



UNIVERSITAT DE
BARCELONA

Carbazole-Based Materials for Organic Thin-Film Transistors and Organic Light-Emitting Diodes

Marta Reig Canyelles

ADVERTIMENT. La consulta d'aquesta tesi queda condicionada a l'acceptació de les següents condicions d'ús: La difusió d'aquesta tesi per mitjà del servei TDX (www.tdx.cat) i a través del Dipòsit Digital de la UB (diposit.ub.edu) ha estat autoritzada pels titulars dels drets de propietat intel·lectual únicament per a usos privats emmarcats en activitats d'investigació i docència. No s'autoritza la seva reproducció amb finalitats de lucre ni la seva difusió i posada a disposició des d'un lloc aliè al servei TDX ni al Dipòsit Digital de la UB. No s'autoritza la presentació del seu contingut en una finestra o marc aliè a TDX o al Dipòsit Digital de la UB (framing). Aquesta reserva de drets afecta tant al resum de presentació de la tesi com als seus continguts. En la utilització o cita de parts de la tesi és obligat indicar el nom de la persona autora.

ADVERTENCIA. La consulta de esta tesis queda condicionada a la aceptación de las siguientes condiciones de uso: La difusión de esta tesis por medio del servicio TDR (www.tdx.cat) y a través del Repositorio Digital de la UB (diposit.ub.edu) ha sido autorizada por los titulares de los derechos de propiedad intelectual únicamente para usos privados enmarcados en actividades de investigación y docencia. No se autoriza su reproducción con finalidades de lucro ni su difusión y puesta a disposición desde un sitio ajeno al servicio TDR o al Repositorio Digital de la UB. No se autoriza la presentación de su contenido en una ventana o marco ajeno a TDR o al Repositorio Digital de la UB (framing). Esta reserva de derechos afecta tanto al resumen de presentación de la tesis como a sus contenidos. En la utilización o cita de partes de la tesis es obligado indicar el nombre de la persona autora.

WARNING. On having consulted this thesis you're accepting the following use conditions: Spreading this thesis by the TDX (www.tdx.cat) service and by the UB Digital Repository (diposit.ub.edu) has been authorized by the titular of the intellectual property rights only for private uses placed in investigation and teaching activities. Reproduction with lucrative aims is not authorized nor its spreading and availability from a site foreign to the TDX service or to the UB Digital Repository. Introducing its content in a window or frame foreign to the TDX service or to the UB Digital Repository is not authorized (framing). Those rights affect to the presentation summary of the thesis as well as to its contents. In the using or citation of parts of the thesis it's obliged to indicate the name of the author.



UNIVERSITAT DE
BARCELONA

Programa de Doctorat de Química Orgànica

**Carbazole-Based Materials for Organic Thin-Film Transistors
and Organic Light-Emitting Diodes**

Marta Reig Canyelles

Supervised by:

Dra. Dolores Velasco Castrillo

Dept. Química Inorgànica i Orgànica

Secció de Química Orgànica

Facultat de Química

Universitat de Barcelona

A la meva família

Al Víctor

ACKNOWLEDGEMENTS/AGRAÏMENTS

M'agradaria que aquestes línies servissin per expressar el meu agraïment a totes aquelles persones que d'alguna manera o altra han participat en la realització d'aquesta tesi.

En primer lloc, vull agrair a la Dra. Dolors Velasco la possibilitat de realitzar aquesta tesi doctoral sota la seva direcció. Vull donar-li les gràcies per tot l'ajut i suport que m'ha donat en totes les etapes d'aquesta tesi, per la confiança que ha dipositat en mi, així com per totes i cadascuna de les oportunitats que m'ha donat al llarg d'aquests anys.

Agraeixo a tota la gent del Departament de Química Orgànica que d'alguna manera o altra també han col·laborat en la realització d'aquest treball. Agraeixo l'ajut rebut per part de tots els companys del grup que m'han anat acompanyant al llarg d'aquest temps i especialment, vull agrair al Jaume, l'Alba, el Raoul i el Cristian tot el suport que m'han donat, així com les bones estones que també hem compartit.

Moltes gràcies al Dr. Joaquim Puigdollers del grup de Micro i Nanotecnologies (MNT) de la Universitat Politècnica de Catalunya (UPC) per permetre'm realitzar la fabricació i mesura dels OTFTs presentats en aquesta tesi en els seus laboratoris i per la seva tan bona acollida. Li agraeixo tot el seu suport, les seves explicacions, els seus consells i la seva sempre bona disposició per ajudar-me. Vull agrair també l'ajut i el suport rebut per part de l'Albert Marsal, que em va introduir en la fabricació i mesura dels transistors orgànics, així com també del Sergi Galindo i del Guillermo Gerling.

Voldria agrair també al Dr. Lluís Julià de l'Institut de Química Avançada de Catalunya (CSIC) per introduir-me en l'estudi de les propietats dels radicals i de la seva química, així com per tots els seus consells i suport al llarg d'aquest temps.

I would like to thank Dr. Juozas Vidas Grazulevicius from the Department of Polymer Chemistry and Technology at Kaunas University of Technology for giving me the opportunity of working in his laboratories during my two predoctoral stays, as well as for his kind reception. I want to

acknowledge Dr. Dmytro Volyniuk, Dr. Nataliya Kostiv and Dr. Khrystyna Ivaniuk for their assistance on the realization of the measurements during my stay in Lithuania.

I would like to thank Dr. Vyintas Jankauskas from the Department of Solid State Electronics from Vilnius University for his collaboration in the XTOF measurements presented along this thesis, as well for his advices and kind disposition to explain me the technique.

I am very grateful to Dr. Gintautas Bagdziunas at Kaunas University of Technology for his collaboration in the realization of the theoretical calculations presented in this thesis during my stay in Lithuania.

Vull agrair a la Dra. Eugenia Martínez del Centre Tecnològic de Catalunya Eurecat, el Dr. Emilio Palomares i el Werther Cambarau de l'Institut Català d'Investigació Química (ICIQ) per la seva col·laboració i per la possibilitat de realitzar la fabricació i mesures d'OLEDs en els seus laboratoris.

A la Dra. Elisa Vallés i a la Dra. Elvira Gómez per deixar-me realitzar les mesures electroquímiques en el seu laboratori i pel seu assessorament.

A la Dra. Concepción López, pels ànims que m'ha donat sempre i per la col·laboració en diferents projectes durant la realització d'aquesta tesi que m'han permès endinsar-me en altres àmbits.

Per últim, m'agradaria donar les gràcies a tot el personal dels Serveis Científicotècnics de la UB per la seva bona disposició en tot moment i pel seu assessorament. En especial, vull agrair tots els consells i explicacions que tant pacientment m'han brindat la Dra. Mercè Font, el Dr. Josep Maria Bassas i el Dr. Xavier Alcobé de la Unitat de Difracció de Raigs X, així com el Dr. Jordi Díaz de la Unitat de Tècniques Nanomètriques.

CONTENTS

INTRODUCTION	1
OBJECTIVES.....	13
GENERAL PART	19
Part 1. Characterization of organic semiconductors.....	21
1.1. Thermal properties	21
1.2. Optical properties	24
1.3. Electrochemical properties.....	28
Part 2. Charge transport properties in organic semiconductors.....	31
2.1. Charge carrier mobility	31
2.2. Time-of-flight technique	31
2.3. Xerographic time-of-flight technique	33
Part 3. Electronic and optoelectronic devices.....	34
3.1. Organic Thin-Film Transistors (OTFTs).....	34
3.2. Organic Light-Emitting Diodes (OLEDs).....	38
Part 4. Surface characterization techniques	43
4.1. X-ray diffraction	43
4.2. Atomic Force Microscopy	45
RESULTS AND DISCUSSION.....	47
<u>Chapter 1.</u> Blue-emitting materials for organic light-emitting diodes	49
1.1. Introduction	51
1.2. Monocarbazole derivatives containing thienyl and phenyl groups as blue emitters	52
1.2.1. Synthesis	53
1.2.2. Crystal structures	56
1.2.3. Characterization of the organic semiconductors.....	58
1.2.4. Charge transport properties	65
1.2.5. Organic Light-Emitting Diodes	66

1.3. Tricarbazole derivatives containing ethynylene linkers as deep-blue emitters	69
1.3.1. Synthesis.....	70
1.3.2. Characterization of the organic semiconductors	72
1.3.3. Charge transport properties	75
1.3.4. Organic Light-Emitting Diodes.....	75
1.4. A bicarbazole derivative as a deep-blue emitter	78
1.4.1. Synthesis.....	78
1.4.2. Characterization of the organic semiconductor and future work	79
1.5. Conclusions	81
<u>Chapter 2.</u> Stable radicals with ambipolar charge transport.....	83
2.1. Introduction	85
2.2. Synthesis	87
2.3. Characterization of the organic semiconductors.....	89
2.4. Charge transport properties	95
2.5. Xerographic single-layered photoreceptors	98
2.6. Conclusions	99
<u>Chapter 3.</u> n-Type and ambipolar materials: the role of the tricyanovinyl group	101
3.1. Introduction	103
3.2. <i>Ortho</i> -methoxy substituted carbazole derivatives	104
3.2.1. Synthesis.....	104
3.2.2. Crystal structures	105
3.2.3. Characterization of the organic semiconductors	106
3.2.4. Charge transport properties	111
3.3. A series of tricyanovinyl derivatives with different <i>N</i> -alkyl chain length	117
3.3.1. Synthesis.....	117
3.3.2. Characterization of the organic semiconductors	118
3.3.3. Single-crystal X-ray analyses	122
3.3.3. Organic Thin-Film Transistors.....	125
3.3.4. Molecular order and morphology of the thin films	126

3.4. Extension of the π -conjugated carbazole system by introduction of the thienyl unit	129
3.4.1. Synthesis	130
3.4.2. Characterization of the organic semiconductors.....	131
3.4.3. Organic Thin-Film Transistors	134
3.5. Conclusions	136
<u>Chapter 4. Role of the molecular order in π-extended carbazole derivatives for p-type OTFTs.....</u>	<u>139</u>
4.1. Introduction	141
4.2. Carbazole derivatives with extended π -conjugated systems: the cases of indolo[3,2- <i>b</i>]carbazole and triindole semiconductors	143
4.2.1. Synthesis	143
4.2.2. Crystal structures	145
4.2.2. Characterization of the organic semiconductors.....	147
4.2.3. Organic Thin-Film Transistors	150
4.2.4. Molecular order and morphology of the thin films	153
4.3. Tricyanovinyl-substituted triindole derivatives	159
4.3.1. Synthesis	159
4.3.2. Characterization of the organic semiconductors.....	160
4.3.3. Organic Thin-Film Transistors	162
4.4. Conclusions	164
CONCLUSIONS	167
REFERENCES	171
EXPERIMENTAL PART	183
1. Materials, solvents and reagents	185
2. Instrumentation and methods	185
3. Synthetic procedures and compound characterization data	197
RESUM.....	233
LIST OF PUBLICATIONS	261
APPENDIX A.....	269
APPENDIX B	CD (back cover)

ABBREVIATIONS AND SYMBOLS

A	acceptor
A	absorbance
AFM	atomic force microscopy
Alq ₃	tris-(8-hydroxyquinoline)aluminum
ATR	attenuated total reflectance
BPhen	bathophenanthroline
<i>c</i>	concentration
CB	chlorobenzene
Cbz	carbazole
Cbz-TTM	[4-(<i>N</i> -carbazolyl)-2,6-dichlorophenyl]bis(2,4,6-trichlorophenyl)methyl radical
CI	chemical ionization
CIE	<i>Commission Internationale de l'Eclairage</i>
C _{ox}	capacitance per unit area of the dielectric
CV	cyclic voltammetry
D	donor
D	drain electrode
d	doublet
<i>d</i>	distance
<i>d</i>	thickness
DCM	dichloromethane
dd	doublet of doublets
DDQ	2,3-dichloro-5,6-dicyano- <i>p</i> -benzoquinone
DFT	density functional theory
<i>d</i> _{hkl}	interplanar spacing
DMF	<i>N,N</i> -dimethylformamide
DMSO	dimethylsulfoxide
dp ^{ph}	2,2-diphenyl-1-picrylhydrazyl radical
DSC	differential scanning calorimetry
<i>E</i>	electric field

E_{ox}^0	oxidation standard potential
E_{red}^0	reduction standard potential
EA	electron affinity
EBU	European Broadcast Union
E_{gap}	HOMO/LUMO energy gap
EL	electroluminescence
E_{onset}	onset potential
E_{pa}	anodic peak potential
E_{pc}	cathodic peak potential
EPR	electron paramagnetic resonance
EQE	external quantum efficiency
ESI	electrospray ionization
ETL	electron-transporting layer
F	electric field
Fc	ferrocene
FT-IR	Fourier-transformed infrared
G	gate electrode
g	g factor
GIXRD	grazing incidence X-ray diffraction
H	coupling integral
hfc	hyperfine coupling
HOMO	highest occupied molecular orbital
ΔH_{pp}	peak to peak line width
HRMS	high resolution mass spectrometry
HTL	hole-transporting layer
IC	internal conversion
ICT	intramolecular charge transfer
I_{D}	drain-source current
IP	ionization potential
ISC	intersystem crossing
ITO	indium tin oxide
J	coupling constant
J	current density
k_{B}	Boltzmann's constant
L	length

<i>L</i>	luminance
<i>l</i>	absorption path length
LE	locally excited
LUMO	lowest unoccupied molecular orbital
<i>m</i>	medium
<i>m</i>	multiplet
MS	mass spectrometry
<i>n</i>	refractive index
NBS	<i>N</i> -bromosuccinimide
NMR	nuclear magnetic resonance
NTSC	National Television System Committee
OLED	organic light-emitting diode
ORTEP	oak ridge thermal ellipsoid plot
OTFT	organic thin-film transistor
OTS	octadecyltrichlorosilane
<i>P</i>	polarization energy
PCZ	bisphenol Z polycarbonate
PEDOT:PSS	poly(3,4-ethylenedioxythiophene)-poly(styrenesulfonate)
PES	potential energy surface
p_i	probability of charge migration
PL	photoluminescence
ppm	parts per million
PS	polystyrene
<i>q</i>	quadruplet
QY	fluorescence quantum yield
RISC	reverse intersystem crossing
rpm	revolutions per minute
RT	room temperature
<i>S</i>	source electrode
<i>s</i>	strong
S_0	singlet ground state
S_1	singlet first excited state
SAM	self assembled monolayer
SCLC	space charge limited current
SOMO	singly occupied molecular orbital
<i>t</i>	triplet

T_1	triplet first excited state
TADF	thermally activated delayed fluorescence
TBAH	tetrabutylammonium hydroxide
TBAP	tetrabutylammonium perchlorate
TBAPF ₆	tetrabutylammonium hexafluorophosphate
T_c	crystallization temperature
TCNE	tetracyanoethylene
T_d	decomposition temperature
TD-DFT	time-dependent density functional theory
T_g	glass transition temperature
TGA	thermogravimetric analysis
THF	tetrahydrofuran
T_m	melting point
TOF	time of flight
TPBi	2,2',2''-(1,3,5-benzinetriyl)-tris(1-phenyl-1- <i>H</i> -benzimidazole)
t_t	transient time
TTA	triplet-triplet annihilation
TTM	tris(2,4,6-trichlorophenyl)methyl radical
UV	ultraviolet
V_D	drain voltage
V_G	gate voltage
V_t	turn on voltage
V_{th}	threshold voltage
W	width
w	weak
XRD	X-ray diffraction
XTOF	xerographic time of flight
α	field dependence parameter
α	isotropic polarizability
δ	chemical shift
ε	molar absorption coefficient
ε	permittivity
η_c	current efficiency
η_{ext}	external quantum efficiency
η_{int}	internal quantum efficiency
η_{out}	light out-coupling efficiency

η_P	power efficiency
θ	incident angle
λ	reorganization energy
λ	wavelength
$\lambda_{\text{abs,max}}$	wavelength of maximum absorption
$\lambda_{\text{em,max}}$	wavelength of maximum emission
λ_{exc}	excitation wavelength
μ	charge carrier mobility
μ_0	zero-field mobility
μ_e	electron mobility
μ_h	hole mobility
v	drift velocity of the charge carriers
ν	wavenumber
ρ	charge balance of injected holes and electrons
Σ	positional disorder
ϕ	efficiency of radiative exciton production
Φ_f	fluorescence quantum yield



by LG^[1]

INTRODUCTION

INTRODUCTION

The research and development of molecular materials for electronics began during the end of the last century. In 1977, A. J. Heeger, A. G. MacDiarmid and H. Shirakawa discovered that the electrical conductivity of polyacetylene films could be increased by doping with halogens.^[2] For the discovery and development of conductive polymers, they were awarded with the Nobel Prize in Chemistry in 2000.^[3,4] Taking into account that hitherto polymers were considered as insulating materials in the electronics industry, this discovery is often considered as the starting point of the field of organic electronics.

In the last years there has been an important effort in the preparation of new organic semiconductors for its application in electronic and optoelectronic devices. Specifically, the development of novel organic semiconductors with effective charge transport capability is an attractive topic in the field of organic electronics, for many applications such as organic thin-film transistors (OTFTs), organic light-emitting diodes (OLEDs) and organic solar cells, among others.^[5-8] Compared to inorganic materials, the use of organic semiconductors is attractive because these materials offer many advantages, such as low cost and capability of forming thin films, which enable the fabrication of large-area and flexible devices. Organic semiconductors include both small molecules and polymers. Small molecules have advantages such as easier synthetic procedures, purification methods and characterization due to their small size and well defined structure.^[9] In addition, their optical and electronic properties can be easily tuned by means of molecular design.

Molecular materials used in organic electronics consist of π -conjugated systems. Conjugated materials are constituted of alternating single and double carbon-carbon bonds. This molecular structure gives rise to the overlap of the π orbitals, which allows the π -electrons to be delocalized over the molecule. It should be considered that organic materials used as active layers in organic-based devices are involved in different processes, such as the introduction of charge carriers into the system, charge transport within the active materials, and collection of charges. According to the nature of the charge carriers, organic semiconductors can be classified into hole-transporting (p-type) or electron-transporting (n-type) materials.

When charge carriers are induced in the organic semiconductor film, that is charges are placed on conjugated molecules, they are rapidly delocalized over the π -orbital system of the corresponding molecules. The delocalization leads not only to a fast conduction within the molecule, but also facilitates the charge transport between molecules. Hence, the intermolecular charge transport is favoured as the strongest is the orbital overlap between neighbouring molecules.^[10]

Charge transport can be explained in terms of the band model in the case of inorganic semiconductors, in which they form energy band structures: the valence and the conduction bands. In contrast, this model is not useful for organic materials, which show weaker intermolecular interactions. To describe the charge transport in organic disordered systems, the hopping model has been developed.^[9] In this model, the charge carriers, *i.e.* holes and electrons, are related to the cation and anion radicals of the species, respectively. In the case of hole transport, electrons are sequentially transferred from a neutral molecule to a cation radical through the highest occupied molecular orbital (HOMO), whereas in the case of electron transport, electrons are sequentially transferred from an anion radical to a neutral molecule through the lowest unoccupied molecular orbital (LUMO).

Thus, the conjugated π -electron system is the responsible for the inherent electronic and optoelectronic properties of the organic semiconductors, which can be easily tuned by the attachment of electron-donating or electron-withdrawing groups. In addition, the introduction of side chains induce solubility and impacts on the film-forming properties of the organic semiconductor. Hence, the chemical nature of the organic semiconductor determines the HOMO and LUMO energy levels, the bandgap (energy difference between the HOMO and the LUMO energy levels), the solubility and the intermolecular interactions, being the latter the responsible of the molecular packing in the solid state. In view of this, when designing new suitable organic compounds for molecular electronics, the selection of an appropriate core structure is a significant aspect to take into account in order to achieve enhanced device performance.^[11] Besides, it should be pointed that just as important as the selection of an appropriate core structure is the processing of the materials, the device design and the control of the film morphology.

This thesis deals with the preparation and characterization of novel organic semiconductors for OTFTs and OLEDs. A brief overview of the current state of organic semiconductors as charge-transporting layers in OTFTs and as emitting layers in OLEDs, together with the basic strategies for

their molecular design, are given below. The different OTFT and OLED device architectures, device operation and characterization will be explained in the General Part.

- **Organic Thin-Film Transistors**

OTFTs are electronic devices that amplify and switch electrical signals. Currently, OTFTs are a key component of organic electronic circuits and are considered for applications in radio frequency identification tags, electronic paper, OLED displays and sensor devices, among others.^[12] In addition, they can be also used as a tool to determine the electrical characteristics of organic semiconductors. A high OTFT device performance implies high charge carrier mobility (μ), large on/off current ratio, low operating voltage and air stability.

The first OTFT device was fabricated in 1986 by A. Tsumura *et al.* by using an electrochemically prepared polythiophene thin film as the semiconducting layer.^[13] The performance of OTFTs has improved considerably over the last decades, achieving charge carrier mobilities comparable to that of amorphous silicon with mobilities of $0.1\text{--}1\text{ cm}^2\text{ V}^{-1}\text{ s}^{-1}$, and in some cases approaching to that of crystalline silicon with mobilities higher than $10\text{ cm}^2\text{ V}^{-1}\text{ s}^{-1}$.^[11] In terms of charge carrier mobility and air stability, the development and performance of p-type semiconducting materials has been higher relative to their n-type or their ambipolar counterparts, which show both hole and electron conduction. However, n-type and ambipolar semiconductors are also required as components in ambipolar transistors and complementary circuits.

As it was mentioned above, efficient charge transport in small molecules is related to strong intermolecular interactions. Therefore, in terms of molecular design, planar and large π -conjugated structures with extended π - π stacking interactions are required for efficient charge transport. The chemical structure of the organic materials determine not only the electronic properties, but also the stability and durability of the fabricated devices under ambient conditions. Many OTFTs show device degradation when operating in air, implying that the device should be encapsulated, which constitutes an undesirable extra processing step, increasing the final cost of the device production. In order to overcome this trouble, materials with high air stability are actually sought. For p-type semiconductors, this implies the obtaining of new compounds with low-lying HOMO levels, or high ionization potential (IP), in order to get stable materials against oxidative doping by atmospheric oxygen.^[14]

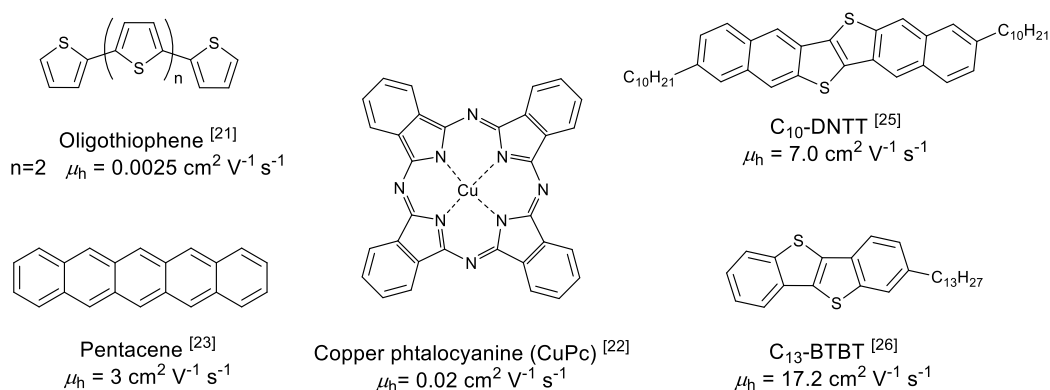
For the design of new n-type organic semiconductors low LUMO energy levels, or high electron affinities (EA), to facilitate charge injection and ambient stability are required. The push-pull electronic structure generates low band gap materials with the possibility to control the ionization potential and the electron affinity. Electron affinities of n-type materials higher or close to 4.0 eV are necessary to achieve acceptable charge carrier injection and air stability.^[10,15] The instability of n-type OTFT devices under ambient conditions arises from the electron charge carrier trapping by H₂O or O₂.^[16] Device air stability can be also favoured by promoting a dense molecular packing in the thin film to resist the penetration of these species.^[17] In this way, the thin film morphology should be taken into account, since thin films with high crystallinity, large grain size and low density of grain boundaries also favour the stability of the device operating under ambient conditions.^[15]

Ambipolar OTFTs can be fabricated by different ways. Their active layer can be a combination of electron- and hole-transporting semiconductors, prepared as a bilayer or as a blend. However, single-component transistors show the advantage of working with only one layer. For ambipolar single-layer OTFT devices, semiconducting materials with ionization potential values higher than 5.0 eV and electron affinity values higher or close to 4.0 eV, as well as bandgaps smaller than 1.6 eV, are required in order to achieve stable hole and electron transport and avoid charge injection barriers.^[18]

Crystalline films are expected to display higher charge carrier mobilities than amorphous films or randomly oriented crystalline films.^[10] Whereas highly oriented crystalline films can be prepared by the vacuum evaporation technique, it is difficult to achieve comparable crystallinity by means of solution-processed methods such as spin coating, which usually gives films with amorphous domains. Huge research efforts are currently focused to develop strategies to afford highly oriented crystalline films from solution-processed techniques. Specifically, the introduction of flexible side chains on the π -conjugated materials to favour intermolecular interactions has recently attracted more and more attention as a strategy to control the molecular packing in the solid state and the film morphology.^[19,20]

Scheme 1 shows some representative examples of p-type organic semiconductors as active layers in vacuum-deposited OTFTs. Some of the most studied p-type organic semiconductors for OTFTs are oligomer-based materials, such as oligothiophenes,^[21] and macrocyclic compounds, such as copper phthalocyanine (CuPc).^[22] The search of high mobility organic semiconductors yielded

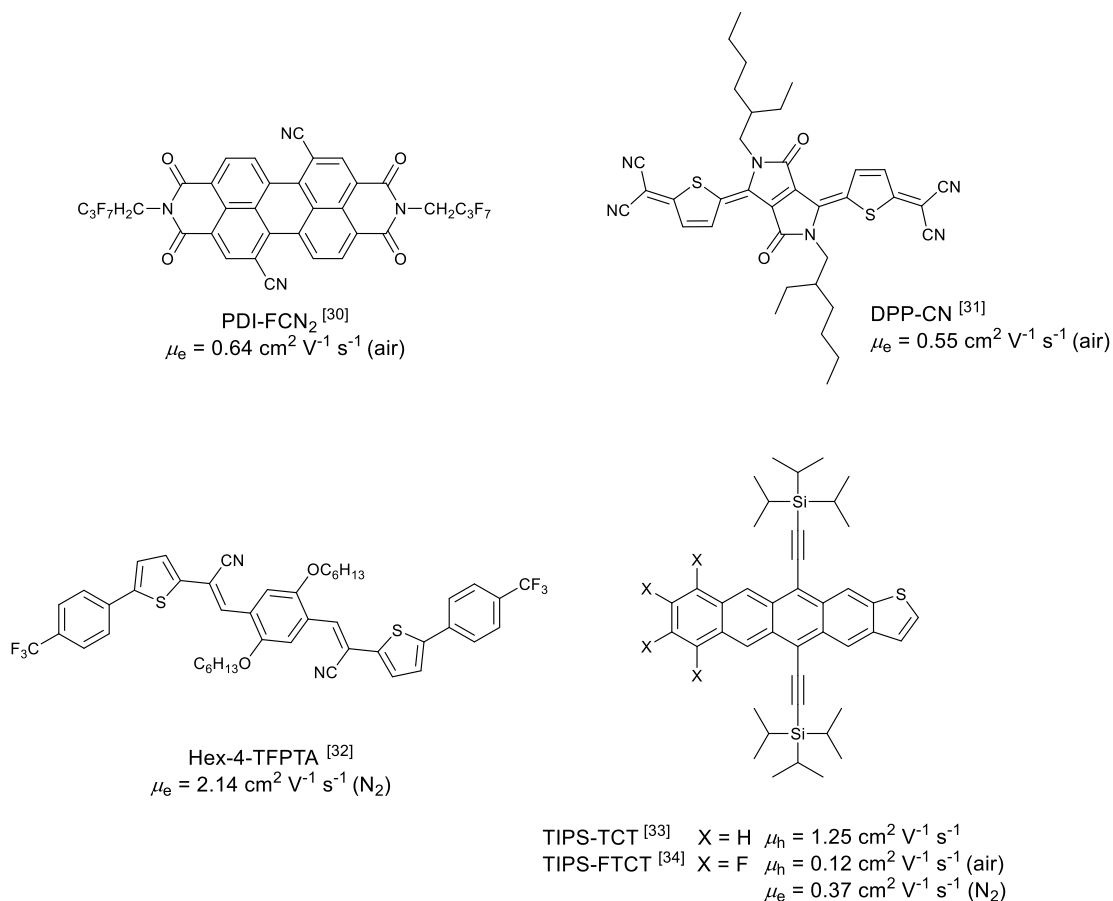
pentacene as one of the most promising p-type materials, achieving high hole mobilities of $3 \text{ cm}^2 \text{ V}^{-1} \text{ s}^{-1}$ for vacuum-deposited OTFTs.^[23] Nevertheless, pentacene-based devices present several drawbacks for practical applications due to a lack of air stability and fast device degradation.^[24] More recently, some examples have been reported in the literature showing high OTFT performance with superior hole mobilities than $0.1\text{--}1 \text{ cm}^2 \text{ V}^{-1} \text{ s}^{-1}$.^[11,25] Among them, it can be highlighted the use of 2-tridecyl[1]benzothieno[3,2-*b*][1]-benzothiophene (C_{13} -BTBT) that afforded a high hole mobility up to $17.2 \text{ cm}^2 \text{ V}^{-1} \text{ s}^{-1}$.^[26]



Scheme 1. Examples of π -conjugated small molecules employed as p-type semiconducting layers in vacuum-deposited OTFT devices. (μ_h : hole mobility).

The introduction of electron-withdrawing groups on the π -conjugated core, such as the case of fluoro atoms, usually leads to a transition from p-type to n-type semiconductors.^[27,28] Copper hexadecafluorophthalocyanine (F_{16}CuPc) is the first example of n-type semiconducting material with high electron mobility ($\mu_e = 0.03 \text{ cm}^2 \text{ V}^{-1} \text{ s}^{-1}$) that showed stability under ambient conditions in vacuum-deposited OTFTs.^[29] Scheme 2 displays some representative examples of n-type materials for OTFTs. π -Conjugated molecules with electron-withdrawing cyano groups have been also used as electron-transporting materials. For example, air-stable OTFTs based on perylene diimide PDI- FCN_2 afforded high electron mobilities up to $0.64 \text{ cm}^2 \text{ V}^{-1} \text{ s}^{-1}$.^[30] More recently, the diketopyrrolopyrrole-containing quinoidal derivative with dicyanomethylene groups (DPP-CN) showed an electron mobility as high as $0.55 \text{ cm}^2 \text{ V}^{-1} \text{ s}^{-1}$ in air.^[31] The combination of cyanovinyl and trifluoromethyl groups as in the case of derivative Hex-4-TFPTA, yielded a high electron mobility of $2.14 \text{ cm}^2 \text{ V}^{-1} \text{ s}^{-1}$ for OTFT devices, but tested under nitrogen atmosphere.^[32] An example of an ambipolar semiconducting material based on the π -conjugated tetraceno[2,3-*b*]thiophene core (TCT) is also shown in Scheme 2. Whereas the trialkylsilylethynyl-functionalized TCT material shows

only hole mobility of $1.25 \text{ cm}^2 \text{ V}^{-1} \text{ s}^{-1}$ in p-channel OTFTs,^[33] the TIPS-TCT, resulting from the partial fluorination of the TCT core, shows hole and electron mobilities up to 0.12 and $0.37 \text{ cm}^2 \text{ V}^{-1} \text{ s}^{-1}$ measured in air and nitrogen, respectively.^[34]



Scheme 2. Examples of n-type and ambipolar semiconductors for vacuum-deposited OTFTs. The experimental conditions of the OTFT device measurements are displayed in parenthesis. (μ_e : electron mobility, μ_h : hole mobility).

• Organic Light-Emitting Diodes

Electroluminescence (EL) is the basic principle of OLEDs and consists of a physical phenomenon in which materials emit light in response to an applied electric field. In the 1950s, Bernanose *et al.* observed for the first time this phenomenon in organic materials by applying a high-voltage alternating current to thin films of gonacrine and acridine orange E adsorbed upon a sheet of Cellophane.^[35] Later, in the 1980s, Tang and VanSlyke from the Research Laboratories of Eastman Kodak Company made a significant progress in the field of OLEDs, by preparing the first efficient double-layered OLED device by vacuum evaporation using an aromatic diamine as hole-

transporting layer and tris-(8-hydroxyquinoline)aluminum (Alq_3) as electron-transporting and emitting layer, which showed a high luminance of $\sim 10^3 \text{ cd m}^{-2}$.^[36] Since then, OLEDs have evolved into commercial applications as flat-panel displays and artificial sources of solid-state lighting. Figure 1 collects a series of examples of commercially available panels and products based on the OLED technology. However, further improvement of power efficiency, colour purity and longer operational lifetimes are still required to produce efficient industrial devices.

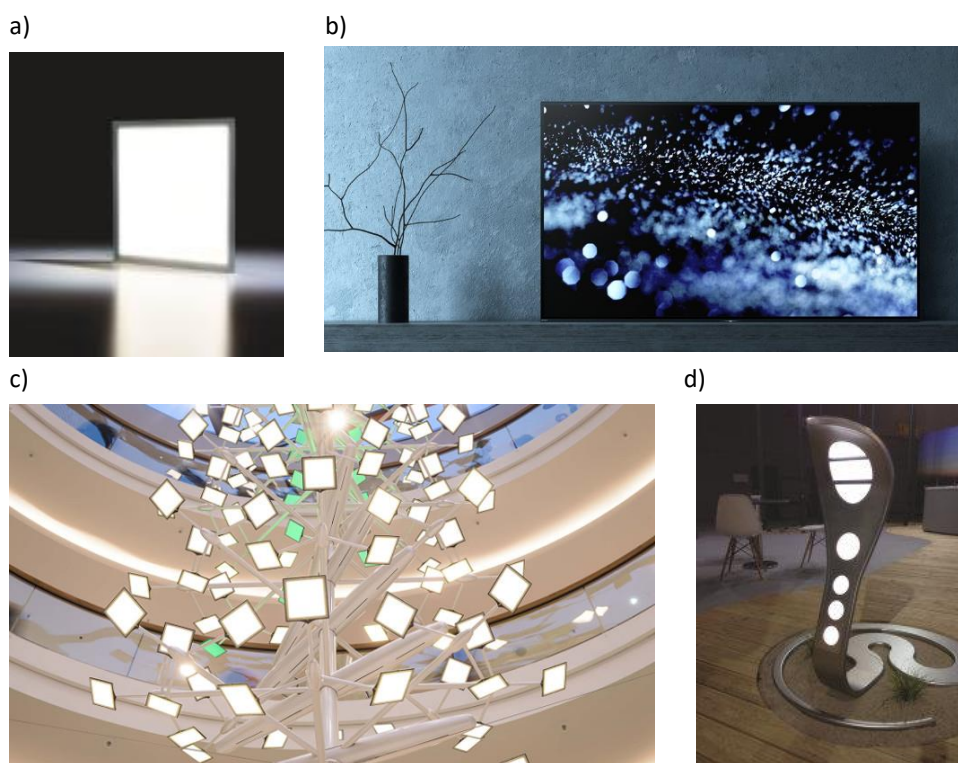


Figure 1. Representative example of commercial OLEDs panels and products: a) Second generation of ORBEOS panel, by OSRAM.^[37] b) BRAVIA OLED TV, by SONY.^[38] c) “Lumiblade” OLEDs, by Philips.^[39] d) OLED design luminaire, “Cobra”, by OSRAM.^[40]

The development of OLEDs that emit in the blue region has attracted intensive research, since these materials can be applied in combination to green and red colour emitters, according to the primary-colour theory, in full-colour displays and white OLEDs (WOLEDs).^[41] Taking into account the inferior performance of blue OLEDs in front of the red and green ones, many research efforts are still currently put forward to the development of new luminescent dyes with blue emission.^[42] Indeed, proper operation of OLED devices with blue-emitting materials is subjected to its intrinsic large band gaps that difficult the injection of charges into the emitting layer, and the lower sensitivity of the human eye in this part of the electromagnetic spectrum, which decreases the

efficacy.^[43] In addition, blue OLEDs are more prone to degradation showing poor long-term stability and shorter lifetimes.^[44]

Blue fluorescent OLEDs can be fabricated by doping with blue fluorescent dyes a host matrix in order to suppress the fluorescence quenching or by using non-doped blue fluorescent emitters.^[43] Although the host-guest system can produce high efficiency, the intrinsic phase separation could deteriorate the device performance during operation. In addition, a strict control of the doping concentration is required for optimal device performance. For these reasons, the use of non-doped emitters is more convenient for practical applications.

The emission colour of the OLED devices can be described by the *Commission Internationale de l'Éclairage* (CIE) chromaticity coordinates (x, y) , which locate the emission colour of the electroluminescent spectrum in the CIE 1931 chromaticity diagram (Figure 2). Considering the application of OLEDs as full-colour displays, the standard CIE coordinates of the blue colour are $(x = 0.14, y = 0.08)$ or $(x = 0.15, y = 0.06)$ as specified by the National Television System Committee (NTSC) and the European Broadcast Union (EBU), respectively.^[44] Thus, the development of efficient OLEDs that emit in the blue region, in particular in the deep-blue region (defined by CIE y value less than 0.1), is still required in order to give rise to OLED devices with high power efficiencies and longer operational lifetimes.

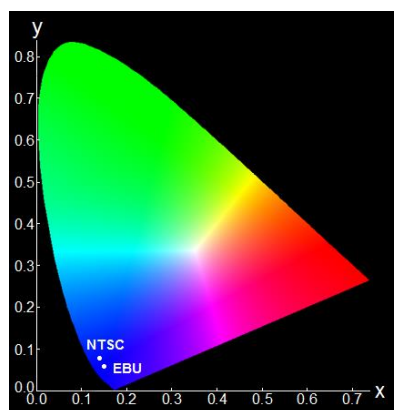
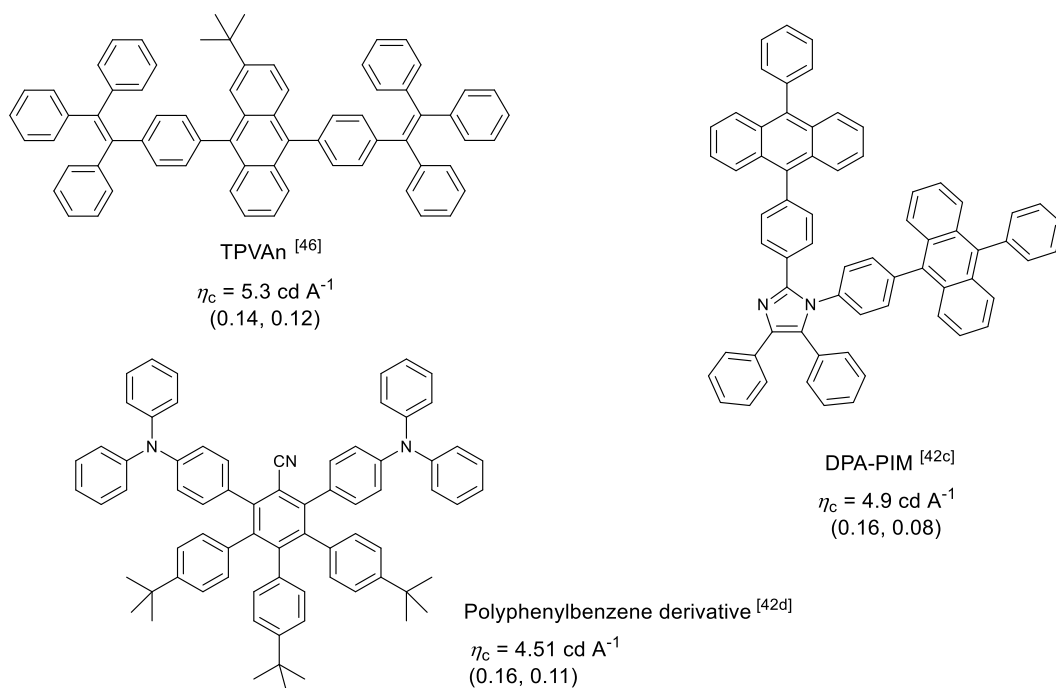


Figure 2. CIE 1931 chromaticity diagram indicating the position of the standard blue coordinates (x, y) specified by the NTSC and the EBU.

For the successful operation of OLEDs, an appropriate π -conjugated core with high emission efficiencies, good thermal stability and capability to form continuous and morphologically stable

films with the absence of grain boundaries are usually sought. Therefore, amorphous molecular materials with glass transition temperatures (T_g) above room temperature are required.^[45]

In general, photoluminescence quantum yields of emitting materials are high in solution, but decrease considerably in the solid state due to aggregation. In order to reduce the fluorescence quenching in the solid state, one strategy consists on the preparation of non-planar molecular structures by introduction of rigid and bulky substituents that hinder the intermolecular interactions in the solid state. Scheme 3 displays some representative examples of deep-blue emitters. For example, the use of tetraphenylethylene as a bulky substituent in the anthracene derivative TPVAn afforded a significant increase of the photoluminescence quantum yield from solution (0.06) to the solid state (0.89).^[46] Some recent examples of non-doped deep-blue OLEDs based on anthracene, polyphenylbenzene or fluorene cores, among others, have reached high device performances with maximum current efficiencies (η_c) around 2–5 cd A^{-1} and external quantum efficiencies (EQE) up to ~6%.^[42b–d] The current efficiency and the CIE values of the OLED devices based on the corresponding emitters are also indicated in Scheme 3.



Scheme 3. Examples of derivatives used as deep-blue emitters in OLEDs. (η_c : current efficiency, CIE values are shown in parenthesis).



by BASF^[47]

OBJECTIVES

OBJECTIVES

The aim of this thesis is the preparation and characterization of novel organic semiconductors based on the carbazole heterocycle for electronic and optoelectronic devices. The carbazole moiety possess a series of advantages relative to other building blocks of organic electroactive materials, for instance low cost and easy availability, high thermal stability, easy chemical functionalization and film-forming capability.^[48] Moreover, it should be highlighted the high fluorescence quantum yields and excellent hole-transporting properties associated to its electron-donating ability, which make of carbazole-based compounds promising candidates for OLEDs^[49] and OTFTs.^[50]

This work involves in the first instance the molecular design, synthesis and characterization of the organic materials, followed by the study of the thermal, optical, electrochemical and charge-transporting properties, and concludes with the application of the prepared materials as active layers in OLEDs and OTFTs. The main objectives and organization of this work are described in more detail below.

The first part of this thesis (Chapter 1) deals with the preparation and characterization of a series of carbazole-based blue emitters for their application as emitting layers in non-doped OLEDs. In order to obtain blue-emitting materials with hole-transporting properties, it was considered to extend the π -conjugated carbazole system by introducing donor moieties at 3,6 position of the carbazole core. Besides, taking into account that π -conjugated linkers can significantly modulate the conjugation connectivity of the molecules and the photophysical properties,^[51] the effect of the insertion of a triple bond as a π -conjugated linker between the carbazole and the donor units was also analysed. As a last structural variation and with the purpose of obtaining amorphous molecular materials, the introduction of bulky substituents on the nitrogen atom of the carbazole core was considered. A study of the structure-properties relationship of this series of compounds afforded the most feasible candidates for their study as blue emitting layers in non-doped OLEDs. To gain insight into the structure-properties relationship of this series of carbazole derivatives, solid state structures were analysed by X-ray diffraction (XRD) and density functional theory (DFT) calculations were performed.

The main objective of Chapter 2 and 3 is the development of new n-type and ambipolar semiconducting materials. For the design of n-type and ambipolar organic materials, high electron affinities to facilitate electron injection and ambient stability are required. For this purpose, the strategy followed in this thesis consisted on the modification of the characteristic hole-transporting behaviour of the electron-donating carbazole moiety by the attachment of electron-withdrawing substituents in order to downshift the LUMO levels to increase the electron affinity, resulting in derivatives with n-channel or ambipolar conduction.

Chapter 2 is based on a previous work developed in our research group, in which the introduction of the carbazole or indole moiety into the stable electron acceptor tris(2,4,6-trichlorophenyl)methyl radical (TTM) fragment afforded charge-transfer radical adducts that exhibited ambipolar charge transport properties, with hole and electron mobilities around $10^{-4} - 10^{-3} \text{ cm}^2 \text{ V}^{-1} \text{ s}^{-1}$.^[52] With the objective to develop new derivatives with enhanced and better balanced hole and electron mobilities, the preparation and characterization of a series of new radical adducts derived from the already known parent compound [4-(*N*-carbazolyl)-2,6-dichlorophenyl]bis(2,4,6-trichlorophenyl)methyl radical (Cbz-TTM) have been considered. In this new series of radicals, the substitution patterns of the carbazole core have been varied in order to modulate the push-pull character of the resulting materials and study the effect on the charge transport properties by the xerographic time-of-flight (XTOF) technique. In addition, the prepared radicals have been studied as active layers in xerographic single-layered photoreceptors.

Chapter 3 is focused on the modification of the characteristic hole-transporting properties of the carbazole derivatives by the introduction of the strong electron-withdrawing tricyanovinyl group affording a push-pull system with high electron affinity. Different approaches have been considered to develop three different series of push-pull derivatives. In the first series of compounds, the substitution patterns of the carbazole core have been varied in order to modulate the electron-donating character of the carbazole moiety. The second series consists of tricyanovinyl-substituted carbazole-based materials that differ only in the length of the *N*-alkyl chain of the carbazole moiety. In the last series of tricyanovinyl derivatives, it has been considered to extend the π -conjugated system by introduction of the thienyl heterocycle between the carbazole moiety and the tricyanovinyl group. The effect of the substitution patterns of the carbazole core in terms of thermal, optical, electrochemical and charge-transporting properties has been analysed. In addition, the relationship between the molecular structure of the organic

semiconductors and the charge mobilities determined by the TOF technique and by the fabrication and measurement of OTFTs was examined by X-ray diffraction studies and theoretical calculations.

Even though p-type materials have reached a more successful development than the n-type and ambipolar counterparts, new types of π -conjugated materials for p-type OTFTs are still required in order to achieve enhanced device performance. With this idea in mind, Chapter 4 has been focused on a series of p-type carbazole-based materials, in which the extension of the π -conjugated core was progressively varied in order to study the effect on the charge-transporting properties. A series of compounds based on the carbazole, the 3,3'-bicarbazole, the indolo[3,2-*b*]carbazole and the triindole cores, were synthesized and characterized. The indolo[3,2-*b*]carbazole and triindole cores show larger molecular structures than carbazole and 3,3'-bicarbazole. Accordingly, a higher molecular order could be expected from them, and therefore, better charge carrier transport. In addition, the effect of the *N*-alkyl chain length of the triindole moiety on the charge-transporting properties has been also analysed. Chapter 4 deals with not only the OTFT performance of this series of carbazole containing compounds, but also the determination of the molecular packing in the organic semiconductor layer of the devices by means of X-ray diffraction studies. Therefore, the aim of this chapter is to determine the correlation of the device performance with the molecular order in the semiconducting thin films as a function of the π -conjugated core design of the organic semiconductors.



GENERAL PART

GENERAL PART

This chapter deals with the basic concepts about the techniques employed for the characterization of organic semiconductors (Part 1) and for the study of their charge-transporting properties (Part 2). Moreover, a brief introduction to OTFTs and OLEDs in terms of device fabrication, operation and characterization is given (Part 3), followed by the description of the techniques employed for the study of the molecular order and morphology of the semiconducting layers of the organic devices (Part 4).

PART 1. Characterization of organic semiconductors

1.1. Thermal properties

The study of the thermal properties of materials consists in measuring their properties as a function of the temperature. The corresponding changes of the properties of the materials observed by increasing the temperature and in an inert atmosphere are named *thermal events*. Thermal events are described by the enthalpy change (ΔH), which quantifies the heat flowing into or out of a solid under constant pressure. Thermogravimetric analysis (TGA) and differential scanning calorimetry (DSC) are two of the most widely used techniques to study the thermal properties of materials.^[53]

- **Thermogravimetric analysis (TGA)**

TGA is commonly used to study the *thermal decomposition* of materials by measuring the change of the absolute amount in weight of a sample with the temperature in a controlled environment. Different properties can be measured from the TGA analysis, such as thermal and oxidative stability of the materials, but also the composition of a sample in the case of multi-component systems or the evaluation of chemical reactions.

In this technique, the weight change of the sample is monitored by a thermobalance, which consists of a microbalance, a furnace, a temperature programmer and a computer. The sample is

heated in the furnace in a controllable environment at a given heating rate, and the microbalance measures the weight change, which in general is able to measure a weight change of $\pm 1 \mu\text{g}$.

Figure 1 displays a typical TGA curve, in which the weight change expressed in percent is plotted *versus* the temperature. The TGA curve shows a one-stage decomposition curve. The decomposition of the sample is characterized by the initial temperature at which a change of the absolute amount in weight is detected (T_i) and the lowest temperature at which the weight change is completed (T_f). The temperature at which decomposition (T_d) starts can be expressed as the onset decomposition temperature, which can be estimated from the intersection point as shown in Figure 1. As an alternative, T_d can be defined as the temperature corresponding to the 5% weight loss.

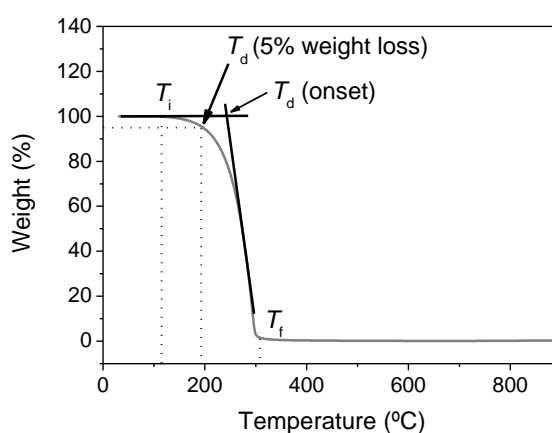


Figure 1. Thermogravimetric curve of 9-methyl-9H-carbazole recorded at a scan rate of $20 \text{ }^\circ\text{C min}^{-1}$ under a nitrogen atmosphere. The initial and final temperature (T_i and T_f), the decomposition temperature (T_d) corresponding to the 5% weight loss and the onset decomposition temperature are indicated.

- **Differential scanning calorimetry (DSC)**

DSC is a widely used technique for studying the phase changes of materials, such as *solid-phase transformation*, *melting* and *glass transition*. Solids that have different equilibrium crystalline phases in different temperature ranges may show solid-phase transformation when heating the sample in an inert atmosphere. Glass transition can be observed in the case of polymeric materials and amorphous molecular materials (or molecular glasses), which are low molar mass compounds with a stable amorphous phase above room temperature. Glass transition consists of the change of a rigid non-crystalline solid in a glass phase to a rubber-like solid. The glassy state can be achieved

by cooling materials from the melt or by solvent evaporation from solution. In some cases, compounds can be isolated directly from the reaction mixtures as amorphous solid materials.^[45]

The instrumentation is similar to that of the TGA technique. A DSC instrument measures the difference of the heat flow between the sample and a reference. For this purpose, the sample is introduced in a furnace, where it can be heated or cooled in a controllable environment. Then, a transducer monitors the changes of the properties of the materials.

Figure 2 displays typical DSC curves for both crystalline and amorphous molecular materials, in which the heat flow (in W g^{-1}) is plotted *versus* the temperature. The endothermic events are indicated as a downward feature, whereas the exothermic events are indicated as an upward feature. In general, DSC curves are recorded over a temperature range by heating and cooling the sample in different cycles with a constant rate. The DSC curve corresponding to the crystalline sample (Figure 2a) shows a melting process during the first heating scan, together with a crystallization process at a lower temperature during the cooling scan. Otherwise, the DSC curve shown in Figure 2b shows a melting process during the first heating scan, but after cooling and heating again, the glass transition is observed, indicating that the glassy state is achieved by cooling the material from the melt.

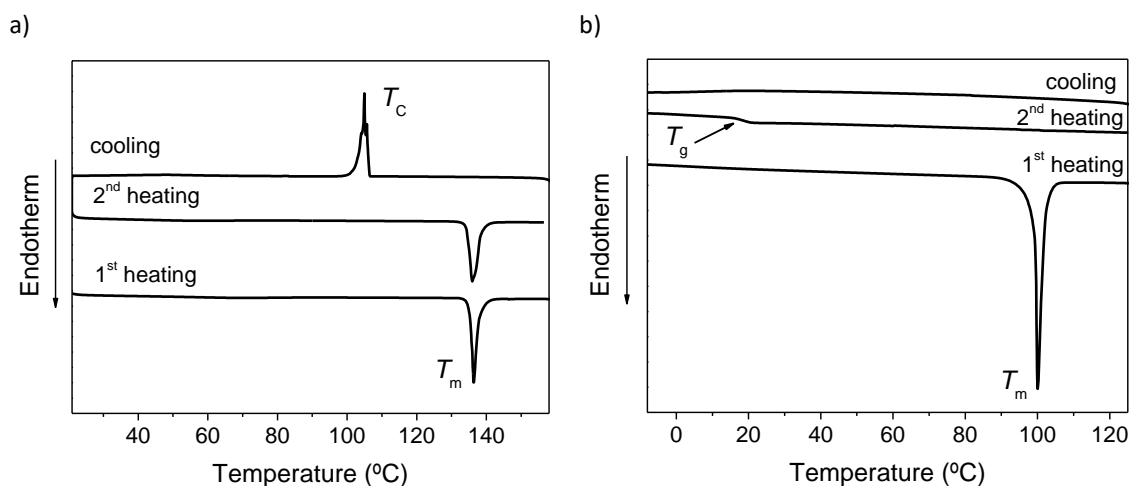


Figure 2. Representative DSC curves of a) crystalline and b) amorphous molecular material recorded at a heating rate of 10 °C min^{-1} under a nitrogen atmosphere. (T_m : melting point, T_c : crystallization temperature and T_g : glass transition temperature).

It should be taken into account that several experimental aspects can influence both TGA and DSC curves, such as the sample mass and dimension, the atmosphere (reactive or nonreactive) and the applied heating rate.

1.2. Optical properties

Jablonski's diagram illustrates the possible processes that occur between the absorption and emission of light (Figure 3). The singlet electronic states are denoted by S_0 for the ground state and S_1 and S_2 for the excited states, whereas the triplet states are named T_1 , T_2 , etc. At each of these electronic energy levels the fluorophores can exist in a number of vibrational levels.

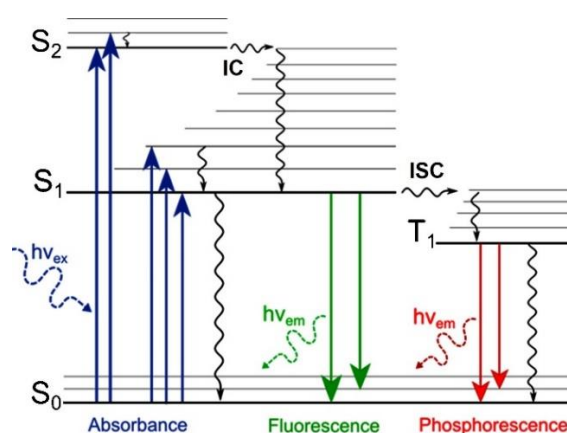


Figure 3. Jablonski's diagram showing the electronic transitions involved during absorption and emission of light.

Some basic concepts about the electronic transitions involved during the absorption and emission of light shown in Figure 3 are given below.^[54]

- **Absorbance**

For a molecule with a closed-shell structure bearing two electrons of opposite spins in a molecular orbital in the ground state, the total spin quantum number ($S = \sum s_i$, where $s_i = +\frac{1}{2}$ or $-\frac{1}{2}$) is equal to zero and the multiplicity of the ground state is equal to 1 ($M = 2S + 1$). When the molecule absorbs a photon of the appropriate energy, one of the electrons is promoted from the orbital of the molecule in its electronic ground state to an unoccupied orbital of higher energy, without altering the initial spin of the molecule. Hence, both ground and excited states are called *singlet states*

(Figure 4a and b). This transition occurs in about 10^{-15} s, which is very quick in comparison to all other processes. Therefore, and according to the Franck-Condon principle, the electronic transition occurs without changes in the positions of the nuclei in the molecular entity and its environment. The $S_0 \rightarrow S_1$ electronic transition can be usually related to the electron promotion from the HOMO to the LUMO, which is energetically favoured. The energy difference between the HOMO and the LUMO, *i.e.* the *optical energy gap*, can be estimated from the onset of the absorption band assigned to the $S_0 \rightarrow S_1$ transition. The extension of the conjugated π -system implies a lower energy gap, that is, the corresponding absorption band will be shifted to longer wavelengths.

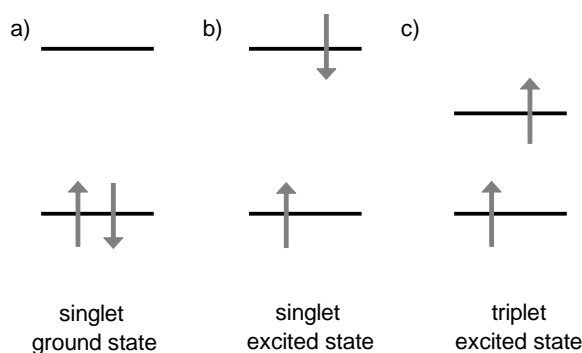


Figure 4. Representation of singlet and triplet states.

The *absorbance* (A) characterizes the efficiency of light absorption by matter at a given wavelength (λ) and can be defined by eqn (1):

$$A(\lambda) = \log \frac{I^0}{I} \quad (1)$$

where I^0 and I are the light intensities of the beams entering and leaving the absorbing medium, respectively. At low concentrations, the absorbance of a sample follows the Lambert-Beer Law (eqn (2)):

$$A(\lambda) = \varepsilon(\lambda)lc \quad (2)$$

where ε is the *molar absorption coefficient* with units $M^{-1} \text{ cm}^{-1}$, when the concentration of the absorbing species (c) is given in molarity (M) and the absorption path length (l) in cm. Deviation of the Lambert-Beer Law can be found in case of light scattering by the sample or aggregation in highly concentrated samples, implying that the measured absorbance does not increase linearly with the concentration.

- **Internal conversion**

After absorption of light, a fluorophore is usually excited to an energy level higher than the lowest vibrational level of the first singlet electronic state. In general, the electron relaxes to the lowest vibrational level of S_1 by the non-radiative transitions called *vibrational relaxation* and *internal conversion* (IC) in the case that the singlet excited state is higher than S_1 .

- **Fluorescence**

Fluorescence is the emission of photons associated to the $S_1 \rightarrow S_0$ relaxation. Apart from a few exceptions, fluorescence generally results from the lowest vibrational level of the first singlet electronic state. In this case and if a unique species exists in the ground state, the characteristics of the fluorescence emission will not depend on the excitation wavelength. Due to the energy loss in the excited state caused by vibrational relaxation, the fluorescence spectrum is located at lower energy than the absorption spectrum. Emission of a photon occurs in the same time scale as the absorption of a photon (10^{-15} s). However, molecules stay in the excited state S_1 for $10^{-10} - 10^{-7}$ s before emitting a photon or undergoing other de-excitation processes.

In the excitation of a fluorophore, the electronic transition is accompanied by an almost instantaneous change in the dipole moment of the fluorophore. In the case of push-pull molecules, the increase of the dipole moment can be considerable. Thus, the excited state, *i.e.* locally excited (LE) state, is not in equilibrium with the solvent molecules if the later are polar and the system reaches a relaxed *intramolecular charge transfer* (ICT) state that in some cases occurs through conformational changes.^[55] As a result, push-pull molecules can display *dual fluorescence*, that is, emission from both LE and ICT states.

The *fluorescence quantum yield* is one of the most important characteristics of a fluorophore. The quantum yield is the number of emitted photons relative to the number of adsorbed photons. Fluorophores that show high quantum yields, approaching unity, display brighter emissions. The fluorescence quantum yield (Φ_f) can be determined experimentally either by using an integrating sphere or regarding to the quantum yield of a reference compound according to eqn (3):^[56]

$$\Phi_{f(x)} = \Phi_{f(r)} \frac{A_r n_x^2 D_x}{A_x n_r^2 D_r} \quad (3)$$

where A is the absorbance of the solution, n is the refractive index of the solvent, D is the integrated area under the emission spectrum and x and r refer to the sample and reference solutions, respectively. The selected reference compound should absorb and emit at similar wavelengths to that of the studied compound.

- **Intersystem crossing (ISC)**

Intersystem crossing (ISC) is a non-radiative transition, in which a molecule in an excited state can undergo conversion into a state where the promoted electron has changed its spin, as in the case of the crossing from the first singlet excited state S_1 to the first triplet state T_1 . The resulting electronic structure is called a *triplet state*, since the total spin quantum number is 1 and the multiplicity is 3 (Figure 4c). The time scale of ISC can be fast enough (10^{-9} – 10^{-7} s) to compete with fluorescence. Transitions between states of different multiplicities are in principle forbidden. However, crossing from S_1 to T_1 is possible thanks to *spin-orbit coupling*, that is, the coupling between the orbital magnetic moment and the spin magnetic moment. The presence of heavy atoms, such as Br, I, Pb or Ir, increases the spin-orbit coupling and favours intersystem crossing.

- **Phosphorescence**

Emission from the first triplet state to the singlet ground state ($T_1 \rightarrow S_0$) is called *phosphorescence*. The phosphorescence spectrum is generally shifted to longer wavelengths in comparison to the fluorescence spectrum, because the energy of the lowest vibrational level of T_1 is lower than the energy of S_1 . Although the $T_1 \rightarrow S_0$ transition is forbidden, phosphorescence can be observed at low temperatures and/or in a rigid medium. Under these conditions, the lifetime of the triplet state can be long enough to observe phosphorescence (10^{-6} –1 s).

- **Delayed fluorescence**

Another possible de-excitation process from T_1 is called *delayed fluorescence* (Figure 5). If the energy difference between S_1 and T_1 (ΔST) is small and the lifetime of T_1 is long enough, *reverse intersystem crossing* (RISC) ($T_1 \rightarrow S_1$) can occur. Since the energy of T_1 is lower than that of S_1 , the RISC process can be thermally activated. The resulting emission corresponds to that of the normal fluorescence but with a longer decay time constant, since the molecules stay in the triplet state before emitting from S_1 . This process is called *thermally activated delayed fluorescence* (TADF).

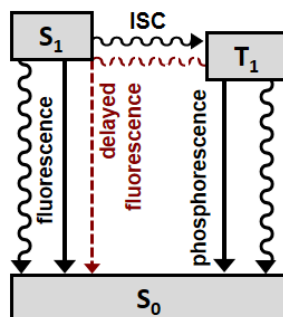


Figure 5. Electronic transitions indicating the delayed fluorescence process.

When the energy gap between S_1 and T_1 (ΔST) is large, two molecules in the T_1 state can provide enough energy to allow one of them to return to the S_1 state through the *triplet-triplet annihilation* (TTA) process, leading also to a delayed fluorescence emission.

Materials that show TDAF or TTA processes have attracted great interest as emitting layers in non-doped OLEDs. The luminescent efficiency of the OLED device can be enhanced due to the contribution in the fluorescence emission ($S_1 \rightarrow S_0$) of the additional singlet excitons provided by the non-radiative triplet excitons.^[57]

1.3. Electrochemical properties

Information of the energy levels of organic semiconductors is essential for designing electronic or optoelectronic devices and for understanding the processes which occur in the devices.

Cyclic voltammetry (CV) is a widely used methodology to estimate the ionization potential (IP) and the electron affinity (EA) of organic semiconductors.^[58-60] In standard CV experiments, a three-electrode cell containing a solution of the compound under study in the presence of a supporting electrolyte at a much higher concentration is used. The three electrodes are: the working electrode, the reference electrode and the counter electrode. This technique consists on the application of a forward and reverse potential between the working electrode and the reference electrode under quiescent conditions and under an inert atmosphere. At the same time, the current is measured between the working electrode and the counter electrode. From this measurement, a current *versus* voltage curve can be obtained as it is shown in Figure 6, which displays the cyclic voltammogram of a solution of ferrocene in acetonitrile as an example. In this case, ferrocene undergoes an oxidation process. First, an anodic wave appears on the positive

forward scan, followed by the corresponding cathodic wave on the reverse scan, corresponding to the oxidation of the neutral molecule to a radical cation and its subsequent reduction to the neutral state, respectively. Similarly, the reduction process of a redox couple corresponds to the reduction of the neutral molecule into a radical anion and its consecutive oxidation to the neutral molecule.

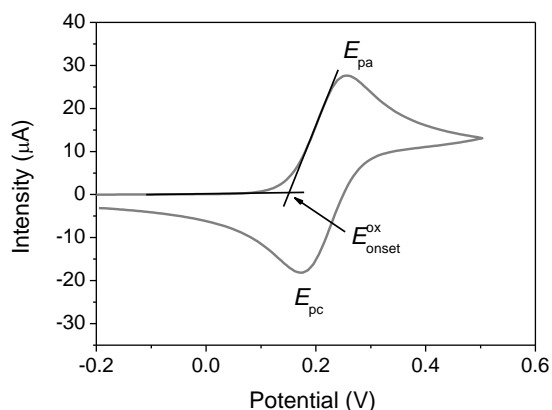


Figure 6. Cyclic voltammogram of an argon-purged ferrocene solution (~ 1 mM) in acetonitrile with tetrabutylammonium hexafluorophosphate (0.1 M) as the supporting electrolyte recorded at a scan rate of 100 mV s^{-1} . The working electrode was a glassy-carbon electrode; a platinum wire was employed as the counter electrode; and a Ag/Ag^+ electrode (0.01 M AgNO_3 in acetonitrile) was used as the reference electrode. (E_{pc} : potential of the cathodic peak, E_{pa} : potential of the anodic peak and $E_{\text{onset}}^{\text{ox}}$: onset oxidation potential).

The oxidation of ferrocene is an example of a reversible process (Figure 6). For reversible couples, which are those redox couples that exhibit fast electron transfer, the cathodic and anodic peak currents should be approximately the same. In addition, the potential difference between the cathodic (E_{pc}) and anodic (E_{pa}) peaks $|E_{pc} - E_{pa}|$ should be $57 \text{ mV}/n$, where n is the number of electrons transferred in the process. The average of the peak potentials of the anodic and cathodic waves of the reversible process is taken as an approximation of the standard potential (E^0) as it is shown in eqn (4).

$$E^0 = \frac{E_{pa} + E_{pc}}{2} \quad (4)$$

The ionization potential of the compound (IP) can be determined by CV from the standard potential of the redox couple of the oxidation process (E_{ox}^0). In a similar way, the electron affinity (EA) can be determined from the standard potential of the redox couple of the reduction process (E_{red}^0). When cyclic voltammograms of organic semiconductors show reversible or *quasi*-reversible redox couples, the determination of E^0 is unequivocal. However, cyclic voltammograms may be

more complex and the peaks of the oxidation to radical cations and reduction to radical anions become irreversible. In this case E^0 cannot be determined, but the oxidation and reduction potentials can be estimated by the onset potential of the first oxidation (E_{onset}^{ox}) or reduction (E_{onset}^{red}) peaks, respectively (Figure 6). Therefore, IP values can be determined from the onset oxidation potential and EA values from the onset reduction potential. For the estimation of EA and IP values it is necessary to express these potentials in the absolute potential scale, *i.e.* with respect to the vacuum level. IP and EA values can be calculated on the basis of the reference energy level of ferrocene as it is shown in eqn (5) and eqn (6):

$$IP \text{ (eV)} = E_{onset}^{ox} - E^0(\text{Fc}^+/\text{Fc}) + 5.39 \quad (5)$$

$$EA \text{ (eV)} = E_{onset}^{red} - E^0(\text{Fc}^+/\text{Fc}) + 5.39 \quad (6)$$

where $E^0(\text{Fc}^+/\text{Fc})$ is the redox potential for the oxidation of ferrocene *versus* the used reference electrode and the value of 5.39 eV corresponds to the formal potential of the Fc^+/Fc redox couple in the Fermi scale.^[58]

Ionization energies of thin films of the organic semiconductor can be determined by the photoelectron emission technique.^[61] In this technique, UV light is incident on a thin film sample, which causes the emission of electrons from its surface. The photocurrent *versus* the photon energy ($h\nu$) is then plotted as shown in Figure 7. The IP value can be determined from the intersection point of the linear part of the spectrum with the abscissa axis. It should be pointed out the differences between the experimental conditions of the photoemission spectroscopy and the cyclic voltammetry measurements. Whereas the IP values from CV are determined in solution, those from the photoelectron emission technique are measured in solid samples.

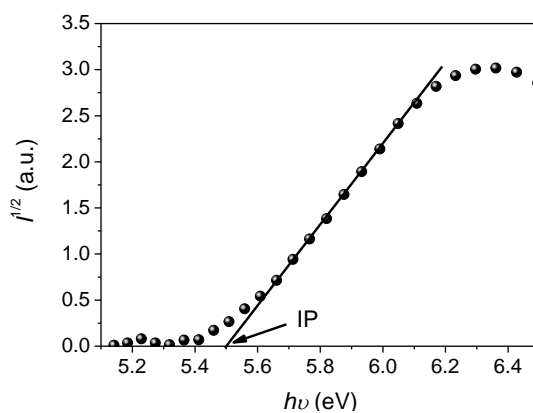


Figure 7. Representative electron photoemission spectrum of a semiconducting organic thin film.

PART 2. Charge transport properties in organic semiconductors

2.1. Charge carrier mobility

When a voltage is applied to an organic semiconductor layer sandwiched between two electrodes, charge carriers are transported across the sample under the applied electric field. The *charge carrier mobility* (μ) characterises how fast these charge carriers are transported across the semiconducting layer of a given thickness under the applied electric field and is defined by eqn (7):

$$\mu = \frac{v}{E} \quad (7)$$

where v is the drift velocity of the charge carriers and E is the applied electric field.

There are several techniques for measuring the charge carrier mobility in organic semiconductors such as time of flight (TOF), space-charge-limited current (SCLC), carrier extraction by linearly increasing voltage (CELIV), double injection (DOI) and impedance spectroscopy (IS).^[62] In addition, charge carrier mobility can be determined from the electrical characteristics of organic thin film transistors (OTFTs). Some basic concepts about the TOF technique and about the fabrication and characterization of OTFTs will be here presented, whereas the other techniques are beyond the scope of this thesis.

2.2. Time-of-flight technique

A brief introduction to the TOF technique is given below.^[62] This technique is based on the measurement of the *carrier transient time* (t_t), that is, the time the charge carriers need to travel across the sample under an applied electric field. A schematic diagram of a TOF experiment is shown in Figure 8. The sample for the TOF measurements usually consists of an organic semiconductor layer (>1 μm in thickness) sandwiched between two electrodes. Since the charge carriers are photogenerated, one of the two electrodes should be transparent or semitransparent.

Charge carriers are generated by photo-excitation through irradiation with a short light pulse. The photon energy of the light should be selected depending on the absorption spectra of the studied materials. Charge carriers are generated in a spatial region close to the transparent or semitransparent electrode, which should be much smaller than the thickness of the organic semiconductor layer. In addition, the duration of the light pulse should be short as compared to the

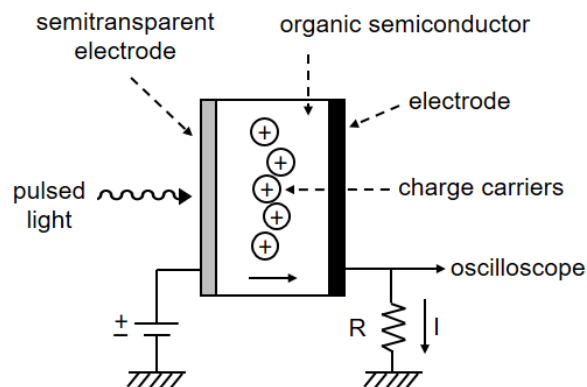


Figure 8. Schematic diagram of a TOF experiment indicating the measurement of hole drift mobility.

transit time of the charge carriers. An additional requirement of the TOF technique is that the transient time should be shorter than the dielectric relaxation time, defined as the time for the photogenerated charges to relax back to the original state. Depending on the polarity of the applied electric field, either electrons or holes will be transported across the sample from the front to the back electrode. This is one of the main advantages of the TOF technique, that is, holes and electrons can be measured separately by using the same sample. For example, for measuring a hole drift mobility (Figure 8), the transparent electrode is held at a positive potential with respect to the ground, while the other electrode is grounded through a resistor R with a smaller resistance than the sample. This leads to an applied potential V in the sample and the photogenerated charge carriers (holes) will start moving towards the negative electrode. An important requirement for determining the transient time and the mobility by the TOF technique is that the time constant CR (C the total capacitance across resistance R) should be lower than the transient time. If this condition is accomplished, the voltage across R is proportional to the current flowing in the sample, which can be measured using an oscilloscope.

A typical photocurrent transient for materials displaying non-dispersive charge transport is displayed in Figure 9a. After excitation of the sample through the transparent or semitransparent electrode, the transient current increases instantaneously. Next, the photogenerated carriers travel through the material and the current level stay constant. When the carriers reach the other electrode, the current decreases rapidly. The transient time can be determined from the cusp of the photocurrent transient as shown in Figure 9a. However, charge transport in organic semiconductors can be dispersive, due to the existence of a distribution of charge trapping sites in

the material. In this case, the characteristic plateau is not observed in the photocurrent transient (Figure 9b), but the transient time can be determined from the inflection point of the photocurrent transient represented in the log–log scale.

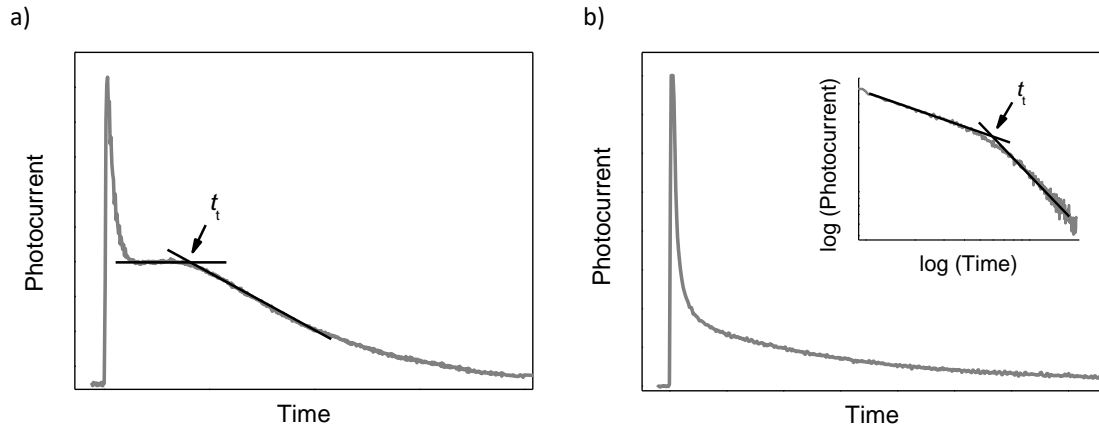


Figure 9. Typical photocurrent transients: a) non-dispersive and b) dispersive. Inset shows the transient curve in the log-log scale.

The transient time (t_t) can be expressed according to eqn (8):

$$t_t = \frac{d}{\nu} \quad (8)$$

where d is the sample thickness and ν is the velocity of the charge carriers. The charge carrier mobility (μ) can be determined by combining equations (7) and (8) as follows:

$$\mu = \frac{d}{Et_t} \quad (9)$$

where E corresponds to the applied electric field and it can be calculated as:

$$E = \frac{V}{d} \quad (10)$$

2.3. Xerographic time-of-flight technique

The xerographic time-of-flight technique (XTOF) show similarities with the TOF technique. The XTOF sample consists of an organic semiconducting layer deposited on a metallic electrode, usually aluminium. Figure 10 shows a representation of a XTOF experiment. In this technique, the surface

of the semiconducting layer is charged by a corona charging device and then exposed to a short pulse of radiation, which creates a sheet of charge carriers. Depending on the applied electric field, holes or electrons move towards the conductive substrate (metallic electrode), observing a decrease of the surface potential.^[63] Since the interpretation of the XTOF transient signals is the same as for the TOF signals, the mobility can be determined from the photocurrent *versus* time plot. The main advantages of the XTOF method are that higher electric fields can be achieved together with the simpler sample preparation.

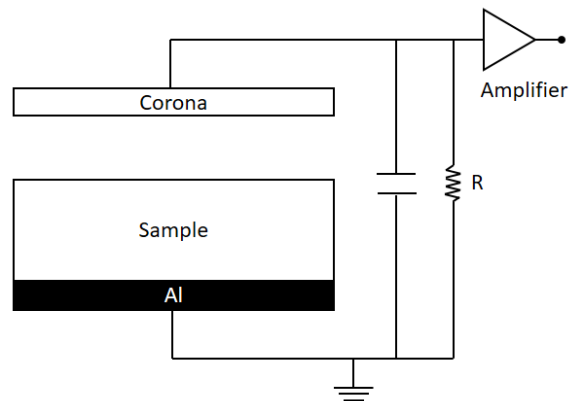


Figure 10. Schematic diagram of a XTOF experiment.

PART 3. Electronic and optoelectronic devices

3.1. Organic Thin-Film Transistors (OTFTs)

- **Geometry and fabrication of OTFTs**

A typical OTFT consists of the following elements: three electrodes (gate, drain and source), a dielectric layer and an organic semiconducting layer. The two most commonly employed geometries for OTFTs are known as top contact and bottom contact (Figure 11). In both cases, the gate electrode is defined on the substrate, which can be rigid, such as a silicon wafer, or flexible, such as plastic or even paper. The gate is in contact with the dielectric layer. In the top-contact architecture, the organic layer is deposited on the dielectric followed by the deposition of the metal contacts, whereas in the bottom-contact case this sequence is inverted.

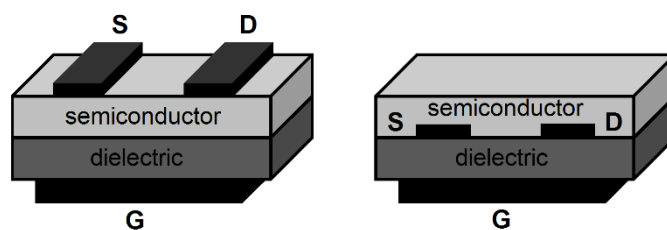


Figure 11. Schematic of typical OTFT architectures: top contact (left) and bottom contact (right). S: Source; D: Drain; G: Gate.

The organic layer (usually with thickness around 25–100 nm) can be deposited either by the vacuum thermal evaporation technique or *via* solution-processing methods such as spin coating or drop casting. In the vacuum evaporation technique, the material is placed in a crucible in a vacuum chamber with a base pressure below 10^{-6} mbar. When the crucible is heated, the semiconductor is sublimated and deposited forming a film onto the substrate. During the evaporation process, some parameters such as the evaporation rate, the thickness and the substrate temperature, can be controlled. In the spin-coating technique, the organic material is dissolved in a suitable solvent and deposited onto the centre of the substrate, which is spun at 500–10000 rpm. During the process, the solvent is evaporated and a thin film is obtained. The thickness of the layer depends on the initial concentration of the sample and of the parameters chosen for the spin process.

Taking into account that the properties of the interface between the semiconductor and the dielectric layers play an important role in the electrical characteristics of the OTFT, the surface of the dielectric may be treated prior to the deposition of the organic semiconductor, as with a self-assembled monolayer (SAM). The treatment of the dielectric surface has been found to effect on the semiconductor film morphology due to the impact on the growth of the semiconductor layer.^[64]

- **Operation and electrical characterization of OTFTs**

The application of a gate voltage (V_G) induces the accumulation of charges in the interface between the dielectric and the semiconducting film as shown in Figure 12.^[10,12] Much of this charge is mobile and moves in response to the voltage applied between the source and the drain (V_D). Charge carriers are injected and collected from the source and drain electrodes. If no gate voltage is applied, the device is found in the *off state*, since ideally there are no mobile charge carriers. On the contrary, when a gate voltage is applied, mobile charges are induced, and the transistor is in the *on state*. Here, it should be mentioned that although a gate voltage is applied, the current flow

between the source and the drain does not start until a *threshold voltage* (V_{th}) is reached. The threshold voltage depends on the material nature and also is related to the presence of traps in the film, among others. If there are a large number of deep electron traps in the film, they will have to be filled before the channel can conduct.^[10]

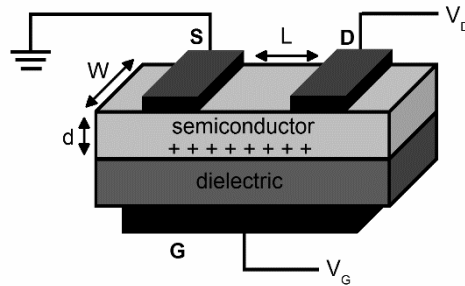


Figure 12. Relevant voltages for an OTFT.

The nature of the charge carriers, holes or electrons, accumulated at the interface between the dielectric and the semiconductor layers can be controlled by the V_G applied. In the case of p-type semiconductors (Figure 12), the application of a negative gate voltage ($V_G < 0$) induces the accumulation of holes in the interface that upon application of a negative drain voltage ($V_D < 0$), results in current circulation along the channel (L) between the source and drain electrodes. For n-type semiconductors, a positive gate voltage ($V_G > 0$) causes the accumulation of electrons in the interface and a positive drain voltage ($V_D > 0$) produces the current circulation.

There are three principal characteristics that describe the operation of a transistor: the output, the transfer and the saturation curves (Figure 13).

The *output curves* (also referred as I_D - V_D curves) consist of a set of plots of the drain-source current (I_D) versus the drain voltage (V_D), in which each individual curve is measured at a fixed gate voltage (V_G) (Figure 13a). The output curves are characterized by the linear and the saturation regions. The linear region is defined at low drain voltages, at $V_D < (V_G - V_{th})$. In this region, the drain-source current (I_D) follows Ohm's Law, being the I_D current proportional to V_D at a fixed V_G . The linear regime of the curve is defined as:

$$I_D = \frac{W}{L} C_{ox} \mu \left[(V_G - V_{th}) - \frac{V_D}{2} \right] V_D \quad (11)$$

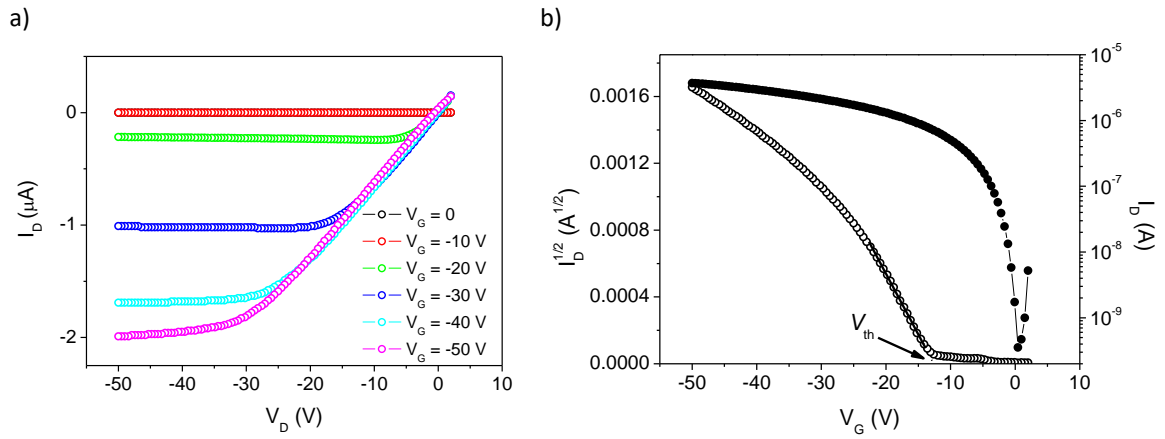


Figure 13. a) Output characteristics of an OTFT. b) Saturation (left) and transfer characteristics at $V_D = -50$ V (right).

where W and L correspond to the channel width and length, respectively, and C_{ox} is the capacitance per unit area of the dielectric.

As V_D is increased, the concentration of accumulated charge carriers in the channel region between the source and the drain becomes non-uniform. When $V_D = V_G - V_{th}$ the channel becomes “pinched”, that is, the region near the drain is found depleted of the accumulated charges and the drain-source current (I_D) remains constant although V_D is increased. Thus, at $V_D > (V_G - V_{th})$, a saturation region is observed as shown in Figure 13. In the saturation regime, I_D can be expressed by eqn (12), which is obtained by substituting $V_D = V_G - V_{th}$ in eqn (11).

$$I_D = \frac{W}{2L} C_{ox} \mu (V_G - V_{th})^2 \quad (12)$$

In the *transfer curves* (Figure 13b, right), the drain-source current I_D is plotted as a function of V_G for a constant value of V_D . An important parameter can be obtained from the transfer curves, the I_{on}/I_{off} ratio. This parameter indicates the ratio between the drain-source current I_D values in the on and off states and is indicative of the switching performance of the device.

Finally, the *saturation curves* can be obtained by applying the same voltage to the drain and the gate ($V_D = V_G$), since under this condition the device works in the saturation regime. The mobility in the saturation regime can be measured from the saturation characteristics when plotted as $I_D^{1/2}$ vs V_G ($V_G = V_D$) as shown in Figure 13b (left). For this purpose, eqn (12) can be written as follows:

$$\sqrt{I_D} = \sqrt{\frac{W}{2L} C_{ox} \mu V_G} - \sqrt{\frac{W}{2L} C_{ox} \mu V_{th}} = AV_G - B \quad (13)$$

where the value of the mobility and the threshold voltage can be graphically extracted from the linear fit to eqn (13), where:

$$\mu = \frac{2L}{WC_{ox}} A^2 \quad (14)$$

$$V_{th} = -\frac{B}{A} \quad (15)$$

One should be careful when comparing the mobility values obtained by different methods, for example from TOF and OTFT measurements. Charge generation methods are different (photogeneration and field effect, respectively), as well as the thickness of the sample. In addition, the configuration of the sample device differs considerably. In TOF samples, the conduction of the charges is perpendicular to the substrate surface, whereas in OTFT devices takes place within the plane of the substrate surface. It should be noted that the configuration of the sample is irrelevant in the case of amorphous semiconducting layers, but becomes fundamental in the study of the charge-transporting properties of crystalline or liquid crystalline materials.

3.2. Organic Light-Emitting Diodes (OLEDs)

- Structure, operation and fabrication of OLEDs

The simplest structure of an OLED consists of only one emitting layer (EML) sandwiched between two electrodes (Figure 14a). The electroluminescence (EL) process involves the injection, migration

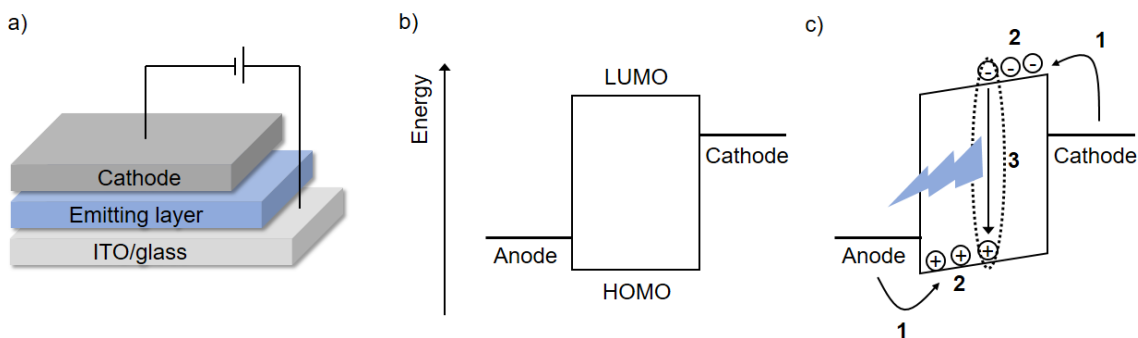


Figure 14. a) Schematic of a typical single-layer OLED device. b) Energy level diagram of a single-layer OLED device. c) Energy level diagram under applying an electric field indicating the basic steps of light generation: (1) injection, (2) migration and (3) recombination of charge carriers and emission of light.

and recombination of charge carriers, followed by the emission of light. The colour of the generated light is determined by the band gap of the emitter. Figure 14b displays the energy level diagram of a single-layer OLED device and the main steps involved in the EL process are outlined in Figure 14c.

The principles of OLED operation^[65,66] are further detailed in Figure 15. This scheme displays the HOMO and LUMO energy levels of molecules of the emitting layer sandwiched between the anode and the cathode electrodes. In Figure 15a all molecules are in the singlet ground

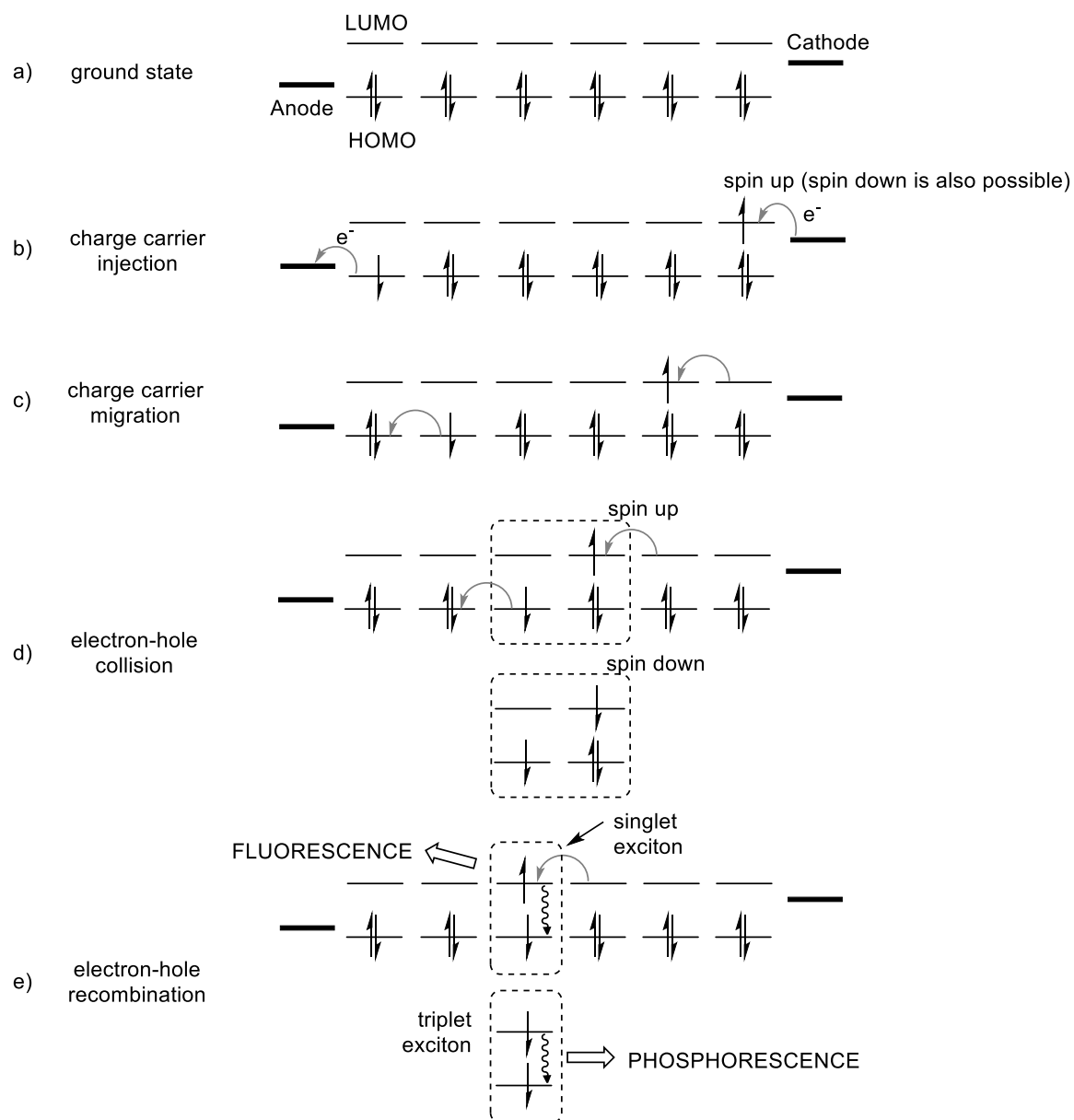


Figure 15. Scheme of EL generation in an organic emitting layer sandwiched between the anode and the cathode electrodes.

state (S_0). When a voltage is applied between the two electrodes, electrons are injected from the cathode into the LUMO of the emitter and holes are injected from the anode into the HOMO (Figure 15b). ITO is usually used as the anode due to its high work function (4.8 eV) and its optical transparency, which allows the extraction of the electrogenerated light. For the cathode, a low work function material is required to facilitate electron injection. The charge carriers migrate across the emitting layer to the opposite electrodes *via* the hopping mechanism (Figure 15c). For this reason, luminescent materials for OLEDs are required to display hole and/or electron transport.

When electrons and holes are close to each other, they are attracted and form *excitons* (Figure 15d and e). Here, it should be noted that electrons and holes have arbitrary spin from the beginning of the process. In Figure 15b, a spin-down hole and a spin-up electron are created as an example, being the electron-hole pair in the singlet spin state (Figure 15e). If the electron and hole have parallel spins, the electron-hole pair will have a triplet spin state (Figure 15e). Both singlet and triplet pair formation are equally probable, since we are not considering here spintronic devices, which are able to inject spin-polarized charge carriers. By statistics, the ratio of the triplet and singlet excitons induced by the applied voltage is 3:1, since the triplet state consists of three spin-sublevels and the singlet state of only one. Thus, 25% of formed excitons are singlet and 75% are triplet excitons, which cannot emit light in most organic compounds as the $T_1 \rightarrow S_0$ transition is spin forbidden.

Compared with fluorescent OLEDs, which use only singlet excitons for light emission, *phosphorescent OLEDs* can use both singlet and triplet excitons for light emission, which increases the quantum efficiency of the devices. The most used phosphorescent emitters are organometallic complexes with heavy metals such as Ir, Pt and Os, in which the $T_1 \rightarrow S_0$ transition can be allowed due to spin-orbit coupling. In general, in these devices the emitting layer consists of the phosphorescent emitter doped in a host material.^[67]

Although the single-layer OLED structure shown in Figure 14a would be desirable from a practical point of view, enhanced device performance can be achieved by introducing additional layers between the electrodes and the emitting layer to facilitate the charge carrier injection and transport. Figure 16 shows the structure of a multi-layer OLED device containing additional hole- and electron-transporting layers (HTL and ETL, respectively). The thickness of the layers ranges from a few nanometres to a few tens of nanometres. It should be remarked that the fabrication of multi-layer devices hinders the fabrication process in solution-processed OLEDs, due to interlayer mixing

can occur during the deposition steps. The advantage of small molecules is that they can be processed by vacuum evaporation, which allows the fabrication of multi-layer devices avoiding the problems of intermixing.

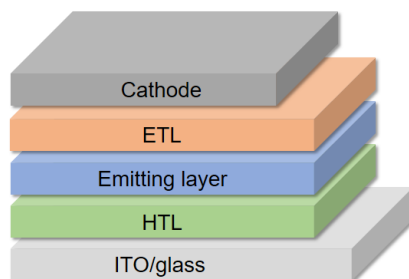


Figure 16. Schematic of a typical multi-layer OLED device (ETL: electron-transporting layer, HTL: hole-transporting layer).

- **Electro-optical characterization of OLEDs**

OLEDs act as a diode and should have a high rectification ratio and a minimal leakage current, which do not contribute to electroluminescence emission.^[65] A typical current density (J) versus voltage curve is shown in Figure 17.

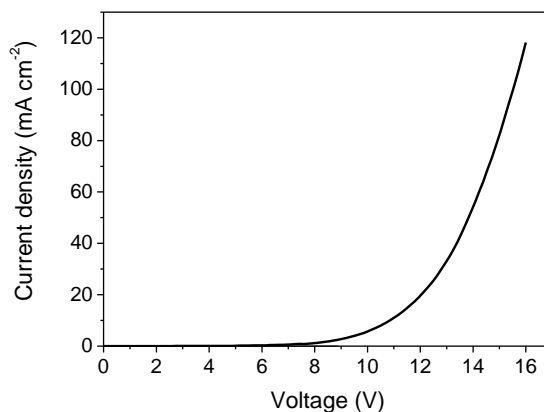


Figure 17. Typical current density vs. voltage curve for an OLED device.

The parameters used to describe the performance of OLED devices are defined below.^[41,65] The emission intensity of an OLED is characterized by the *luminance* (L), given in candela per square metre (cd m⁻²), which is the luminous intensity per unit area of light emitted by the OLED surface.

Under the assumption of Lambertian emission, the surface emission of an OLED is independent of the viewing direction.

The *turn-on voltage* (V_t) describes the voltage at which the device turns on at a given luminance. The turn-on voltage is related to the energy barriers at the organic/organic and organic/electrode interfaces, as well as to the charge transport properties and thickness of the active layers.

The *current efficiency* (η_c) in candelas per ampere (cd A^{-1}) is the ratio between the luminous intensity of the emitted light in forward direction and the current through the device as it is shown by eqn (16):

$$\eta_c = \frac{AL}{I} \quad (16)$$

where A is the area and I is the current of the device. The *power efficiency* (η_p) in lumen per watt (lm W^{-1}) is the output luminous flux (in lumens, the unit of light intensity perceived by the human eye) per electrical power input (measured in watts). The power efficiency can be calculated from the current efficiency according to eqn (17) under the assumption of Lambertian emission:

$$\eta_p = \eta_c \times \frac{\pi}{V_{\text{appl.}}} \quad (17)$$

As it can be seen from eqn (17), if the driving voltage ($V_{\text{appl.}}$) is low, the η_p will be high and consequently, the OLED will be more efficient, which is of particular interest for lighting applications.

The *external quantum efficiency* (EQE or η_{ext}) is the ratio between the total number of photons emitted from the device and the number of electrons injected. EQE can be determined experimentally with an integrating sphere. On the other hand, the *internal quantum efficiency* (η_{int}) is the ratio between the total number of photons produced within the device and the number of electrons injected. Eqn (18) shows the correlation between the external and internal quantum efficiencies:

$$\text{EQE} = \eta_{\text{out}} \times \eta_{\text{int}} \quad (18)$$

$$\eta_{\text{out}} = 1/(2n^2) \quad (19)$$

where η_{out} is the *light out-coupling efficiency*, being n the refractive index of the glass substrates, assumed to be ~ 1.5 .

The EQE of OLEDs can be described by eqn (20):

$$EQE = \rho \times QY \times \phi \times \eta_{out} \quad (20)$$

where ρ is the charge balance of injected holes and electrons, QY is the quantum yield of the emitting material and ϕ is the efficiency of electrically generated excitons conversion into light or efficiency of radiative exciton production ($\phi = 0.25$ for fluorophores and $\phi = 1$ for phosphorophores since the singlet exciton can be converted to a triplet exciton by intersystem crossing). Based on eqns (18) and (20), and considering that fluorophores can reach a maximum internal quantum efficiency of 25%, fluorescent OLEDs can reach a maximum EQE of $\sim 5\%$. Thus, fluorescent materials that can convert the non-radiative triplet excitons into singlet excitons, such as those that can undergo delayed fluorescence *via* either reverse intersystem crossing (RISC) in TADF molecules^[68] or triplet-triplet annihilation (TTA),^[69] have been recently attracting more and more attention in fluorescent OLEDs to increase the EL efficiency of the devices.

At this point, it should be remarked that the current efficiency (η_c) and the power efficiency (η_p) of an OLED device take into account the sensitivity of the human vision to the different wavelengths of the visible spectrum, whereas the external quantum efficiency weights all photons equally. Therefore, EQE can be used as a general measure of device efficiency, whereas η_c and η_p of devices with different emission colours should be compared with caution.

PART 4. Surface characterization techniques

4.1. X-ray diffraction (XRD)

X-ray diffraction (XRD) methods are very useful to study not only the crystallographic structure, but the chemical composition and physical properties of materials and thin films as well.^[70]

X-rays are electromagnetic waves, being the X-ray wavelength of the order of 0.1 nm. Two waves of the same wavelength and traveling in the same direction can show constructive or destructive interference, that is, waves are in phase (with a phase difference of $n\lambda$, where n is an

integer) or out of phase, respectively. When X-ray beams impact on a crystalline solid, they are diffracted by the crystallographic planes as displayed in Figure 18.

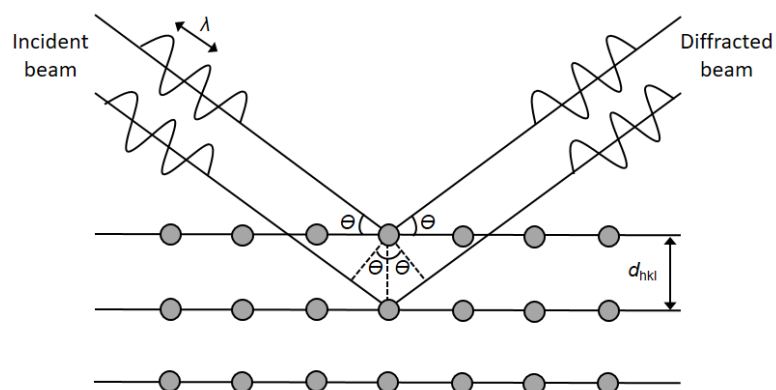


Figure 18. Bragg diffraction by crystal planes.

In Figure 18, two in phase incident waves are deflected by two crystal planes. The deflected waves will be in phase only when the Bragg's Law is accomplished:^[53]

$$n\lambda = 2d_{hkl} \sin\theta \quad (21)$$

where λ is the wavelength of the X-ray source, d_{hkl} is the spacing between the parallel crystal planes, *i.e.* the interplanar spacing, and θ is the incident angle.

The crystal structure of materials can be solved by XRD from single crystals determining the spacings of the crystallographic planes (d_{hkl}), which can be deduced according to Bragg's Law. The Miller indices (hkl) represent a series of parallel planes in a crystal with a spacing of d_{hkl} . To distinguish between the different planes, a coordinate system is used with unit vectors denoted as a , b and c , which are the edges of the *unit cell*.

The XRD technique is also widely used to characterize powder solid samples. Here, it should be noted that a tendency of orientations of one or more particular crystallographic planes is possible, which is known as *preferred orientation*. The combination of the XRD spectra of the thin films with the single crystal structures and the powder XRD data provides valuable information such as the molecular packing and orientation of the organic material in the thin films.^[71]

In some cases, XRD measurements using conventional scanning methods of thin films of a few tens of nanometres, such as those of OTFTs, only afford a weak signal from the film and an

intense signal from the substrate. As an alternative, the grazing incidence X-ray diffraction (GIXRD) technique can be used. In this technique, the measurement is performed at a small incident angle lower than a critical angle relative to the surface plane in order to attenuate the corresponding X-rays reflection of the substrate.^[70]

4.2. Atomic Force Microscopy (AFM)

The study of the morphology of the active organic layers renders information about the device performance, since aspects such as crystallinity and growth mode are directly related. The surface topography of thin films can be examined by using the AFM technique. In this way, the surface layer roughness and the grain size and boundaries of thin films can be analysed. The AFM scan images can range from a few nanometres to tens of micrometres.

In this technique, a cantilever with a fixed sharp tip is used to scan the sample surface. When the tip is close to the sample surface, forces between the tip and the sample lead to a deflection of the cantilever according to Hooke's law. The deflection is measured using a laser spot reflected from the top surface of the cantilever into an array of photodiodes. AFM can be operated in the contact or the tapping mode. In the *contact mode* (or static model), the tip is in permanent contact with the sample during the scanning and can collide with the surface, causing damage. For this reason, a piezoelectric actuator is used to keep a constant force between the tip and the sample and control the corresponding distance between them.^[70,72] In the *tapping mode*, while the tip interacts with the sample, the cantilever oscillates with a constant resonant frequency, resulting in a change in the dynamic parameters of the cantilever. Thus, due to the intermittent contact between the tip and the sample, AFM images can be obtained without damaging the sample.



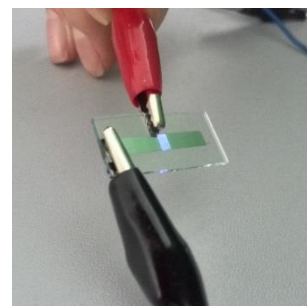
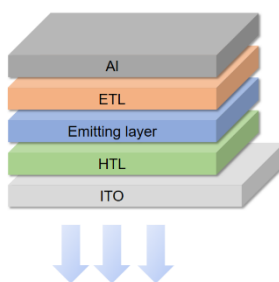
RESULTS AND DISCUSSION

Inside cover

J. Mat. Chem. C **2015**, *3*, 506–513

Chapter 1

Blue-emitting materials for Organic Light-Emitting Diodes



Part of this chapter has been published in:

Dyes Pigm. **2017**, *137*, 24–35

RSC Adv. **2016**, *6*, 9247–9253

CHAPTER 1

Blue-emitting materials for Organic Light-Emitting Diodes

Three different series of carbazole-based compounds have been developed as blue emitters for non-doped OLEDs. In a first instance, the role of the substitution patterns of the carbazole core on the thermal, optical, electrochemical and charge-transporting properties was systematically examined and interpreted according to their corresponding single-crystal structures and by DFT calculations. Hence, the extension of the π -conjugated system by introduction of one or two additional carbazole units and by using the triple bond as a π -conjugated linker afforded materials with hole mobilities and with the desired deep-blue emission in the solid state. The prepared OLEDs demonstrate the feasibility of the new molecules as effective emitters in the blue region yielding devices with low turn-on voltages and a maximum luminance up to $1.4 \times 10^4 \text{ cd m}^{-2}$. A high efficiency of radiative exciton production was calculated, and accordingly, the mechanism through which emission occurs was elucidated by means of DFT calculations.

1.1. Introduction

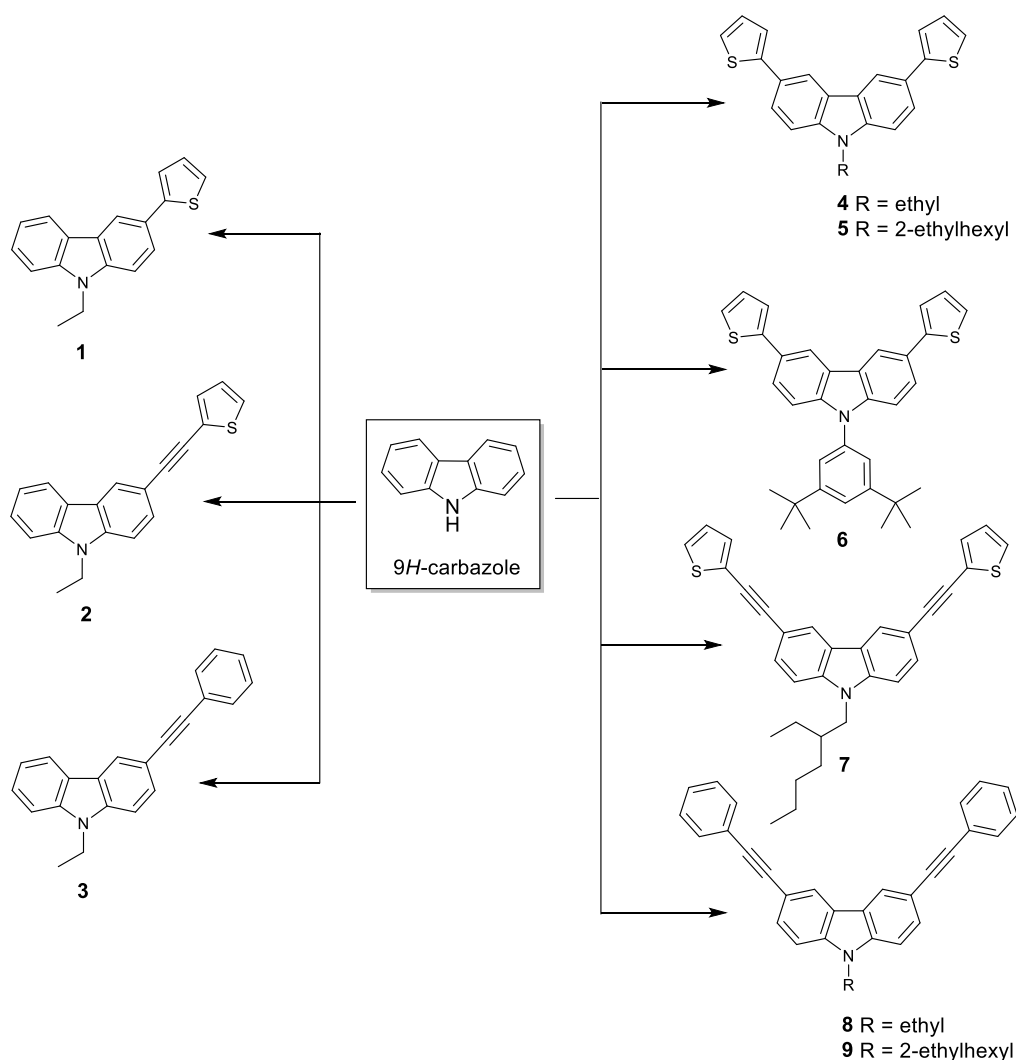
OLEDs have been studied extensively due to their promising applications in flat panel displays and solid-state lighting. However, further improvement of power efficiency, colour purity and longer operational lifetimes are still required to produce more efficient industrial devices. The development of OLEDs that emit in the blue region and in particular in the deep-blue region, with the CIE y value lower than 0.1 as required by the National Television System Committee (NTSC) and the European Broadcast Union (EBU), have attracted intensive research, since these materials can be applied in combination with green and red colour emitters in white OLEDs and full-colour displays.

Among the many known luminescent materials with blue emission, carbazole derivatives are found to be promising as emitting layers in non-doped blue OLED devices.^[73] Carbazole-based

materials are well-known for its luminescent and hole-transporting properties. This heterocycle shows an emission band in the UV zone of the spectrum that can be shifted to lower energies by extending its π -conjugated system. Thus, the design of new carbazole-based dyes that could present both blue fluorescent properties and charge transport characteristics is an attractive challenge.

1.2. Monocarbazole derivatives containing thienyl and phenyl groups as blue emitters

As a first approach to obtain blue-emitting materials with hole-transporting properties, the structural modification of the efficient carbazole UV emitter was considered. The π -conjugated



Scheme 1.1. Chemical structures of compounds 1–9.

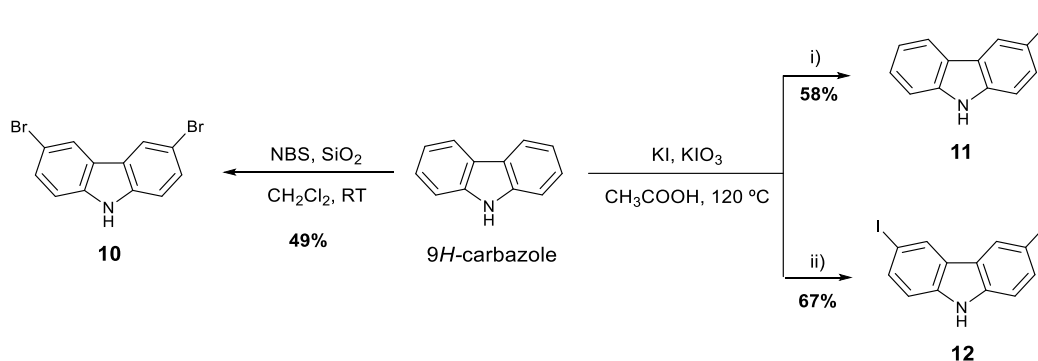
carbazole system was extended by introducing the thienyl or phenyl donor moieties at 3,6 positions of the carbazole core. In this way, an easy accessible series of mono and disubstituted carbazole derivatives (**1–9**) was synthesized (Scheme 1.1). Besides, the effect of the insertion of the ethynylene linker between the carbazole and the donor units was also analysed, as well as the nature of the *N*-substitution of the carbazole core, which was modified from the alkyl chains, ethyl and 2-ethylhexyl, to the bulky 3,5-di-*tert*-butylphenyl fragment in order to obtain amorphous molecular materials.

1.2.1. Synthesis

All the compounds were prepared starting from commercially available 9*H*-carbazole. Compounds **1**^[74], **4**^[75], **5**^[76], **8**^[77] and **9**^[78] have been previously reported in the literature. However, they are here described following an alternative methodology.

Synthesis of intermediates **10–12**

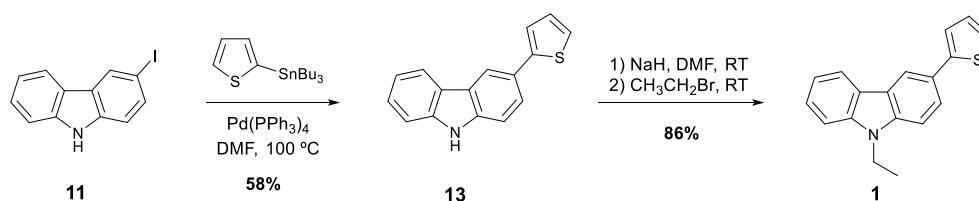
The first synthetic step for obtaining compounds **1–9** consisted on the functionalization of 3,6 positions of the carbazole core via either the bromination or the iodination reactions. Scheme 1.2 displays the synthetic route to the halogenated derivatives **10–12**. 3,6-Dibromo-9*H*-carbazole (**10**) intermediate was prepared using *N*-bromosuccinimide (NBS) in the presence of silica gel in dichloromethane via an electrophilic addition reaction.^[79] 3-Iodo-9*H*-carbazole (**11**) and 3,6-diiodo-9*H*-carbazole (**12**) were prepared in the presence of KI and KIO₃ in glacial acetic acid at 120 °C by the Tucker reaction.^[80] 3-Iodo-9*H*-carbazole was obtained in a lower yield (58%) owing to the simultaneous formation of 3,6-di-iodo-9*H*-carbazole in the reaction mixture.



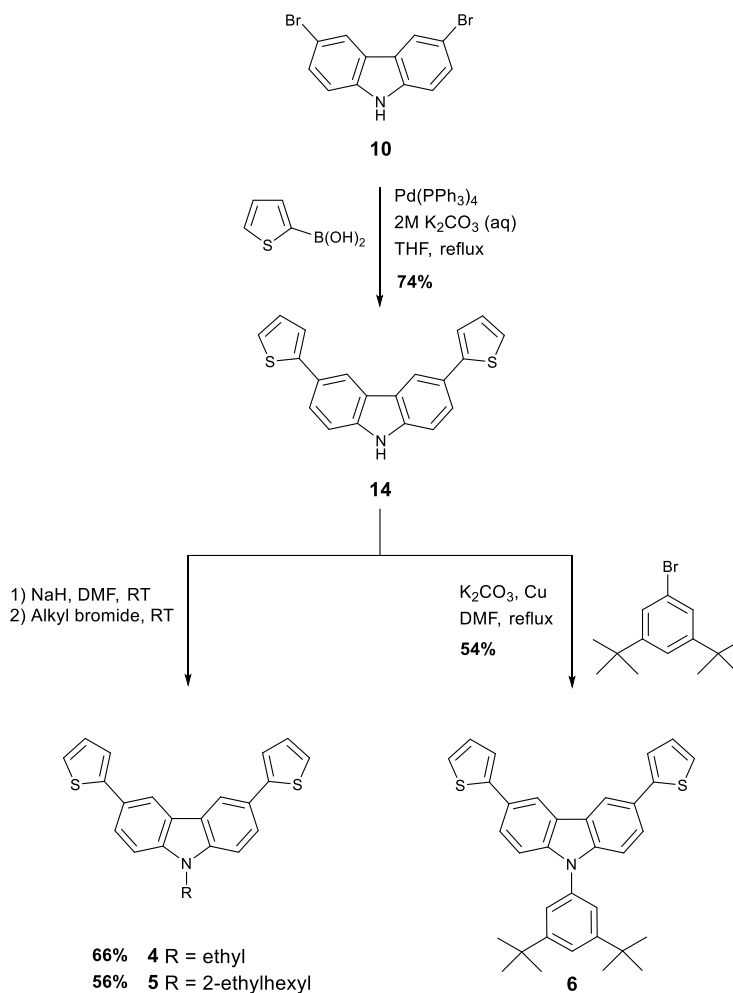
Scheme 1.2. Synthesis of bromo- and iodo-substituted intermediates **10–12**. Reaction conditions: (i) KI (0.7 eq.), KIO₃ (0.8 eq.), 30 min. (ii) KI (1.4 eq.), KIO₃ (1.5 eq.), 20 min.

Synthesis of thienyl derivatives 1 and 4–6

Scheme 1.3 displays the synthetic route to the thienyl-based compound **1**. 9-Ethyl-3-(2-thienyl)-9*H*-carbazole (**1**) was prepared from 3-iodo-9*H*-carbazole **11** and 2-(tributylstannyl)thiophene by the Stille coupling reaction^[81] catalysed by Pd(PPh₃)₄ in anhydrous DMF at 100 °C, followed by alkylation with bromoethane using NaH as a base in anhydrous DMF at room temperature.



Scheme 1.3. Synthesis of the monosubstituted thienyl-based compound **1**.

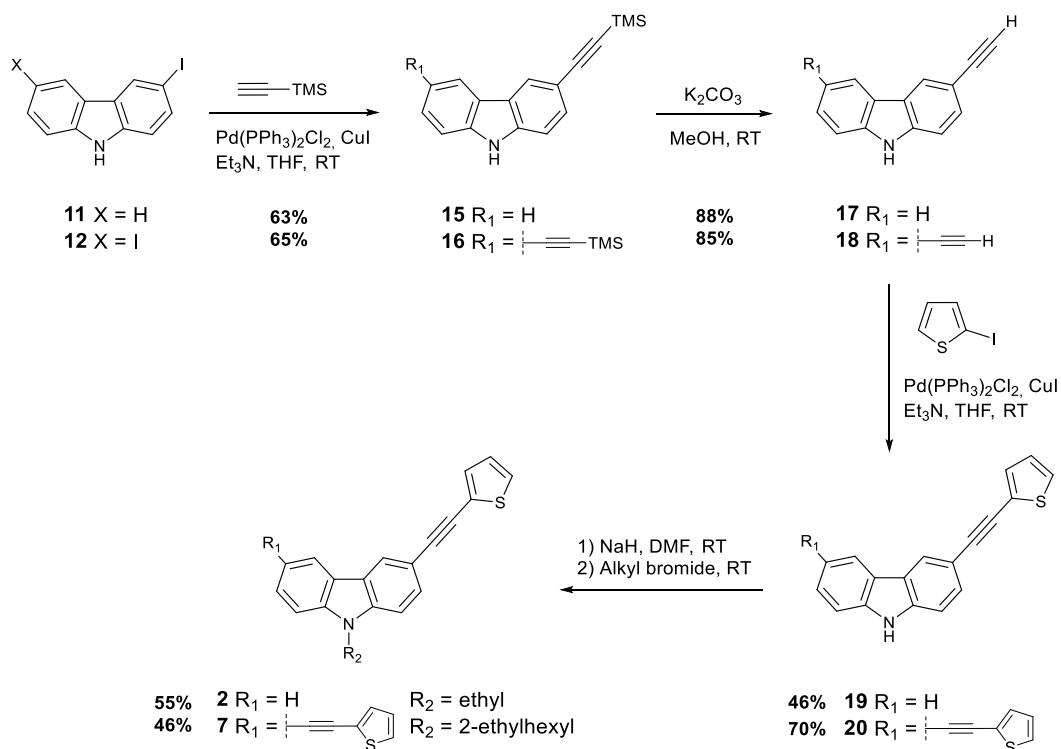


Scheme 1.4. Synthesis of 3,6-disubstituted thienyl-based compounds **4–6**.

3,6-Disubstituted thienyl derivatives **4–6** were obtained from 3,6-dibromo-9*H*-carbazole (**10**) as it is shown in Scheme 1.4. The Suzuki coupling reaction^[82] of **10** with 2-thienylboronic acid gave the intermediate 3,6-di-2-thienyl-9*H*-carbazole (**14**). The reaction was performed using Pd(PPh₃)₄ as a catalyst and an aqueous solution of K₂CO₃ as a base in THF. Compound **14** was subsequently alkylated either with bromoethane or 2-ethylhexyl bromide under standard conditions yielding the final products 9-ethyl-3,6-di-2-thienyl-9*H*-carbazole (**4**) and 9-(2-ethylhexyl)-3,6-di-2-thienyl-9*H*-carbazole (**5**), respectively. The Ullmann coupling reaction of **14** with 1-bromo-3,5-di-*tert*-butylbenzene in the presence of copper powder and K₂CO₃ in anhydrous DMF under reflux conditions furnished the new product 9-(3,5-di-*tert*-butylphenyl)-3,6-di-2-thienyl-9*H*-carbazole (**6**).

Synthesis of thienylethynyl derivatives **2** and **7**

The novel thienylethynyl compounds **2** and **7** were prepared as shown in Scheme 1.5 *via* the Sonogashira coupling reaction^[83] as key step. The Sonogashira coupling was performed in THF at room temperature using Pd(PPh₃)₂Cl₂ as a catalyst, CuI as a cocatalyst and triethylamine as a base.



Scheme 1.5. Synthesis of thienylethynyl derivatives **2** and **7**.

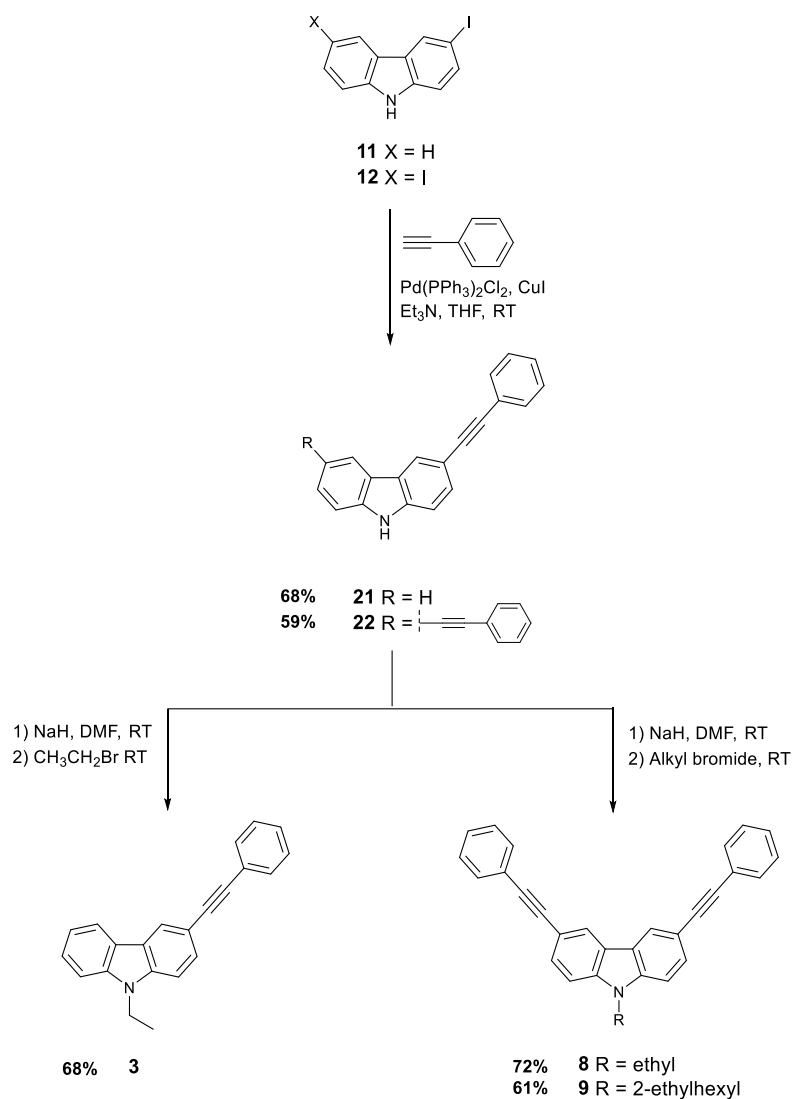
Firstly, a Sonogashira coupling of either 3-iodo-9*H*-carbazole (**11**) or 3,6-diiodo-9*H*-carbazole (**12**) with (trimethylsilyl)acetylene and further deprotection of the trimethylsilyl group in the presence of K₂CO₃ in methanol^[84] furnished the intermediates 3-ethynyl-9*H*-carbazole (**17**) and 3,6-diethynyl-9*H*-carbazole (**18**), respectively. Then, a second Sonogashira coupling from the above mentioned intermediates **17** and **18** with 2-iodothiophene and subsequent *N*-alkylation under standard conditions with bromoethane and 2-ethylhexyl bromide, respectively, yielded the corresponding final products 9-ethyl-3-[2-(2-thienyl)ethynyl]-9*H*-carbazole (**2**) and 9-(2-ethylhexyl)-3,6-bis[2-(2-thienyl)ethynyl]-9*H*-carbazole (**7**).

Synthesis of phenylethynyl derivatives **3**, **8** and **9**

Finally, in order to obtain phenylethynyl derivatives **3**, **8** and **9** (Scheme 1.6), the intermediate products 3-(2-phenylethynyl)-9*H*-carbazole (**21**) and 3,6-bis(2-phenylethynyl)-9*H*-carbazole (**22**) were prepared *via* the Sonogashira coupling reaction^[85] between either 3-iodo-9*H*-carbazole or 3,6-diiodo-9*H*-carbazole and phenylacetylene. Then, *N*-alkylation of 3-(2-phenylethynyl)-9*H*-carbazole (**21**) with bromoethane under standard conditions yielded the final product 9-ethyl-3-(2-phenylethynyl)-9*H*-carbazole (**3**). Similarly, *N*-alkylation of the 3,6-disubstituted counterpart **22** with either bromoethane or 2-ethylhexyl bromide furnished the final products 9-ethyl-3,6-bis(2-phenylethynyl)-9*H*-carbazole (**8**) and 9-(2-ethylhexyl)-3,6-bis(2-phenylethynyl)-9*H*-carbazole (**9**), respectively.

1.2.2. Crystal structures

Single crystal structures of the monosubstituted phenylethynyl derivative **3**, the disubstituted thienyl derivative **6** and the disubstituted thienylethynyl derivative **7** were determined by single-crystal X-ray analysis. Suitable single crystals for X-ray diffraction studies were obtained by the slow evaporation of acetone solutions of compounds **3**, **6** and **7**. The Oak Ridge Thermal Ellipsoid Plot (ORTEP) projections and representative intermolecular interactions of compounds **3**, **6** and **7** are depicted in Figure 1.1. Crystallographic data are collected in Appendix B. Compound **3** crystallized in space group P2₁/n of the monoclinic system with unit-cell dimensions of a = 13.7242(6) Å, b = 7.9549(3) Å, c = 15.3895(7) Å, β = 111.582(2)° and volume = 1562.35(11) Å³. Compound **6** crystallized in space group I-4 of the tetragonal system with unit-cell dimensions of a = 30.176(3) Å, b = 30.176(3) Å, c = 5.9741(5) Å and volume = 5440.0(12) Å³. Finally, compound **7** crystallized in



Scheme 1.6. Synthesis of phenylethynyl derivatives **3**, **8** and **9**.

space group *C2/c* of the monoclinic system with unit-cell dimensions of $a = 22.942(2) \text{ \AA}$, $b = 5.9810(6) \text{ \AA}$, $c = 37.788(4) \text{ \AA}$, $\beta = 93.314(3)^\circ$ and volume = $5176.4(9) \text{ \AA}^3$.

In the three crystal structures the phenyl and thienyl rings are not coplanar with the carbazole core. Specifically, the phenyl ring in compound **3** exhibits the highest deviation of planarity with a twist angle of 63.3° , whereas the two thienyl rings are only twisted 9.7° and 15.2° in the thienyl derivative **6** and 7.7° and 24.4° in the thienylethynyl derivative **7**. S1–C3 and S2–C18 atoms of the thienyl rings in the crystal structure of compound **6** and S1–C3 and S2–C22 atoms of compound **7** were found to be disordered. A similar behaviour was previously reported for the crystal structure of compound **4**,^[86] where it was stated that thienyl rings could freely rotate along

the bond with the carbazole core and consequently the S atom of the thienyl ring could interchange its position with that of the corresponding C atom.

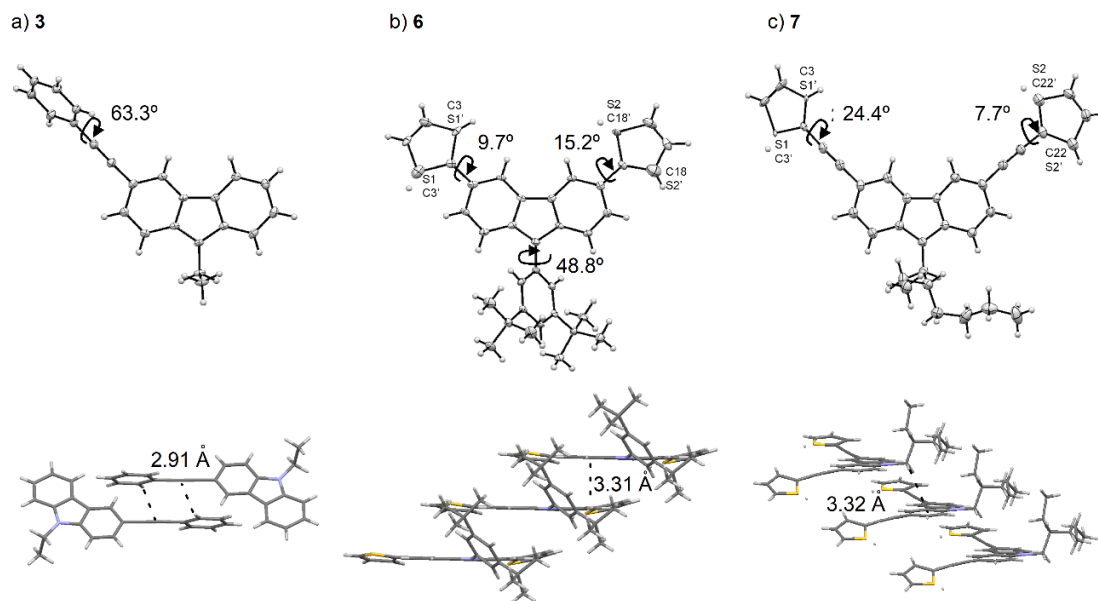


Figure 1.1. X-ray crystal structures, showing the 50% probability displacement, and representative intermolecular interactions of compounds a) **3**, b) **6** and c) **7**.

The molecular packing of the monosubstituted phenylethynyl compound **3** is characterized by numerous short intermolecular contacts, consisting on C–H \cdots π interactions, whereas no significant π – π stacking interactions are observed. Disubstituted thienylethynyl compound **7** also shows C–H \cdots π interactions. In addition, the sulphur atoms S1 and S2 of the thienyl units also show short intermolecular contacts with the carbazole core of neighbouring molecules with distances of 3.00 and 3.57 Å, respectively. Nevertheless, short contacts responsible for significant π – π stacking interactions are neither observed. On the contrary, the disubstituted thienyl-based molecule **6** shows slipped π – π stacking interactions with a distance of 3.31 Å between two adjacent carbazole planes.

1.2.3. Characterization of the organic semiconductors

Thermal properties

Thermal properties of compounds **1–9** were examined by thermogravimetric analysis (TGA) and differential scanning calorimetry (DSC) under a nitrogen atmosphere (Table 1.1; DSC curves can be

found in Appendix B). Thermal decomposition starts at higher temperatures ($T_d > 300$ °C) for the disubstituted derivatives **4–6** and **8–9** than for the corresponding monosubstituted ones (**1–3**) (240 to 263 °C). The nature of the substitution on the nitrogen atom of the carbazole core has no significant influence on the decomposition temperature.

Table 1.1. Thermal properties of carbazole-based compounds **1–9**.

Compound	T_d (°C) [a]	T_m (°C) [b]	T_g (°C) [b]
1	240	81	5
2	263	100	18
3	256	108	11
4	299	217	–
5	307	101	8
6	324	219	–
7	182	96	11
8	329	167	51
9	344	107	19

[a] Decomposition temperature (T_d) corresponding to the 5 % weight loss obtained from TGA performed at a heating rate of 20 °C min⁻¹. [b] Melting point (T_m) and glass transition temperature (T_g) obtained from DSC performed at a scan rate of 10 °C min⁻¹.

DSC measurements reveal that the here studied compounds are able to form amorphous molecular materials, except derivatives **4** and **6**. The length of the *N*-alkyl chain influences significantly the glass transition temperatures. Indeed, dithienyl derivative **5**, with the longer *N*-alkyl 2-ethylhexyl chain shows a T_g of 8 °C, in front of the crystalline behaviour of analogues **4** and **6**. In a similar way, diphenylethynyl derivative **8**, with the shorter *N*-alkyl chain, the ethyl one, exhibits a higher glass transition temperature at 51 °C than the corresponding 2-ethylhexyl substituted analogue **9** ($T_g = 19$ °C). Consequently, for the OLED application of this series of compounds, derivative **8** arises as the unique candidate with improved film-forming capability and morphological stability due to its thermal stability and enhanced T_g value above room temperature.

Optical properties

Table 1.2 collects the optical properties for compounds **1–9** determined in 10 μM THF solutions and in vacuum-evaporated thin films. The UV-vis absorption spectra of the monosubstituted compounds **1–3** display the absorption maximum at lower wavelengths than the corresponding

disubstituted counterparts **4–9** in both THF solution and in the solid state. For all of them a bathochromic shift of the wavelength of maximum absorption in the range of 1–14 nm is registered for the vacuum-evaporated solid samples in comparison to THF solutions. The largest bathochromic shift corresponds to the compounds with the stronger electron-donating thienyl unit and without the ethynylene spacer. Indeed, in agreement with the single-crystal X-ray data, thienyl-based compounds show a more planar molecular structure leading to a more extended π -conjugation.

Figure 1.2 displays the emission spectra of THF solutions and vacuum-deposited thin films of compounds **1–9**. Those compounds that incorporate the triple bond in its structure exhibit in general a hypsochromic shift of the emission band. PL quantum yields are not influenced by the nature of the *N*-substitution of the carbazole core. Phenylethynyl-based derivatives **3**, **8** and **9** show the highest PL quantum yields of all the series of compounds. In the solid state, the fluorescence emission can be expected to decrease due to strong intermolecular π - π stacking interactions and non-radiative decay processes.^[87] As deduced from the single crystal data, a close molecular packing

Table 1.2. Optical properties of compounds **1–9**.

Compd.	Solution			Solid state		
	$\lambda_{\text{abs,max}}$ (nm) [a,b] [ϵ ($\text{M}^{-1} \text{cm}^{-1}$)]	$\lambda_{\text{em,max}}$ [a,b] (nm)	Φ_f [c]	$\lambda_{\text{abs,max}}$ [a,d] (nm)	$\lambda_{\text{em,max}}$ [a,d] (nm)	Φ_f [e]
1	299 (35 925)	376, 395	0.12	313	400	0.09
2	304 (37 944)	368, 386	0.04	310	404	0.09
3	299 (42 835)	365, 383	0.33	308	400	0.12
4	315 (42 710)	388, 409	0.05	328	418	0.05
5	314 (40 978)	388, 408	0.05	325	421	0.05
6	313 (54 696)	385, 405	0.05	318	410	0.04
7	312 (53 400)	380, 398	0.15	320	398	0.06
8	312 (55 546)	374, 394	0.27	318	402	0.11
9	312 (64 737)	374, 394	0.28	313	405	0.10

[a] Wavelength of maximum absorption ($\lambda_{\text{abs,max}}$), molar absorption coefficient (ϵ), and wavelength of maximum emission ($\lambda_{\text{em,max}}$). Emission spectra were recorded after excitation at the wavelength of maximum absorption.

[b] Determined in 10 μM THF solutions at room temperature. [c] Fluorescence quantum yield (Φ_f) measured in THF solution using 1,4-bis(5-phenyl-2-oxazolyl)benzene as the standard ($\Phi_f = 0.93$ in cyclohexane solution) after excitation at 300 nm. [d] Measured from vacuum-evaporated thin films on quartz substrates at room temperature.

[e] Fluorescence quantum yield (Φ_f) of thin films recorded in an integrating sphere.

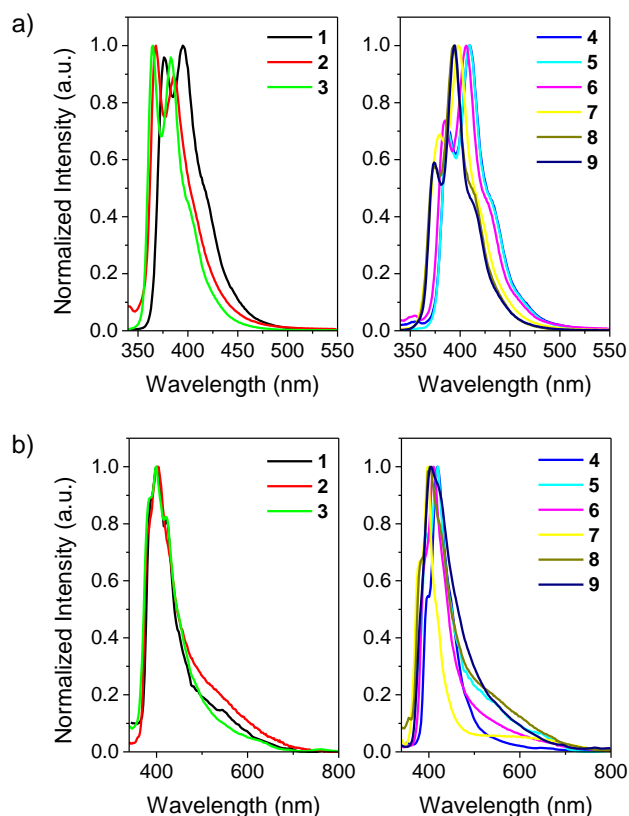


Figure 1.2. Emission spectra of the monosubstituted derivatives **1–3** (left) and of the disubstituted derivatives **4–9** (right) a) in 10 μM THF solutions and b) of vacuum-evaporated thin films.

of the phenylethynyl compound **3** is hindered in the solid state due to the larger twist angle of the phenyl moiety. Therefore, phenylethynyl based compounds could be expected to display higher emission efficiencies than the thienyl or thienylethynyl analogues.

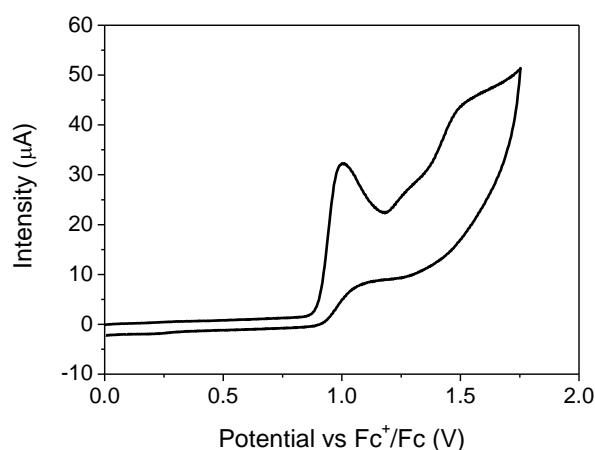
Electrochemical properties

Table 1.3 collects the electrochemical data for compounds **1–9**. Cyclic voltammogram of compound **8** is shown in Figure 1.3 as a representative example; cyclic voltammograms for all the series of compounds are collected in Appendix B. All the compounds underwent irreversible oxidation processes, whereas no reduction processes were observed. Ionization potentials (IP) were estimated from the onset oxidation potentials, and electron affinities (EA) as the difference between IP and the optical gap energies ($E_{\text{gap}}^{\text{opt}}$), where $E_{\text{gap}}^{\text{opt}}$ was obtained from the UV-vis absorption spectra.

Table 1.3. Electrochemical properties of compounds 1–9.

Compd.	$E_{\text{onset}}^{\text{ox}}$ (V) [a]	$E_{\text{gap}}^{\text{opt}}$ (eV) [b]	IP (eV) [c]	EA (eV) [d]	$-E_{\text{HOMO}}^{\text{DFT}} / -E_{\text{LUMO}}^{\text{DFT}}$ (eV)	IP (eV) [e]
1	0.50	3.50	5.89	2.39	5.13 / 0.79	5.53
2	0.65	3.43	6.04	2.61	5.05 / 1.13	5.48
3	0.67	3.57	6.06	2.49	5.12 / 0.98	5.54
4	0.48	3.40	5.87	2.47	5.09 / 0.91	5.38
5	0.48	3.39	5.87	2.48	–	5.42
6	0.54	3.41	5.93	2.52	5.06 / 0.87	5.19
7	0.68	3.35	6.07	2.72	–	5.67
8	0.69	3.42	6.08	2.66	5.10 / 1.18	5.69
9	0.70	3.43	6.09	2.66	–	5.54

[a] Onset oxidation potential ($E_{\text{onset}}^{\text{ox}}$) vs. Fc^+/Fc determined from CV in 1 mM acetonitrile solutions at a scan rate of 100 mV s^{-1} . [b] Optical energy gap ($E_{\text{gap}}^{\text{opt}}$) estimated from the absorption spectra. [c] Ionization potential (IP) estimated from CV as $\text{IP} = E_{\text{onset}}^{\text{ox}} \text{ vs. } \text{Fc}^+/\text{Fc} + 5.39$. [d] Electron affinity (EA) estimated as $\text{EA} = \text{IP} - E_{\text{gap}}^{\text{opt}}$. [e] Ionization potential of vacuum-evaporated thin films determined by the photoelectron emission technique in air.

**Figure 1.3.** Cyclic voltammogram of compound 8 recorded at a scan rate of 100 mV s^{-1} in 1 mM acetonitrile solution.

Mono- and disubstituted thienylethynyl derivatives **2** and **7** show slightly higher IP values (6.04 and 6.07 eV) in comparison to those of the thienyl analogues **1** and **5** (5.89 and 5.87 eV). On the other hand, compounds that incorporate the phenylethynyl unit show similar IP values to the thienylethynyl-based compounds. Therefore, the ethynylene spacer yields materials with higher ionization potentials, that is, with slightly more stable HOMO levels.

DFT calculations

To gain insight into the structure-properties relationship of this series of compounds at the molecular level, density functional theory (DFT) calculations (B3LYP, 6-31G(d,p)) were carried out for compounds **1–4**, **6** and **8**. Compounds with the shorter *N*-alkyl ethyl chain and the *N*-aryl 3,5-di-*tert*-butylphenyl group were selected for theoretical calculations. Potential energy surface (PES) scans were conducted on compounds **1–3** by rotating the thienyl and phenyl moieties from 0 to 360° in steps of 20° (Figure A1 in Appendix A). The lowest energy structures correspond to rotation angles about 30°/150° for **1** and 0°/180° for **2** and **3**. The theoretical approach shows good correlation with the single crystal data of the thienyl-based molecules **6** and **7** with twist angles between 10 and 24° (Figure 1.1). On the contrary, the phenyl group of **3** in the crystal structure shows a twist angle of 63°. A similar geometry was described in the crystal structure of 3,6-di(4-pyridylethynyl)carbazole.^[88] To explain this phenomenon, the rotation barriers of the thienyl and phenyl moieties were estimated from PES. The rotation barriers for **1–3** were estimated to be 12, 2.8 and 3.6 kJ mol⁻¹, respectively. Similar rotation barriers for the disubstituted compounds can be expected. For all the calculated compounds these energies are higher than the thermal energy at room temperature, which is defined as $k_B T = 2.48$ kJ mol⁻¹ (or 25.7 meV), where k_B is the Boltzmann constant. Thus, stabilization of the twisted structures via intermolecular interactions in the solid state was proposed. The interaction energies between molecules with C–H··· π or π – π contacts were estimated as –34.1, –40.5 and –46.2 kJ mol⁻¹ for compounds **3**, **6** and **7**, respectively, which are higher than the rotation barriers of the thienyl and phenyl moieties. These results suggest that the supramolecular interactions should be the responsible of the twisted conformers found in the crystal structures. PES scans of HOMO and LUMO energies were predicted from DFT calculations by rotating the thienyl and phenyl moieties from 0 to 360° in steps of 20° (Figure A1 in Appendix A). LUMO energies remain almost unaltered and only HOMO energies change with rotation of the thienyl and phenyl groups, corresponding the lowest HOMO energies to the perpendicular disposition of the two aryl moieties.

Figure 1.4 displays the HOMO and LUMO orbitals of compounds **1–4**, **6** and **8**. DFT studies indicate that the HOMO levels are delocalized over the aromatic molecule, which benefits the hole-transporting properties. The LUMO levels remain on the carbazole fragment in the thienyl-based molecules **1**, **4** and **6**. On the other hand, the LUMO levels in molecules containing the ethynylene spacer are extended to both the carbazole and the thienylethynyl or phenylethynyl units. Both the LUMO energies acquired from DFT calculations and from CV measurements of the thienyl-based

compounds **1**, **4** and **6** are higher than the LUMO energies of the compounds containing the triple bond connector (compounds **2**, **3** and **8**).

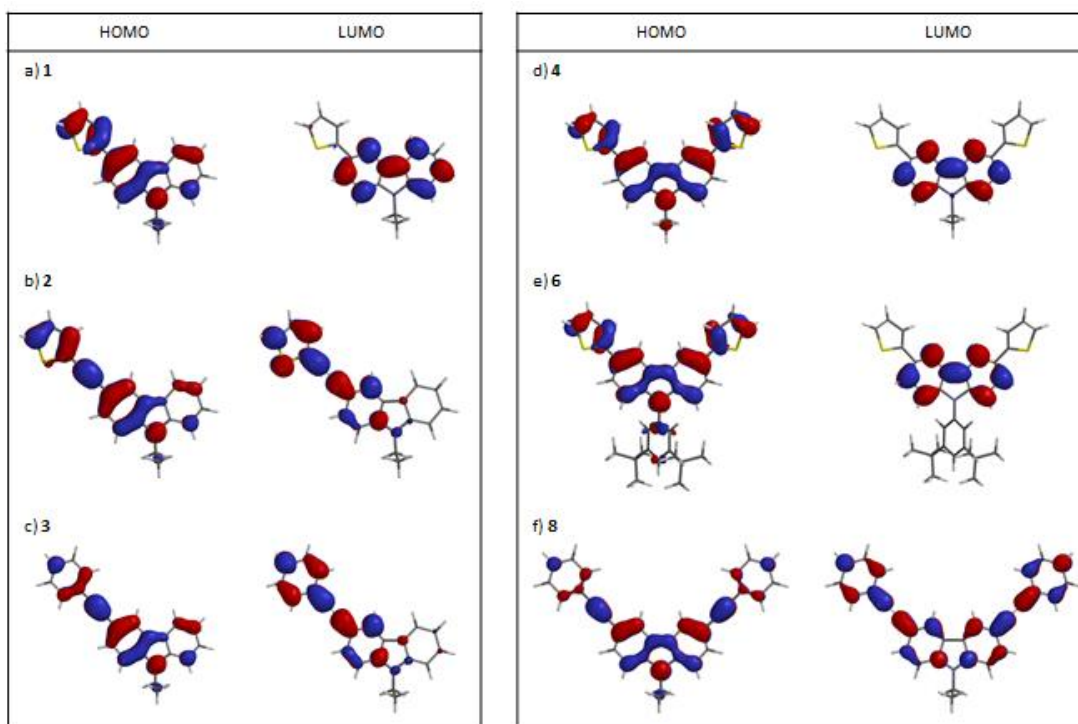


Figure 1.4. Computed spatial distributions of HOMO and LUMO orbitals for compounds **1–4**, **6** and **8**.

Ionization potentials (IP) of vacuum-deposited thin films of compounds **1–9** were determined by the electron photoemission method in air (Table 1.3 and Appendix B) giving lower values (5.19–5.69 eV) than those determined in solution (5.87–6.09 eV). This differential behaviour has been previously reported.^[89]

All the here reported materials display suitable ionization potentials and high optical gaps, showing potential behaviour as hole-transporting materials. Among the structural parameters discussed herein, the one that seems to perform a major influence on the properties of this series of luminescent organic semiconductors is the presence of the ethynylene linker, which concerns the molecular geometry and as a consequence the crystal packing and the photoluminescence properties. With regard to the nature of the donor unit (thienyl or phenyl), although there is no influence on the electrochemical properties, it should be taken into account that the phenyl unit provides enhanced emission efficiencies, both in solution and in the solid state.

1.2.4. Charge transport properties

Charge-transporting properties of vacuum-deposited layers of this series of compounds were studied by the time-of-flight (TOF) technique (Table 1.4). Representative TOF transients for hole transport in the log-log scale of compound **8** are displayed in Figure 1.5. TOF transients and the dependency of hole drift mobilities on the square root of the electric field for the series of compounds are shown in Appendix B. Not good quality amorphous films could be prepared from compounds **3** and **7**, neither by vacuum evaporation nor by drop casting technique.

Table 1.4. Hole mobility data of compounds **1**, **2**, **4–6**, **8** and **9** determined by means of the TOF technique.

Compound	μ_h ($\text{cm}^2 \text{V}^{-1} \text{s}^{-1}$) [E (V cm^{-1})] [a]	μ_0 ($\text{cm}^2 \text{V}^{-1} \text{s}^{-1}$) [b]	α (cm V^{-1}) ^{1/2} [c]
1	8×10^{-5} [3.1×10^5]	3×10^{-5}	0.0018
2	4×10^{-4} [2.6×10^5]	3×10^{-6}	0.0096
4	2×10^{-4} [1.9×10^5]	5×10^{-7}	0.0135
5	2×10^{-4} [3.2×10^5]	2×10^{-5}	0.0041
6	4×10^{-4} [3.7×10^5]	6×10^{-5}	0.0032
8	6×10^{-4} [4.6×10^5]	9×10^{-6}	0.0060
9	2×10^{-3} [5.2×10^5]	1×10^{-5}	0.0071

[a] Hole mobilities (μ_h) at the corresponding electric field (E). [b] Zero-field mobilities (μ_0). [c] Field dependences (α). Measurements were determined in air and at room temperature. Layers with thicknesses around 0.56–2.52 μm were prepared by vacuum evaporation of the organic materials.

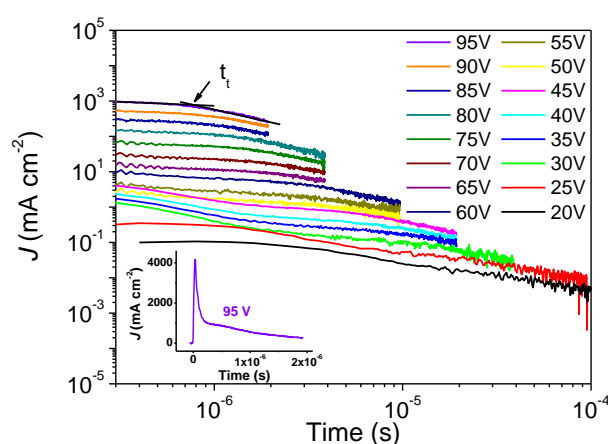


Figure 1.5. TOF transients in the log-log scale for **8** vacuum-deposited layer with thickness of 2.04 μm . Inset shows one transient curve in the linear scale.

Transient curves in the linear scale show a dispersive behaviour, being the vacuum-deposited layers of diphenylethynyl compounds **8** and **9** those with the lowest dispersive transport. Nevertheless, transient times have been determined in the log-log scale. Hole mobilities around $10^{-4} - 10^{-3} \text{ cm}^2 \text{ V}^{-1} \text{ s}^{-1}$ were achieved at high electric fields of $2-5 \times 10^5 \text{ V cm}^{-1}$.

1.2.5. Organic Light-Emitting Diodes

The performance of a non-doped OLED device based on compound **8** was investigated and furthermore, the emission mechanism of the OLED device was elucidated by means of DFT studies. Compound **8** exhibited a high thermal stability ($T_d = 329 \text{ }^\circ\text{C}$) and the highest glass transition temperature of all the series of monocarbazole derivatives **1-9** ($T_g = 51 \text{ }^\circ\text{C}$), which is crucial for the morphological stability of the film. Besides, compound **8** exhibited blue photoluminescence with a maximum emission peak centred at 402 nm in the solid state with CIE chromaticity coordinates at (0.21, 0.18). On the other hand, although compounds **1-9** showed low emission efficiencies in the solid state, the quantum yield of phenylethynyl derivative **8** is among the highest values ($\Phi_f = 0.11$) of all the series.

Non-doped OLED device with structure ITO/MoO₃ (5 nm)/**8** (45 nm)/BPhen (15 nm)/Ca (14 nm)/Al (85 nm) was fabricated by a step-by-step deposition process of the different layers by the vacuum evaporation technique (10^{-6} mbar). MoO₃ was used as hole-transporting layer^[90] and BPhen (Bathophenanthroline) as electron-transporting layer. The energy band diagram is shown in Figure 1.6a.

Figure 1.6b-d displays the current density-voltage-luminance characteristics and efficiencies of the OLED device. It should be highlighted the very low and competitive turn-on voltage of only 4 V achieved for the device, indicating an efficient and balanced charge injection, transport and recombination. A high maximum brightness of 14305 cd m^{-2} was attained at 12 V. OLED device exhibited a high maximum current efficiency of 3.3 cd A^{-1} , a maximum power efficiency of 1.2 lm W^{-1} and a maximum external quantum efficiency (EQE) of 1.0%. Although further optimization of the device configuration should be done, these results indicate that compound **8** exhibits competitive device performance in comparison to literature reported OLED devices based on carbazole derivatives with blue emission.^[73]

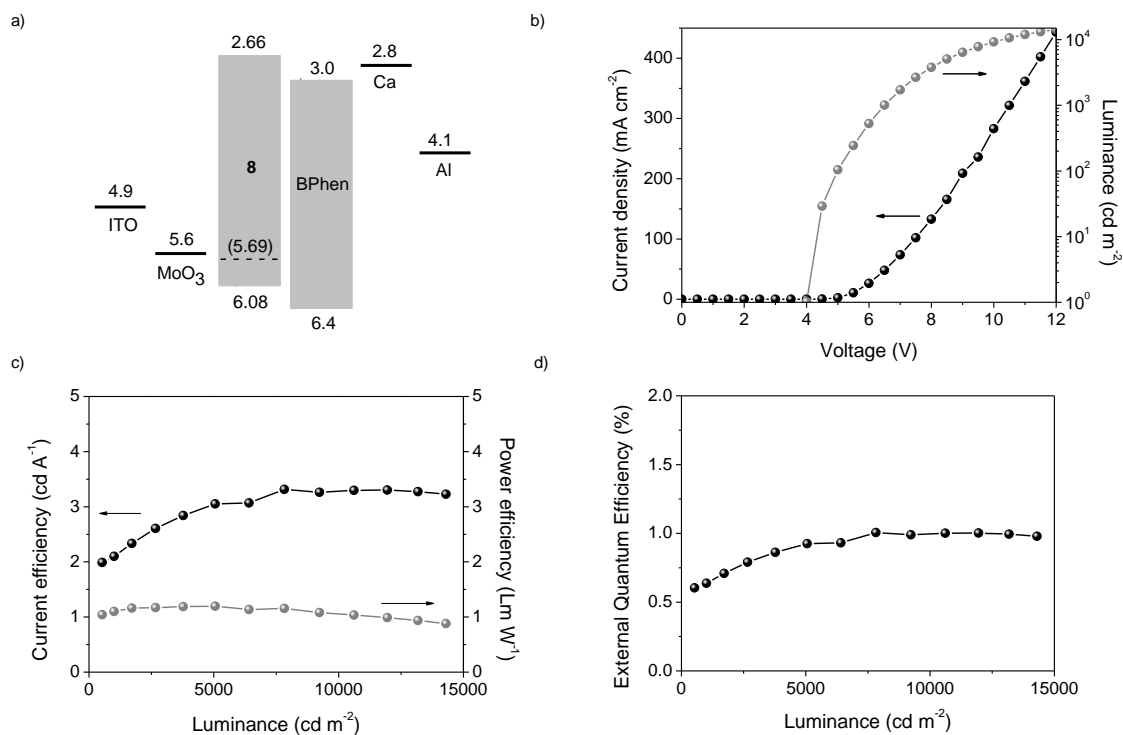


Figure 1.6. a) Energy level diagram of the device of compound **8**. The dashed line in **8** component indicates the ionization potential obtained from the photo-emission in air technique. This value is displayed in parentheses. b) Current density-voltage-luminance characteristics. c) Current efficiency and power efficiency *versus* luminance. d) External quantum efficiency *versus* luminance.

The external electroluminescence quantum efficiency (EQE) of OLEDs can be described according to eqn (20), which was presented in section 1.2 of the General Part:

$$\text{EQE} = \rho \times QY \times \phi \times \eta_{out} \quad (20)$$

Considering the ideal of $\rho = 1$, $QY = 11\%$, and estimating η_{out} as $\sim 20\%$ at maximum EQE of the device, the efficiency of electrically generated excitons conversion to light (ϕ) was calculated to be 45%. This result clearly indicates that the here presented device overcame the theoretical limit of 25% for the singlet exciton production efficiency that is assumed for fluorescence-based OLEDs. In the case of the triplet-triplet annihilation (TTA) or of thermally activated delayed fluorescence (TADF) mechanisms, that can harvest both singlet and triplet excited states, the theoretical limits are 62.5%^[91] and 100%,^[57] respectively. However, the possibilities of the TTA mechanism seem to be excluded in view of the linear growth of the luminance - current density curve. On the other hand, the TADF mechanism is excluded due to the large energy difference between the first excited singlet and triplet states ($\Delta ST = 0.58$ eV) of compound **8**. The ΔST value was

estimated from the first peak of the low-temperature fluorescence spectrum and the first vibronic peak of the low-temperature phosphorescence spectrum (Figure A2 in Appendix A). The high ϕ of **8** could be attributed to the triplet exciton contribution from the reverse intersystem crossing (RISC) process along the possible high-lying excited state (hot excitons) channel.^[92]

TD-DFT calculations were performed in order to prove this statement. Taking into account the twist angle of the phenyl moiety of 63° from the single crystal data of **3** (Figure 1.1), the rotation barriers of S_1 and T_1 states for compound **3** were theoretically estimated to be 24 and 26 kJ mol^{-1} , respectively, being lower than the intermolecular interaction energy (see section 1.2.3 of Chapter 1). Therefore, it could be stated that the conformation of **3** is fixed in the excited states. This behaviour was assumed as a model for compound **8** in the solid state and a conformer of **8** was optimised considering twist angles of 63° for the corresponding phenyl moieties. TD-DFT calculations were performed, using both the twisted and flatted structure coordinates of **8** in the ground state, in order to estimate the excitation energies of the six lowest excitation states, corresponding to the singlet-singlet ($S_n \rightarrow S_0$) and triplet-singlet ($T_n \rightarrow S_0$) electronic transitions, together with their respective transition strengths (Figure 1.7). For the twisted structure of **8**, which

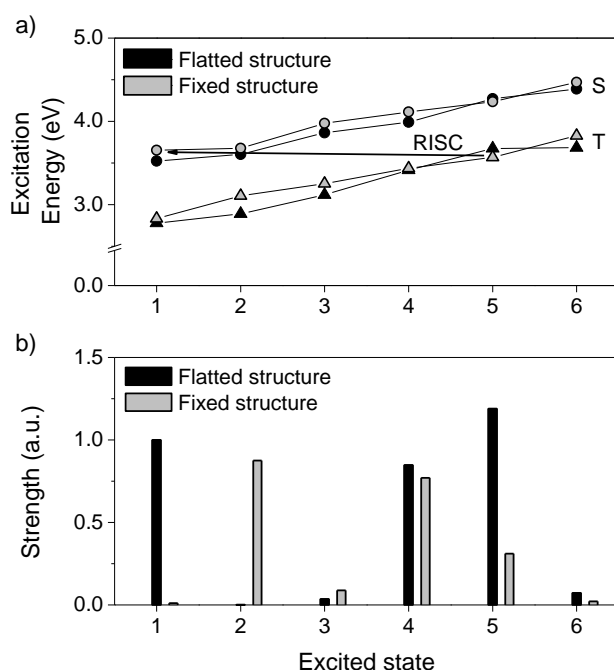
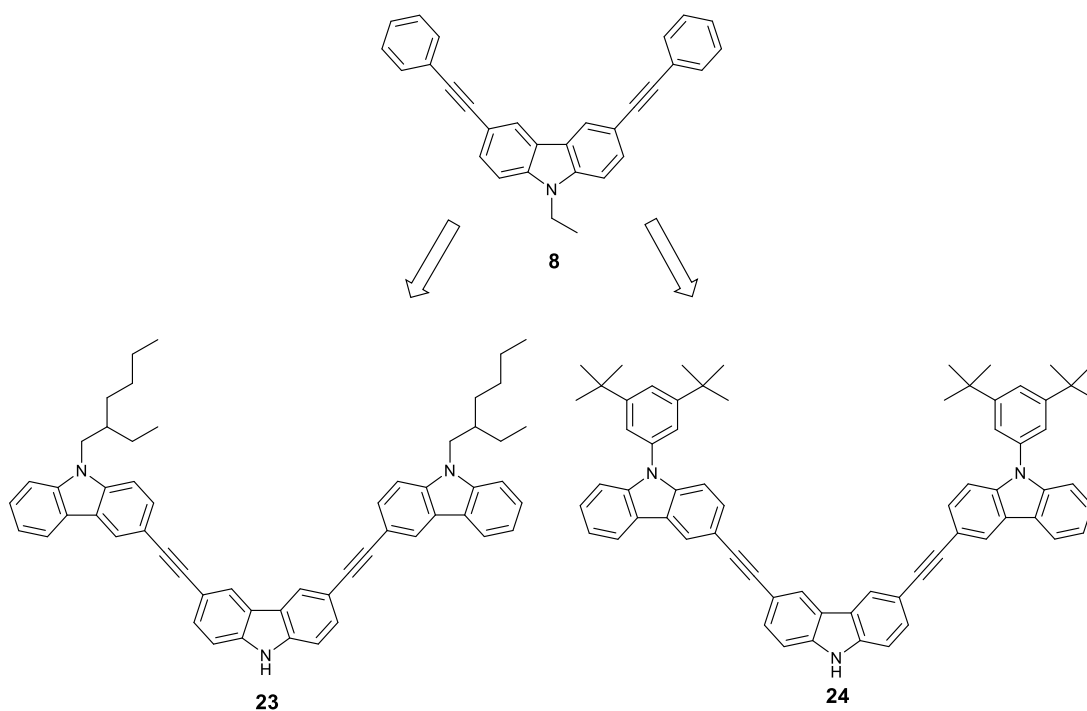


Figure 1.7. a) Calculated harvesting singlet and triplet excitons for luminescence for flatted (black symbols) and fixed (grey symbols) structures of **8**, corresponding to $S_n \rightarrow S_0$ and $T_n \rightarrow S_0$ electronic transitions. b) Calculated transition strengths of $S_n \rightarrow S_0$ electronic transitions for flatted (black symbols) and fixed (grey symbols) structures of **8**.

is fixed in the solid state due to intermolecular interactions, the transition strength of $S_1 \rightarrow S_0$ is low (0.0106 a.u.) because it is a symmetry-forbidden transition of the carbazole moiety, whereas the $S_2 \rightarrow S_0$ transition has a much higher probability and strength of 0.875 a.u.^[93] These results suggest that emission occurs from S_1 and S_2 states. Moreover, for the twisted structure of **8**, an energy transfer from the T_5 "hot exciton" to S_1 state via RISC is here proposed, because the energy difference between these states was estimated to be of only 85 meV.

1.3. Tricarbazole derivatives containing ethynylene linkers as deep-blue emitters

This section is focused on obtaining materials with emission in the solid state at longer wavelengths than monocarbazole derivatives **1–9** but in the deep-blue region of the visible spectrum, with the CIE y coordinate lower than 0.1. Deep-blue emitters in OLEDs are of vital importance for full-color display and lighting applications. Thus, two new dyes were prepared based on compound **8** by replacing the peripheral phenyl groups for carbazole units in order to extend the π -conjugated system and to increase the emission efficiencies in the solid state (Scheme 1.7).

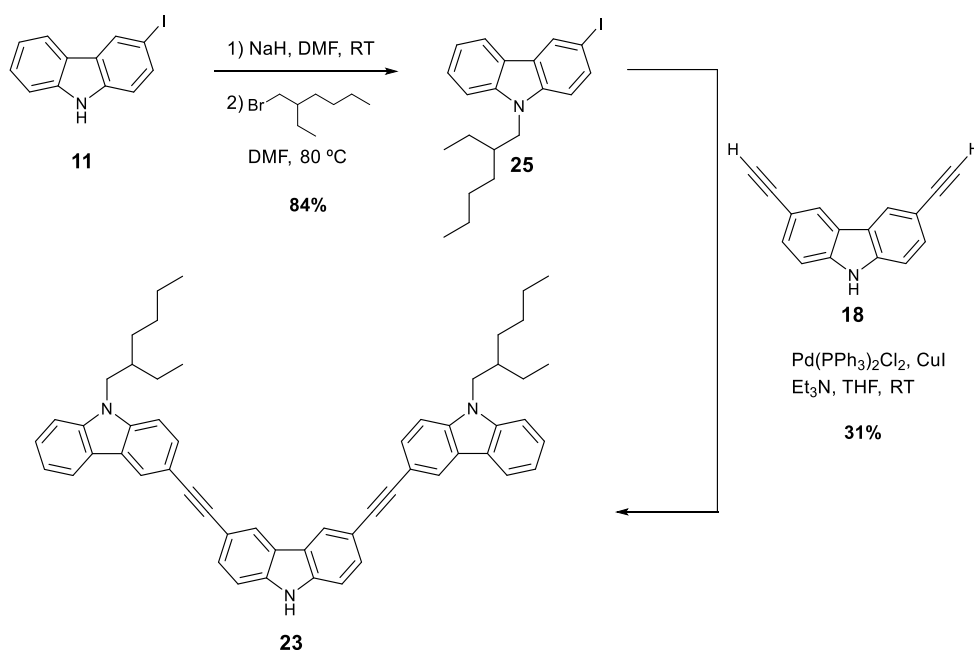


Scheme 1.7. Chemical structures of tricarbazole derivatives **23** and **24**.

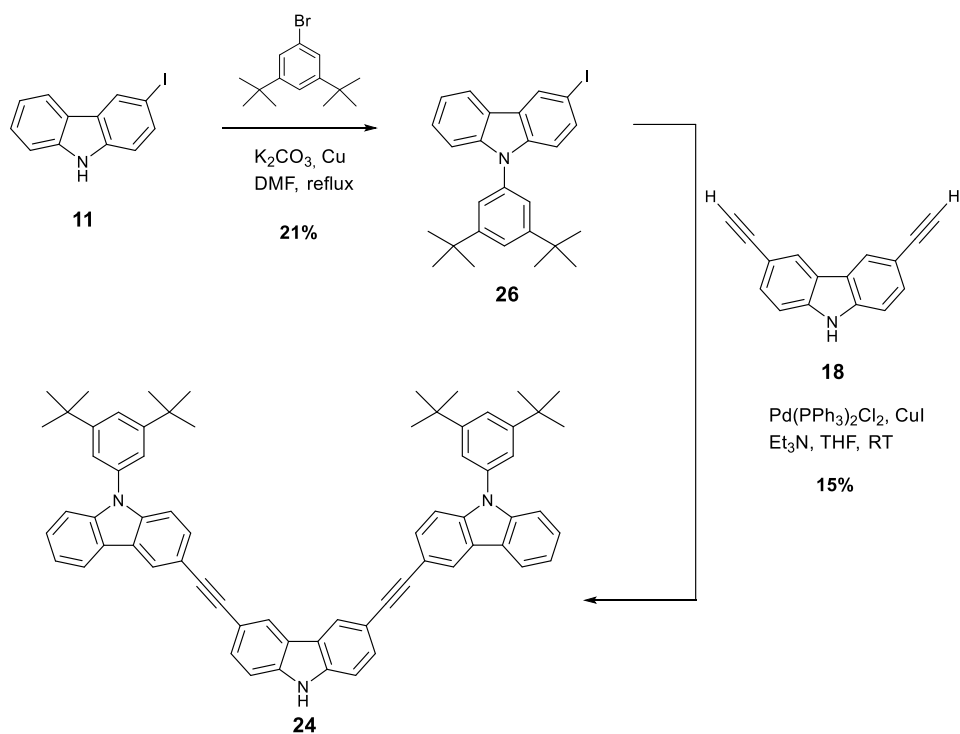
The ethynylene linkers were retained in order to promote luminescence in the deep-blue zone of the visible spectrum. Whereas the central carbazole unit was left with no substitution in the nitrogen atom to favour electronic delocalization, the two external carbazole units connected to the 3,6 positions of the central core were substituted in the nitrogen atom by two different groups to introduce steric hindrance to obtain materials with a stable amorphous phase above room temperature and higher quantum yields.

1.3.1. Synthesis

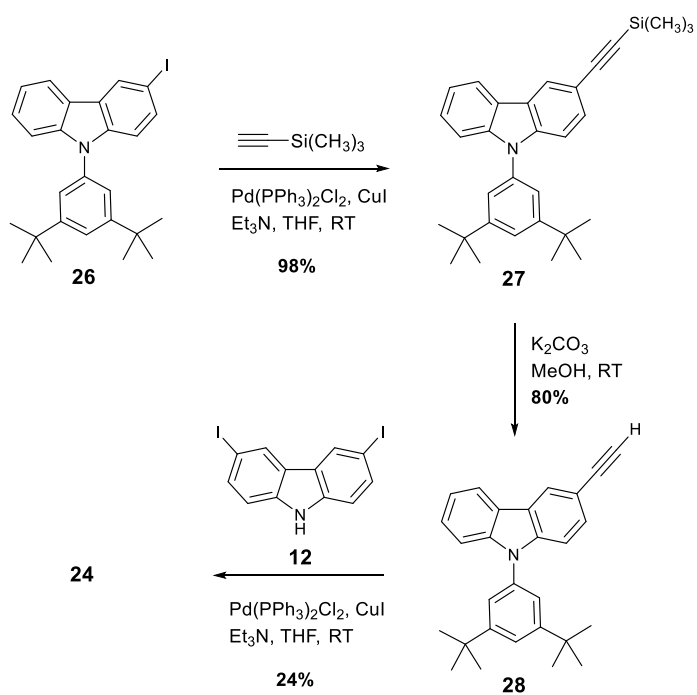
Scheme 1.8 and 1.9 display the synthetic route to 3,6-bis[2-(9-(2-ethylhexyl)-9H-carbazol-3-yl)ethynyl]-9H-carbazole (**23**) and 3,6-bis[2-(9-(3,5-di-*tert*-butylphenyl)-9H-carbazol-3-yl)ethynyl]-9H-carbazole (**24**), respectively. Sonogashira couplings between either **25** or **26** and 3,6-diethynyl-9H-carbazole (**18**) in the presence of triethylamine under Pd(PPh₃)₂Cl₂ catalysis gave final derivatives **23** and **24**, respectively. Previously, compounds **25**^[94] and **26** were prepared from 3-iodo-9H-carbazole (**11**) via the alkylation reaction with 2-ethylhexyl bromide under standard conditions and the Ullmann coupling reaction with 1-bromo-3,5-di-*tert*-butylbenzene, respectively.



Scheme 1.8. Synthesis of compound **23**.



Scheme 1.9. Synthesis of compound **24** (Method A).



Scheme 1.10. Synthesis of compound **24** (Method B).

In order to get coupling product **24** in higher yield, a second synthetic route was investigated (Scheme 1.10). For that purpose, 9-(3,5-di-*tert*-butylphenyl)-3-[2-(trimethylsilyl)ethynyl]-9*H*-carbazole (**27**) and 9-(3,5-di-*tert*-butylphenyl)-3-ethynyl-9*H*-carbazole (**28**) were firstly prepared from compound **26** and then coupled to 3,6-diiodo-9*H*-carbazole (**12**), affording a slight increase in the yield from 15 to 24% in the last Sonogashira reaction. It should be mentioned that this last route involved enhanced yields in the previous synthetic steps.

1.3.2. Characterization of the organic semiconductors

Thermal properties

Compound **23** exhibits higher thermal stability ($T_d = 431$ °C) than monocarbazole derivative **8** ($T_d = 329$ °C) as revealed by TGA experiments. On the other hand, tricarbazole **23** show an enhanced glass transition temperature of 67 °C in comparison to **8** ($T_g = 51$ °C), which can be attributed to the increase of the molecular size and weight. Therefore, the introduction of three carbazole units into the molecular structure affords materials with enhanced thermal stability and with a stable amorphous phase above room temperature.

Optical properties

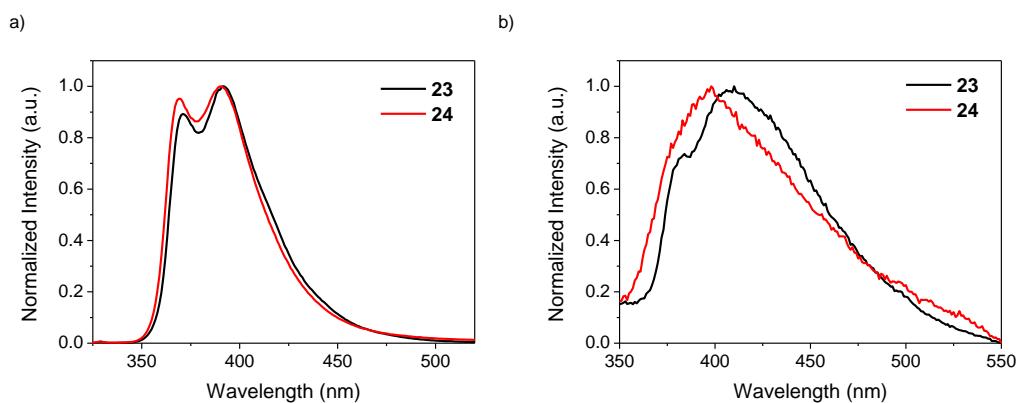
The photophysical properties of dyes **23** and **24** in solution and in the solid state are summarized in Table 1.5. Fluorescence measurements in dichloromethane solution, after excitation at 300 nm, show maximum fluorescent peaks centred at 371 and 392, and at 369 and 390 nm, for **23** and **24**, respectively. The emission in solid state samples after photoexcitation renders a single peak in both cases located at 410 and 398 nm, respectively (Figure 1.8). The bathochromic shift observed in the solid state emission, compared to the measurements in solution, is more evident on the **23** molecule, allowing better van der Waals interactions between neighbouring molecules, in comparison to compound **24** with the 3,5-di-*tert*-butylphenyl group,.

The quantum yield of the *N*-aryl substituted **24** solid state thin films drops from 0.31 in solution to 0.11 in the solid state, while the *N*-alkylated analogue **23** maintain substantially unchanged its fluorescence efficiency. Therefore, the introduction of the 2-ethylhexyl substitution on the carbazole units has demonstrated to be more efficient to avoid the quenching of the fluorescence, than the introduction of a steric hindrance demanded 3,5-di-*tert*-butylphenyl group.

Table 1.5. Optical properties of compounds **23** and **24**.

Compd.	Solution			Solid state		
	$\lambda_{\text{abs,max}}$ (nm) [a] [ϵ ($\text{M}^{-1} \text{cm}^{-1}$)]	$\lambda_{\text{em,max}}$ [b,c] (nm)	Φ_f [d,e]	$\lambda_{\text{em,max}}$ [b,f] (nm)	Φ_f [d,g]	CIE [h]
23	305 (84 451)	371, 392	0.39	410	0.31	(0.17, 0.07)
24	305 (80 919)	369, 390	0.31	398	0.11	(0.18, 0.11)

[a] Wavelength of maximum absorption ($\lambda_{\text{abs,max}}$) and molar absorption coefficient (ϵ) determined in 10 μM CH_2Cl_2 solutions at room temperature. [b] Wavelength of maximum emission ($\lambda_{\text{em,max}}$). Emission spectra were recorded after excitation at 300 nm. [c] Determined in 10 μM CH_2Cl_2 solutions at room temperature. [d] Fluorescence quantum yield (Φ_f) measured using 1,4-bis(5-phenyl-2-oxazolyl)benzene as the standard ($\Phi_f = 0.93$ in cyclohexane solution) after excitation at 300 nm. [e] Determined in CH_2Cl_2 solution. [f] Measured from thin films on quartz substrates. Films were prepared by spin coating from a 1 mM dichloromethane solution at 1500 rpm for 20 s and at 3500 rpm for 10 s followed by 5 min of thermal annealing at 50 $^\circ\text{C}$. [g] Determined from solid films. [h] Colour rendering indexes (CIE) of thin films were calculated after excitation at 310 nm.

**Figure 1.8.** Emission spectra of compounds **23** and **24** a) in dichloromethane at a concentration of 10 μM and b) in the solid state.

It is worth to take into account that the three carbazole units in molecules **23** and **24** are linked by a triple bond. When the triple bond is used as a π -spacer the Stokes Shift is reduced in comparison to the double bond analogue^[51b] keeping the fluorescence emission wavelength in the blue zone. It is interesting to highlight that both compounds present a CIE y coordinate in the range of the deep-blue region (CIE y coordinate lower than 0.1).

Electrochemical properties

Electrochemical properties of compounds **23** and **24** were analysed. Both compounds showed one irreversible oxidation process by cyclic voltammetry (Appendix B), being both stable to the

reduction processes, similarly to the characteristics of all the carbazole dyes until now synthesized. Table 1.6 displays the electrochemical characteristics. Similarly to compounds **1–9**, high IP values (~ 5.9 eV) and high optical energy gap values (~ 3.3 eV) were estimated for compounds **23** and **24**, which are indicative of potential hole conduction properties.

Table 1.6. Electrochemical properties of compounds **23** and **24**.

Compound	$E_{\text{onset}}^{\text{ox}}$ (V) [a]	$E_{\text{gap}}^{\text{opt}}$ (eV) [b]	IP (eV) [c]	EA (eV) [d]	IP (eV) [e]
23	0.50	3.32	5.89	2.57	5.33
24	0.56	3.33	5.95	2.62	5.44

[a] Onset oxidation potential ($E_{\text{onset}}^{\text{ox}}$) vs. Fc^+/Fc determined from CV in 1 mM dichloromethane solutions at a scan rate of 100 mV s^{-1} . [b] Optical energy gap ($E_{\text{gap}}^{\text{opt}}$) estimated from the absorption spectra. [c] Ionization potential (IP) estimated from cyclic voltammetry as $\text{IP} = E_{\text{onset vs. Fc}^+/\text{Fc}}^{\text{ox}} + 5.39$. [d] Electron affinity (EA) estimated as $\text{EA} = \text{IP} - E_{\text{gap}}^{\text{opt}}$. [e] Ionization potentials of solid films determined by the photoelectron emission technique in air.

Ionization potentials were also determined in the solid state for compounds **23** and **24** by the photoemission in air method (Table 1.6, Figure 1.9). IP values for compounds **23** and **24** are 5.33 and 5.44 eV, respectively, close to that of indium tin oxide (4.8 eV). The nature of the *N*-substituents of the carbazole core has only a slight influence on the ionization potential values. This observation is in agreement with previous reports where it was found that the modification of the substitution patterns of the carbazole moiety practically does not affect the ionization energy values.^[93,95]

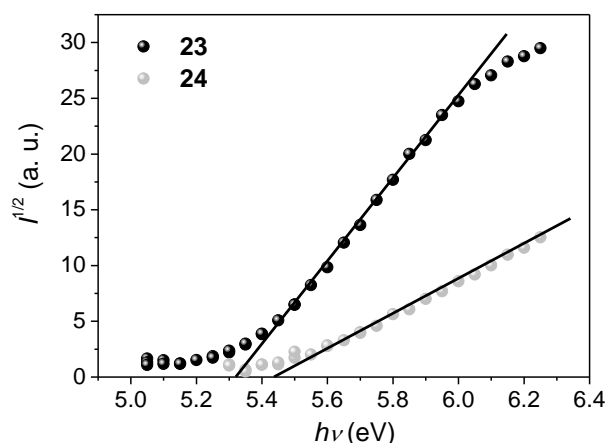


Figure 1.9. Photoemission spectra of the amorphous films of compounds **23** and **24** measured in air at 25°C .

1.3.3. Charge transport properties

For the estimation of hole transport properties, amorphous layers of the synthesized materials were prepared and subjected to the Xerographic Time-of-Flight (XTOF) measurements. Representative XTOF transients for hole transport of compound **23** are displayed in Figure 1.10, showing a dispersive pattern. The attempts to estimate the hole mobility for compound **24** were unsuccessful, due to the much more dispersive mobility registered for that compound.

The hole-transit times (t_t) of **23** were established from intersection points of two asymptotes from the double-logarithmic plots (Figure 1.10a). The dependency of hole drift mobilities on the square root of the electric field for compound **23** is represented in Appendix B. Compound **23** showed a zero field hole drift mobility (μ_0) of $2.6 \times 10^{-7} \text{ cm}^2 \text{ V}^{-1} \text{ s}^{-1}$ and a field dependence parameter (α) of $\sim 0.0087 \text{ (cm V}^{-1})^{1/2}$. Compound **23** showed a hole charge mobility of $2.8 \times 10^{-4} \text{ cm}^2 \text{ V}^{-1} \text{ s}^{-1}$ at an electric field of $6.4 \times 10^5 \text{ V cm}^{-1}$, which is relatively high and useful for practical applications.

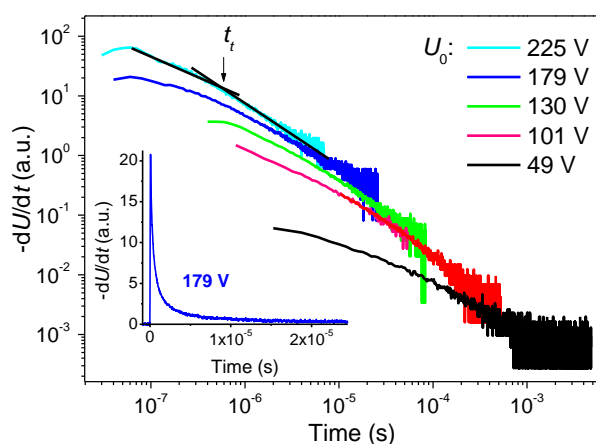


Figure 1.10. XTOF transients for compound **23** measured at 25°C. Insert shows one transient curve in linear plot.

1.3.4. Organic Light-Emitting Diodes

The optical and electrochemical properties of compound **23**, the high quantum yield in the solid state, together with the suitable blue CIE coordinates and hole mobility values confer to **23** the sought characteristics for an efficient luminescent dye in the deep blue emission range. In addition, derivative **23** is soluble in many solvents, overcoming the insolubility of small molecules and

opening the door to the construction of OLEDs by solution processing. Solution-processing methods are attractive in the fabrication of OLED devices because they are associated to low cost and fast productivity. However, as it was mentioned previously, interlayer mixing during the deposition steps can occur when fabricating multilayer devices by solution-processing methods. In order to overcome this trouble, a careful choice of the solvents is required.

Tapping mode Atomic Force Microscopy (AFM) was performed in order to characterize the morphology of the thin film based on compound **23** (Figure 1.11). 25 nm thick films were prepared by spin casting of a chlorobenzene solution of compound **23** on a PEDOT:PSS treated ITO substrate. AFM images show homogeneous and continuous thin films of compound **23** prepared by solution processing with a root-mean-square (rms) roughness of ~ 1.46 nm, showing appropriate morphology layer characteristics.

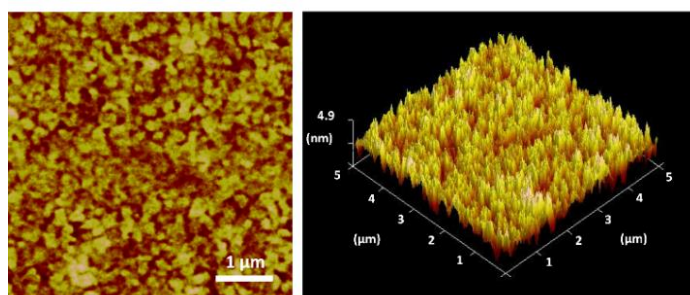


Figure 1.11. AFM image of a solution-processed **23**-based thin film from two different points of view ($5 \times 5 \mu\text{m}^2$).

In this section, non-doped OLEDs were prepared using the solution-processable material **23** as the emitting layer. The OLED configuration consisted on ITO/PEDOT:PSS (25 nm)/**23** (25–55 nm)/TPBi (10 nm)/LiF (1 nm)/Al (100 nm) as shown in Figure 1.12. In order to optimize the performance of the devices different thicknesses, from 25 to 55 nm, of the **23** layer were prepared from chlorobenzene solution by spin coating. Deposition of the emissive layer of compound **23** was also tested from different solvents, such as dichloromethane and tetrahydrofuran.

The performance characteristics of the different devices are summarized in Table 1.7 and Figure 1.13. All the devices show competitive turn-on voltages between 2.6 and 3.6 V indicating small injection barriers from the transporting layers in the device. The luminance increases upon voltage application, reaching the maximum values below 5 V. The maximum luminance values are

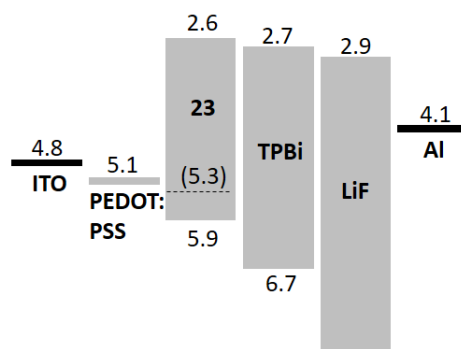


Figure 1.12. Energetic scheme of the different components of the device structure used in this study. The dashed line in **23** component indicates the ionization potential obtained from the photoemission in air technique. This value is displayed in parentheses.

dependent on the thickness of the active layer, reaching the optimum ratio between luminance and current efficiency at 50 nm. Further increase of the thickness leads to a decrease of the maximum luminance and efficiency together with an increase of the turn-on voltage, pointing to growing unbalance of the charge transport in the device. On the other hand, the devices prepared from DCM and THF solutions show poorer performances suggesting the influence of the solvent on the final morphology of the active layer.

Table 1.7. Data of OLED devices based on compound **23**.

Device	Solvent ^[a]	<i>d</i> (nm) ^[b]	<i>V_t</i> (V) ^[c]	<i>L_{max}</i> (cd m ⁻²) ^[d]	<i>η_c</i> (cd A ⁻¹) ^[e]
1	CB	25	2.80	35.59	0.08
2	CB	30	2.68	37.52	0.09
3	CB	40	2.88	40.98	0.09
4	CB	50	3.23	39.46	0.17
5	CB	55	3.62	33.49	0.05
6	DCM	25	2.61	24.75	0.03
7	THF	25	2.62	26.47	0.03

[a] Solvent used for preparing the **23** based layer by spin-coating (CB: chlorobenzene, DCM: dichloromethane, THF: tetrahydrofuran). [b] Thickness of the **23** based layer measured with a profilometer. [c] Turn-on voltage defined as voltage corresponding to a luminance of 0.1 cd m⁻². [d] Maximum luminance. [e] Maximum current efficiency.

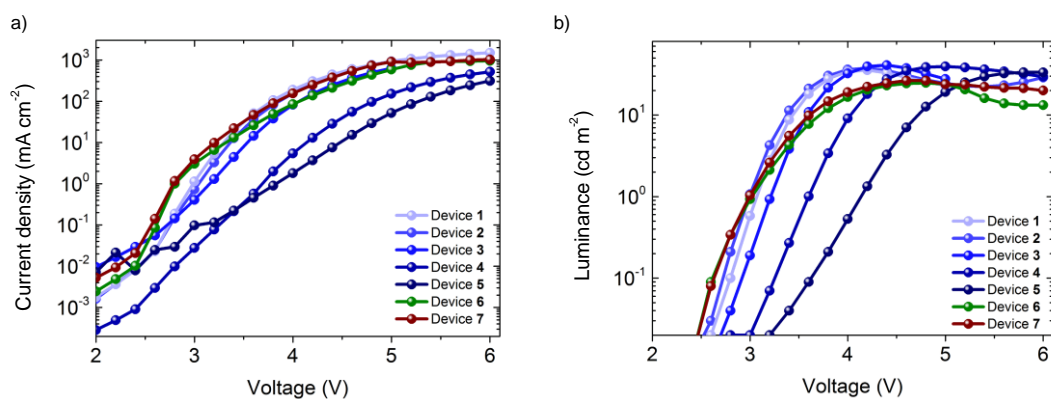
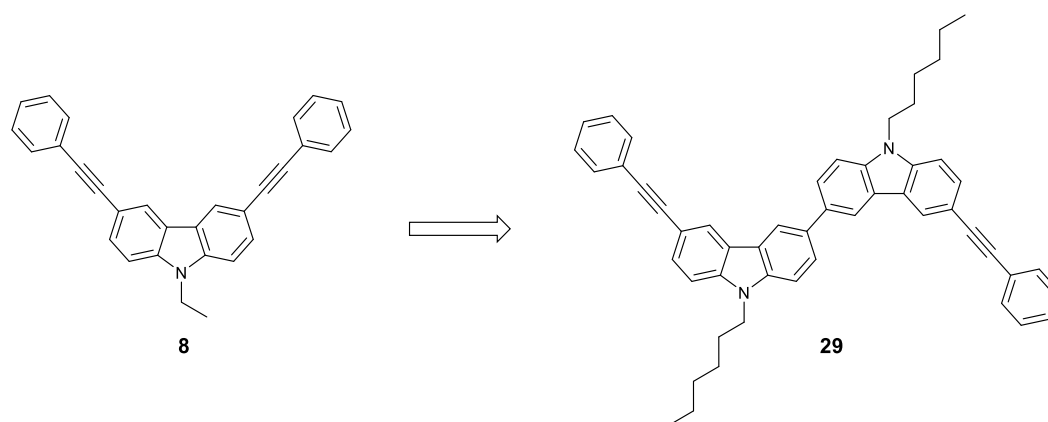


Figure 1.13. a) Current density-voltage and b) luminance-voltage characteristics of the devices summarized in Table 1.7.

1.4. A bicarbazole derivative as a deep-blue emitter

In this section, a new dye was also prepared based on the structure of compound **8** in order to develop a new deep-blue emitter in the solid state. In this case, the extension of the π -conjugated system was accomplished by substituting the carbazole core for the bicarbazole one, while maintaining the phenylethynyl peripheral groups (Scheme 1.11).



Scheme 1.11. Chemical structure of bicarbazole derivative **29**.

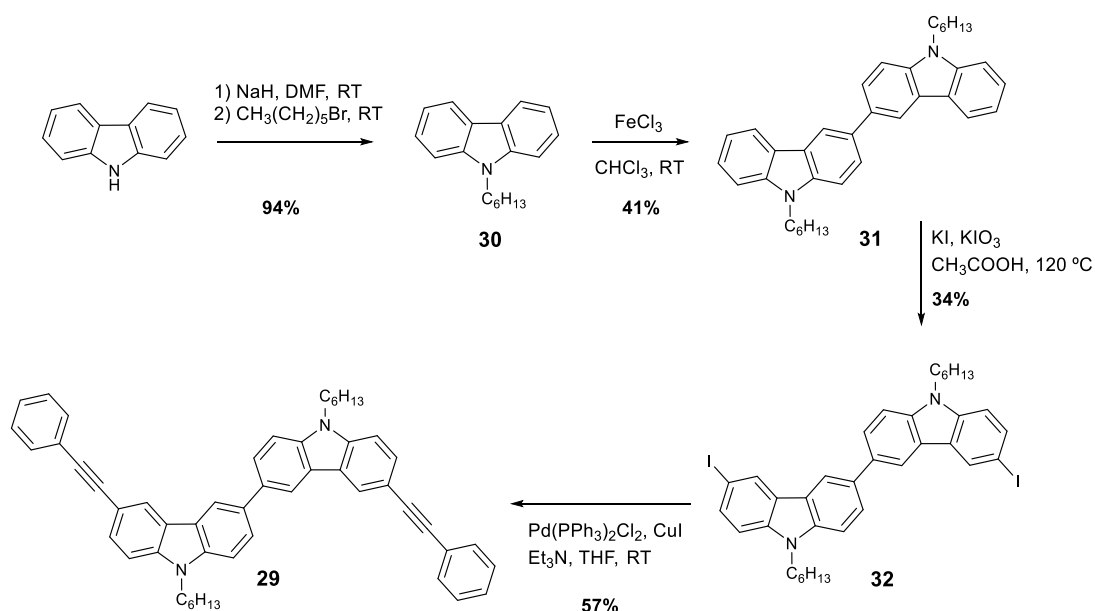
1.4.1. Synthesis

9,9'-Dihexyl-6,6'-bis(2-phenylethynyl)-3,3'-bi-9H-carbazole (**29**) was prepared via a four-step process (Scheme 1.12). First, the alkylation of 9H-carbazole with hexyl bromide under standard conditions yielded the intermediate 9-hexyl-9H-carbazole (**30**).^[96] Next, 9,9'-dihexyl-3,3'-bi-9H-

carbazole (**31**) was prepared by oxidative dimerization of **30** with FeCl₃ in anhydrous chloroform at room temperature.^[97] The iodination reaction of 3,3'-bicarbazole **31** in 6,6' positions under the Tucker reaction conditions^[80] afforded the intermediate 9,9'-dihexyl-6,6'-diiodo-3,3'-bi-9*H*-carbazole (**32**). Finally, the Sonogashira coupling reaction between **32** and phenylacetylene furnished the final compound **29**.

1.4.2. Characterization of the organic semiconductor and future work

Bicarbazole **29** exhibits higher thermal stability ($T_d = 440$ °C) in comparison to compound **8** ($T_d = 329$ °C), due to the incorporation of two carbazole units into the molecular structure. Similarly to **8**, compound **29** exhibited an amorphous behaviour with a glass transition temperature of 59 °C.



Scheme 1.12. Synthesis of compound **29**.

Table 1.8 collects the optical properties of bicarbazole **29** determined in 10 μ M THF solution and in vacuum-evaporated thin film (Figure 1.14). The optical data for compound **8** is also shown for comparison. The emission spectra of **29** both in solution and in the solid state are significantly bathochromically shifted in comparison to that of **8**, which can be attributed to the extended π -conjugated bicarbazole core. Accordingly, compound **29** displays the CIE coordinates in the deep-blue zone (0.17, 0.10) as tricarbazole derivatives **23** and **24** (Insert image in Figure 1.14b). In

Table 1.8. Optical properties of compounds **8** and **29**.

Compd.	Solution			Solid state		
	$\lambda_{\text{abs,max}}$ (nm) [a,b] [ϵ ($\text{M}^{-1} \text{cm}^{-1}$)]	$\lambda_{\text{em,max}}$ [a,b] (nm)	Φ_{f} [c]	$\lambda_{\text{abs,max}}$ [a,d] (nm)	$\lambda_{\text{em,max}}$ [a,d] (nm)	Φ_{f} [e]
8	312 (55 546)	374, 394	0.27	318	402	0.11
29	313 (86 011)	416	0.11	315	428	0.21

[a] Wavelength of maximum absorption ($\lambda_{\text{abs,max}}$), molar absorption coefficient (ϵ) and wavelength of maximum emission ($\lambda_{\text{em,max}}$). Emission spectra were recorded after excitation at the wavelength of maximum absorption. [b] Determined in 10 μM THF solutions at room temperature. [c] Fluorescence quantum yield (Φ_{f}) measured in THF solution using 1,4-bis(5-phenyl-2-oxazolyl)benzene as the standard ($\Phi_{\text{f}} = 0.93$ in cyclohexane solution) after excitation at 300 nm. [d] Determined from vacuum-evaporated thin films on quartz substrates at room temperature. [e] Fluorescence quantum yield (Φ_{f}) of thin films recorded in an integrating sphere.

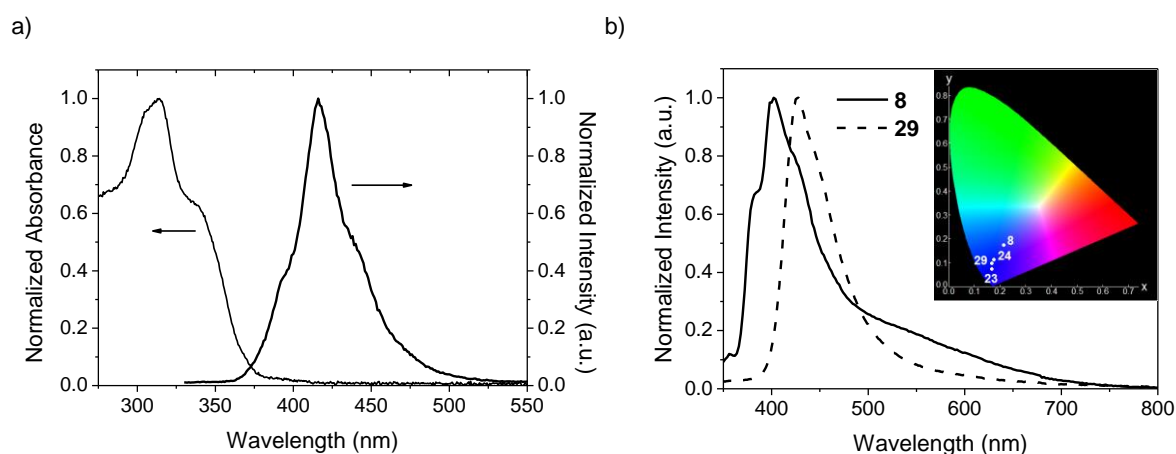


Figure 1.14. a) Absorbance and emission spectra of a 10 μM THF solution of compound **29**. b) Emission spectra of vacuum-deposited thin films of compounds **8** and **29**. Inset shows the CIE chromaticity diagram indicating the coordinates of **8**, **23**, **24** and **29**.

addition, the fluorescence quantum yield in the solid state is enhanced for bicarbazole derivative **29** ($\Phi_{\text{f}} = 0.21$) in comparison to that of the monocarbazole analogue **8** ($\Phi_{\text{f}} = 0.11$), and is also higher than that determined in solution. Thus, this species show enhanced emission in contrast to the more usual effect of fluorescence quenching in the solid state.

Figure 1.15 displays the cyclic voltammogram of compound **29**, which shows one quasi-reversible oxidation wave at $E_{\text{onset}}^{\text{OX}} = 0.48$ V vs. Fc^+/Fc , followed by a second irreversible one. Thus, **29** is more easily oxidized than monocarbazole **8** ($E_{\text{onset}}^{\text{OX}} = 0.69$ V vs. Fc^+/Fc) according to the enhanced electron-donating nature of the bicarbazole core. The IP and the EA values of **29** were estimated to be 5.87 and 2.52 eV, respectively. The ionization potential in the solid state

determined for **29** by means of the photoemission in air technique is 5.11 eV. A hole mobility up to $1.7 \times 10^{-3} \text{ cm}^2 \text{ V}^{-1} \text{ s}^{-1}$ was achieved at an electric field of $5.9 \times 10^6 \text{ V cm}^{-1}$ by the TOF technique (Appendix B).

Therefore, bicarbazole **29** maintains the desired characteristics required for the successful operation of OLEDs as compound **8**, but additionally exhibits the sought photoluminescence characteristics for deep-blue emission, as well as an enhanced fluorescent quantum yield, which makes of **29** a promising candidate for OLEDs. Currently, compound **29** is being examined as the deep-blue emitting layer in non-doped OLEDs.

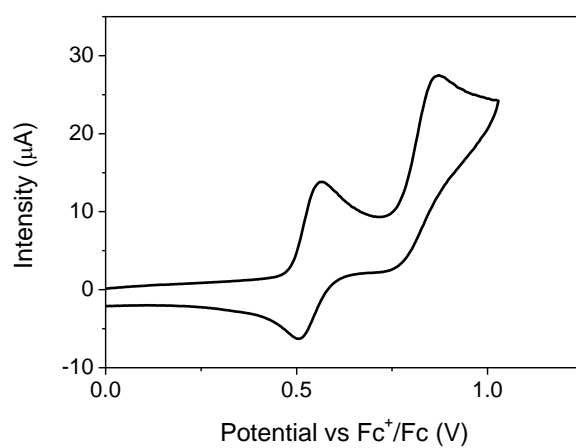


Figure 1.15. Cyclic voltammogram of compound **29** recorded at a scan rate of 100 mV s^{-1} in 1 mM acetonitrile solution.

1.5. Conclusions

An easy synthetically accessible series of aryl substituted monocarbazole-based fluorescent organic semiconductors has been deeply investigated. The ethynylene spacer between the carbazole moiety and the donor unit (phenyl or thienyl) influences on the molecular structure and as a consequence in the crystal packing and modulates the optical properties. The nature of the *N*-substitution of the carbazole core practically does not influence on the optical and electrochemical properties, but impacts considerably on the glass transition temperatures and as a result on the film-forming capability of these compounds. This series of compounds shows hole-transporting properties with mobilities up to $10^{-3} \text{ cm}^2 \text{ V}^{-1} \text{ s}^{-1}$. A non-doped OLED based on 9-ethyl-3,6-bis(2-phenylethynyl)-9*H*-carbazole (**8**) as the emitting layer, shows a very low turn-on voltage of only 4 V together with a high luminance up to $1.4 \times 10^4 \text{ cd m}^{-2}$ and a current efficiency of 3.3 cd A^{-1} . A high

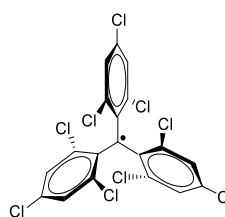
efficiency of radiative exciton production (ϕ) of 45% has been calculated and, in combination with DFT studies, it can be stated that the operated emission mechanism of the OLED device proceeds from S_1 and S_2 states of the carbazole-based emitter **8**, with the contribution of energy transfer from T_5 "hot exciton" to S_1 state through reverse intersystem crossing process.

Tricarbazoles **23** and **24** show the sought deep blue emission in the solid state, as a result of linking the three carbazole units by a triple bond as a π -spacer. In addition, alkylation of the nitrogen positions of the lateral carbazole units with 2-ethylhexyl chains helps to transfer the quantum yield determined in solution to that in the solid state without significant reduction. Solution processed non-doped OLED devices from compound **23** demonstrates its potential as a deep-blue emitter in non-doped devices, reaching luminances of up to 40 cd m⁻² and current efficiency of 0.2 cd A⁻¹.

The extended π -conjugated system from the bicarbazole core **29** afforded a promising candidate for non-doped OLEDs with a CIE y coordinate in the range of the deep-blue region emission in the solid state.

Chapter 2

Stable radicals with ambipolar charge transport



Part of this chapter has been published in:

Chem. Eur. J. **2016**, *22*, 18551–18558

CHAPTER 2

Stable radicals with ambipolar charge transport

This chapter deals with the study of the charge transport properties of a series of neutral long-lived purely organic radicals based on the stable [4-(N-carbazolyl)-2,6-dichlorophenyl]bis(2,4,6-trichlorophenyl)methyl radical adduct (Cbz-TTM). All the compounds exhibit ambipolar charge transport properties under ambient conditions owing to their radical character. High electron and hole mobilities up to 10^{-2} and 10^{-3} $\text{cm}^2 \text{V}^{-1} \text{s}^{-1}$, respectively, were achieved. Xerographic single-layered photo-receptors were fabricated from the radicals studied herein, exhibiting good xerographic photosensitivity across the visible spectrum.

2.1. Introduction

In the field of organic electronics, new organic semiconductors are currently required as active layers in optoelectronic devices. For instance, many research efforts are focused on obtaining new organic materials with high absorption coefficients or efficient light-emitting properties for their use as components in organic solar cells or OLEDs, respectively. In this way, in Chapter 1 a new family of carbazole derivatives was prepared and studied as blue emitting layers for OLEDs, leading to non-doped blue OLED devices with very low turn-on-voltages and even achieving a high luminance up to 1.4×10^4 cd m^{-2} in the case of the OLED device based on material **8**.

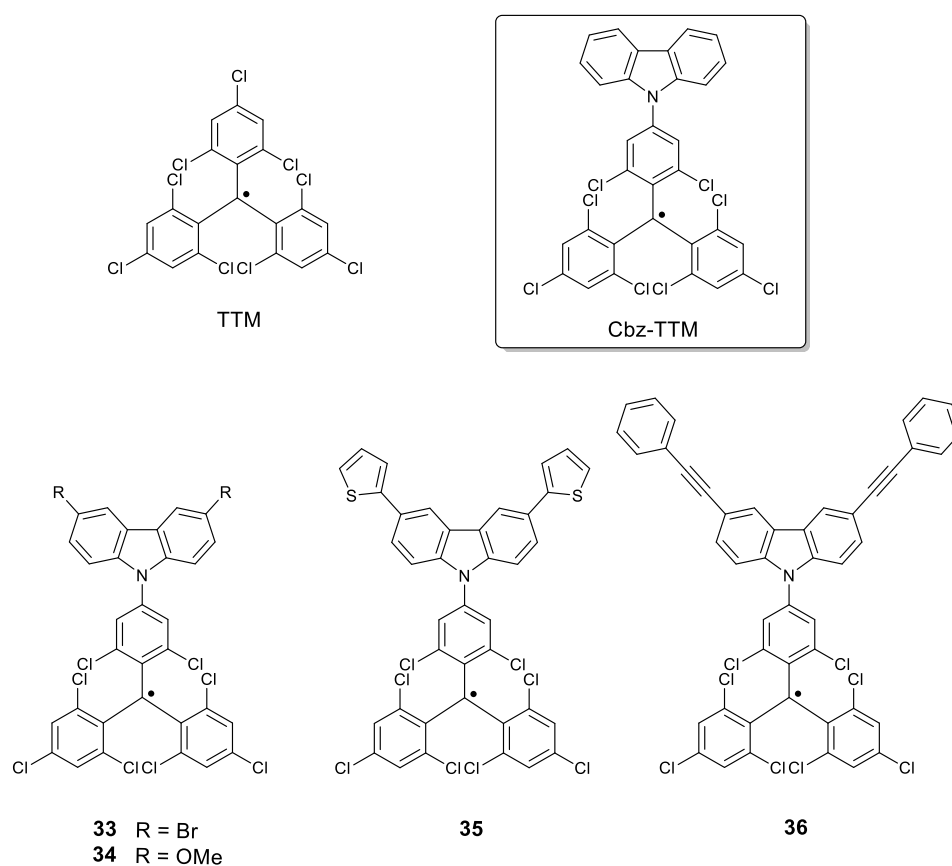
In general, the successful operation of OLEDs depends on several aspects, including the thermal stability, film-forming properties and the fluorescence quantum yield of the organic emitter as discussed in Chapter 1, but also on its charge-transporting properties. Indeed, higher efficiencies of OLEDs can be obtained by optimizing the charge balance in multilayer devices.^[7,98] This implies the improvement of the charge injection and transport characteristics of the emitting layer but also the use of appropriate and effective hole- and electron-transporting layers.^[99] Thus, organic semiconductors with effective hole and/or electron-transporting properties are essential

for the fabrication of OLEDs, OTFTs, organic solar cells and complementary logic circuits, among others. Keeping this idea in mind, the following chapters deal with the study of the charge transport properties of different series of organic semiconductors, being Chapters 2 and 3 focused on the development of new charge-transfer compounds with n-type or ambipolar properties. Specifically, the present Chapter 2 involves the study of the ambipolar properties of a series of neutral long-lived organic radicals based on the tris(2,4,6-trichlorophenyl)methyl (TTM) radical.

Organic radicals are open-shell molecules, that is, they bear an unpaired electron. In order to ensure the stability of this kind of species, the unpaired electron can be stabilized with bulky substituents. Given that organic radicals are paramagnetic systems, they have been usually sought as components for obtaining materials with magnetic properties. Stable organic radicals are then promising building blocks in the preparation of molecular magnetic materials for applications such as spintronics or sensing devices, among others.^[100] Moreover, the semiconducting properties of the stable organic radicals are attractive due to the ability of the unpaired electrons of undergoing simple and reversible redox reactions.^[101] As mentioned in the introduction, charge carrier transport in layers of compounds with a closed-shell electron configuration can be explained *via* the hopping model, involving the cationic or anionic radical species, for hole or electron transport, respectively. In contrast, hole and electron transport in open-shell molecules is expected to take place between the neutral radical molecule and the formed cationic or anionic species, respectively, involving the singly-occupied molecular orbital (SOMO).^[52,102,103]

The neutral organic TTM radical exhibits an extremely high air and thermal stability in the solid state, due to the steric hindrance induced by the six chlorine atoms around the trivalent carbon atom.^[104,105] Charge-transfer radical adducts have been previously reported by our research group by coupling the electron-acceptor TTM core to electron-donor heterocycles.^[106–109] Remarkably, the radical adducts resulting from the introduction of the carbazole or the indole moiety into the TTM fragment exhibited ambipolar charge transport properties with hole and electron mobilities around $10^{-4} - 10^{-3} \text{ cm}^2 \text{ V}^{-1} \text{ s}^{-1}$.^[52] Neutral organic radicals with p- or n- type charge-transporting properties have been previously reported,^[102,110] but to the best of our knowledge, no further examples of organic radicals with ambipolar properties have been described. Ambipolar materials are attractive for practical applications, since the use of a single layer of an organic material that exhibits balanced electron and hole mobilities is most cost-effective.

In this chapter, the charge transport properties of a series of radical adducts based on the ambipolar [4-(*N*-carbazolyl)-2,6-dichlorophenyl]bis(2,4,6-trichlorophenyl)methyl radical (Cbz-TTM) are presented (Scheme 2.1). In this series of compounds, the electron-donating capability of the carbazole moiety, and hence, the push-pull electronic character of the radical adducts, has been modulated by the introduction of different electron-donating or electron-withdrawing groups on the carbazole core (**33**, **34**).^[108] In addition, the extension of the conjugated π -system has been also considered (**35**, **36**). The nature of the substitution patterns of the carbazole moiety was found to have a great impact on the bipolar charge transport properties of the final organic semiconductor material.



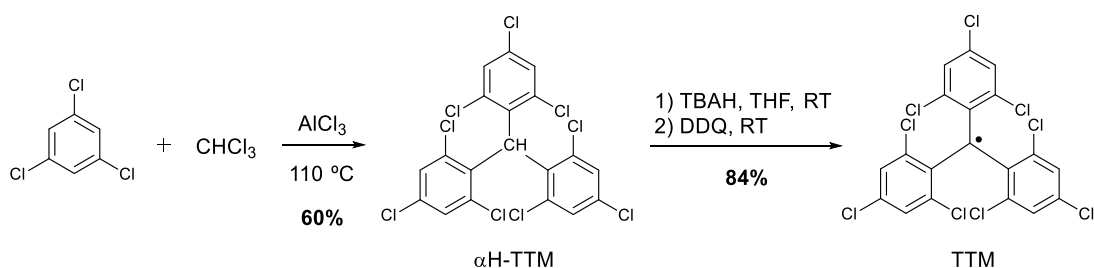
Scheme 2.1. Chemical structures of radical adducts Cbz-TTM and **33–36**.

2.2. Synthesis

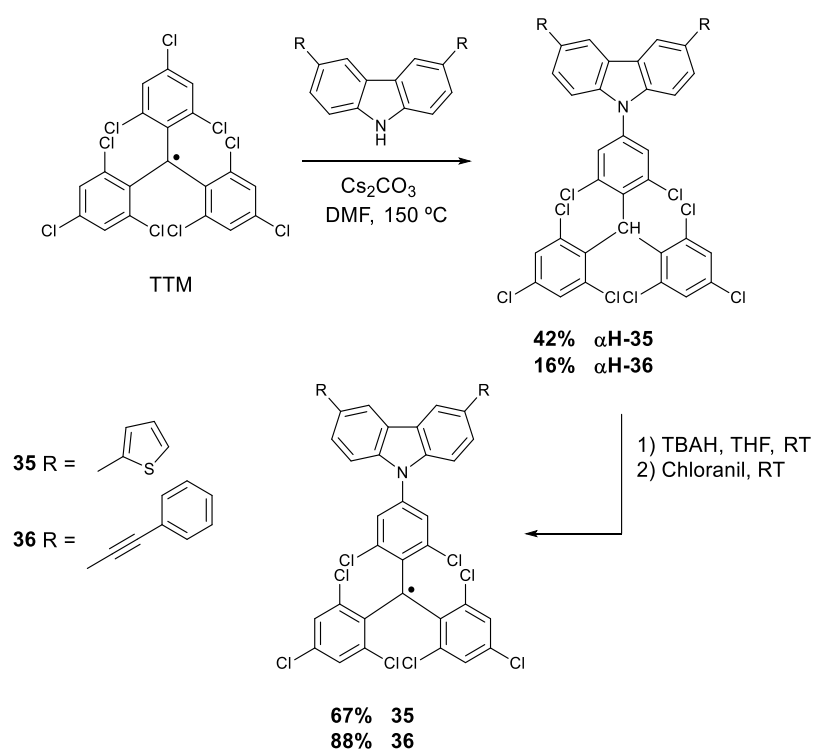
Radical adducts Cbz-TTM,^[109] **33**^[108] and **34**^[108] were already synthesized in our research group and therefore their detailed syntheses are not included in the present work. The novel radicals **35** and

36 were synthesised by coupling the corresponding 3,6-disubstituted carbazole derivative to the TTM radical following the methodology used to prepare the parent compound Cbz-TTM.

The radical TTM was prepared through a two-step process as previously reported (Scheme 2.2).^[104,111] First, a Friedel-Crafts condensation between 1,3,5-trichlorobenzene and chloroform as the alkylating agent at 110 °C and in the presence of AlCl₃ furnished the intermediate tris(2,4,6-trichlorophenyl)methane (α H-TTM). Next, α H-TTM was treated with an aqueous solution of tetrabutylammonium hydroxide (TBAH) in THF followed by oxidation with 2,3-dichloro-5,6-dicyano-*p*-benzoquinone (DDQ) rendering the pure radical TTM.



Scheme 2.2. Synthesis of radical tris(2,4,6-trichlorophenyl)methyl (TTM).



Scheme 2.3. Synthesis of radical adducts **35** and **36**.

Intermediates **α H-35** and **α H-36** were obtained by treating TTM with an excess of the 3,6-disubstituted carbazole derivative, 3,6-di-2-thienyl-9H-carbazole (**14**) and 3,6-bis(2-phenylethynyl)-9H-carbazole (**22**), respectively, in the presence of cesium carbonate in DMF at 150 °C (Scheme 2.3). Subsequently, intermediates **α H-35** and **α H-36** were treated with an aqueous solution of tetrabutylammonium hydroxide (TBAH) followed by oxidation with chloranil yielding the pure radical adducts **35** and **36**, respectively.

2.3. Characterization of the organic semiconductors

Electron paramagnetic resonance studies

The electron paramagnetic resonance (EPR) technique is a highly sensitive technique that allows the characterization of radicals both in solution and in the solid state. This technique consists on the measurement of the energy absorption produced under microwave radiation and varying the magnetic field. From the first derivative of the absorption curve the g factor, the hyperfine structure and the line width can be obtained.

X-band EPR spectra of the new radical adducts **35** and **36** were recorded in dichloromethane solution ($\sim 10^{-4}$ M) at 298 and 180 K (radical **35**, Figure 2.1) and their spectral data are reported in Table 2.1. g values of radicals **35** and **36** were similar to those of TTM ($g = 2.0034$)^[104] and very close to that of the free electron ($g = 2.0023$), in agreement with the expected small spin-orbit interaction. Both spectra at room temperature consisted of a broad and single line (**35**, $\Delta H_{pp} = 3.48$ G; **36**, $\Delta H_{pp} = 3.59$ G) and an equidistant pair of small lines on both sides of the main spectrum. The small pair of lines corresponds to the strong coupling of the free electron with the α -¹³C nucleus.

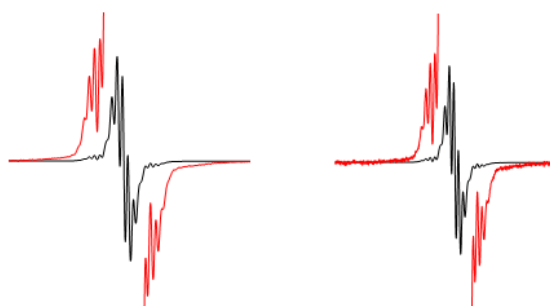


Figure 2.1. Left: Experimental EPR spectrum of radical adduct **35** ($\sim 10^{-4}$ M) in CH_2Cl_2 at 180 K. Scan range: 55 G; $\Delta H_{pp} = 0.69$ G; $a(6\text{H, arom}) = 1.21$ G; $a(^{13}\text{C bridge}) = 12.71$ G. Right: Simulated spectrum with these parameters.^[112] The red lines are y-axis expanded spectra.

Table 2.1. *g* values and hyperfine coupling constants in gauss for triphenylmethyl radicals **35** and **36** in dichloromethane ($\sim 10^{-4}$ M).

Radical	<i>g</i> [a]	¹ H [b]	¹³ C(α) [b,c]	¹³ C(arom) [b,c]	ΔH_{pp} [b]
35	2.0035 \pm 0.0001	1.21	27.2	12.71	0.69
36	2.0035 \pm 0.0001	1.20	27.4	12.74	0.69

[a] *g* values were measured against 2,2-diphenyl-1-picrylhydrazyl (dpph) (2.0037 \pm 0.0002) at 298 K. [b] The hyperfine coupling (hfc) constants for six ¹H in meta, ¹³C(α) and ¹³C(arom) (adjacent to α -carbon), and values for ΔH_{pp} (peak to peak line width) were determined at 180 K and checked by computer simulation. [c] Natural abundance of ¹³C isotope: 1.10%.

At low temperature, the spectra of **35** and **36** showed an overlapped multiplet of very close 7 lines related to the weak coupling with the six equivalent aromatic *meta*-hydrogen atoms, and two weak multiplets on both sides of the central multiplet attributed to the coupling with the three bridgehead-¹³C nuclei adjacent to the α -carbon atom. The relatively large values of the coupling of the free electron with α and bridgehead ¹³C atoms, and the small values with the *meta*-hydrogen atoms suggest that the spin density is mainly localized in the central carbon, due to the out-of-plane torsions of the phenyl rings. All the coupling values are displayed in Table 2.1. X-band EPR spectra of radicals Cbz-TTM, **35**, and **36** have been previously reported.^[108,109] EPR quantitative measurements of all these radical adducts in solid state confirm that the radical character remains unaltered at room temperature under air conditions in the dark for months. This stability is a specific characteristic of these radical compounds based on the TTM core that furnishes its derivatives with the appropriate physicochemical properties for their use as potential organic materials for electronic devices.

Thermal and optical properties

Thermal properties of the neutral radicals TTM, Cbz-TTM and **33–36** were examined by TGA. Table 2.2 collects the data of TGA measurements of the neutral radicals Cbz-TTM and **33–36** and TGA curves of all compounds can be found in Appendix B. The decomposition temperature (T_d) range between 261 and 364 °C, with a decomposition pattern similar to that of the TTM radical ($T_d = 324$ °C). Phenylethynyl-based radical adduct **36** exhibits the highest thermal stability.

The optical properties of radical compounds Cbz-TTM and **33–36** are summarized in Table 2.2. The absorption band located between 291 to 316 nm corresponds to the carbazole moiety and that peaked around 374 nm is characteristic of radicals of the TTM series. For all the compounds,

the additional absorption band at longer wavelengths (589–648 nm) is attributed to the charge transfer from the electron-donor carbazole moiety to the electron-acceptor TTM fragment. The methoxy-substituted radical adduct **34** exhibits the charge-transfer band peaked at longer wavelengths, with a red-shift of 50 nm with respect to the non-substituted parent compound Cbz-TTM. The absorption spectra of the new radicals **35** and **36** in chloroform solutions are displayed in Figure 2.2.

Table 2.2. Thermal and optical properties of radical adducts Cbz-TTM and **33–36**.

Radical	T_d [a] (°C)	$\lambda_{abs,max}$ (nm) [b] [ϵ ($M^{-1} cm^{-1}$)]	$\lambda_{em,max}$ [c] (nm)	Φ_f [d]
Cbz-TTM	325	291 (14 400), 374 (25 600), 598 (2940)	628	0.64
33	261	297 (20 219), 375 (29 591), 553 (sh) (2437), 589 (3036)	615 [e]	0.45 [e]
34	282	309 (20 977), 376 (29 018), 648 (3970)	728	<0.01
35	277	316 (41 898), 376 (33 876), 626 (3752)	684	0.14
36	364	313 (73 860), 375 (43 520), 609 (4820)	654	0.39

[a] Decomposition temperature (T_d) corresponding to the 5% weight loss determined from TGA at a scan rate of 20 °C min^{-1} . [b] Wavelength of maximum absorption ($\lambda_{abs,max}$) and molar absorption coefficient (ϵ) determined in chloroform solution (10^{-4} M). [c] Wavelength of maximum emission ($\lambda_{em,max}$) determined in cyclohexane solution (10^{-4} M) after excitation at 450 nm. [d] Fluorescence quantum yield (Φ_f) measured in cyclohexane solution using tris(2,2'-bipyridyl)ruthenium(II) chloride in water as a standard after excitation at 450 nm. [e] Values taken from ref. [108].

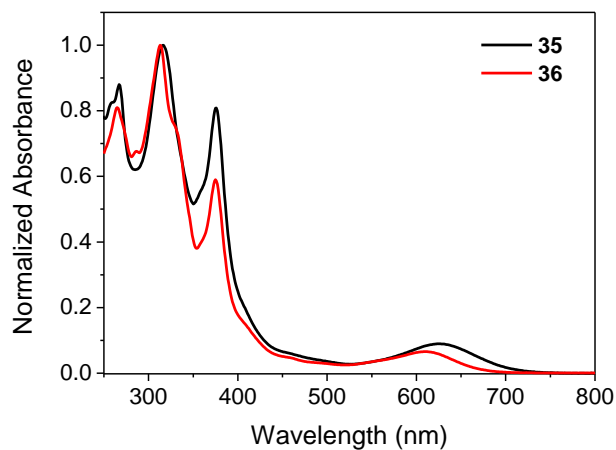


Figure 2.2. Absorption spectra of radical adducts **35** and **36** in chloroform solutions ($\sim 10^{-5}$ M).

Figure 2.3 displays the emission spectra of all radical compounds recorded in cyclohexane. All compounds exhibit an emission band centered in the range of 615 to 728 nm (Table 2.2), which

is significantly influenced by the substitution patterns of the carbazole core. Compounds **34–36** show the maximum emission band redshifted by 100, 56 and 26 nm, respectively, with respect to that of the non-substituted derivative Cbz-TTM, confirming the enhanced electron-donating strength of the methoxy substituent in adduct **34**, which shows the most red-shifted emission. On the contrary, radical adduct **33**, with the electron-withdrawing bromo atoms in the 3,6-positions, shows an hypsochromic shift of 13 nm of the maximum emission peak. Non-substituted Cbz-TTM shows the highest fluorescence quantum yield value of all the series in cyclohexane ($\Phi_f = 0.64$), which decreases according to the electron-donating strength of the substituents of the carbazole moiety.

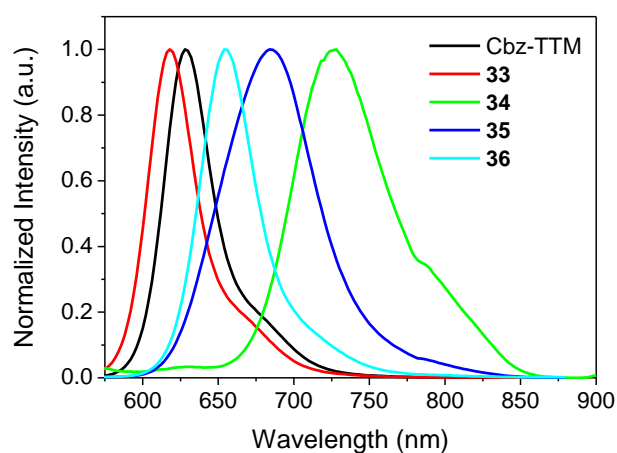


Figure 2.3. Emission spectra of radical adducts Cbz-TTM and **33–36** in cyclohexane solutions (10^{-4} M).

Cation and anion species were chemically obtained from the corresponding neutral radicals. The absorption spectra of the neutral radicals **35** and **36** after being treated with an oxidant, a copper(II) salt, to afford the corresponding cations, and a reductant, TBAH, to give the respective anions, are displayed in Figure 2.4 and 2.5, respectively. For the new compounds **35** and **36**, the intensity of the absorption bands of the oxidized species at $\lambda = 538$ and 998 nm for **35** and $\lambda = 551$ and 967 nm for **36** increases with the concentration of the oxidant, and the intensity of the absorption bands of the reduced species at $\lambda = 513$ nm for both **35** and **36** increases with the concentration of the reductant. The more intense and broader band in the spectra of the oxidized species is assigned to a photoinduced electron transfer from the carbazole nitrogen atom to the carbocation of the triphenylmethyl moiety of the radical adduct. This band is remarkably shifted to the infrared region of the spectrum with respect to that of the non-substituted Cbz-TTM ($\lambda = 789$ nm).^[106] The presence of isosbestic points in all spectra, when going from radical to charged

species, proves the stoichiometry and the presence of only two species in all the redox processes. This behaviour shows the implicit stability of all these species, in accordance with previous insights reported for compounds **33** and **34**.^[106,108]

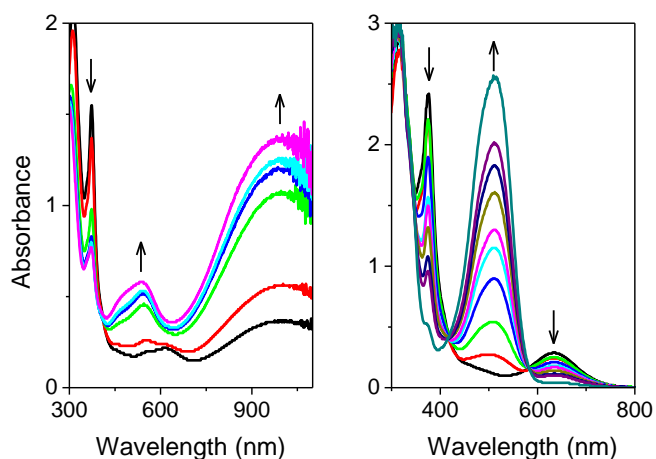


Figure 2.4. Left: Absorption spectra of the solution of radical adduct **35** in CH₃CN/CHCl₃ (9:1) ($\sim 10^{-4}$ M) at different concentrations of Cu(ClO₄)₂ (emerging bands $\lambda = 538, 998$ nm). Right: Absorption spectra of the solution of radical adduct **35** in THF ($\sim 10^{-4}$ M) at different concentrations of TBAH aqueous solution (emerging band $\lambda = 513$ nm).

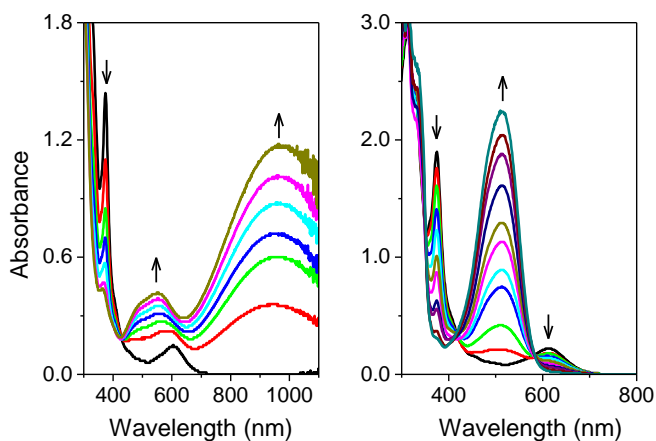


Figure 2.5. Left: Absorption spectra of radical adduct **36** in CH₃CN/CHCl₃ (9:1) ($\sim 10^{-4}$ M) at different concentrations of Cu(ClO₄)₂ (emerging bands $\lambda = 551, 967$ nm). Right: Absorption spectra of the solution of radical adduct **36** in THF ($\sim 10^{-4}$ M) at different concentrations of TBAH aqueous solution (emerging band $\lambda = 513$ nm).

Electrochemical properties

Electrochemical properties of dichloromethane solutions of all radical compounds were analysed by CV (Table 2.3). The cyclic voltammograms of radical adducts show quasi-reversible oxidation and reduction processes (Figure 2.6 and Appendix B). The oxidation standard potentials of the carbazole-based radicals Cbz-TTM and **33–36** range from 0.32 to 0.60 V. A significant influence of the substitution patterns of the carbazole moiety on the oxidation and reduction potentials was found. Radical **34**, with the presence of the electron-donating methoxy substitution

Table 2.3. Electrochemical properties and ionization energies of radical adducts Cbz-TTM and **33–36**.

Radical	E_{ox}^0 (V) [a] (($E_{\text{pa}}-E_{\text{pc}}$) (mV)) [b]	E_{red}^0 (V) [c] (($E_{\text{pa}}-E_{\text{pc}}$) (mV)) [b]	IP [d] (eV)	EA [e] (eV)	E_{gap} [f] (eV)	IP [g] (eV)
Cbz-TTM	0.52 (122)	-1.03 (122)	5.91	4.36	1.55	5.78
33	0.60 (125)	-1.00 (117)	5.99	4.39	1.60	5.87
34	0.32 (159)	-1.04 (159)	5.71	4.35	1.36	5.58
35	0.51 (112)	-1.01 (95)	5.90	4.38	1.52	5.72
36	0.59 (90)	-0.99 (95)	5.98	4.40	1.58	5.92

[a] Oxidation standard potential (E_{ox}^0) vs. Fc^+/Fc for the redox oxidation couple determined in 0.5 mM dichloromethane solutions at a scan rate of 50 mV s^{-1} . [b] Difference between the anodic (E_{pa}) and cathodic (E_{pc}) peak potentials. [c] Reduction standard potential (E_{red}^0) vs. Fc^+/Fc for the redox reduction couple determined in 0.5 mM dichloromethane solutions at a scan rate of 50 mV s^{-1} . [d] Ionization potential (IP) determined as $\text{IP} = E_{\text{ox}}^0 \text{ vs } \text{Fc}^+/\text{Fc} + 5.39$. [e] Electron affinity (EA) determined as $\text{EA} = E_{\text{red}}^0 \text{ vs } \text{Fc}^+/\text{Fc} + 5.39$. [f] Electrochemical gap calculated as the difference between IP and EA values. [g] Ionization potential determined from the photoemission technique under a N_2 atmosphere.

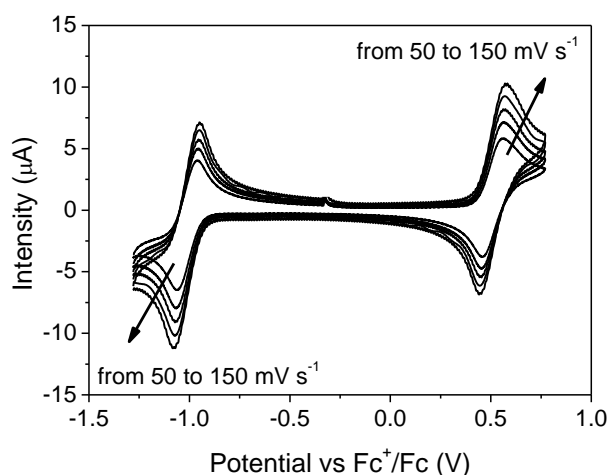


Figure 2.6. Cyclic voltammograms for the oxidation and reduction of radical adduct **35** in dichloromethane solution (0.5 mM) at room temperature at different scan rates ($50, 75, 100, 125$ and 150 mV s^{-1}).

on the carbazole core, appears to be the most easily oxidized and the less easily reduced adduct of all the series. On the contrary, the attachment of the electron-withdrawing bromo atoms at the 3,6 positions of the carbazole unit (**33**) produce an increase of the oxidation standard potential (0.60 V) in comparison to that of the non-substituted radical Cbz-TTM (0.52 V).^[108] These results are in agreement with the onset oxidation potentials of 9*H*-carbazole and 3,6-dibromo-9*H*-carbazole, which were estimated by CV to be 0.71 and 0.90 V, respectively. In addition, a cooperative effect between the fragment 9*H*-carbazole ($E_{\text{onset}}^{\text{ox}} = 0.71$ V) and the TTM radical ($E_{\text{ox}}^0 = 0.79$ V) should be involved to explain the final oxidation standard potential of the Cbz-TTM adduct ($E_{\text{ox}}^0 = 0.52$ V). On the contrary, the reduction standard potentials of all the radical adducts are very similar, independently of the substitution of the carbazole core and very close to that of the TTM radical ($E_{\text{red}}^0 = -1.04$ V), suggesting that the reduction potentials of the radical adducts are highly influenced by the TTM fragment and not by the carbazole moiety.

Ionization potential (IP) and electron affinity values (EA) were estimated from the standard potential values. IP values of this series of radicals depend on the electron-donor nature of the substituents attached at the carbazole core as previously mentioned, whereas EA values were found to be very similar (4.35–4.40 eV). It is worth pointing out that materials that present EA values higher than 4.0 eV are desirable for air-stable electron-transporting semiconductors as it was mentioned previously in the introduction.

IP values of solid samples as thin films from radicals **33–36** were determined by the electron photoemission method under a nitrogen atmosphere (Table 2.3). The IP values determined in the solid state confirmed the tendency observed by cyclic voltammetry, showing the radical adduct **34**, with the presence of methoxy groups, the lowest value (5.58 eV) of all the series. The presented series of radical adducts fulfill all the required conditions to act as ambipolar semiconductors under ambient conditions. For single-layer devices, semiconducting materials with ionization potential values higher than 5.0 eV and electron affinity values higher or close to 4.0 eV are required to achieve stable hole and electron transport.

2.4. Charge transport properties

The parent compound Cbz-TTM exhibited relatively high hole and electron mobilities of 4.6×10^{-4} and $4.7 \times 10^{-3} \text{ cm}^2 \text{ V}^{-1} \text{ s}^{-1}$, respectively.^[52] To explore the charge transport properties of this series of compounds, thin films of radicals **33–36** were subjected to the measurements by the xerographic

time-of-flight (XTOF) technique. Table 2.4 displays the charge drift mobility of the thin films of the radical materials **33–36** prepared either by vacuum thermal evaporation or by casting of the tetrahydrofuran solutions of the corresponding materials on Al-coated glasses. Figure 2.7 shows, as a representative example, the electrons and holes XTOF transients in the log-log scale of a thermal vacuum evaporated layer of compound **33**. The XTOF transients and the dependency of hole and electron drift mobilities on the square root of the electric field for the other compounds of the series are collected in Appendix B.

Table 2.4. Zero-field mobilities (μ_0), mobilities (μ) at an electric field strength (E), and field dependences (α) of holes and electrons in Cbz-TTM and **33–36**-based films.

Radical	Holes			Electrons			E (V cm^{-1})
	μ_0 ($\text{cm}^2 \text{V}^{-1} \text{s}^{-1}$)	μ_h ($\text{cm}^2 \text{V}^{-1} \text{s}^{-1}$)	α (cm V^{-1}) ^{1/2}	μ_0 ($\text{cm}^2 \text{V}^{-1} \text{s}^{-1}$)	μ_e ($\text{cm}^2 \text{V}^{-1} \text{s}^{-1}$)	α (cm V^{-1}) ^{1/2}	
Cbz-TTM [a]	8.0×10^{-5}	4.6×10^{-4}	0.0023	7.5×10^{-4}	4.7×10^{-3}	0.0025	0.64×10^6
33 [b]	1×10^{-4}	1.4×10^{-3}	0.0033	5.4×10^{-3}	1.7×10^{-2}	~ 0.0014	0.64×10^6
33/PCZ [c]	4.2×10^{-8}	3.5×10^{-7}	~ 0.002	1.2×10^{-7}	4.7×10^{-6}	~ 0.0036	1×10^6
34 [b]	2×10^{-5}	3.7×10^{-4}	0.0037	2.3×10^{-4}	2.4×10^{-3}	0.0029	0.64×10^6
34/PCZ [c]	1.2×10^{-6}	2.8×10^{-6}	~ 0.001	2.1×10^{-6}	4×10^{-5}	~ 0.003	1×10^6
35 [b]	5.2×10^{-5}	1.3×10^{-3}	~ 0.004	6.6×10^{-9}	7×10^{-7}	~ 0.0055	0.64×10^6
36 [b]	4.3×10^{-4}	3×10^{-3}	~ 0.0025	2.7×10^{-3}	7×10^{-3}	~ 0.0012	0.64×10^6
36/PCZ [c]	1.5×10^{-6}	8×10^{-6}	~ 0.0022	1.5×10^{-6}	1.8×10^{-5}	~ 0.0031	0.64×10^6

[a] Values taken from ref. [52]. Layer prepared by casting a THF solution of the pure radical adduct Cbz-TTM. [b] Thin films prepared by vacuum evaporation. [c] Thin films prepared by casting a THF solution of the molecular mixtures of radical adduct/polycarbonate (PCZ) in weight proportion 1:1.

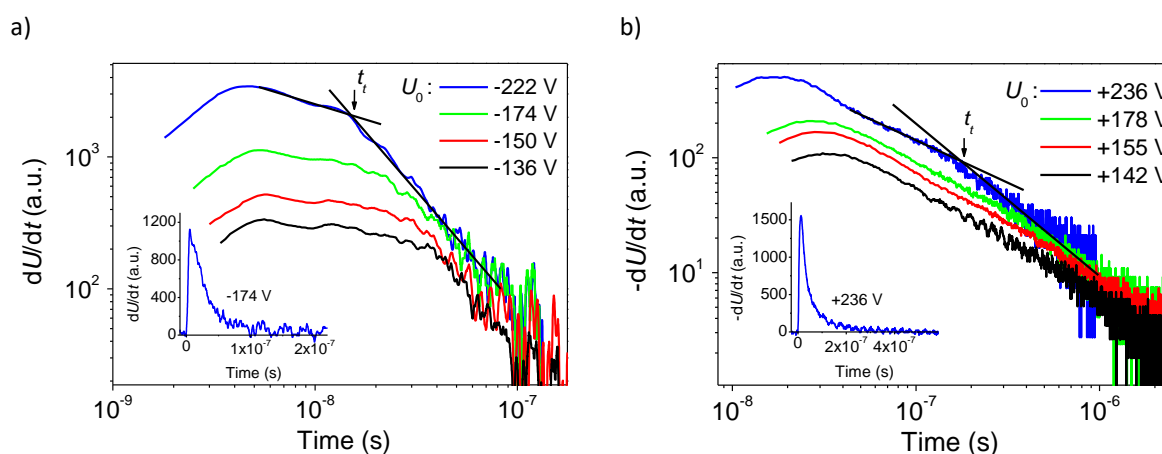


Figure 2.7. a) Electrons and b) holes XTOF transients of a 2.9 μm thick vacuum evaporated layer based on radical adduct **33**. Inset shows one of the transient curves in the linear plot.

From the values displayed in Table 2.4, it can be seen that radical adducts **33–36** exhibit ambipolar charge transport with balanced hole and electron mobilities under ambient conditions, except the thienyl-substituted radical **35**, with much more lower electron mobility. Charge-transporting properties of materials **33–36** are highly influenced by the deposition method, with the vacuum-deposited samples showing a better performance than the solution processed ones. Indeed, only films of compound **34** prepared by casting a THF solution of the pure material could be subjected to the XTOF measurements and only hole mobility of $3 \times 10^{-4} \text{ cm}^2 \text{ V}^{-1} \text{ s}^{-1}$ at an electric field of $0.64 \times 10^6 \text{ V cm}^{-1}$ could be detected, with a zero-field hole drift mobility (μ_0) of $1.3 \times 10^{-5} \text{ cm}^2 \text{ V}^{-1} \text{ s}^{-1}$ and a field dependence parameter (α) of $\sim 0.0039 \text{ (cm V}^{-1})^{1/2}$. XTOF measurements of the corresponding blends of the casted radical adducts **33**, **34** and **36** with bisphenol Z polycarbonate (PCZ) exhibited again both electron- and hole-transporting properties, although with lower values of electron and hole drift mobilities, as expected. In all cases, XTOF transients for hole and electron transport showed a dispersive pattern.

The modification of the substitution patterns of the carbazole moiety impacts on the charge transport properties of this series of neutral radicals. The electron-withdrawing substitution on the carbazole core favours the ambipolar charge transport with improvement of both electron and hole transport characteristics. Bromo-substituted radical adduct **33** exhibits the highest electron mobility value of $1.7 \times 10^{-2} \text{ cm}^2 \text{ V}^{-1} \text{ s}^{-1}$ at an electric field of $0.64 \times 10^6 \text{ V cm}^{-1}$ of the entire series without losing its hole transport properties. Taking into account that carbazole-based compounds have been usually defined as hole-transporting materials, the electron transport determined for the radical adduct Cbz-TTM and the series of derivatives here studied, should be related to the presence of the radical TTM fragment, which is easily and reversibly reduced.^[52] Accordingly, the introduction of electron-withdrawing groups on the carbazole core should influence the transporting properties of both positive and negative charges. When an electron-withdrawing group like the bromo substituent, with not only inductive electron-withdrawing character but also with electron-donating mesomeric properties, is attached to the carbazole moiety, it could be expected that the oxidation process would not be favoured, as is in fact reflected by the determined oxidation potential value (Table 2.3). Nevertheless, the stabilization of the electron-deficient oxidized species, which intervenes in the hole transport process according to the proposed hopping model, can occur due to the electro-donating mesomeric character. Thereby the hole transport mobility could be increased. At the same time, the bromo-substituted carbazole heterocycle behaves as a less electron-donating group in its substitution to the radical TTM unit. In this way,

the already electron-deficient radical tends to be easily reduced and thus the electron transport in the material could be favoured.

The increase of the donor strength of the carbazole core with methoxy groups in the radical adduct **34** shows no significant variations of hole and electron mobilities, although slightly lower mobility values of both charge carriers are detected in comparison to the parent radical Cbz-TTM. The vacuum-deposited layer of radical adduct **35**, with the strong electron-donating thienyl heterocycles, showed dispersive electron transport with a low mobility value of $7 \times 10^{-7} \text{ cm}^2 \text{ V}^{-1} \text{ s}^{-1}$ in comparison with the hole mobility one ($1.3 \times 10^{-3} \text{ cm}^2 \text{ V}^{-1} \text{ s}^{-1}$), resulting in a nonbalanced ambipolar system. On the contrary, the extension of the π -conjugated system of the carbazole core with the phenylethynyl group in radical adduct **36**, afforded a better-balanced ambipolar system with enhanced hole and electron mobilities in comparison to those of the parent compound Cbz-TTM. It should be mentioned that this strategy afforded the maximum hole transport mobility value of all the series ($3 \times 10^{-3} \text{ cm}^2 \text{ V}^{-1} \text{ s}^{-1}$).

These results suggest that the introduction of electron-withdrawing groups, as in the case of compound **33**, and the extension of the conjugation of the carbazole core through 3,6-positions, as in the case of compound **36**, improves both hole and electron-transporting properties with respect to those of the parent compound Cbz-TTM.

2.5. Xerographic single-layered photoreceptors

Taking into account the ambipolar charge transport properties of radical adducts **33–36**, they were evaluated in xerographic single-layered photoreceptors. Such photoreceptors need photogeneration and bipolar conductivity transporting materials.^[113] The best results were obtained with the bromo-substituted radical adduct **33**. Figure 2.8 shows the photosensitivity spectral distribution of the amorphous layer of compound **33**. Both polarities exhibit enough good xerographic photosensitivity across a wide region of the visible spectrum with a maximum near 600 nm. Photodischarge transients (Figure A3 in Appendix A) are very similar at positive and negative photoreceptor charging, according to its high electron and hole mobilities. The discharge is rather faster for negative electrification, consistent with the higher electron mobility in both the pure **33** and in the PCZ composition layers. Although these results do not improve the photosensitivity of the best reported phthalocyanine photoreceptors,^[113] they show fast discharging under

appropriate strong lighting, indicating the promising application of these materials in xerographic photoreceptors.

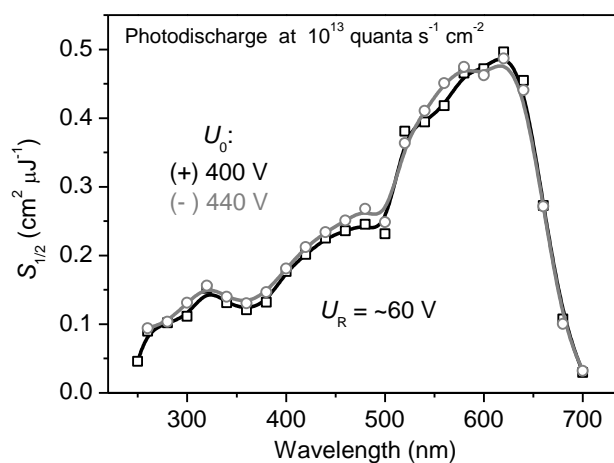


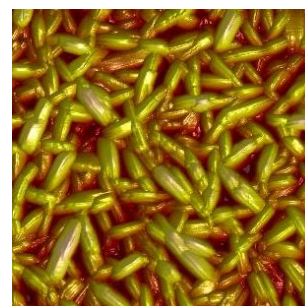
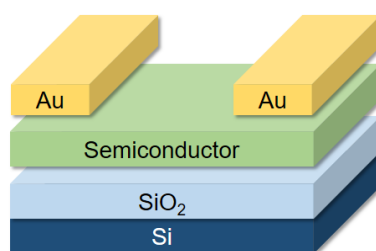
Figure 2.8. Xerographic photosensitivity spectra of the layer of **33**/PCZ (1:1) at positive and negative charging.

2.6. Conclusions

The ambipolar charge transport properties of a series of room-temperature stable all-organic radical compounds based on the coupling of the electron-acceptor tris(2,4,6-trichlorophenyl)methyl radical to the electron-donor heterocycle carbazole with substituents of different electronic characteristics have been determined. The extension of the conjugation of the carbazole core or the introduction of electron-withdrawing groups in the carbazole moiety enhanced both hole and electron mobilities, affording ambipolar materials with good balanced charge mobilities. Xerographic single-layered photoreceptors were fabricated from this series of radical adducts, exhibiting good xerographic photosensitivity across the visible spectrum for both positive and negative charging, attributed to their well-balanced charge transport properties.

Chapter 3

n-Type and ambipolar materials: the role of the tricyanovinyl group



Part of this chapter has been published in:

Phys. Chem. Chem. Phys. **2017**, *19*, 6721–6730

CHAPTER 3

n-Type and ambipolar materials: the role of the tricyanovinyl group

This chapter deals with the charge-transporting properties of a series of push-pull carbazole-based compounds. The introduction of the strong electron-withdrawing tricyanovinyl group in the carbazole core affords electron-transporting ability in addition to the characteristic hole-transporting properties exhibited by donor carbazole derivatives. Electron mobilities up to

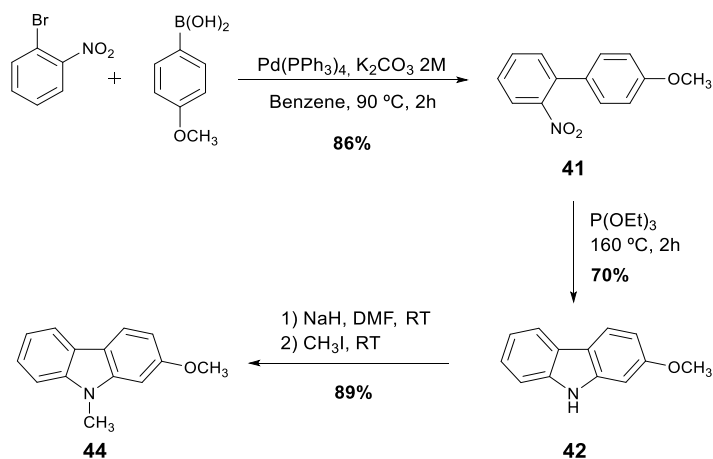
$5 \times 10^{-5} \text{ cm}^2 \text{ V}^{-1} \text{ s}^{-1}$ were achieved in vacuum-evaporated OTFTs. The effect of the substitution patterns of the carbazole core on the thermal, optical, electrochemical and charge-transporting properties is here analysed in combination with X-ray diffraction studies and theoretical calculations.

3.1. Introduction

In the previous Chapter 2, the electron acceptor TTM radical was selected to be coupled to the electron-donating carbazole heterocycle. This resulted in a new family of ambipolar materials with well-balanced hole and electron transport depending on the 3,6 substitution of the carbazole fragment. In the present Chapter, and with the aim of obtaining new n-type or ambipolar materials, the carbazole unit has been maintained as the electron-donating group, whereas the tricyanovinyl group has been selected as the electron acceptor unit instead of the TTM radical.

The incorporation of the strong electron-withdrawing tricyanovinyl group in push-pull organic compounds has been explored in combination with various π -systems giving promising materials for organic electronics.^[114–117] Carbazole derivatives incorporating the tricyanovinyl group have been previously reported showing high nonlinear optical (NLO) responses,^[114] but to the best of our knowledge the charge transport properties of this type of materials are here described for the first time. This chapter is focused on the modification of the characteristic hole-transporting

The synthesis of the 2-methoxy-substituted carbazole parent compound required for the preparation of tricyanovinyl-based compounds **38** and **40** is shown in Scheme 3.2. Firstly, the Suzuki coupling reaction of 1-bromo-2-nitrobenzene and 4-methoxyphenylboronic acid afforded the intermediate 4'-methoxy-2-nitro-1,1'-biphenyl (**41**) that followed by the Cadogan cyclization reaction of **41** with triethyl phosphite gave 2-methoxy-9*H*-carbazole (**42**) through an alternative methodology as described in the literature.^[118] Compound **42** rendered 9-methyl-2-methoxy-9*H*-carbazole^[119] (**44**) after methylation process under standard conditions.



Scheme 3.2. Synthesis of 2-methoxy-9*H*-carbazole intermediates **42** and **44**.

3.2.2. Crystal structures

The crystal structures of compounds **39** and **40** were determined by single-crystal X-ray analysis. Suitable single crystals were grown by slow evaporation from the corresponding chloroform solutions. Figure 3.1 shows the ORTEP projections of molecules **39** and **40**. The detailed crystallographic data can be found in Appendix B.

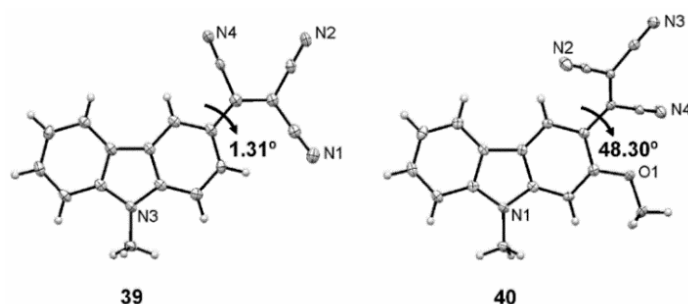


Figure 3.1. X-ray crystal structures of **39** and **40**, showing the 50% probability displacement.

The introduction of the methoxy group in the *ortho* position with respect to the tricyanovinyl unit influences the twist angle between the tricyanovinyl and the carbazole planes. While molecule **39**, containing no methoxy substituent, adopts an almost planar conformation with an angle of 1.31°, the *ortho* methoxy-substituted analogue **40** shows a deviation of the planarity with a twist angle of 48.30°, because of the steric hindrance caused by the methoxy group.

3.2.3. Characterization of the organic semiconductors

Thermal properties

Thermogravimetric analysis (TGA) and differential scanning calorimetry (DSC) measurements were performed to investigate the thermal properties of carbazole derivatives **37–40** (Table 3.1, Figure 3.2 and Appendix B). All the compounds possess high thermal stabilities with high onset decomposition temperatures in the range of 248 to 305 °C, allowing its handling for the preparation of thin films by the vacuum thermal evaporation technique. DSC thermograms confirmed the crystalline nature of this series of tricyanovinyl derivatives. *N*-Methyl derivatives **39** and **40** showed a melting process during the first heating scan owing to the crystallization process, whereas the non-alkylated analogues **37** and **38** melted with decomposition (Figure 3.2).

Table 3.1. Thermal properties of tricyanovinyl-substituted derivatives **37–40**.

Compound	T_d (°C) [a]	T_m (°C) [b]	T_c (°C) [b]
37	289	309 [c]	–
38	248	255 [c]	–
39	301	245	231
40	305	249	197

[a] Onset decomposition temperature (T_d) obtained from TGA performed at a heating rate of 20 °C min⁻¹. [b] Melting point (T_m) and crystallization temperature (T_c) obtained from DSC performed at a scan rate of 10 °C min⁻¹. [c] Melting with decomposition.

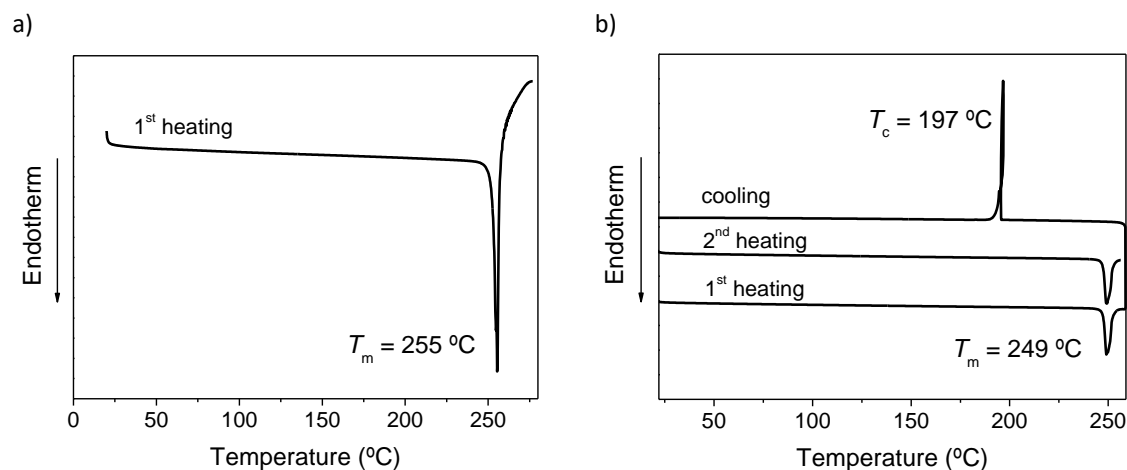


Figure 3.2. DSC curves of compounds a) **38** and b) **40** recorded at 10 °C min^{-1} under a nitrogen atmosphere.

Optical properties

The UV-Vis absorption spectra of $10\text{ }\mu\text{M}$ dichloromethane solutions of compounds **37–40** are shown in Figure 3.3 and the corresponding optical data are collected in Table 3.2. All compounds exhibit similar absorption spectra with absorption in the UV zone with a maximum peaking around 288–295 nm, characteristic of the carbazole moiety, and a second broad and intense absorption band centred in the range of 464 to 490 nm, which is assigned to the intramolecular charge transfer from the electron-donating carbazole moiety to the electron-withdrawing tricyanovinyl group. *N*-Alkyl derivatives **39** and **40** show a red-shift of the charge transfer absorption band of 23 and 22 nm, respectively, in comparison to the non-alkylated counterparts **37** and **38**. The strong push-pull character of these molecules allows the coverage of the UV and a wide part of the visible region of the electromagnetic spectrum.

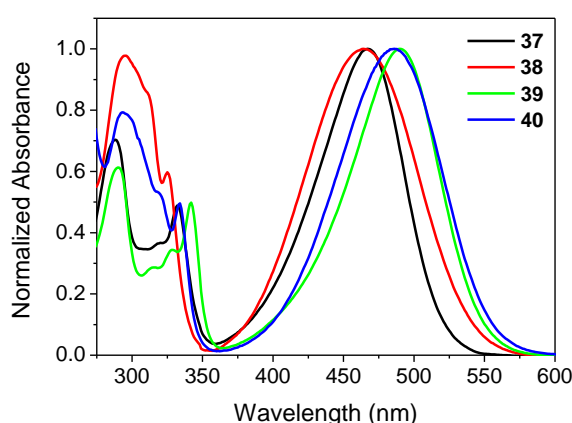


Figure 3.3. UV-Vis absorption spectra of $10\text{ }\mu\text{M}$ solutions of compounds **37–40** in dichloromethane.

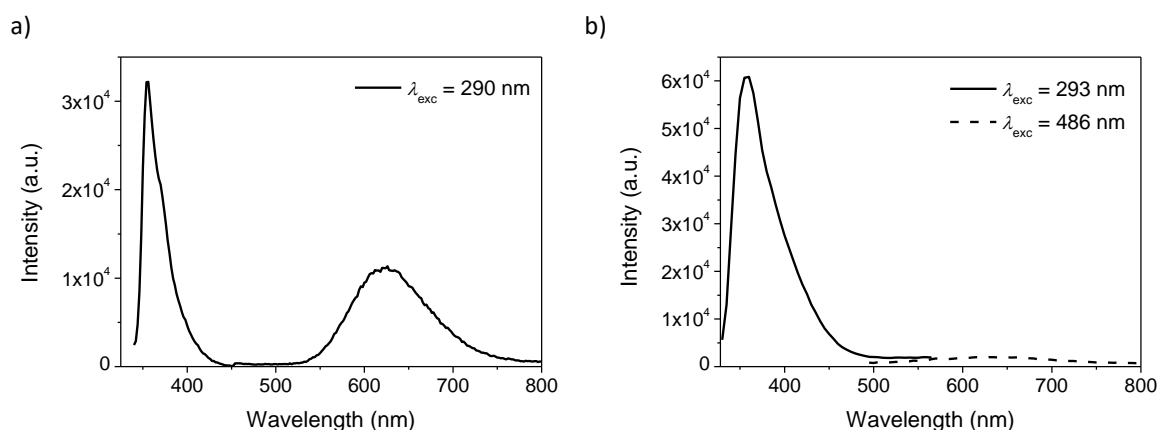
Table 3.2 Optical properties of tricyanovinyl-substituted derivatives **37–40**.

Compound	$\lambda_{\text{abs,max}}$ (nm) [ϵ ($\text{M}^{-1} \text{cm}^{-1}$)] [a]	$\lambda_{\text{em,max}}$ (nm) [a]	Φ_f [b]
37	288 (19 044), 467 (27 062)	354, 604	0.02
38	295 (19 147), 464 (19 580)	347, –	< 0.01
39	290 (19 667), 490 (32 090)	355, 625	0.02
40	293 (17 947), 486 (22 627)	360, –	< 0.01

[a] Wavelength of maximum absorption ($\lambda_{\text{abs,max}}$), molar absorption coefficient (ϵ) and wavelength of maximum emission ($\lambda_{\text{em,max}}$) determined in 10 μM dichloromethane solutions at room temperature. Emission spectra were recorded after excitation at the wavelength of maximum absorption.

[b] Fluorescence quantum yield (Φ_f) measured in dichloromethane solution using an integrating sphere after excitation at $\lambda = 290$ nm.

The emission spectra of compounds **37** and **39** in dichloromethane solutions show one emission band in the UV zone and a second emission band around 600 nm (Table 3.2 and Figure 3.4a). The emission band located at the UV zone corresponds to the emission from the locally excited (LE) state, whereas the emission band located at longer wavelengths is related to the emission from an intramolecular charge transfer (ICT) state. However, the ICT emission band is not observed in the emission spectra of methoxy-substituted derivatives **38** and **40** (Figure 3.4b). The electron-donating methoxy substituent in **38** and **40** influences on the push-pull character of the molecule enhancing its polarity, which could be related to the quenching of the ICT emission band through a non-radiative deactivation process.

**Figure 3.4.** Emission spectra of 10 μM dichloromethane solutions of a) **39** and b) **40** recorded at room temperature.

Electrochemical properties

Electrochemical properties were investigated by cyclic voltammetry (Table 3.3 and Appendix B). Figure 3.5 displays the cyclic voltammograms of compound **39** as a representative example of the series. Compounds **37–40** show two reduction waves, with the first one being quasi-reversible and the second one irreversible, together with an irreversible oxidation wave. Consistent with the strong electron-donating capability of the 2-methoxy group, compounds 2-methoxy substituted **38** and **40** are less easily reduced and more easily oxidized, exhibiting lower EA and IP values, than the non-substituted counterparts **37** and **39**. Ionization potentials and electron affinities range from 6.34 to 6.46 and from 4.32 to 4.40 eV, respectively. The amphoteric redox properties indicate the potential behaviour of this series of compounds for both hole and electron transport.

Table 3.3. Electrochemical properties of tricyanovinyl derivatives **37–40**.

Compd.	$E_{\text{red},1}^0$ [a] (V)	$E_{\text{onset}}^{\text{red}}$ [b] (V)	$E_{\text{onset}}^{\text{ox}}$ [b] (V)	EA [c] (eV)	IP [c] (eV)	E_{gap} [c] (eV)	EA ^{DFT} [d] (eV)	IP ^{DFT} [d] (eV)
37	-1.07	-0.99	1.07	4.40	6.46	2.06	4.03	6.07
38	-1.14	-1.06	0.95	4.33	6.34	2.01	3.96	5.94
39	-1.08	-1.00	1.06	4.39	6.45	2.06	4.03	5.98
40	-1.14	-1.07	0.98	4.32	6.37	2.05	3.96	5.94

[a] Reduction standard potential ($E_{\text{red},1}^0$) vs. Fc^+/Fc for the redox reduction couple determined from CV in 1 mM dichloromethane solutions at a scan rate of 100 mV s^{-1} . [b] Onset reduction potential ($E_{\text{onset}}^{\text{red}}$) and onset oxidation potential ($E_{\text{onset}}^{\text{ox}}$) vs. Fc^+/Fc estimated from CV in 1 mM dichloromethane solutions at a scan rate of 100 mV s^{-1} . [c] Estimated from cyclic voltammeteries as $\text{EA} = E_{\text{onset}}^{\text{red}} \text{ vs. } \text{Fc}^+/\text{Fc} + 5.39$, $\text{IP} = E_{\text{onset}}^{\text{ox}} \text{ vs. } \text{Fc}^+/\text{Fc} + 5.39$ and $E_{\text{gap}} = \text{IP} - \text{EA}$. [d] Estimated adiabatic EA and IP values by B3LYP/6-31+G(d) and PCM models in dichloromethane.

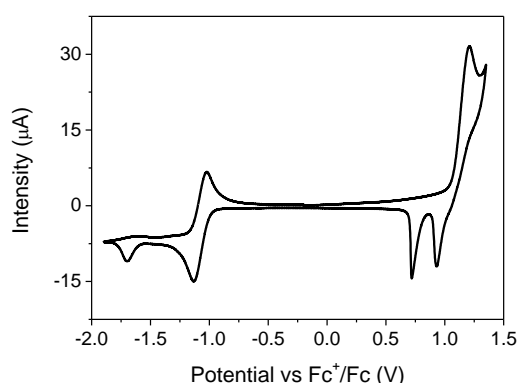


Figure 3.5. Cyclic voltammogram of compound **39** recorded at a scan rate of 100 mV s^{-1} in 1 mM dichloromethane solution.

DFT calculations

The structures of compounds **37–40** were explored by full optimization of the molecular structure by density functional theory (DFT) calculations employing the B3LYP/6-31+G(d) level of theory in vacuum. The twist angles between the tricyanovinyl and carbazole planes of the optimized molecular structures were calculated to be 19.7° and 41.0° for **39** and **40**, respectively. The difference between the above-mentioned twist angles with those of the crystal forms (1.31° and 48.3° for **39** and **40**, respectively) could be attributed to the established interactions between molecules in the solid state.

The highest occupied molecular orbitals (HOMOs) are mainly localized at the electron rich carbazole moiety with some contribution of the tricyanovinyl and the methoxy moieties, evidencing their influence on the energy of IP (Figure 3.6). Compounds **38** and **40** show the lowest values of theoretical adiabatic IP levels (*i.e.* 5.94 eV) due to the attached electron-donating methoxy group (Table 3.3). These values follow the same trend and are close (± 0.3 eV) to the IP values experimentally obtained from the electrochemical measurements (Table 3.3). The efficient withdrawing effect of the tricyanovinyl moiety leads to localization of the lowest unoccupied molecular orbital (LUMO) mainly on the tricyanovinyl group. Compounds **37** and **39**, without the methoxy substitution, exhibit the highest EA energy values (*i.e.* 4.03 eV).

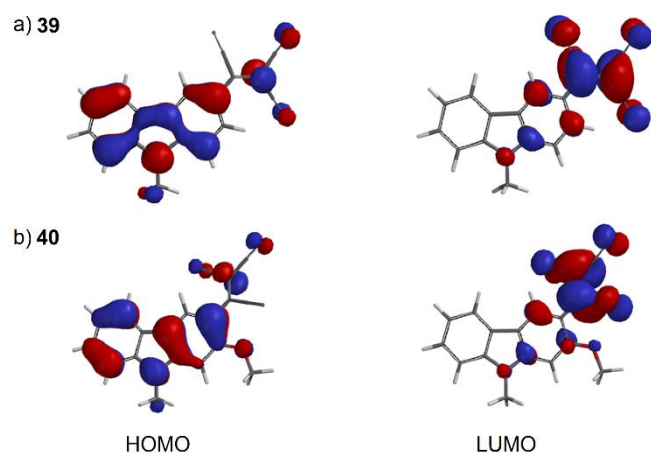


Figure 3.6. Computed spatial distributions of HOMOs and LUMOs of a) **39** and b) **40** (isovalue is 0.032).

The relationship between the IP and EA energy, or probability of the band gap engineering between the frontier molecular orbitals, and the rotation probability of the tricyanovinyl group in the neutral, cationic and anionic states of molecules **39** and **40** were estimated using the potential

energy surfaces (PES) scans. The PES scans of the neutral, cationic and anionic states of molecules **39** and **40** were conducted by rotating the tricyanovinyl moiety in steps of 20° from 0 to 360° (Figure A4 in Appendix A). The rotation barriers for **39** and **40** were estimated to be 23 and 14 kJ mol⁻¹, respectively. From PES analysis, the tricyanovinyl moiety vibrations for all states of **39** and **40** within the intervals of twist angles from -40° to +40° for **39**, and -60° to -30° together with 30° to 60° for **40** are possible in vacuum at room temperature, because the rotation barriers at these intervals are lower than the thermal energy $k_B T = 2.48$ kJ mol⁻¹, where k_B is the Boltzmann constant and T is the temperature.

3.2.4. Charge transport properties

The charge transport properties of the vacuum-evaporated layers of compounds **37–40** were studied by the time-of-flight (TOF) technique (Table 3.4). The attachment of the strong electron-withdrawing tricyanovinyl group to the carbazole moiety impacts the charge-transporting properties and as a result, electron transport is observed in the layers of these carbazole-based compounds. Representative TOF transients for electron transport of compound **38** and the dependency of hole and electron drift mobilities on the square root of the electric field are displayed in Figure 3.7. TOF characteristics for this series of compounds are collected in Appendix B. Transient curves in the linear scale for all compounds show a dispersive pattern. Nevertheless, transit times could be determined in the log–log scale.

Table 3.4. Hole and electron mobility data for the layers of tricyanovinyl-based compounds **37–40** obtained by the TOF technique.

Compd.	Electrons			Holes			E [a] (V cm ⁻¹)
	μ_e [a] (cm ² V ⁻¹ s ⁻¹)	μ_0 [b] (cm ² V ⁻¹ s ⁻¹)	α [c] (cm V ⁻¹) ^{1/2}	μ_h [a] (cm ² V ⁻¹ s ⁻¹)	μ_0 [b] (cm ² V ⁻¹ s ⁻¹)	α [c] (cm V ⁻¹) ^{1/2}	
37	2.6×10^{-4}	6.4×10^{-7}	0.0087	–	–	–	4.7×10^5
38	3.1×10^{-5}	2.3×10^{-8}	0.0072	1.8×10^{-4}	4.4×10^{-7}	0.0061	9.5×10^5
39	7.2×10^{-4}	1.3×10^{-4}	0.0027	–	–	–	4.0×10^5
40	9.3×10^{-5}	2.6×10^{-6}	0.0042	2.4×10^{-4}	7.2×10^{-6}	0.0042	7.1×10^5

[a] Electron (μ_e) and hole (μ_h) mobilities at the corresponding electric field (E). [b] Zero-field mobilities (μ_0). [c] Field dependence parameter (α). Measurements were determined in air and at room temperature. The thickness of the vacuum-evaporated layers varied from 0.85 to 5.0 μ m.

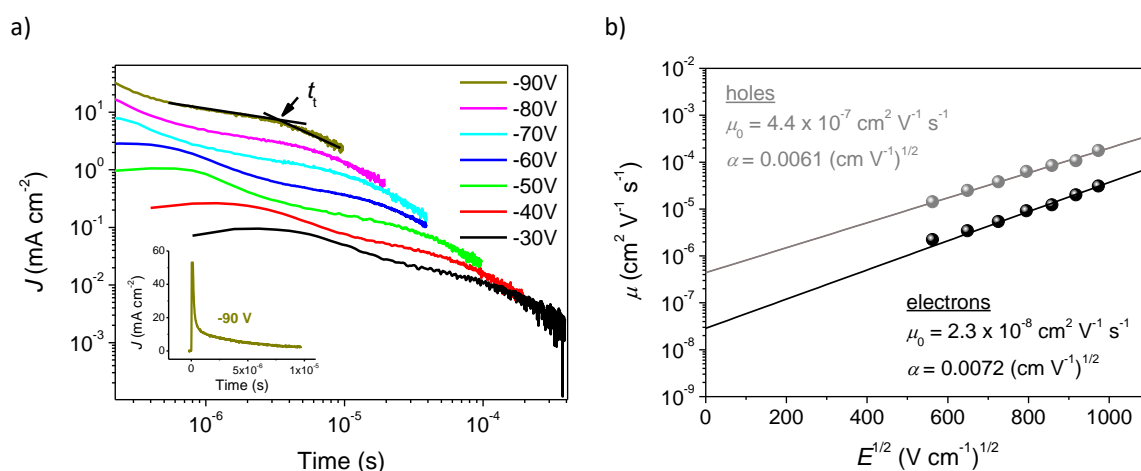


Figure 3.7. a) TOF transients for electron transport of the vacuum-evaporated layer of compound **38** ($d = 0.95 \mu\text{m}$). Inset shows one of the transient curves in the linear plot. b) Electric field dependences of the hole and electron mobilities of the vacuum-evaporated layer of **38**.

The layers of tricyanovinyl derivatives **37** and **39** showed only electron transport. *N*-Methyl-substituted compound **39** exhibited the highest electron mobility among the series of $7.2 \times 10^{-4} \text{ cm}^2 \text{ V}^{-1} \text{ s}^{-1}$ (Table 3.4). Hole transport was not detected in the layers of these compounds by the TOF technique. Remarkably, the introduction of the electron-donating methoxy group in the *ortho* position with respect to the tricyanovinyl fragment in compounds **38** and **40** afforded ambipolar properties. The *N*-alkylated derivative **40** showed more balanced electron and hole mobilities of 9.3×10^{-5} and $2.4 \times 10^{-4} \text{ cm}^2 \text{ V}^{-1} \text{ s}^{-1}$, respectively, than the non-alkylated analogue **38**. Significant differences in the charge mobility parameters, specifically the zero-field mobility (μ_0) and the Poole-Frenkel field dependence parameter (α), were observed for the layers of compounds **37–40** (Table 3.4). The electric field dependences for organic materials were previously described by the Gaussian disorder model, according to the following equation:^[120]

$$\mu = \mu_0 \exp \left[- \left(\frac{2\hat{\sigma}}{3} \right)^2 \right] \exp \left[C(\hat{\sigma}^2 - \Sigma^2) E^{1/2} \right] \quad (3.1)$$

where σ is the energy width of the hopping site manifold, Σ is the positional disorder, C is an empirical constant, and $\hat{\sigma} = \sigma/k_B T$. The field dependence parameter (α) (Table 3.4) is related to the energetic disorder parameters ($\hat{\sigma}$ and Σ), which at the same time depend on the molecular structure.^[121] Therefore, the differences in the charge mobility parameters at low fields (μ_0) among the derivatives studied here can be attributed to the differences in the above mentioned energetic disorder parameters.

In order to gain insight into the fundamentals of the relationship between the chemical structure and the above mentioned electrical properties of this series of compounds, DFT calculations were performed. In the first instance, the reorganization energies (λ) for holes and electrons were estimated for *N*-methyl compounds **39** and **40**. The reorganization energy is defined as the relaxation energy of a molecule from the geometry of the neutral state to the charged (anion and cation) state and from the charged to the neutral state. The reorganization energies in vacuum for holes (λ_+) were calculated to be 75.4 and 289 meV and for electrons (λ_-) 344 and 352 meV for **39** and **40**, respectively. However, it should be remembered that the structures of molecules **39** and **40** found in the solid state are different than those predicted in vacuum, because the rotation of the groups attached to the carbazole core should be fixed in the solid state by intermolecular forces. Indeed, Vaissier *et al.*^[122] showed that performing DFT calculations on the isolated molecules systematically underestimates the energy barrier to charge transfer, which is important to be taken into consideration when designing conductive molecular materials. Thus, the twist angles from the single crystal structures (*i.e.* 1.31° for **39** and 48.3° for **40**, Figure 3.1) for the solid state, the calculation of the reorganization energies was carried out again as previously, showing values for holes (λ_+) of 64.4 and 249 meV and for electrons (λ_-) of 310 and 369 meV for **39** and **40**, respectively, following the same trend as the obtained values estimated in vacuum. Thus, the calculated reorganization energies for holes and electrons are similar in the methoxy-substituted derivative **40**, but differ considerably for the non-methoxy substituted analogue **39**, expecting to more balanced charge transport characteristics for the layers of compound **40**.

The charge mobilities of compounds **39** and **40** were theoretically estimated in order to establish the relationship between the molecular origin and the different hole and electron transport behaviour across layers of compounds **39** and **40** determined by the TOF technique. For this purpose, the crystal structures of **39** and **40** were used to generate a wide variety of possible hopping pathways between neighbouring molecules with intermolecular interactions, as shown in Figure 3.8 and Figures A5–A7 in Appendix A. It should be mentioned that the crystal structure of compound **39** presented in this work is different from the one previously reported.^[123] Therefore, both structures have been considered for the determination of the hopping pathways. According to the Holstein small polaron limit, a charge is localized on a single organic molecule.^[124] The rate of charge transfer between molecules was estimated by the Marcus theory.^[125] All data of charge mobility calculations are summarized in Table A1 in Appendix A and the details of the theoretical calculations are given in the Experimental part.

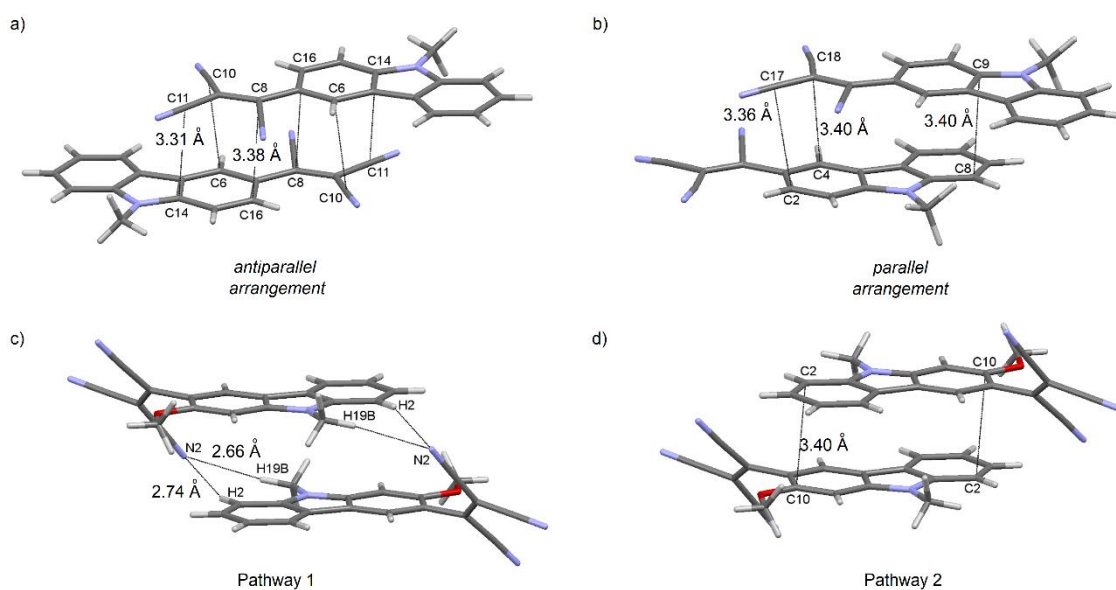


Figure 3.8. Selected carrier hopping pathways between neighbouring molecules and intermolecular interactions for a) the crystal structure of **39** reported here, b) the previously reported crystal structure^[123] of **39** and the two selected pathways for the crystal structure of **40**: c) pathway 1 and d) pathway 2.

The carrier hopping pathways shown in Figure 3.8 for compounds **39** and **40** were considered to be the most effective and they were selected for the charge carrier mobility calculations. Compounds **39** and **40** exhibit a layered organization. Neighbouring molecules of **39** obtained from the crystal structure described here and the previously reported one^[123] are interlinked via π - π interactions to produce antiparallel and parallel arrangements, respectively, showing the strongest intermolecular interactions among all the proposed pathways, with interaction energies of -111 and -76.9 kJ mol⁻¹, respectively. Hence, these two carrier hopping pathways, from the crystal structure of **39** described here and the previously reported one,^[123] were considered for the charge carrier mobility calculations. On the other hand, for compound **40**, among all the considered pathways (Figures 3.8c and d and Figure A7 in Appendix A), only pathway 1 and 2 were taken into account for the charge carrier mobility calculations due to the significant site probabilities of 0.76 and 0.24, respectively. Adjacent molecules in pathways 1 and 2 are connected *via* C-H...NC hydrogen bonding and π - π interactions to produce an antiparallel arrangement, showing the highest interaction energies of -99.7 and -96.8 kJ mol⁻¹, respectively, among all the proposed pathways.

For the selected pathways shown in Figure 3.8 from the crystal structure of **39** described here and the previously reported one,^[123] the calculated coupling integral values for electrons were

found to be higher (140 and 166 meV) than those for holes (47.4 and 83.2 meV, respectively), pointing out that for compound **39** electron transport is favoured relative to hole transport. On the other hand, for compound **40**, the coupling integrals for pathway 1, which showed the highest site probability value, were estimated to be 21.8 meV for electrons and 63.1 meV for holes, respectively, indicating that for compound **40** hole transport is more favoured. Compound **40** shows electronic coupling values for holes between neighbouring molecules (63.1 meV) comparable to those for compound **39** (47.4 and 83.2 meV). According to the experimental results obtained by the TOF technique, compound **39** has negligible hole mobility, whereas compound **40** has values even larger than its electron mobility. In order to explain this phenomenon, the theoretical hole and electron charge mobilities for **39** and **40** versus the polarization energies, reorganization energies and the coupling integrals were analysed and are collected in Figure 3.9. First of all, it is worth mentioning that compounds **39** and **40** show a notable difference in the reorganization energies for holes (64.4 versus 249 meV, respectively). On the one hand, Figure 3.9a and c show that the polarization energies have a great impact on the charge mobilities in comparison to the coupling integrals. On the other hand, for compound **39**, an inverted Marcus region (*i.e.* $\lambda < \Delta G$) is observed for the hole mobility. In that case, the low reorganization energy of **39** reduces the hole mobility (Figure 3.9b). Normal Marcus regions for all the other processes were estimated. Thus, from a theoretical point of view, the charge mobilities are calculated from the different above-mentioned parameters, that is, the reorganization and polarization energies, the coupling integrals and the sites probabilities.

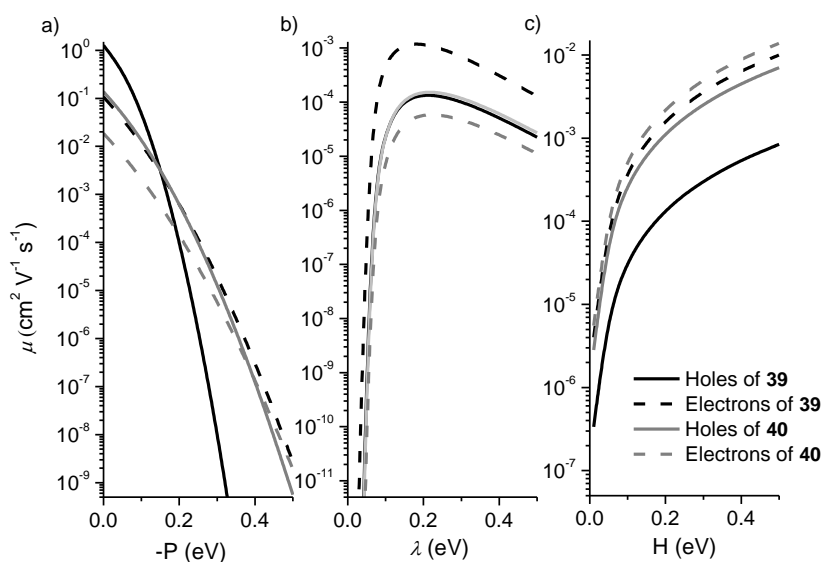


Figure 3.9. Visualization of the predicted hole and electron charge mobilities when changing only the polarization energies (a), reorganization energies (b) and the coupling integrals (c) for compounds **39** and **40** at $1.1 \times 10^7 \text{ V m}^{-1}$ electric field.

The calculated mobility dependence on the applied electric field for the modelled layers shows a very good agreement with the data obtained from TOF experiments (Figure 3.10). The experimental and theoretical charge mobilities of electrons for **39** at the highest experimental electric field of $4.0 \times 10^5 \text{ V cm}^{-1}$ were determined and calculated to be 7.2×10^{-4} and $6.6 \times 10^{-4} \text{ cm}^2 \text{ V}^{-1} \text{ s}^{-1}$, respectively. Hole mobilities for compound **39** were not detected by the experimental TOF method, in accordance with the prediction of our theoretical model, through which were estimated to be very low on the order of $10^{-6} \text{ cm}^2 \text{ V}^{-1} \text{ s}^{-1}$. For compound **40**, the experimental and theoretical charge mobilities of holes and electrons at the highest experimental electric field of $7.1 \times 10^5 \text{ V cm}^{-1}$ were determined and estimated to be 2.4×10^{-4} and 2.1×10^{-4} for holes and 9.3×10^{-5} and $5.8 \times 10^{-5} \text{ cm}^2 \text{ V}^{-1} \text{ s}^{-1}$ for electrons, respectively.

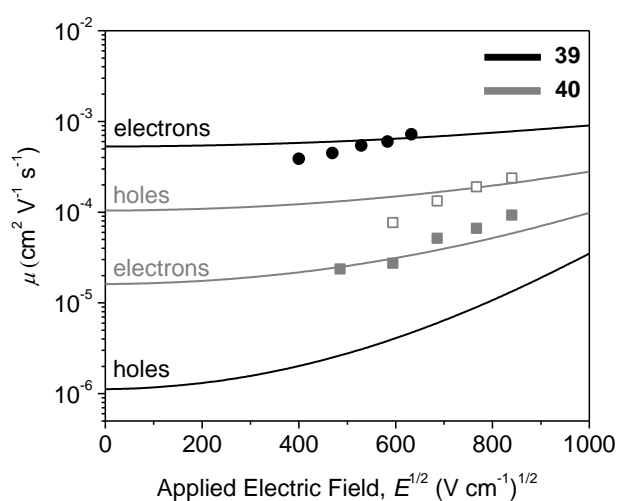


Figure 3.10. Visualization of the experimental (symbols) and predicted (lines) charge mobilities of **39** and **40**.

The presented results suggest that the charge transport throughout layers of compounds **37–40** depend considerably on the supramolecular organization, which is highly influenced by the *ortho*-methoxy substituent on the carbazole core with respect to the tricyanovinyl group. Indeed, the tricyanovinyl fragment in compound **40** is placed out of the molecular plane due to the steric hindrance caused by the methoxy fragment. Taking into account that the HOMO is localized mainly at the electron rich carbazole moiety for both **39** and **40** compounds (Figure 3.6), the twisted structure of compound **40** implies a face-to-face interaction between adjacent donor carbazole fragments, whereas for compound **39** the planar structure shows slipped cofacial interactions between the adjacent donor carbazole units (Figure 3.8). From the charge transport point of view, theoretical calculations pointed that the inverted Marcus region of **39** could explain the

enhancement of the hole mobility observed for **40** in comparison to that recorded for **39**. On the other hand, considering that the LUMO is mainly localized in the tricyanovinyl unit, a greater overlap between the LUMOs of neighbouring molecules is expected for the planar compound **39** than for compound **40**, since the accepting tricyanovinyl groups of neighbouring molecules are closer in compound **39** (Figure 3.8 and Table A1 in Appendix A). This feature is corroborated with the higher calculated coupling integral values for electrons for compound **39** with respect to holes. Accordingly, compound **39** showed the highest electron mobilities observed both experimentally and theoretically.

3.3. A series of tricyanovinyl derivatives with different *N*-alkyl chain length

Among the series of push-pull derivatives presented in Section 3.2, *N*-alkylated derivatives **39** and **40** exhibited the highest electron mobilities as determined by the TOF technique. Keeping this idea in mind and considering that flexible side chains can control the molecular packing and order in the solid state, a new series of tricyanovinyl-substituted carbazole-based materials, with varying the *N*-alkyl chain length, was prepared to analyse its influence on the charge-transporting properties (Scheme 3.3). These materials were evaluated as active layers in OTFTs and their performance was correlated to their corresponding molecular packing via XRD studies.

3.3.1. Synthesis

The preparation of 9-alkyl-3-(1,2,2-tricyanovinyl)-9*H*-carbazole derivatives **45–48**, which differ on the length of the alkyl chain located on the nitrogen atom of the carbazole core, is shown in Scheme 3.3. The selected alkyl chain lengths have been of 2, 4, 8 and 12 carbon units to generate the corresponding **45–48** derivatives, respectively. Derivatives **45**^[114a,126] and **46**^[114a] have been previously described in the literature. Compounds **45–48** were easily prepared by heating the corresponding *N*-alkylated carbazole precursor in anhydrous *N,N*-dimethylformamide (DMF) at 50 °C. Previously, *N*-alkyl derivatives 9-butyl-9*H*-carbazole (**49**), 9-octyl-9*H*-carbazole (**50**) and 9-dodecyl-9*H*-carbazole (**51**) were obtained by alkylation^[127–129] of 9*H*-carbazole using NaH as a base in DMF in high yields. Compound **45** was directly prepared from commercially available 9-ethyl-9*H*-carbazole.

Optical properties

UV-vis absorption spectra of compounds **45–48** in dichloromethane solutions and in the respective thin films each show two absorption regions that cover the UV and the visible electromagnetic spectrum (Table 3.6 and Figure 3.11). The optical data of compound **39** is shown again for comparison in Table 3.6. The first absorption region, which is attributed to the carbazole moiety, is located in the UV zone with a maximum at 290–292 nm in solution. The second broad absorption band is centred at lower energy (490–494 nm in solution) and attributed to the intramolecular charge transfer from the electron-donating carbazole moiety to the electron-withdrawing tricyanovinyl group as mentioned previously for compound **39**. In solution, all compounds (**39** and **45–48**) display practically identical absorption spectra independently of the *N*-alkyl substitution of the carbazole moiety. However, some information can be obtained by comparing the absorption spectra in solution and in the solid state. The absorption spectra of thin films show a hypsochromic shift of the maximum of the charge-transfer absorption band in comparison to that observed in solution. The hypsochromic shift is more significant as the *N*-alkyl chain length increases, as revealed by compounds **39** (18 nm), **45** (21 nm), **46** (58 nm), **47** (69 nm) and **48** (67 nm). These results are indicative of the influence of the *N*-alkyl chain length on the molecular packing in the solid state, which will be discussed below through the single-crystal X-ray analysis.

Table 3.6. Optical properties of tricyanovinyl derivatives **39** and **45–48**.

Compd.	Solution			Solid state		
	$\lambda_{\text{abs,max}}$ ^[a,b] (nm)	$\lambda_{\text{em,max}}$ ^[a,b] (nm)	Φ_f ^[c]	$\lambda_{\text{abs,max}}$ ^[a,d] (nm)	$\lambda_{\text{em,max}}$ ^[a,d] (nm)	Φ_f ^[e]
39	290, 490	355, 625	0.02 (0.06)	298, 472	652	0.01
45	292, 493	358/373, 627	0.02 (0.07)	300, 472	647	< 0.01
46	292, 494	353/373, 627	0.02 (0.07)	282, 436	636	0.01
47	292, 494	399, 625	0.02 (0.07)	282, 425	641	0.05
48	292, 494	396, 628	0.02 (0.08)	283, 427	631	0.25

[a] Wavelength of maximum absorption ($\lambda_{\text{abs,max}}$) and emission ($\lambda_{\text{em,max}}$). Molar absorption coefficient (ϵ) can be found in the Experimental Part. [b] Determined in 10 μM dichloromethane solutions at room temperature. Emission spectra were recorded after excitation at $\lambda_{\text{abs,max}}$. [c] Fluorescent quantum yield (Φ_f) determined in dichloromethane solution using an integrating sphere after excitation at 290 nm. The Φ_f determined in toluene solution is shown in parenthesis. [d] Measured in vacuum-evaporated thin films on quartz substrates at room temperature. Emission spectra were recorded after excitation at the wavelength of maximum absorption of the charge-transfer band. [e] Fluorescent quantum yield (Φ_f) determined from vacuum-evaporated thin films after excitation at 450 nm using optically matched solutions of tris(2,2'-bipyridyl)ruthenium(II) chloride in water as the standard.

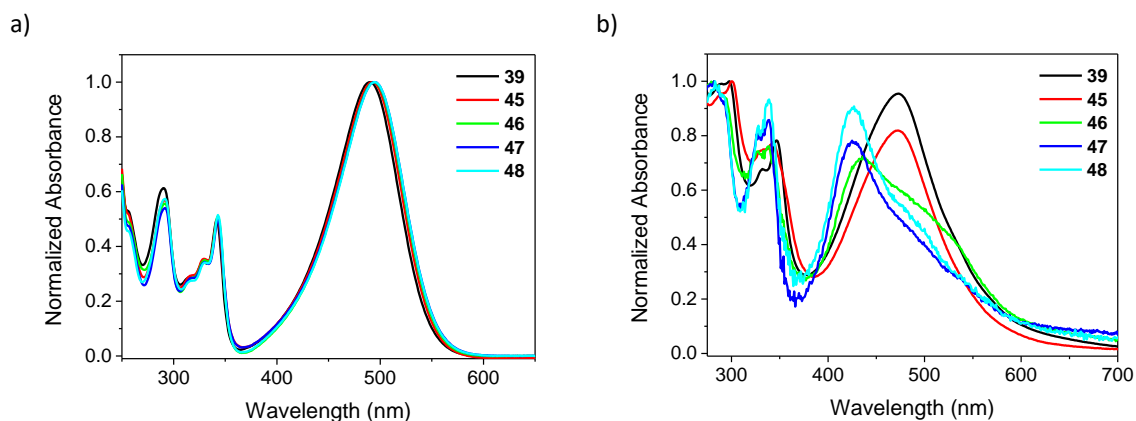


Figure 3.11. UV-vis absorption spectra of compounds **39** and **45–48** in a) 10 μM dichloromethane solutions and b) vacuum-evaporated thin films of 75 nm (right).

The emission spectra of **45–48** recorded in 10 μM dichloromethane solutions are similar to that of *N*-methyl **39** (Figure 3.12). Thus, two emission bands are observed independently of the excitation wavelength. The emission band located at longer wavelengths, which is attributed to the intramolecular charge transfer process, is centred at 625–628 nm and is independent of the *N*-alkyl chain length. Accordingly, quantum yields determined in dichloromethane solution are very similar for this series of compounds. They are very low in dichloromethane ($\Phi_f = 0.02$) and slightly enhanced in toluene solutions ($\Phi_f = 0.06\text{--}0.08$), pointing to the quenching of the fluorescence when using solvents of increasing polarity.

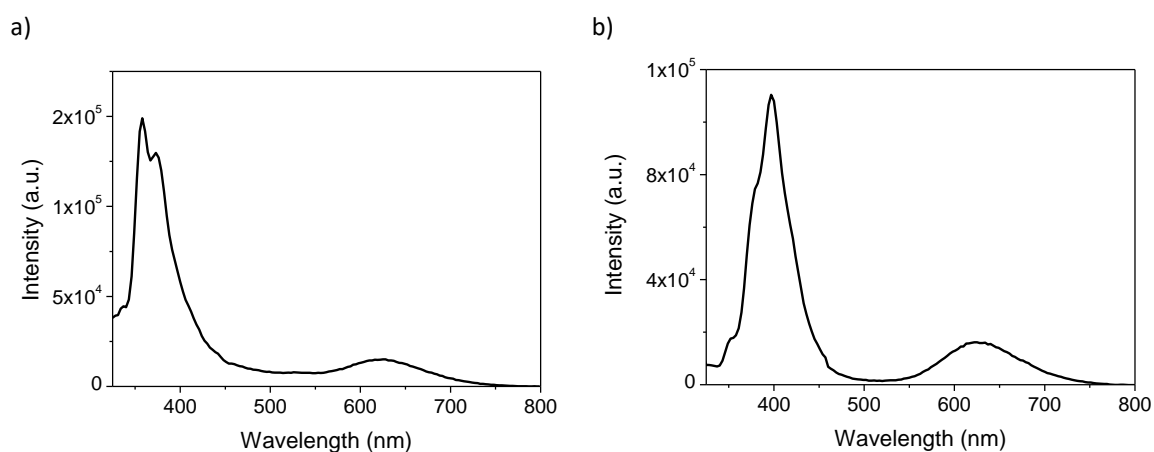


Figure 3.12. Emission spectra of 10 μM dichloromethane solutions of a) **45** and b) **47** recorded at room temperature after excitation at 292 nm.

The emission spectra of vacuum-evaporated thin films of **39** and **45–48** are shown in Figure 3.13. According to the behaviour observed in the absorption spectra, the emission band from the ICT state in the solid state is centred at 631–652 nm and is bathochromically shifted in comparison to the emission band recorded in solution. Quantum yields in the solid state are very low for **39**, **45** and **46**, but they increase as longer is the alkyl chain. Thus, *N*-dodecyl derivative **48** shows enhanced emission in the solid state ($\Phi_f = 0.25$) in comparison to dichloromethane solutions ($\Phi_f = 0.02$).

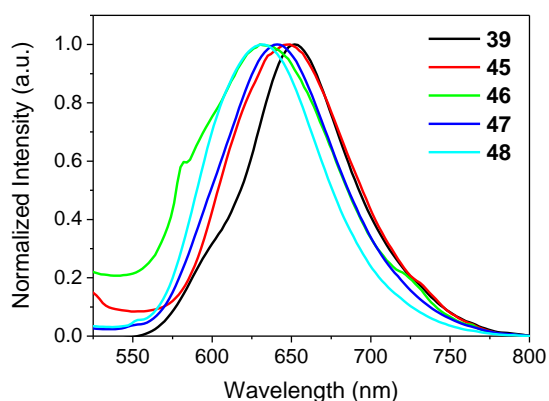


Figure 3.13. Emission spectra of vacuum-evaporated layers of **39**, **45–46** (150 nm) and **47–48** (75 nm).

Electrochemical properties

The electrochemical properties of compounds **45–48** were characterized by cyclic voltammetry (Table 3.7 and Appendix B). All compounds display identical redox behaviour as *N*-methyl derivative

Table 3.7. Electrochemical properties for tricyanovinyl derivatives **39** and **45–48**.

Compd.	$E_{\text{red},1}^0$ (V) [a]	$E_{\text{onset}}^{\text{red}}$ (V) [b]	$E_{\text{onset}}^{\text{ox}}$ (V) [b]	EA (eV) [c]	IP (eV) [c]	E_{gap} (eV) [c]
39	-1.08	-1.00	1.06	4.39	6.45	2.06
45	-1.08	-1.00	1.07	4.39	6.46	2.07
46	-1.08	-1.00	1.06	4.39	6.45	2.06
47	-1.08	-1.00	1.07	4.39	6.46	2.07
48	-1.08	-1.00	1.07	4.39	6.46	2.07

[a] Reduction standard potential ($E_{\text{red},1}^0$) vs. Fc^+/Fc for the redox reduction couple determined from CV in 1 mM dichloromethane solutions at a scan rate of 100 mV s^{-1} . [b] Onset reduction potential ($E_{\text{onset}}^{\text{red}}$) and onset oxidation potential ($E_{\text{onset}}^{\text{ox}}$) vs. Fc^+/Fc determined from cyclic voltammeteries of 1 mM dichloromethane solutions at a scan rate of 100 mV s^{-1} . [c] Estimated from cyclic voltammeteries as $\text{EA} = E_{\text{onset vs. Fc}^+/\text{Fc}}^{\text{red}} + 5.39$, $\text{IP} = E_{\text{onset vs. Fc}^+/\text{Fc}}^{\text{ox}} + 5.39$ and $E_{\text{gap}} = \text{IP} - \text{EA}$.

39. Cyclic voltammograms exhibit two reduction waves, being the first one *quasi*-reversible and the second one irreversible, together with one irreversible oxidation wave. Electron affinities (EA) and ionization potentials (IP) of this series of compounds were estimated to be 4.39 and 6.45–6.46 eV, respectively, in solution. The high EA values of these compounds are indicative of their potential *n*-type properties.

3.3.3. Single-crystal X-ray analyses

The crystal structures of compounds **45–48** were determined by single-crystal X-ray analysis. Suitable single crystals were grown by slow evaporation from the corresponding dichloromethane (**45**), chloroform (**46**) and acetone (**47** and **48**) solutions. The detailed crystallographic data of **45–48** can be found in Appendix B. Molecules **39** and **45–48** adopt an almost planar conformation independently of the length of the *N*-alkyl chain. The twist angles between the tricyanovinyl and the carbazole planes of molecules **45–48** are in the range of 3.31 to 6.36° (Figure 3.14), which are only slightly higher than that for compound **39** (1.31°). Regarding the crystal structure of *N*-ethyl derivative **45**, the tricyanovinyl group is presented in two different conformations (Figure

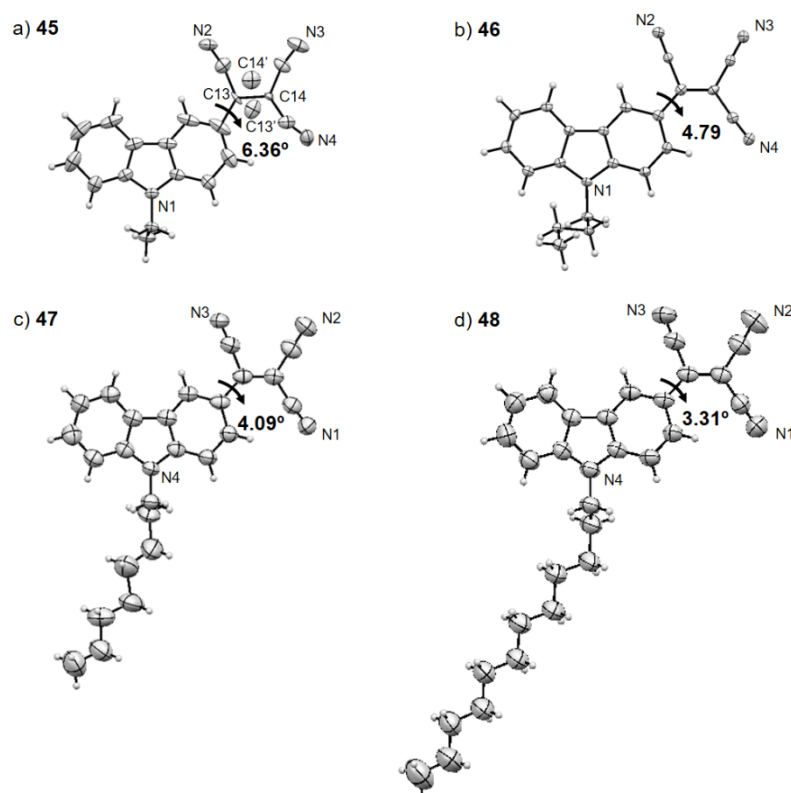


Figure 3.14. X-ray crystal structures of **45–48**, showing the 50% probability displacement.

3.14a), showing a free rotational barrier under the crystallization conditions. This is represented in Figure 3.14a by showing the two different positions that either the atoms C13–C14 or C13'–C14' of the tricyanovinyl fragment can adopt.

The crystal structures of derivatives with the shorter *N*-alkyl chains, from methyl to butyl chains **39**, **45** and **46** (Figure 3.15), show a layered organization with an antiparallel arrangement. Molecules of *N*-methyl derivative **39** show π – π interactions along the *c*-axis and interlayer distances of 3.28 and 3.29 Å (Figure 3.15a). In addition, the molecules adopt a herringbone structure along the *b*-axis through C–H \cdots π and C–H \cdots NC hydrogen bonding intermolecular interactions with distances of 2.84 and 2.54 Å, respectively. In a similar way, the crystal structure of the ethyl analogue **45** shows a herringbone packing motif (Figure 3.15b). Molecules of the π stacks show π – π interactions along the *a*-axis, with slightly larger interlayer distances of 3.35–3.36 Å in comparison to those of **39**. Neighbouring molecules also exhibit C–H \cdots NC hydrogen bonding interactions between adjacent stacks with a minimum distance of 2.58 Å. Finally, the crystal structure of the *N*-butyl substituted compound **46** shows π – π stacking interactions along the *a*-axis with the same interlayer distances as in **45** (3.35 and 3.36 Å) (Figure 3.15c). Molecules exhibit a herringbone structure along the *b*-axis and are connected with the molecules of the adjacent π -stacked arrays via C–H \cdots π and C–H \cdots NC hydrogen bonding interactions (2.73 and 3.04 Å).

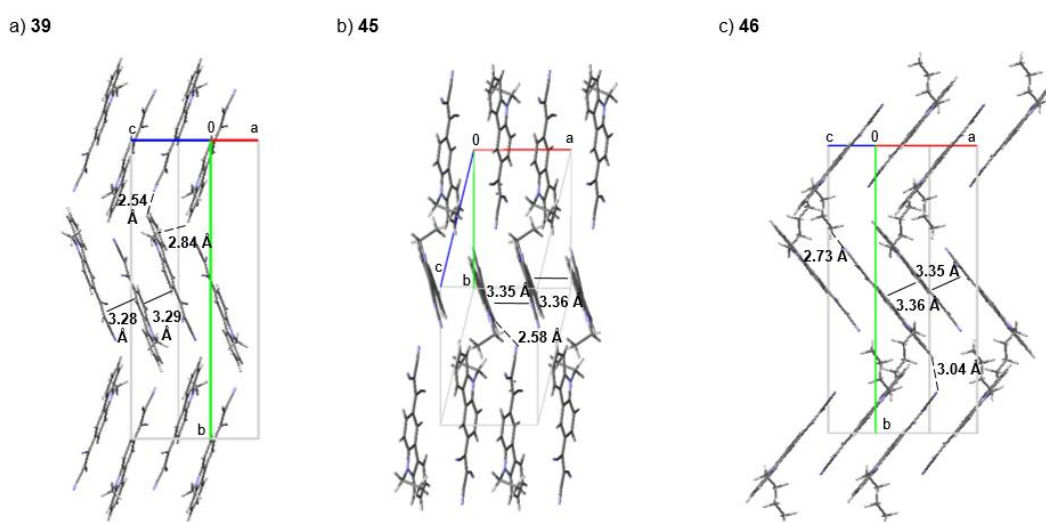


Figure 3.15. Crystal structures of a) **39**, b) **45** and c) **46**.

The crystal structures of *N*-octyl and *N*-dodecyl derivatives **47** and **48** are both very similar as displayed in Figure 3.16. Likewise to **39**, **45** and **46**, molecules are organized in an antiparallel

arrangement showing π - π stacking interactions along the *b*-axis with interlayer distances of 3.40/3.51° and 3.38/3.53° for **47** and **48**, respectively. In contrast to **39**, **45** and **46**, molecules between adjacent π stacks are coplanar and connected through C-H \cdots NC hydrogen bonding interactions, with minimum distances of 2.58 Å for **47** and 2.59 Å for **48**, and interdigitated alkyl chains. Consistent with the length of the alkyl chain, the minimum distances between neighbouring carbazole cores separated by the interdigitated alkyl chains are 7.12 and 11.76 Å for **47** and **48**, respectively. Hence, the π -stacked arrays are more separated due to the longer *N*-alkyl chain introduced.

Therefore, the resulting molecular arrangement of this series of compounds depends on the length of the *N*-alkyl chain. Molecules with the shorter alkyl chains **39**, **45** and **46** adopt a herringbone packing motif, being the aromatic π -system the responsible of the supramolecular assembly. In contrast, the longer alkyl chains in **47** and **48** induce the formation of π stacked layers separated by interdigitated alkyl chains. However, it should be highlighted that for all the compounds, molecules in the π stacks show an antiparallel arrangement with minimum interlayer distances in the range of 3.28–3.40 Å, which are suitable for an efficient charge transport considering the hopping model.

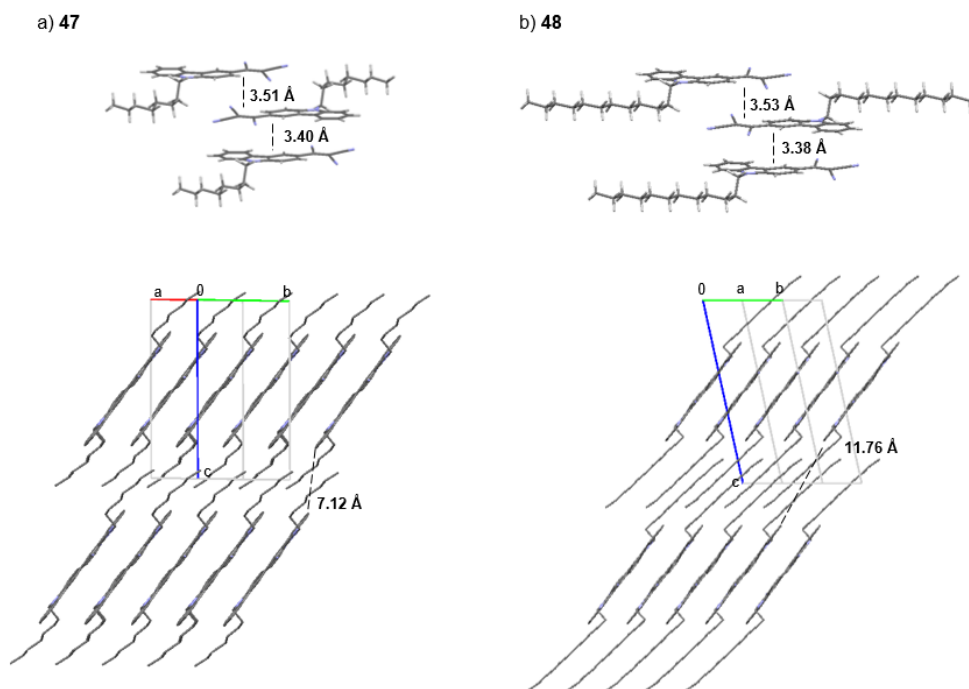


Figure 3.16. Crystal structures of a) **47** and b) **48**. Hydrogen atoms have been removed for clarity in the representation of the molecular packing.

3.3.4. Organic Thin-Film Transistors

Charge-transporting properties of compounds **39** and **45–48** were studied in bottom-gate/top-contact OTFTs by using polystyrene (PS) treated c-Si/SiO₂ gate/dielectric substrates and Au as source and drain electrodes. The semiconductor thin films were deposited by the vacuum evaporation technique (with a base pressure below 10⁻⁶ mbar).

Devices based on **39** and **45–48** showed characteristics of n-type transistors (Table 3.8, Figure 3.17 and Appendix B). OTFT devices with PS-treated substrates based on compounds **39** and **45–48** exhibited similar electron mobilities in the range of 9 × 10⁻⁶ to 5 × 10⁻⁵ cm² V⁻¹ s⁻¹, showing a no clear dependence of the mobility with the *N*-alkyl chain length, according to the antiparallel arrangement in the π stacks with similar interlayer distances that all of them exhibit. Threshold voltages were also similar for all the prepared devices (15.3–25.6 V), but in contrast it can be mentioned that those devices based on the *N*-octyl **47** and *N*-dodecyl **48** materials showed the larger I_{on}/I_{off} ratios ($\sim 10^4$). In order to study the effect of the dielectric treatment on the device performance, an OTFT device with octadecyltrichlorosilane (OTS) treated c-Si/SiO₂ surface based on compound **39** was prepared. Similar electron mobilities were achieved for devices of **39** on PS- and OTS-treated substrates around 2–3 × 10⁻⁵ cm² V⁻¹ s⁻¹. Given that no significant improvement was observed, no further OTFT devices with OTS-treated substrates were prepared for its analogues.

Table 3.8. OTFT characteristics of devices based on tricyanovinyl-carbazole derivatives **39** and **45–48** with PS and OTS-treated c-Si/SiO₂ substrates.

Compound		μ_e (cm ² V ⁻¹ s ⁻¹) [a]	V_{th} (V) [b]	I_{on}/I_{off} (A/A) [c]
39	PS	3 × 10 ⁻⁵	19.7	$\sim 10^2$
39	OTS	2 × 10 ⁻⁵	23.6	$\sim 10^3$
45	PS	9 × 10 ⁻⁶	25.6	$\sim 10^1$
46	PS	2 × 10 ⁻⁵	15.3	$\sim 10^2$
47	PS	3 × 10 ⁻⁵	19.6	$\sim 10^4$
48	PS	5 × 10 ⁻⁵	19.6	$\sim 10^4$

[a] Electron mobility (μ_e). [b] Threshold voltage (V_{th}). [c] I_{on}/I_{off} ratio. Measurements were performed under vacuum and at room temperature.

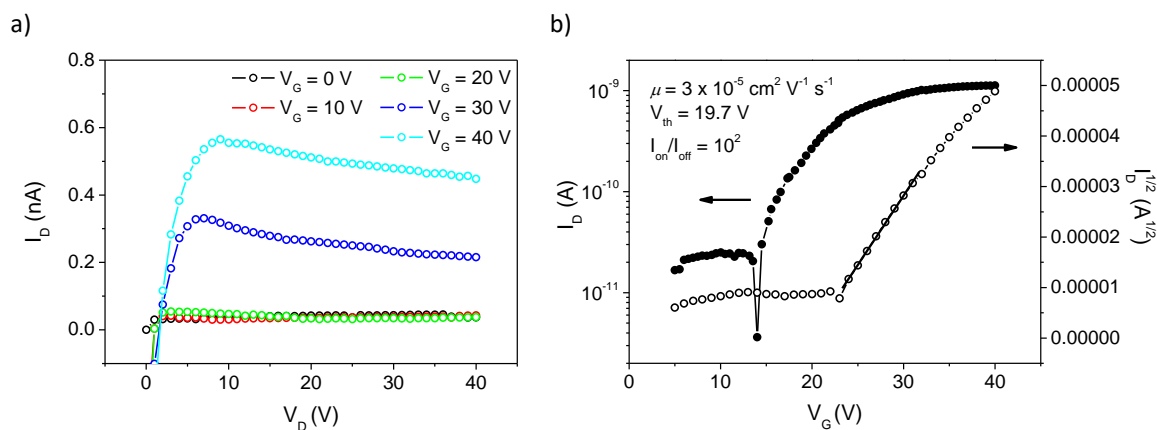


Figure 3.17. OTFT characteristics of a device fabricated with compound **39** as the semiconductor layer and with PS-treated substrate. a) Output characteristics at different gate voltages (V_G). b) Transfer ($V_D = 10$ V) and saturation characteristics.

3.3.5. Molecular order and morphology of the OTFT active layers

In order to correlate the charge transport properties with the molecular structure in the thin films, vacuum-evaporated layers (75 nm) of **39** deposited on PS- and OTS-treated c-Si/SiO₂ substrates and of **45–48** deposited on PS-treated substrates were subjected to Grazing Incidence X-Ray Diffraction (GIXRD) studies. Figure 3.18 displays the GIXRD patterns of the above-mentioned layers of **39** and **45–48**. It should be mentioned that the longer alkyl chains induce more ordered films. In fact, GIXRD spectra of layers of **39**, **45** and **46** show in general multiple weak diffraction peaks, whereas films of **47** and **48** show only one strong diffraction peak.

GIXRD spectrum of the film of **39** deposited on PS-treated c-Si/SiO₂ substrate shows several weak diffraction peaks at $2\theta = 9.28^\circ$, 10.68° and 13.02° . Similarly, the GIXRD spectrum of the layer of **39** deposited on OTS-treated substrate shows the diffraction peaks at $2\theta = 9.22^\circ$, 10.72° and 13.02° . However, the GIXRD spectra of **39** do not correspond neither to the powder XRD spectrum (Appendix B) nor to the single crystal data. Therefore, it was not possible to establish the molecular orientations in the films.

Layers of **45** prepared on PS-treated c-Si/SiO₂ substrates show several weak diffraction peaks and one stronger diffraction peak at $2\theta = 8.88^\circ$, which suggest a preferred orientation in the film. Combining the single crystal data and the powder XRD spectra (Appendix B), this stronger

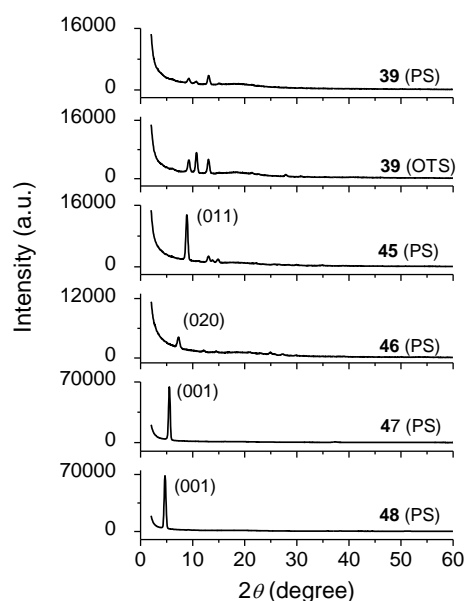


Figure 3.18. GIXRD patterns of vacuum-deposited layers of **39** on PS- and OTS-treated c-Si/SiO₂ substrates and of **45–48** on PS-treated c-Si/SiO₂ substrates.

diffraction peak can be assigned to the reflection 011, indicating that the (011) plane is parallel to the c-Si/SiO₂ substrate, with the *a*-axis also in the parallel plane. In a similar way, the GIXRD spectrum of the layer of **46** on PS-treated substrate shows more than one diffraction peak. The strongest diffraction peak at $2\theta = 7.28^\circ$ can be attributed to the reflection 020, indicating that the (010) plane is parallel to the c-Si/SiO₂ substrate, with the *a*- and *c*-axis also in the parallel plane. The molecular packing in the thin films of **45** and **46** corresponds to that of the corresponding derivatives in the single crystals and as a result, it can be concluded that molecules in layers of **45** and **46** exhibit a preferred orientation as the one displayed in Figure 3.15b and c, respectively, with the π - π stacking direction along the *a*-axis, that is parallel to the substrate surface.

GIXRD spectra of thin films of compounds **47** and **48** show only one strong diffraction peak at $2\theta = 5.52^\circ$ and 4.68° , respectively, indicating that **47** and **48** form well-ordered films under the experimental conditions. Combining the single crystal data and the powder XRD spectra (Appendix B), the diffraction peaks at $2\theta = 5.52^\circ$ for **47** and $2\theta = 4.68^\circ$ for **48** can be assigned to the reflection 001, indicating that the (001) plane is parallel to the c-Si/SiO₂ substrate, *i.e.* with *a*- and *b*-axis also in the parallel plane. The XRD study indicates that the molecular packing in the thin films is in accordance with that of the corresponding derivatives **47** and **48** in the single crystals. Molecules in films of **47** and **48** are oriented with the π - π stacking direction being parallel to the substrate surface as shown in Figure 3.16 (below).

According to the XRD study, molecules in vacuum-evaporated layers of compounds **45–48** show a similar layered organization with π – π stacking interactions and comparable interlayer distances. In addition, they are organized with the π – π stacking direction being parallel to the substrate surface. This kind of molecular organization is recognised to be appropriate for obtaining enhanced charge carrier mobilities in OTFTs. Therefore, this results justify that OTFTs with PS-treated substrates based on **45–48** show similar electron mobilities independently of the alkyl chain length.

Here, it should be highlighted that the distance between adjacent π stacks are significantly increased in compounds with longer alkyl chains **47** and **48** by the interdigitated alkyl chains, showing minimum distances of 7.12 and 11.76 Å, respectively (Figure 3.16). Since these alkyl chains act as insulating parts and do not contribute to the charge transport process,^[19] a decrease in the charge transport properties could be expected for **47** and **48** based devices. Instead, comparable electron mobilities to that of devices based on **39**, **45** and **46** were achieved. These unexpected results suggest that the use of long alkyl chains is not in the opposite direction to obtain enhanced charge carrier mobilities in OTFTs. In fact, the use of long alkyl chains induces better ordered films that could be involved in the improvement of the device performance.

The morphology of the films of **39** and **45–47** was studied by AFM further investigate the film-forming properties of this series of derivatives. Figure 3.19 collects the AFM images taken from vacuum-evaporated films of **39** on PS- and OTS- treated c-Si/SiO₂ substrates and of **45–47** on PS-treated c-Si/SiO₂ substrates. Layers of **39**, **45** and **46** deposited on PS-treated substrates show continuous films with similar granular morphology, being the grain sizes in the range of 0.1–0.5 μm . The film of **39** on OTS-treated substrate shows more elongated crystal grains in comparison to the corresponding film on PS-treated substrate, in accordance to the XRD patterns of **39**, where different relative intensities of the diffraction peaks were observed depending on the substrate treatment. On the other hand, the vacuum-deposited film of *N*-octyl **47** shows grains with a larger size around 0.5–1 μm with a terrace-like structure (Figure 3.19f), which is in accordance to the XRD studies and the long range organization of the molecules in the film.

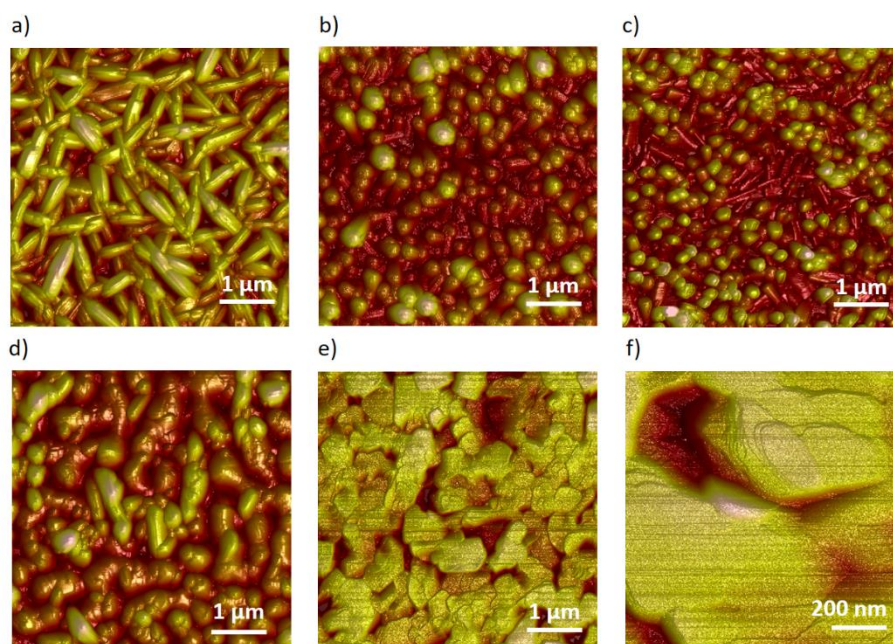


Figure 3.19. AFM images of vacuum-evaporated thin films of a) **39** on OTS-treated SiO₂ (5 × 5 μm²), b) **39** on PS-treated SiO₂ (5 × 5 μm²), c) **45** on PS-treated SiO₂ (5 × 5 μm²), d) **46** on PS-treated SiO₂ (5 × 5 μm²), e) **47** on PS-treated SiO₂ (5 × 5 μm²) and f) **47** on PS-treated SiO₂ (1 × 1 μm²).

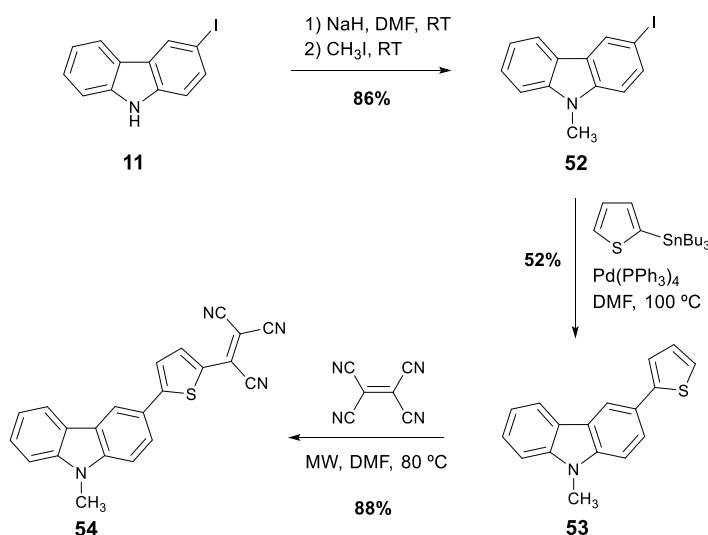
3.4. Extension of the π -conjugated carbazole system by introduction of the thienyl unit

In Section 3.3 it was found that the *N*-alkyl chain length of the carbazole moiety has a negligible effect on the charge-transporting properties. Although the molecular packing motifs of that series of tricyanovinyl derivatives differ according to the *N*-alkyl chain length, all of them show π - π stacking interactions with similar minimum interlayer distances. Thus, the XRD study suggested that all compounds have similar hopping pathways, which is consistent with the comparable electron mobilities determined for the OTFT devices. In order to improve the electron mobilities, it was considered to extend the π -conjugated system by introduction of the thienyl heterocycle as a π -conjugated bridge between the carbazole and the tricyanovinyl groups. The extension of the π -conjugated carbazole system pretends to favour the orbital overlap between neighbouring molecules to improve the charge transport properties.

3.4.1. Synthesis

Scheme 3.4 and 3.5 display the synthetic route to 9-methyl-3-[5-(1,2,2-tricyanovinyl)thiophen-2-yl]-9*H*-carbazole (**54**) and 9-methyl-3,6-bis[5-(1,2,2-tricyanovinyl)thiophen-2-yl]-9*H*-carbazole (**57**), respectively.

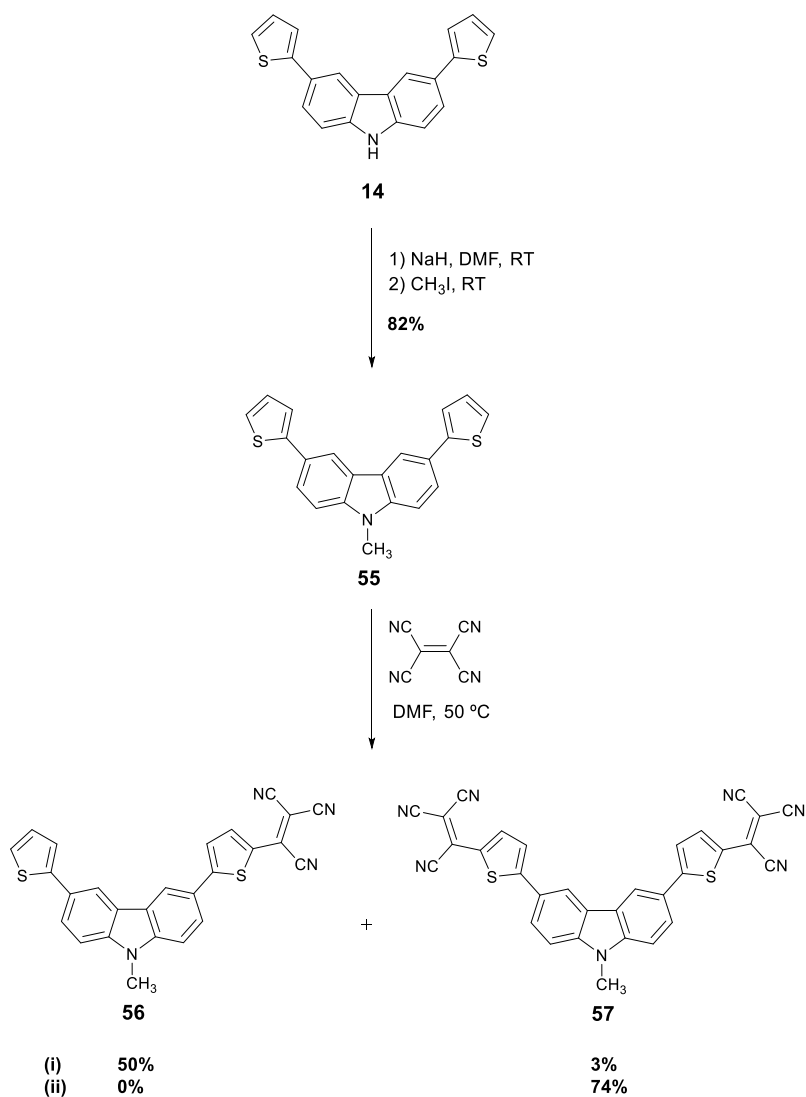
Tricyanovinyl derivative **54** was prepared from 3-iodo-9*H*-carbazole (**11**) (Scheme 3.4), which was firstly alkylated under standard conditions affording the intermediate 3-iodo-9-methyl-9*H*-carbazole (**52**) in high yields. Then, the Stille coupling reaction^[81] of **52** with 2-(tributylstannyl)thiophene catalysed by Pd(PPh₃)₄ in anhydrous DMF at 100 °C gave 9-methyl-3-(2-thienyl)-9*H*-carbazole (**53**). The final product **54** was prepared by heating **53** in anhydrous DMF with tetracyanoethylene under microwave irradiation in high yields.



Scheme 3.4. Synthesis of tricyanovinyl derivative **54**.

Prior to obtaining the target compound bistricyanovinyl **57**, derivative **14** was methylated under standard conditions to afford 9-methyl-3,6-di-2-thienyl-9*H*-carbazole (**55**) as shown in Scheme 3.5. Due to the presence of the two nucleophilic thienyl units in **55**, the introduction of the tricyanovinyl group can take place in one or both thienyl units depending on the reaction conditions. Hence, when **55** was heated in anhydrous DMF with 1 eq. of tetracyanoethylene (TCNE) for 48 h at 50 °C, monotricyanovinyl derivative **56** was obtained as the major product in a 50% yield, whereas bistricyanovinyl **57** was obtained as a sub-product. The desired product **57** was obtained

as the major product in a 74% yield by increasing the TCNE equivalents from 1 to 6 and by extending the reaction time to 72 h.



Scheme 3.5 Synthesis of bistricyanovinyl derivative **57**. Reagents and conditions: (i) tetracyanoethylene (1 eq.), 48 h. (ii) tetracyanoethylene (6 eq.), 72 h.

3.4.2. Characterization of the organic semiconductors

Thermal properties

The thermal properties for thienyl-based compounds **54** and **57** are collected in Table 3.9. TGA and DSC curves can be found in Appendix B. Thermal properties for *N*-methyl derivative **39**, without the

thienyl group, are also shown in Table 3.9 for comparison. Derivatives **54** and **57**, containing one or two tricyanovinylthienyl groups, respectively, exhibited higher thermal stability ($T_d = 341$ and 402 °C, respectively), in comparison to **39** ($T_d = 301$ °C). Compounds **54** and **57** were obtained as crystalline products, but they both melt with decomposition.

Table 3.9. Thermal properties of tricyanovinyl derivatives **39**, **54** and **57**.

Compound	T_d (°C) [a]	T_m (°C) [b]	T_c (°C) [b]
39	301	245	231
54	341	346 [c]	–
57	402	412 [c]	–

[a] Onset decomposition temperature (T_d) obtained from TGA performed at a heating rate of 20 °C min^{-1} . [b] Melting point (T_m) and crystallization temperature (T_c) obtained from DSC performed at a scan rate of 10 °C min^{-1} . [c] Melting with decomposition.

Optical properties

Table 3.10 collects the optical data of compounds **54**, **56** and **57** determined in 10 μM CH_2Cl_2 solutions and in vacuum-evaporated thin films. The optical data of **39** is also shown for comparison. Similarly to **39**, all compounds showed two absorption regions covering a broad range of the UV and visible spectrum. The UV-Vis absorption spectrum of **54**, which includes the thienyl ring between the carbazole core and the tricyanovinyl acceptor group, in dichloromethane solution displays a red shift of 76 nm of the maximum absorption wavelength corresponding to the charge-transfer band in comparison to that of **39** (Figure 3.20a). The electron rich thienyl group reinforces the electron-donating character of the carbazole one providing a strong push-pull system, as deduced from the UV-vis spectrum. The absorption spectra of **56** and **57** was not recorded in solution due to the low solubility of these compounds in common organic solvents.

The UV-Vis absorption spectra of vacuum-evaporated thin films of **54**, **56** and **57** show a bathochromic shift of the maximum of the UV band in agreement with the extension of the π -conjugation of the carbazole core by introduction of thienyl units (Figure 3.20b). Accordingly, the UV absorption band of dithienyl compounds **56** and **57** are 8 and 11 nm bathochromically shifted in comparison to monothienyl derivative **54**. Remarkably, the maximum of the intramolecular charge-transfer band of thienyl derivatives is considerably red-shifted in comparison to **39**, with the absorption maxima peaking at 535 , 575 and 644 nm for **54**, **56** and **57**, respectively. The attachment

of the electron rich thienyl units at the carbazole core enhances the push-pull character of the molecules and lead to extended π -conjugated systems. The UV-Vis absorption spectra of these thienyl-based dyes cover a wide range of the UV and visible spectrum, which make of them plausible candidates to be used as components for organic solar cells.

Table 3.10. Optical properties of tricyanovinyl derivatives **39**, **54**, **56** and **57**.

Compound	$\lambda_{\text{abs,max}}$ (nm) [ϵ ($\text{M}^{-1} \text{cm}^{-1}$)] [a]	$\lambda_{\text{abs,max}}$ (nm) [b]
39	290 (19 667), 490 (32 090)	298, 472
54	294 (22 059), 566 (36 974)	299, 535
56	– [c]	307, 575
57	– [c]	310, 644

[a] Wavelength of maximum absorption ($\lambda_{\text{abs,max}}$) and molar absorption coefficient (ϵ) determined in 10 μM dichloromethane solutions at room temperature. [b] Measured in vacuum-evaporated thin films (25–75 nm) on quartz substrates at room temperature. [c] Not determined due to insolubility in common organic solvents.

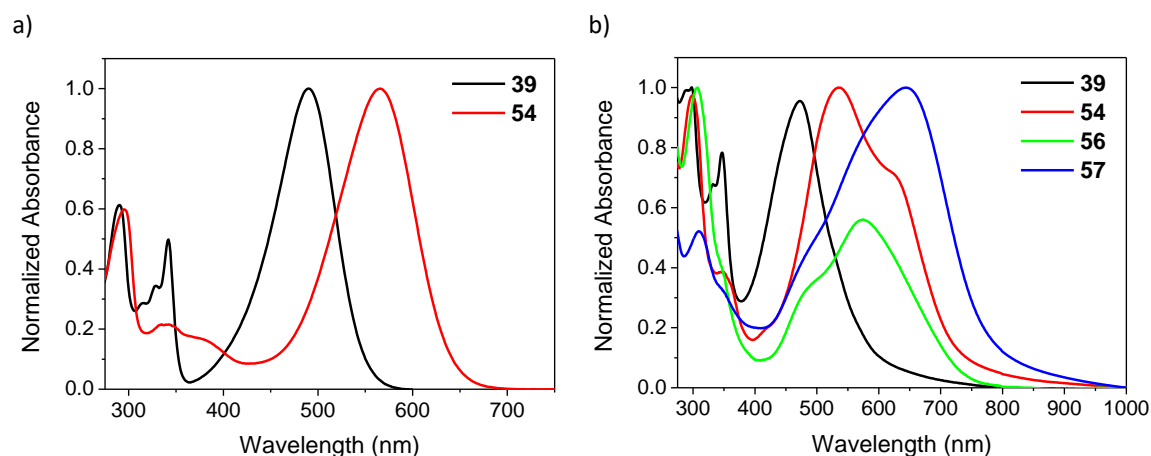


Figure 3.20. UV-vis absorption spectra of a) 10 μM solutions of **39** and **54** and b) vacuum-evaporated thin films of compounds **39** (75 nm), **54** (75 nm), **56** (25 nm) and **57** (75 nm).

Electrochemical properties

Electrochemical properties were investigated by cyclic voltammetry (Table 3.11). CV of **57** was not recorded due to its low solubility under the experimental conditions. The electrochemical data of **39** is also shown for comparison. Derivative **54** show two quasi-reversible reduction waves and one

irreversible oxidation wave (Figure 3.21). Compound **54** is significantly more easily oxidized ($E_{\text{onset}}^{\text{ox}} = 0.78 \text{ V}$) than the non-containing thienyl derivative **39** ($E_{\text{onset}}^{\text{ox}} = 1.06 \text{ V}$) according to the enhanced electron-donating character of the π -conjugated core. Ionization potential and electron affinity of **54** are 6.17 and 4.48 eV, respectively, which are indicative of potential ambipolar transport.

Table 3.11. Electrochemical properties of tricyanovinyl derivatives **39** and **54**.

Compd.	$E_{\text{red},1}^0$ [a] (V)	$E_{\text{red},2}^0$ [a] (V)	$E_{\text{onset}}^{\text{red}}$ [b] (V)	$E_{\text{onset}}^{\text{ox}}$ [b] (V)	EA [c] (eV)	IP [c] (eV)	E_{gap} [c] (eV)
39	-1.08	–	-1.00	1.06	4.39	6.45	2.06
54	-0.98	-1.63	-0.91	0.78	4.48	6.17	1.69

[a] Standard potential of the first ($E_{\text{red},1}^0$) and second ($E_{\text{red},2}^0$) reduction redox couple vs. Fc^+/Fc determined from CV in 1 mM dichloromethane solutions at a scan rate of 100 mV s^{-1} . [b] Onset reduction potential ($E_{\text{onset}}^{\text{red}}$) and onset oxidation potential ($E_{\text{onset}}^{\text{ox}}$) vs. Fc^+/Fc determined from CV in 1 mM dichloromethane solutions at a scan rate of 100 mV s^{-1} . [c] Estimated from cyclic voltammograms as $\text{EA} = E_{\text{onset}}^{\text{red}} \text{ vs. } \text{Fc}^+/\text{Fc} + 5.39$, $\text{IP} = E_{\text{onset}}^{\text{ox}} \text{ vs. } \text{Fc}^+/\text{Fc} + 5.39$ and $E_{\text{gap}} = \text{IP} - \text{EA}$.

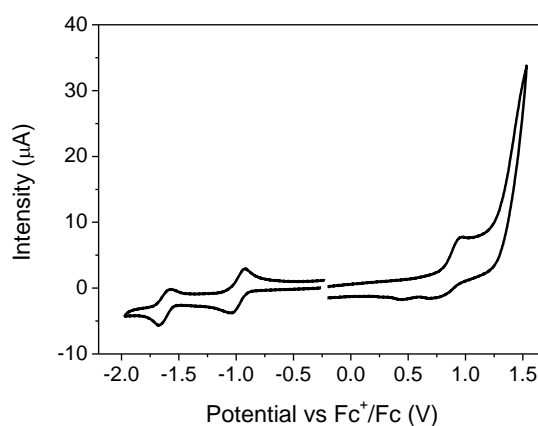


Figure 3.21. Cyclic voltammogram of compound **54** recorded at a scan rate of 100 mV s^{-1} in 1 mM dichloromethane solution.

3.4.3. Organic Thin-Film Transistors

Bottom-gate/top-contact OTFTs based on **54** and **57** were fabricated and measured by using polystyrene (PS) treated c-Si/SiO₂ gate/dielectric substrates and Au as source and drain electrodes. The semiconductor thin films were deposited by the vacuum thermal evaporation technique (with a base pressure below 10^{-6} mbar).

Devices based on **54** and **57** showed typical characteristics of n-type transistors (Table 3.12, Figure 3.22 and Appendix B). OTFT devices with PS- and OTS-treated substrates based on **54** and **57** exhibited similar electron mobilities in the range of $2\text{--}5 \times 10^{-5} \text{ cm}^2 \text{ V}^{-1} \text{ s}^{-1}$ as **39** based devices. Threshold voltages were also similar for all the prepared devices (14.9–24.0 V) as well as the $I_{\text{on}}/I_{\text{off}}$ ratio ($\sim 10^1\text{--}10^3$). These results confirm that the treatment of the dielectric layer with PS or OTS does not influence on the electrical characteristics of the prepared devices of this family of compounds, as previously described for **39**.

Table 3.12. OTFT characteristics of devices based on tricyanovinyl-carbazole derivatives **39**, **54** and **57** with PS and OTS-treated c-Si/SiO₂ substrates.

Compound		μ_e (cm ² V ⁻¹ s ⁻¹) [a]	V_{th} (V) [b]	$I_{\text{on}}/I_{\text{off}}$ (A/A) [c]
39	PS	3×10^{-5}	19.7	$\sim 10^2$
39	OTS	2×10^{-5}	23.6	$\sim 10^3$
54	PS	4×10^{-5}	14.9	$\sim 10^1$
54	OTS	2×10^{-5}	17.3	$\sim 10^3$
57	PS	3×10^{-5}	18.4	$\sim 10^2$
57	OTS	5×10^{-5}	24.0	$\sim 10^2$

[a] Electron mobility (μ_e). [b] Threshold voltage (V_{th}). [c] $I_{\text{on}}/I_{\text{off}}$ ratio. Measurements were performed under vacuum and at room temperature.

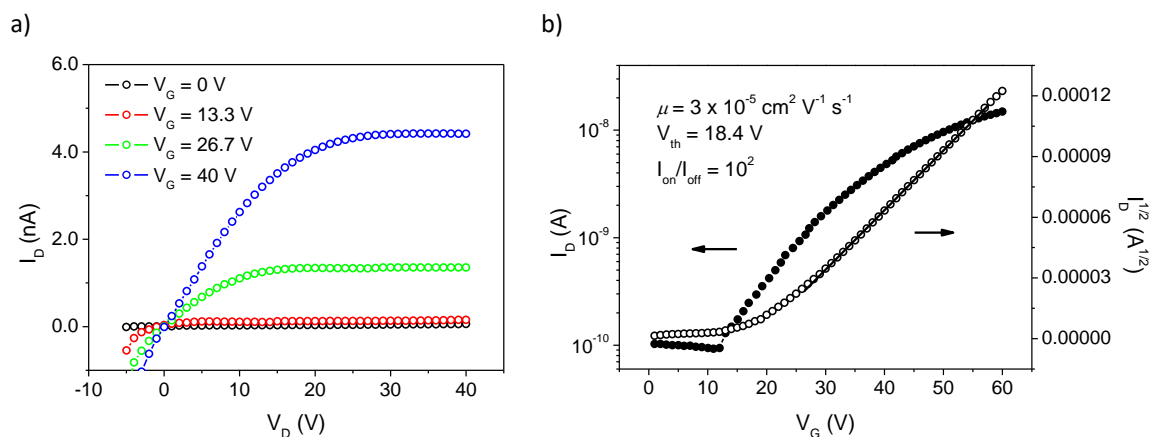


Figure 3.22. OTFT characteristics of a device fabricated with **57** as the semiconductor layer and with PS-treated c-Si/SiO₂ substrate. a) Output characteristics at different gate voltages (V_G). b) Transfer ($V_D = 60 \text{ V}$) and saturation characteristics.

Remarkably, the extension of the π -conjugated core by introducing the thiophene group between the carbazole and the tricyanovinyl group seems to have a negligible effect on the charge-transporting properties. It should be mentioned here that it was not possible to get suitable crystals from neither **54** nor **57**, which would give insights into the molecular packing of these molecules in the solid state. Based on the previous results (Section 3.3), some considerations can be done. Molecules in carbazole derivatives that differed only on the length of the *N*-alkyl chain length showed a similar antiparallel arrangement with π - π stacking interactions and comparable interlayer distances, which justified the similar electron mobilities achieved in OTFT devices. Thus, the molecular organization along the π stacks and the interlayer distances seem to be similar for thienyl-based molecules **54** and **57** to that of **39**, independently of their more π -extended system, given that similar OTFT device performance have been determined.

3.5. Conclusions

The charge transport properties of three series of push-pull carbazole-based compounds bearing the strong electron-withdrawing tricyanovinyl group have been examined. All the compounds exhibited high thermal stability and charge-transfer absorption bands in the visible region, together with hole and electron transport ability due to the amphoteric redox properties. TOF and OTFT measurements confirm that the substitution of the carbazole core with the electron-withdrawing tricyanovinyl group is a useful strategy to achieve electron-transporting materials.

N-Alkylated derivatives **39** and **40** showed enhanced charge transport properties in comparison to the non-alkylated analogues **37** and **38**. In addition, ambipolar properties could be detected by the TOF technique by the additional incorporation of the electron-donating methoxy group in the *ortho* position with respect to the tricyanovinyl fragment. In this way, almost balanced electron and hole mobilities of 9.3×10^{-5} and $2.4 \times 10^{-4} \text{ cm}^2 \text{ V}^{-1} \text{ s}^{-1}$, respectively, were attained for compound **40** at high electric fields under ambient conditions, whereas the non-methoxy substituted carbazole derivatives **37** and **39** exhibited exclusively electron transport. Although the electron-donating methoxy substituent might modulate the charge-transporting properties, as well as the HOMO and LUMO levels, by controlling the donor strength of the carbazole core and the molecular planarity, the analysis of the single-crystal structures by X-ray analysis together with the theoretical calculations suggest that the charge transport properties of the layers of this series of push-pull derivatives are highly influenced by the supramolecular organization. The planar structures of compounds **37** and **39** favour LUMO-LUMO interactions between neighbouring

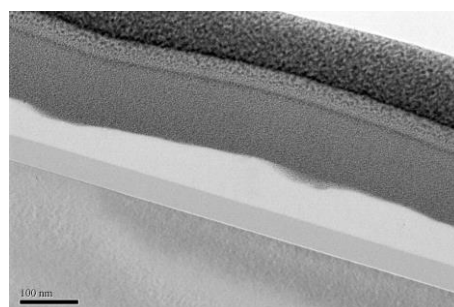
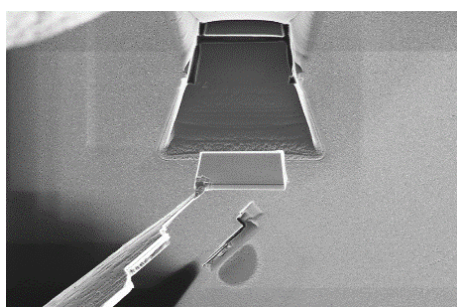
molecules, resulting in the enhancement of the electron transport. The twisted structures of compounds **38** and **40** induce face-to-face π - π interactions between adjacent donor carbazole moieties. For that disposition, hole transport is favoured without losing the electron-transporting properties, affording ambipolar semiconductors.

The *N*-alkyl chain length of the carbazole moiety has a negligible effect on the charge mobility as determined by OTFT measurements. Thus, similar electron mobilities in the range of 9×10^{-6} to $5 \times 10^{-5} \text{ cm}^2 \text{ V}^{-1} \text{ s}^{-1}$ were achieved for OTFT devices based on compounds **39** and **45–48**. The XRD study revealed that all compounds show a layered organization with an antiparallel arrangement and similar minimum interlayer distances (3.28–3.40 Å), independently of the length of the *N*-alkyl chain. In addition, molecules in the films are organized with the π - π stacking direction parallel to the substrate surface, favourable for the charge transport through the active layer in OTFTs. These results are consistent with the similar charge carrier mobilities achieved in the measurement of OTFTs.

A series of compounds containing the thiophene group as a π -conjugated bridge between the carbazole and the tricyanovinyl unit was also synthesized. The charge-transfer absorption bands of the thienyl-based compounds **54** and **57** are remarkably red-shifted in comparison to that of **39**, pointing to the extent of the π -conjugated system. The extension of the π -conjugated core seems to have a negligible effect on the charge-transporting properties, since similar electron mobilities were achieved for **54** and **57**-based OTFTs in comparison to that based on **39**. The electron-transporting characteristics together with the optical properties of these dyes point out that they could be good candidates as components for organic solar cells, since their absorption spectra cover a wide range of the UV and visible spectrum.

Chapter 4

Role of the molecular order in π -extended carbazole derivatives for p-type OTFTs



Part of this chapter has been published in:

J. Mater. Chem. C **2015**, *3*, 506–513

CHAPTER 4

Role of the molecular order in π -extended carbazole derivatives for p-type OTFTs

*In the design of new organic semiconductors, the selection of the appropriate core plays a key role in the molecular packing and charge transport characteristics of the organic device. A series of carbazole derivatives that mainly differ in the extension of the π -conjugated core, including indolo[3,2-*b*]carbazole and triindole derivatives,*

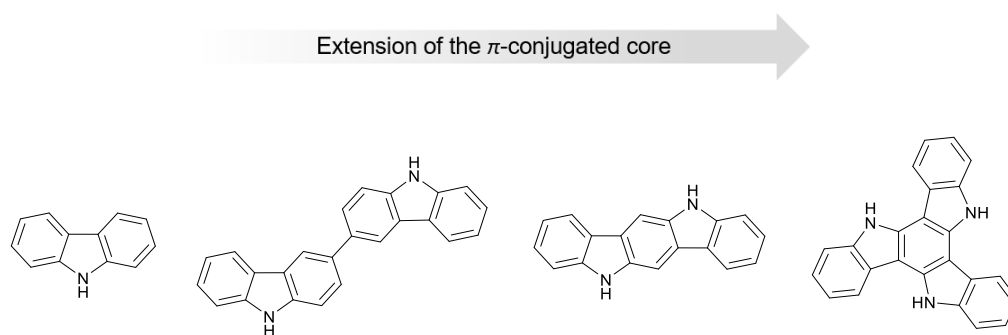
exhibited hole mobilities ranging from 10^{-5} to 10^{-1} $\text{cm}^2 \text{V}^{-1} \text{s}^{-1}$ as active layers in OTFTs. X-ray analysis of single crystals and evaporated thin films gave insights into the molecular packing of the compounds that justified their OTFTs characteristics.

4.1. Introduction

Chapter 2 and 3 were focused on the development of new organic semiconductors with n-type or ambipolar properties, achieving electron mobilities up to $10^{-5} \text{ cm}^2 \text{ V}^{-1} \text{ s}^{-1}$ in vacuum-evaporated OTFTs. To date, p-type OTFTs have reached a more successful development than the n-type and ambipolar counterparts, achieving hole mobilities comparable to those obtained with amorphous silicon. However, new hole-transporting materials are still required in order to achieve enhanced OTFT device performance including temporal and air stability. For this purpose, the selection of an appropriate core structure is crucial, because it could modulate the optical and electronic properties and even determine the stability and durability of the fabricated devices under ambient conditions.

With this in mind, this chapter deals with the study of the charge-transporting properties of a series of hole-transporting carbazole-based materials that differ in the extension of the π -conjugated core, including the carbazole, the 3,3'-bicarbazole, the indolo[3,2-*b*]carbazole and the

triindole cores (Scheme 4.1). Indolo[3,2-*b*]carbazole and triindole show extended π systems, in which two or three carbazole units, respectively, share an aromatic ring. Indolo[3,2-*b*]carbazole and triindole units present a planar structure with two or three N–H units, respectively, which allows easy introduction of alkyl chains, in order to increase the solubility of the systems and to promote the molecular order of the materials during the deposition process. Both heterocycles display large energy band gaps and low-lying HOMO energy levels. In the last years, indolocarbazole has received special attention as a building block in the field of organic electronics,^[130] and recent studies have shown the great potential of indolo[3,2-*b*]carbazole-based derivatives to be used in OTFTs.^[50c,131]

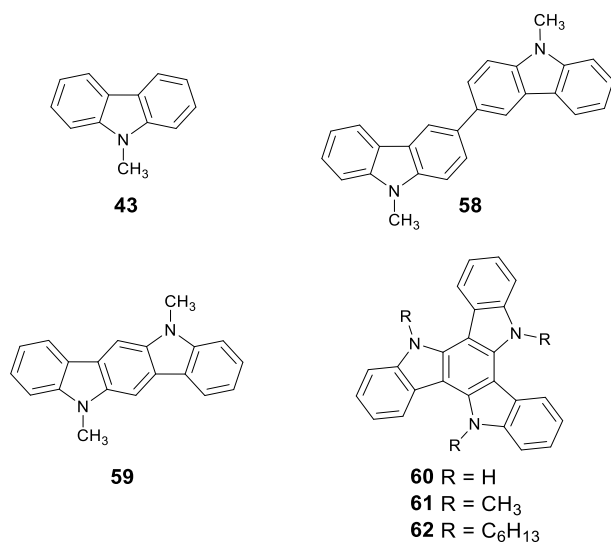


Scheme 4.1. Chemical structures of 9*H*-carbazole, 3,3'-bi-9*H*-carbazole, 5,11-dihydro-indolo[3,2-*b*]carbazole and 10,15-dihydro-5*H*-diindolo[3,2-*a*:3',2'-*c*]carbazole (from left to right).

The triindole core presents a larger molecular structure than the indolocarbazole one. Accordingly, a higher molecular order could be expected from it and therefore, better charge carrier transport. Triindole derivatives have been explored as active layers in organics photovoltaics^[132,133] and OLEDs,^[134] but also as hole-transporting layers in organic solar cells,^[135] perovskite solar cells^[130a,136] and OLEDs,^[137] revealing their promising charge-transporting properties. The easy preparation, high thermal stability, π -stacking capability, high carrier mobilities, and optoelectronic properties of such molecules make indolocarbazole and triindole-based materials very promising organic semiconductors for electronic and optoelectronic applications. The charge transport properties of liquid crystal-based triindole derivatives^[138] and of *N*-trimethyltriindole, as well as that of its non-alkylated counterpart, have been reported by the space-charge-limited-current method (SCLC), yielding values of hole mobilities for the two last mentioned materials ranging from $\sim 1 \times 10^{-4}$ to $\sim 1 \times 10^{-3} \text{ cm}^2 \text{ V}^{-1} \text{ s}^{-1}$.^[135]

4.2. Carbazole derivatives with extended π -conjugated systems: the cases of indolo[3,2-*b*]carbazole and triindole semiconductors

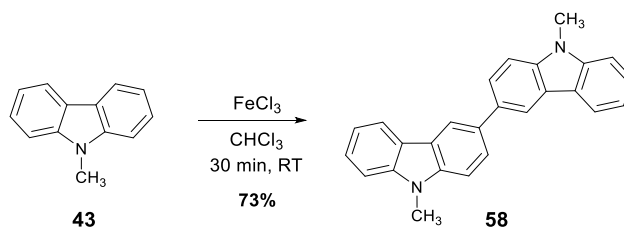
This section deals with the study of 9-methyl-9*H*-carbazole **43**, 9,9'-dimethyl-9*H*,9*H*'-[3,3']bicarbazole **58**, 5,11-dihydro-5,11-dimethylindolo[3,2-*b*]carbazole **59**, and *N*-trimethyltriindole **61** (Scheme 4.2) as active organic semiconductor layers in OTFTs. In addition, the effect of the *N*-alkyl chain length of the triindole moiety on the charge-transporting properties is also presented herein. For this purpose, the non-alkylated triindole **60** and the *N*-hexyl derivative **62** have been also examined as active layers in OTFTs.



Scheme 4.2. Chemical structures of carbazole derivatives **43** and **58–62**.

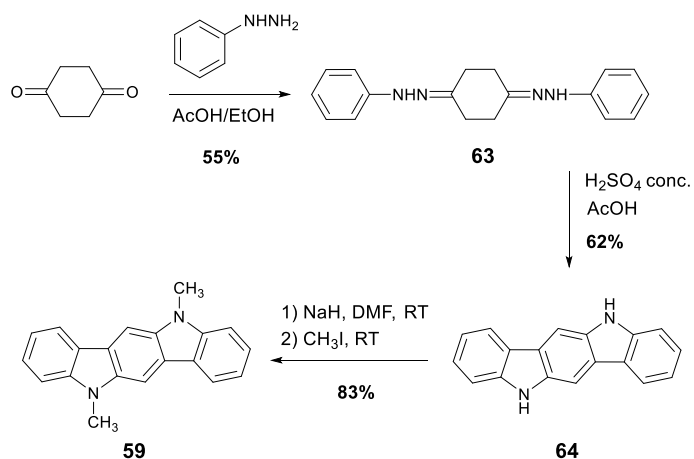
4.2.1. Synthesis

9,9'-Dimethyl-9*H*,9*H*'-[3,3']bicarbazole (**58**) was synthesized by oxidative dimerization^[139] of 9-methyl-9*H*-carbazole (**43**) with FeCl₃ in anhydrous chloroform (Scheme 4.3).

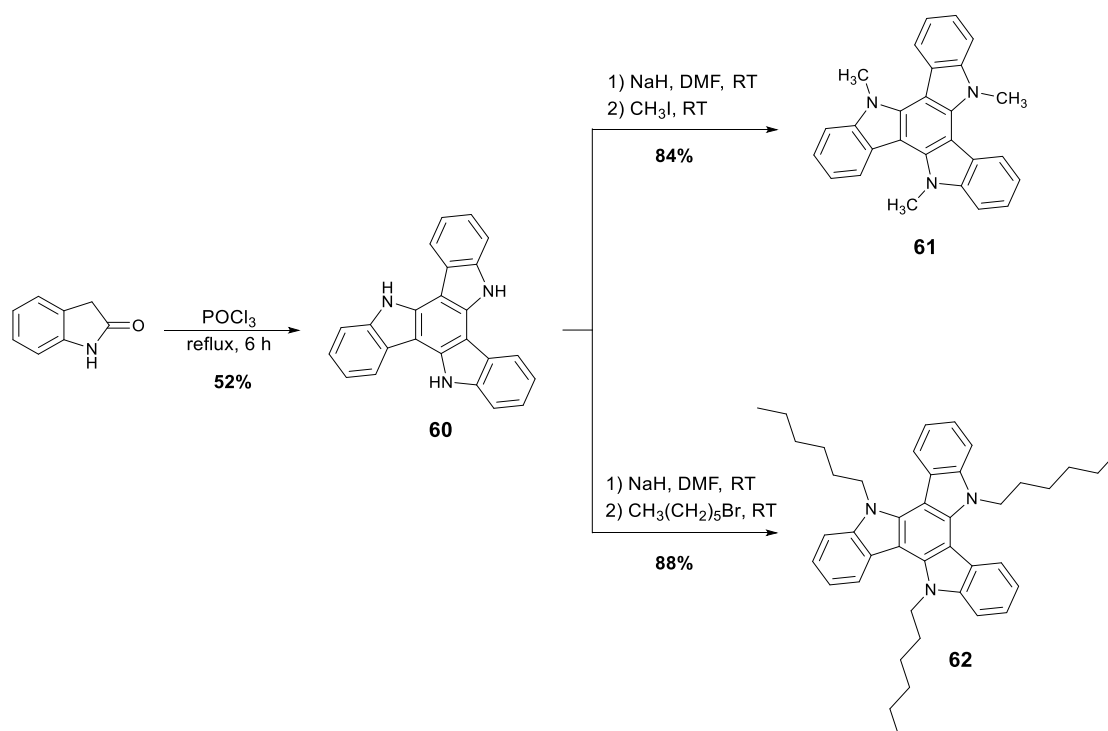


Scheme 4.3. Synthesis of bicarbazole **58**.

The synthesis of 5,11-dihydro-5,11-dimethylindolo[3,2-*b*]carbazole (**59**) is shown in Scheme 4.4. Indolo[3,2-*b*]carbazole **64** was prepared by condensation of 1,4-cyclohexanodione with phenylhydrazine, followed by a double Fischer indolization in a mixture of conc. H₂SO₄ and glacial acetic acid.^[140] The alkylation of **64** with iodomethane under standard conditions using NaH as a base in dry DMF at room temperature afforded the final product **59**.



Scheme 4.4. Synthesis of indolo[3,2-*b*]carbazole **59**.



Scheme 4.5. Synthesis of triindole derivatives **60–62**.

10,15-Dihydro-5*H*-diindolo[3,2-*a*:3',2'-*c*]carbazole **60** was synthesized by the cyclocondensation of 2-oxindole in phosphorus(V) oxychloride (Scheme 4.5) in moderate yield.^[141] The alkylation of **60** with either iodomethane or 1-bromohexane under standard conditions furnished the final triindole derivatives **61** and **62**, respectively.

4.2.2. Crystal structures

The single crystal structures of **59** and **62** were determined by X-ray crystallography, whereas the crystal structure of **61** has been previously reported in the literature.^[142] Indolocarbazole **59** crystallizes in space group *C2/c* of the monoclinic system with unit-cell dimensions of $a = 16.8377(13)$ Å, $b = 5.6889(4)$ Å, $c = 15.3882(11)$ Å, $\beta = 106.671(2)^\circ$ and volume = $1412.05(18)$ Å³. The detailed crystallographic data are provided in Appendix B. The X-ray crystal structure of **59** is shown in Figure 4.1. The molecular structure of indolocarbazole **59** is almost planar, with a small torsion angle around 1.5° (Figure 4.1a). The molecules exhibit a herringbone packing motif with a herringbone angle of 70.96° (Figure 4.1b). Every molecule is surrounded by six molecules showing C-H \cdots π interactions between one of the hydrogen atoms of the methyl groups with the central benzene ring of an adjacent indolocarbazole molecule with a distance of 2.68 Å. Moreover, one of the hydrogen atoms of the methyl groups also interacts with one peripheral benzene ring with a distance of 3.01 Å, being responsible of the herringbone packing motif (Figure 4.1c).

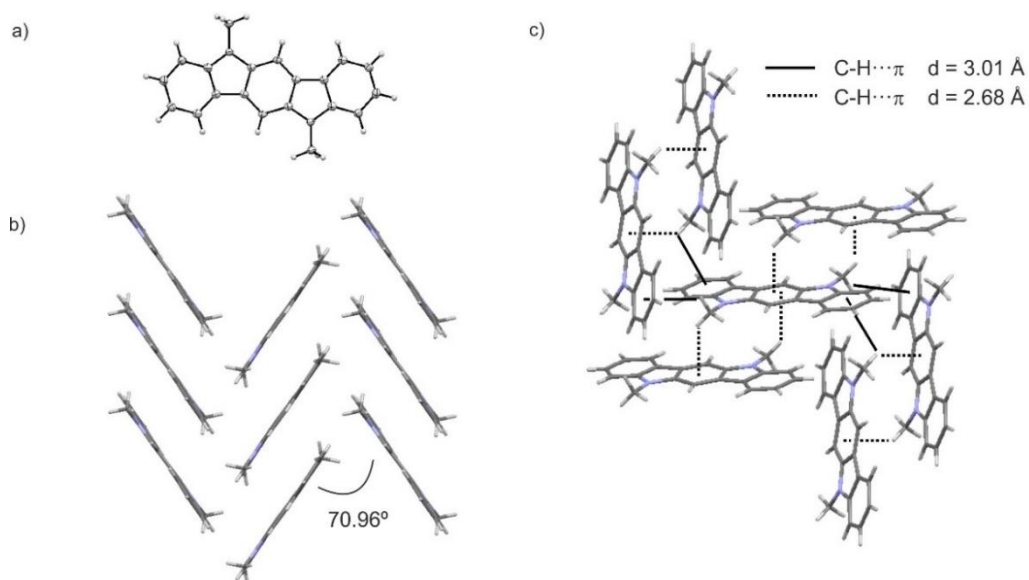


Figure 4.1. X-Ray crystal structure of compound **59**. a) ORTEP projection of **59**, showing the 50% probability displacement, b) herringbone packing motif with its corresponding herringbone angle and c) short contacts given by C-H \cdots π interactions.

For indolo[3,2-*b*]carbazole derivatives, the packing motif in the solid state depends on the length of the alkyl chain in the nitrogen position of the indolocarbazole derivatives. Different packing motifs have been described in the literature, from the non-substituted indolo[3,2-*b*]carbazole^[143] to derivatives with long *N*-alkyl chains.^[143,144]

The previously reported crystal structure of *N*-trimethyltriindole^[142] derivative **61** is displayed in Figure 4.2. The triindole core is not planar, but the external benzene rings bend around 8° out of the plane of the central benzene ring. Molecules adopt a face-to-face packing in an alternate arrangement due to π - π interactions between adjacent triindole molecules. For that compound, two different distances (3.53 Å and 3.68 Å) between two neighbouring molecules were observed due to the steric hindrance induced by the methyl groups.

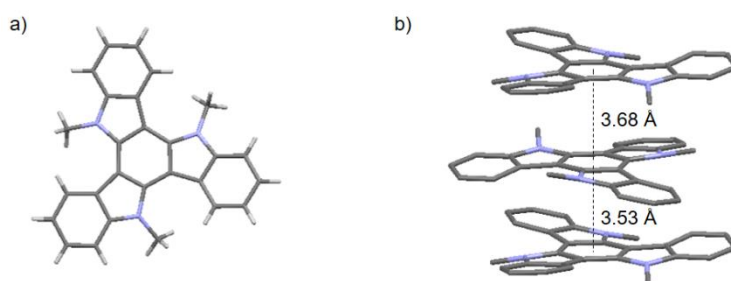


Figure 4.2. X-Ray crystal structure of compound **61**. a) Molecular structure of **61**. b) Molecular packing along the π -stacks indicating the π - π stacking interactions. Hydrogen atoms have been omitted for clarity.

The single crystal structure of *N*-trihexyltriindole derivative **62** was determined by X-ray crystallography. Suitable single crystals were grown by slow evaporation from acetone solution. The compound crystallizes in space group P -1 of the triclinic system with unit-cell dimensions of $a = 8.411(3)$ Å, $b = 15.202(5)$ Å, $c = 26.348(9)$ Å, $\alpha = 86.900(16)^\circ$, $\beta = 89.438(15)^\circ$, $\gamma = 84.427(17)^\circ$ and volume = $3348.2(19)$ Å³. The detailed crystallographic data are provided in Appendix B. The X-ray crystal structure of **62** is shown in Figure 4.3. In comparison to *N*-trimethyltriindole **61**, the triindole core is slightly more twisted, with the three peripheral benzene rings bending with different torsion angles of 9.7°, 13.8° and 15.9° out of the plane of the central benzene ring. Molecules adopt a slipped face-to-face packing with π - π stacking interactions between adjacent triindole molecules, showing minimum distances of 3.75–3.77 Å between the centroid of one peripheral benzene ring of one molecule and the centroid of the central ring of the neighbouring one. C-H \cdots π interactions are also observed between the triindole core and the hexyl chains of adjacent molecules.

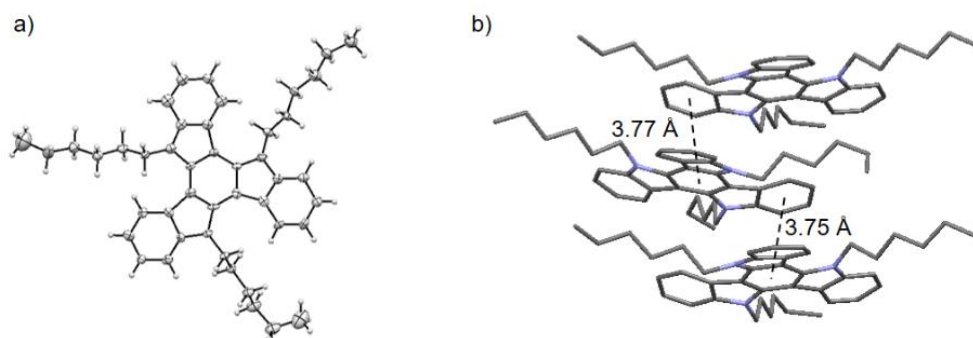


Figure 4.3. X-Ray crystal structure of compound **62**. a) ORTEP projection of **62**, showing the 50% probability displacement. b) Molecular packing along the π -stacks indicating the π - π stacking interactions. Hydrogen atoms have been omitted for clarity.

4.2.3. Characterization of the organic semiconductors

Thermal and optical properties

The thermal properties of compounds **43** and **58–62** were examined by TGA (Table 4.1). Compounds **58–62** exhibited high thermal stability, with enhanced decomposition temperatures ($T_d > 384$ °C) in comparison to 9-methyl-9*H*-carbazole **43** ($T_d = 243$ °C).

Table 4.1. Thermal and optical properties of **43** and **58–62**.

Compound	T_d (°C) [a]	$\lambda_{\text{abs,max}}$ (nm) [ϵ ($\text{M}^{-1} \text{cm}^{-1}$)] [b]	$\lambda_{\text{em,max}}$ (nm) [b]	Φ_f [c]
43	243	263 (32 314), 294 (29 722)	349, 366	0.20
58	456	303 (76 660)	411	0.10
59	384 [d]	283 (52 268), 340 (67 146)	421, 447	0.26
60	492	306 (60 233)	374	0.12
61	461 [d]	317 (79 023)	394	0.19
62	424	318 (71 631)	395	0.19

[a] Onset decomposition temperature (T_d) obtained from TGA performed at a heating rate of 20 °C min⁻¹.

[b] Wavelength of maximum absorption ($\lambda_{\text{abs,max}}$) and emission ($\lambda_{\text{em,max}}$) and molar absorption coefficient (ϵ) determined in 10 μM CH_2Cl_2 solutions at room temperature. Emission spectra were recorded after excitation at the wavelength of maximum absorption. [c] Fluorescence quantum yield (Φ_f) measured in CH_2Cl_2 solutions using 1,4-bis(5-phenyl-2-oxazolyl)benzene as the standard ($\Phi_f = 0.93$ in cyclohexane solution) after excitation at $\lambda = 300$ nm.

[d] Determined at a heating rate of 10 °C min⁻¹.

Table 4.1 collects the optical properties for compounds **43** and **58–62** determined in 10 μM dichloromethane solutions. The UV-vis absorption spectra of bicarbazole **58**, indolocarbazole **59** and triindole **61** display the absorption maximum in the UV zone, but at longer wavelengths than 9-methyl-9*H*-carbazole **43** (Figure 4.4a). Thus, the bathochromic shift of the lowest energy absorption band together with the decrease of the optical band gaps (Table 4.2) in comparison to **43** confirms the extension of the π -conjugated system in these series of derivatives. The alkylation of the nitrogen atoms of triindole derivatives **61** and **62** with the methyl and hexyl chains, respectively, implies a red shift of 11–12 nm of the wavelength of maximum absorption, in comparison to the non-alkylated derivative **60** (Figure 4.4b).

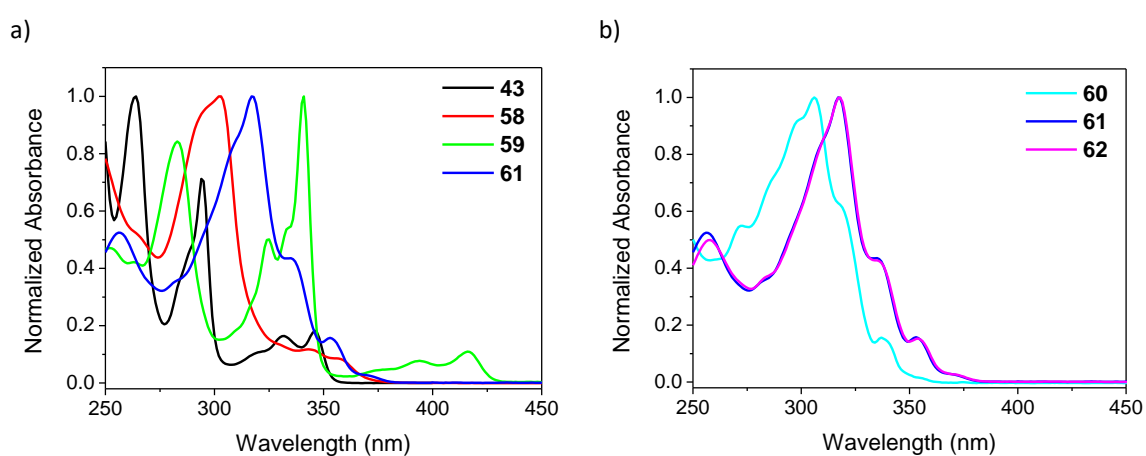


Figure 4.4. UV-Vis absorption spectra of a) **43**, **58**, **59** and **61** and b) **60–62** recorded in 10 μM dichloromethane solutions at room temperature.

Figure 4.5a displays the emission spectra of **43**, **58**, **59** and **61** recorded in 10 μM dichloromethane solutions. Whereas the emission spectra of monocarbazole **43** exhibits the wavelength of maximum emission in the UV region at 349/366 nm, the emission band of **58**, **59** and **61** is centred in the blue region (394–421 nm), due to the more extended π -conjugated systems. According to the behaviour observed in the absorption spectra, *N*-alkylated triindoles **61** and **62** display the emission maxima ~ 10 nm bathochromically shifted in comparison to the non-alkylated counterpart **60**. This series of compounds exhibited fluorescence quantum yields in the range of 0.1–0.2 in dichloromethane solutions.

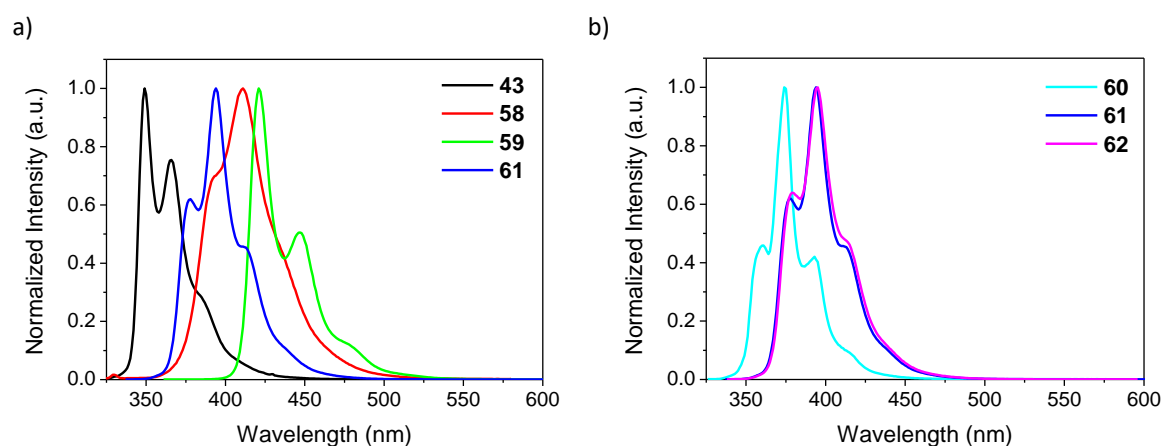


Figure 4.5. Emission spectra of a) **43**, **58**, **59** and **61** and b) **60–62** recorded in 10 μM dichloromethane solutions at room temperature.

Electrochemical properties

Compounds **43** and **58–60** showed irreversible oxidation processes by cyclic voltammetry, whereas *N*-alkylated triindole derivatives **61** and **62** showed two oxidation processes, being the first one quasi-reversible. No reduction processes were observed for any of them. Table 4.2 and Appendix B collect the electrochemical characteristics. In this series of carbazole-based compounds, when increasing the conjugation of the system, the ionization potentials decrease slightly from 6.16 eV for carbazole **43** to 5.56 eV corresponding to triindole derivative **61** (Figure 4.6), that is the HOMO levels are slightly destabilized. Triindoles **60–62** show similar IP values of ~ 5.6 eV, but the alkylation

Table 4.2. Electrochemical properties of **43** and **58–62**.

Compound	$E_{\text{onset}}^{\text{ox}}$ (V) [a]	IP (eV) [b]	EA (eV) [c]	$E_{\text{gap}}^{\text{opt}}$ (eV) [d]
43	0.77	6.16	2.06	4.10
58	0.41	5.80	1.90	3.90
59	0.25	5.64	2.07	3.57
60	0.18	5.57	1.87	3.70
61	0.17	5.56	2.03	3.53
62	0.21	5.60	2.07	3.52

[a] Onset oxidation potential ($E_{\text{onset}}^{\text{ox}}$) vs. Fc^+/Fc determined from CV in 1 mM dichloromethane solutions at a scan rate of 100 mV s^{-1} . [b] Ionization potential (IP) estimated from cyclic voltammeteries as $\text{IP} = E_{\text{onset}}^{\text{ox vs. Fc}^+/\text{Fc}} + 5.39$. [c] Electron affinity (EA) estimated as $\text{EA} = \text{IP} - E_{\text{gap}}^{\text{opt}}$. [d] Optical energy gap ($E_{\text{gap}}^{\text{opt}}$) estimated from the absorption spectra.

of the nitrogen atoms affords materials (**61–62**) with slightly enhanced EA values of ~ 2.0 eV in comparison to non-alkylated derivative **60** (1.87 eV), according to the higher optical energy gap of the latter. The relative high ionization potentials and high optical energy gaps (~ 3.7 eV) of these compounds are indicative of their potential behaviour as hole-transporting materials. Moreover, the energy levels found for the organic semiconductors **43** and **58–62** are perfectly suitable to Au electrode work function (5.1 eV) as it is displayed in Figure 4.6.

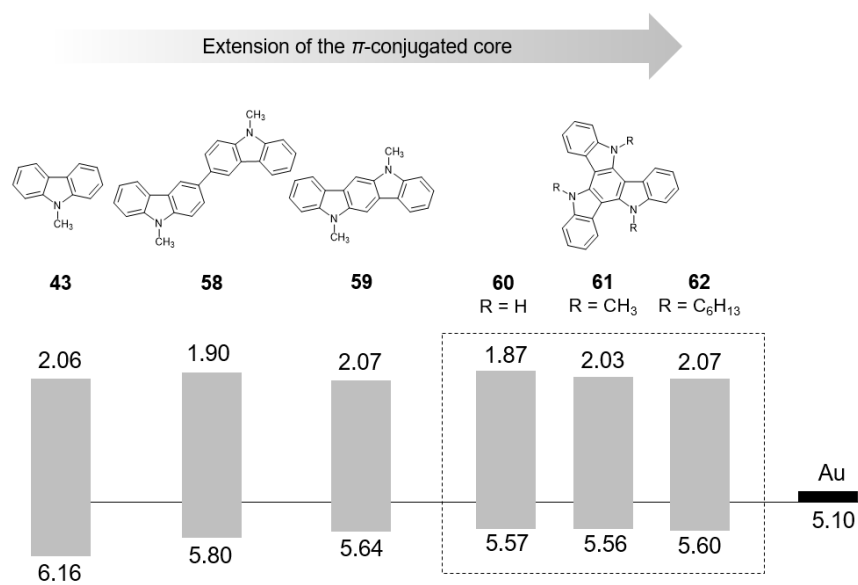


Figure 4.6. Energy levels of materials **43**, **58–62** estimated by cyclic voltammetry. The work function of Au electrode is also shown for comparison.

4.2.4. Organic Thin-Film Transistors

Charge carrier mobilities were measured in standard bottom gate-top contact OTFTs by using the organic materials **43** and **58–62** as vacuum-deposited active layers and gold as the source and drain electrodes. The SiO₂ dielectric surface was treated by adding a layer of polystyrene (PS) or with octadecyltrichlorosilane (OTS).

Fabrication of OTFTs with compound **43** as the organic semiconductor layer was not successful, due to its low sublimation temperature (40 °C at 10⁻⁶ mbar under the experimental conditions during the deposition process). **58**-based devices fabricated with 50 nm thick SiO₂ dielectric presented a low yield and reproducibility: only 17% of the devices fabricated with polystyrene (PS) treated substrates presented OTFT characteristics, with a maximum hole mobility around $2 \times 10^{-5} \text{ cm}^2 \text{ V}^{-1} \text{ s}^{-1}$ and a threshold voltage of -16.0 V (Table 4.3).

Table 4.3. OTFT characteristics of devices based on materials **58–62** with PS and OTS treated c-Si/SiO₂ substrates.

Compound		μ_h (cm ² V ⁻¹ s ⁻¹) [a]	V_{th} (V) [b]	I_{on}/I_{off} (A/A) [c]
58	PS	2×10^{-5}	-16.0	$\sim 10^1$
59	PS	7×10^{-3}	-9.6	$\sim 10^4$
59	OTS	8×10^{-2}	-5.7	$\sim 10^5$
60	PS	1×10^{-5}	-6.0	$\sim 10^2$
60	OTS	1×10^{-4}	-7.4	$\sim 10^3$
61	PS	3×10^{-2}	-12.8	$\sim 10^3$
61	OTS	6×10^{-2}	-0.8	$\sim 10^3$
62	PS	0.1	-13.2	$\sim 10^6$
62	OTS	2×10^{-2}	-7.7	$\sim 10^5$

[a] Hole mobility (μ_h). [b] Threshold voltage (V_{th}). [c] I_{on}/I_{off} ratio. Measurements were performed in air and at room temperature.

Table 4.3 collects the device characterization for OTFTs fabricated with the more extended π -conjugated cores of compounds **59–62**. PS-treated devices based on **59** and **61** fabricated with substrates of 50 nm of SiO₂ presented similar hole mobilities, but lower threshold voltages, than those fabricated from substrates of 110 nm of SiO₂. The reproducibility of the measurements and the yield of the working devices were found to be independent of the thickness of the SiO₂ layer. All the other devices were fabricated with substrates of 110–130 nm of SiO₂. The highest values of charge mobilities were achieved by modifying the dielectric surface with a polystyrene (PS) thin layer or with OTS instead of depositing the organic semiconductor directly over the dielectric SiO₂ surface. It should be mentioned that OTFTs based on **59–62** with PS- or OTS-treated SiO₂ substrates presented a superior yield of working devices around 70–100%, given by the average of the tested devices.

Indolocarbazole **59** exhibited hole mobilities up to 7×10^{-3} and 8×10^{-2} cm² V⁻¹ s⁻¹ for PS- and OTS-treated devices, respectively. Triindole **61** exhibited a considerably higher hole mobility of 3×10^{-2} cm² V⁻¹ s⁻¹ in PS-treated devices in comparison to that of **59**, but a similar hole mobility of 6×10^{-2} cm² V⁻¹ s⁻¹ in OTS-treated devices. The OTFTs characteristics of **59**- and **61**-based devices fabricated on bare SiO₂ surfaces showed lower reproducibility and lower charge mobilities of 7×10^{-5} and 5×10^{-3} cm² V⁻¹ s⁻¹, respectively. A representative output, transfer and saturation characteristics for **61**-based OTFTs prepared with PS-treated SiO₂ surfaces are shown in Figure 4.7 (OTFT characteristics for the other devices can be found in Appendix B). The output characteristics are indicative of the OTFT behaviour of the device in both the linear and saturated regions.

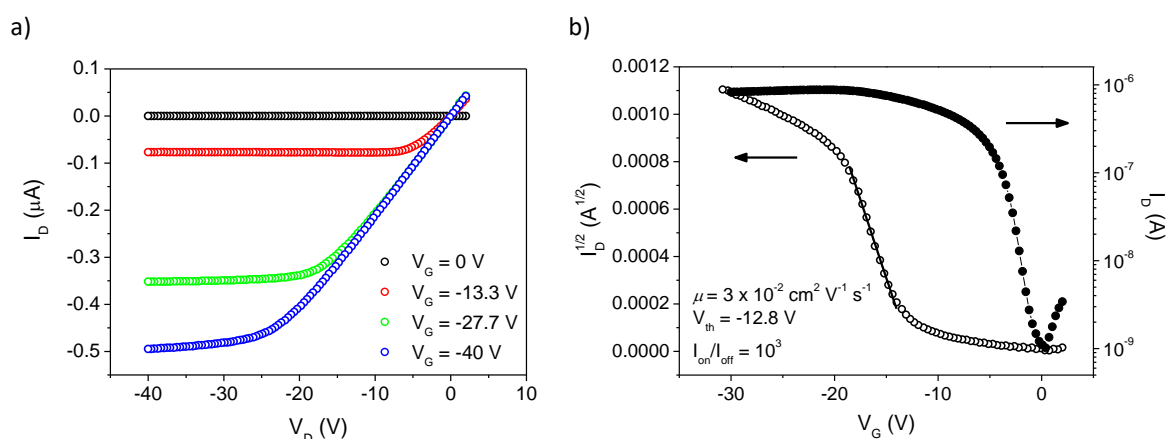


Figure 4.7. OTFT characteristics of a device fabricated with **61** as the semiconductor layer and with PS-treated c-Si/SiO₂ substrate. a) Output characteristics at different gate voltages (V_G). b) Transfer ($V_D = -20$ V) and saturation characteristics.

A considerable effect of the *N*-alkyl chain of triindole derivatives **60–62** was found on the charge-transporting properties. The non-alkylated derivative **60** exhibited the lowest hole mobility values of 1×10^{-5} and $1 \times 10^{-4} \text{ cm}^2 \text{ V}^{-1} \text{ s}^{-1}$ for devices with PS- and OTS-treated substrates, respectively, within this series of triindole derivatives. OTFTs based on **61** both prepared with PS- and OTS-treated SiO₂ surfaces showed enhanced mobilities in comparison to **60** of 3×10^{-2} and $6 \times 10^{-2} \text{ cm}^2 \text{ V}^{-1} \text{ s}^{-1}$, respectively, as previously mentioned. On the other hand, *N*-hexyl derivative **62** afforded the highest hole mobility of all the series as high as $0.1 \text{ cm}^2 \text{ V}^{-1} \text{ s}^{-1}$, a threshold voltage of -13.2 V and an excellent $I_{\text{on}}/I_{\text{off}}$ ratio of around 10^6 for devices with PS-treated SiO₂ surfaces (Figure

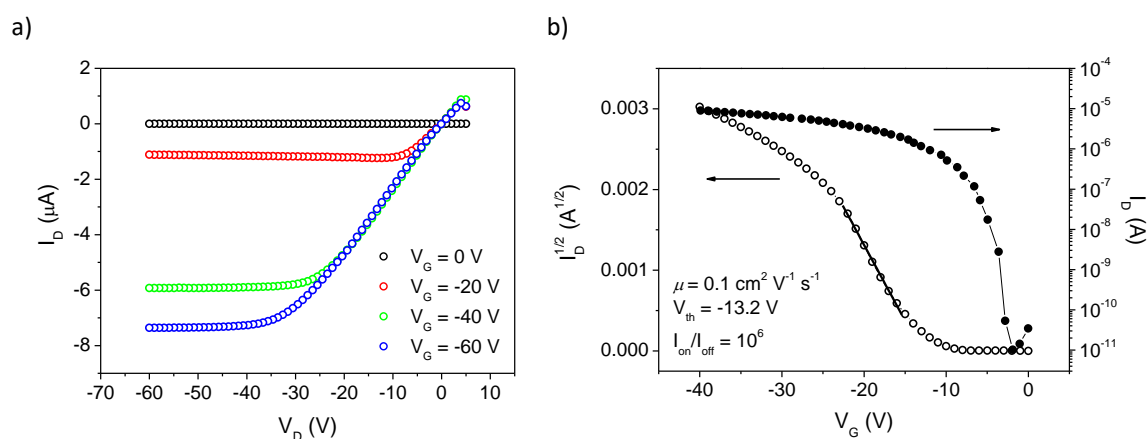


Figure 4.8. OTFT characteristics of a device fabricated with **62** as the semiconductor layer and with PS-treated c-Si/SiO₂ substrate. a) Output characteristics at different gate voltages (V_G). b) Transfer ($V_D = -40$ V) and saturation characteristics.

4.8), whereas OTS-treated devices showed mobilities up to $2 \times 10^{-2} \text{ cm}^2 \text{ V}^{-1} \text{ s}^{-1}$, of the order of those obtained with *N*-methyl derivative **61**. So, **62**-based OTFTs with PS-treated SiO_2 surfaces exhibit a very high performance.

A key requirement in the design of new semiconductors is the stability under ambient conditions. OTFTs fabricated with indolocarbazole and triindole-based semiconductors **59–62** operate well in air, exhibiting remarkable ambient storage stability. Similar threshold voltages, mobilities and $I_{\text{on}}/I_{\text{off}}$ ratios were obtained after 5 months of storage in air and in dark conditions, demonstrating excellent air stability. A representative example based on *N*-trimethyltriindole **61** is shown in Figure 4.9. The increase in charge mobilities after the first days of exposure to air can be attributed to p-doping of the device by O_2 .

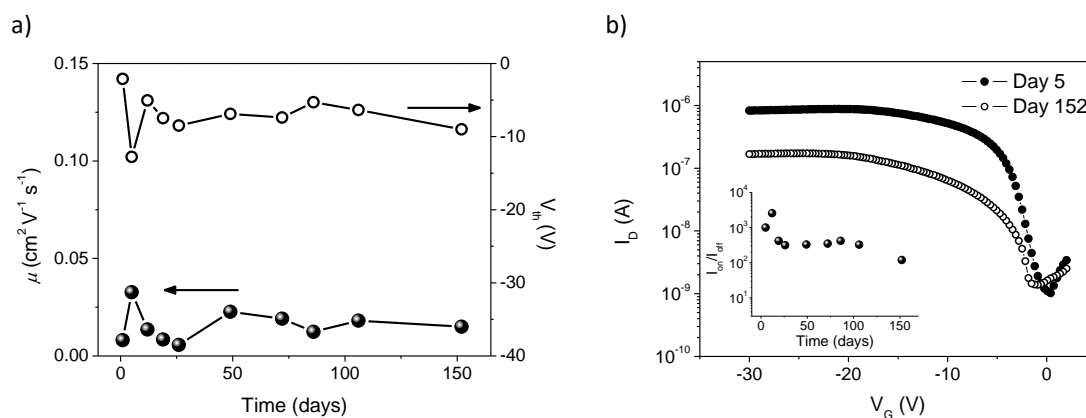


Figure 4.9. a) Mobility and threshold voltage of one representative device (Figure 4.7) fabricated with **61** as the semiconductor layer and PS-treated SiO_2 surface as a function of storage time in the air. b) Transfer characteristics on the 5th day and the 152nd day of the experiment at $V_{\text{b}} = -20 \text{ V}$. Inset figure shows the evolution with time of the $I_{\text{on}}/I_{\text{off}}$ ratio of the selected device.

To date, only a few examples of the application of triindole derivatives in solution-processed OTFTs are found in the literature, showing hole mobilities of $\sim 1 \times 10^{-4} \text{ cm}^2 \text{ V}^{-1} \text{ s}^{-1}$ ^[138a] and $\sim 4 \times 10^{-3} \text{ cm}^2 \text{ V}^{-1} \text{ s}^{-1}$.^[132a] It should be mentioned that these reports were published afterwards the publication of part of the results presented in this Chapter by our group.

4.2.5. Molecular order and morphology of the thin films

For further exploration of the relationship between the OTFTs performance and the role of the molecular order in the thin films, X-ray diffraction (XRD) measurements were performed. For this

purpose, 75-nm thick films were deposited by vacuum evaporation of compounds **59**, **61** and **62** on bare, PS and OTS-treated c-Si/SiO₂ substrates. First of all, the knowledge of the single crystal structure of compounds **59**, **61** and **62** was crucial because it could provide the molecular packing motif and indicate the main intermolecular interactions of these compounds (Section 4.2.2).

As shown in Figure 4.10a, vacuum deposited **59** thin films on bare, PS and OTS-treated c-Si/SiO₂ surfaces presented only one diffraction peak in the XRD patterns at $2\theta = 11.1^\circ$, in comparison to the more complex diffractogram spectra obtained from the powder XRD data (Appendix B). From the single crystal data and the powder XRD pattern, the diffraction peak at $2\theta = 11.1^\circ$ can be assigned to the reflection 200. Thus, the XRD study shows that the plane (100) is parallel to the c-Si/SiO₂ substrate, *i.e.* with *b*- and *c*-axis also in the parallel plane. The molecular packing within the thin film corresponds to that of indolocarbazole **59** in the single crystal. This suggests that the molecules are tilted with an angle of 68° to the substrate (Figure 4.10b). The XRD pattern of the film of **59** on OTS-treated SiO₂ surface shows a stronger diffraction peak than those of films with bare or PS-treated SiO₂ surfaces, suggesting that **59** forms more ordered films on OTS-treated SiO₂ surfaces. These results are in accordance with the hole mobilities measured in OTFTs, where **59** showed higher hole mobilities by treating the SiO₂ surface with OTS (Table 4.3).

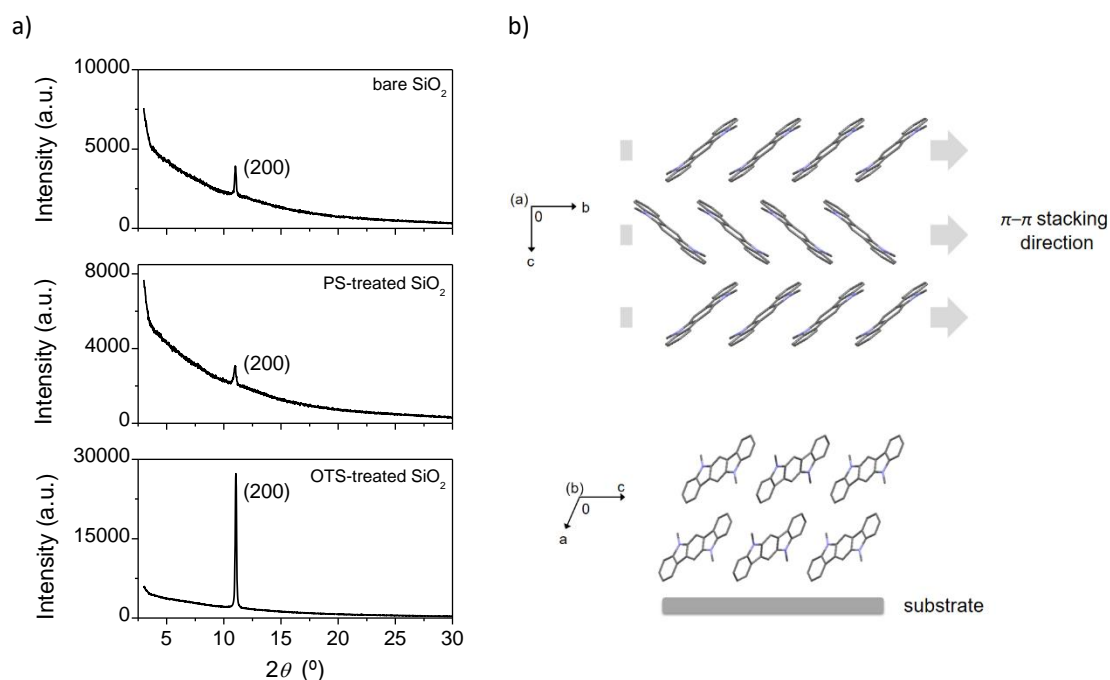


Figure 4.10. a) XRD patterns of vacuum-deposited **59** films on bare, PS and OTS-treated c-Si/SiO₂ surfaces (from top to bottom). b) Molecular packing of compound **59** with the (100) plane situated at 27° (above) and perpendicular (below) to the paper plane, respectively.

The XRD patterns of vacuum-deposited films of *N*-trimethyltriindole **61** on bare and PS-treated substrates displayed one diffraction peak at $2\theta = 8.3^\circ$ (Figure 4.11a). The film of **61** on OTS-treated SiO_2 substrate exhibited a stronger diffraction peak and in addition a second order diffraction peak at $2\theta = 16.6^\circ$, indicating a higher degree of ordering, in accordance with the slightly enhanced hole mobility of **61** on OTS-treated devices (Table 4.3). From the single crystal data,^[142] the powder XRD pattern (Appendix B) and the XRD data of the films, the diffraction peaks at $2\theta = 8.3^\circ$ and $2\theta = 16.6^\circ$ were assigned to the corresponding reflections 110 and 220, respectively, suggesting that the plane (110) is parallel to the substrate with the *c*-axis also in the parallel plane. Consequently, as it is collected in Figure 4.11b, triindole molecules are located totally perpendicular (90°) to the substrate surface with the π - π stacking direction lying parallel to the substrate surface.

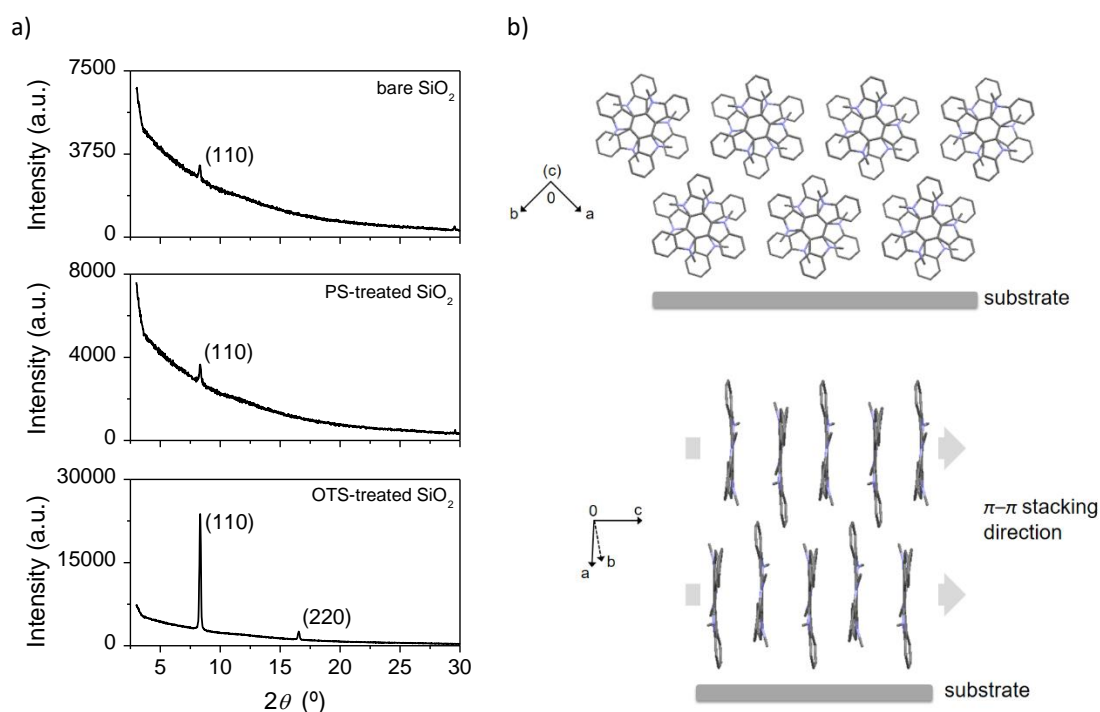


Figure 4.11. a) XRD patterns of vacuum-deposited **61** films on bare, PS and OTS-treated *c*-Si/ SiO_2 surfaces (from top to bottom). b) Molecular packing in the thin film seen from two different perspectives, being the (110) plane situated perpendicular to the paper. The hydrogen atoms were omitted for clarity.

The XRD patterns of vacuum-deposited thin films of *N*-hexyl derivative **62** on bare, PS- and OTS-treated substrates each show one strong diffraction peak at $2\theta = 5.7^\circ$ (Figure 4.12a). From the single crystal data, the powder XRD pattern (Appendix B) and the XRD data of the films, the diffraction peak at $2\theta = 5.7^\circ$ was assigned to the reflection 010, suggesting that the plane (010) is parallel to the *c*-Si/ SiO_2 substrate, *i.e.* with *a*- and *c*-axis also in the parallel plane. As a result,

molecules are located with an angle of 60° to the substrate surface, but also with the π - π stacking direction being parallel to it as displayed in Figure 4.12b. The strongest diffraction peak of the film of **62** on PS-treated substrate is indicative of a more ordered film, which is in accordance with the higher hole mobilities obtained in OTFTs when treating the SiO_2 surface with PS (Table 4.3).

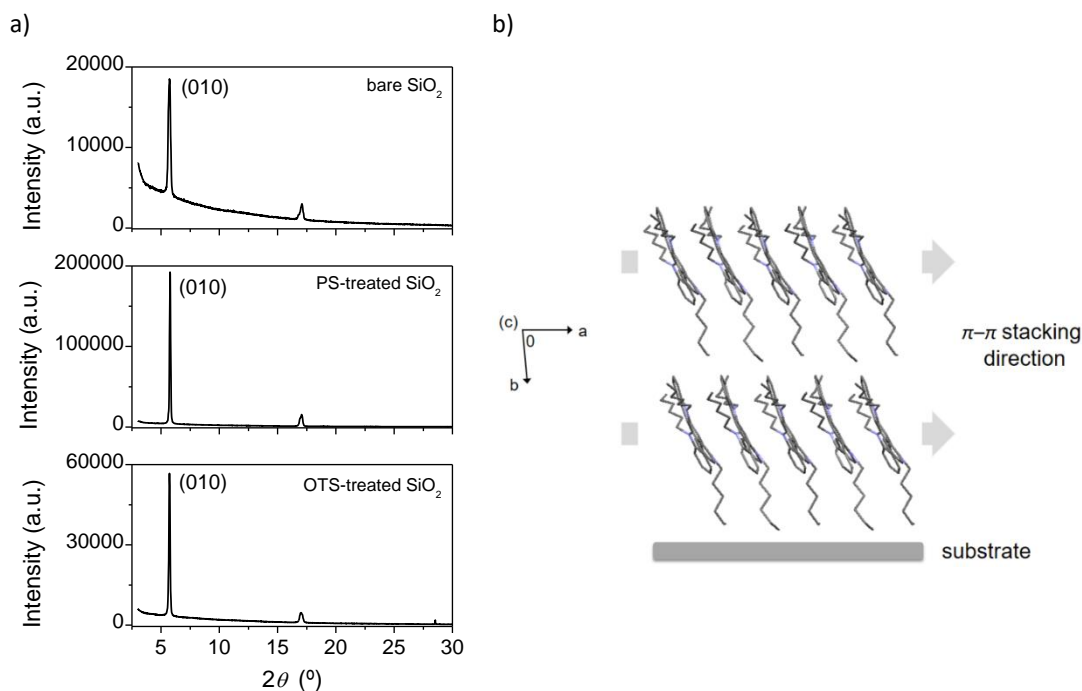


Figure 4.12. a) XRD patterns of vacuum-deposited **62** films on bare, PS and OTS-treated c-Si/SiO₂ surfaces (from top to bottom). b) Molecular packing in the thin film with the (010) plane situated perpendicular to the paper. The hydrogen atoms were omitted for clarity.

Films of **59** and **61** showed a higher degree of molecular ordering by treating the SiO_2 surface with OTS as revealed by XRD, which can be related to the enhanced hole mobilities detected. On the other hand, films of *N*-trihexyltriindole **62** exhibit a higher degree of order in comparison to those of *N*-trimethyltriindole **61**. These results are in accordance with the higher hole mobility up to $0.1 \text{ cm}^2 \text{ V}^{-1} \text{ s}^{-1}$ determined for **62**-based devices with PS-treated SiO_2 surface. Molecules in **62** show a slipped cofacial arrangement with π - π stacking interactions between neighbouring triindole cores, but remarkably with also $\text{C-H}\cdots\pi$ interactions involving the alkyl chains. These additional $\text{C-H}\cdots\pi$ interactions could be responsible of a more favourable packing for enhancing the charge transport.^[145]

In addition to the local intermolecular interactions, the film morphology and the grain sizes and boundaries strongly influence the charge transport properties, particularly at the interface

between the semiconductor and the dielectric. AFM images were taken from **59**, **61** and **62** films deposited by sublimation on bare, polystyrene (PS) and OTS-treated SiO₂ surfaces (Figures 4.13–4.15). Remarkable morphology differences were observed between them.

Thin films based on indolocarbazole **59** deposited on bare, PS- and OTS-treated SiO₂ surfaces showed similar topography profiles (Figure 4.13). Vacuum-deposited **59** films presented a terrace-like step morphology (Figure 4.13c), independently of the modification of the dielectric surface. Films present a similar average grain size, with an average width of 600 nm and lengths that include from 600 nm to around 2 μm. A slight enhancement of the interconnectivity between the grains is observed for films based on **59** deposited on PS- and OTS-treated surfaces, which actually correspond to devices with higher performance (Table 4.3). However, the film of **59** on OTS-treated substrate shows less irregular grain morphology and lower roughness than the PS-treated layer, which could favour the charge transport.

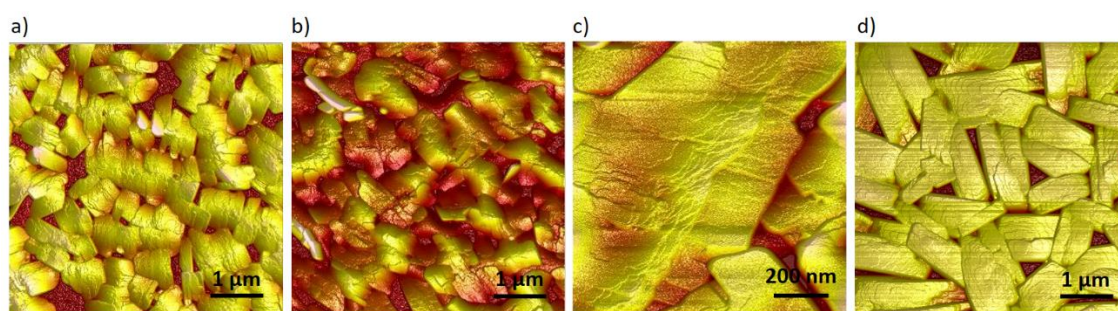


Figure 4.13. AFM images of vacuum-evaporated thin films of indolocarbazole **59** deposited on a) bare SiO₂ (5 × 5 μm²), b) PS-treated SiO₂ (5 × 5 μm²), c) PS-treated SiO₂ (1 × 1 μm²) and d) OTS-treated SiO₂ (5 × 5 μm²).

The AFM images taken from films of triindole derivatives **61** and **62** are displayed in Figures 4.14 and 4.15. Vacuum-deposited **61** films on bare and PS-treated SiO₂ show identical morphologies (Figure 4.14a,b and c). AFM images exhibited protrusions/hillocks, whose average thickness was in the order of 130 nm and their height varied from 50 nm to more than 100 nm. On the contrary, the crystal grains are larger and elongated in shape when the c-Si/SiO₂ substrate was treated with OTS, with average grain sizes about 0.25 μm × 1.3 μm (Figure 4.14d and e). Thus, by treating the SiO₂ surface with OTS, the grains of the film of **61** become larger and the surface is smoother which corresponds to improved OTFT performance (Table 4.3).

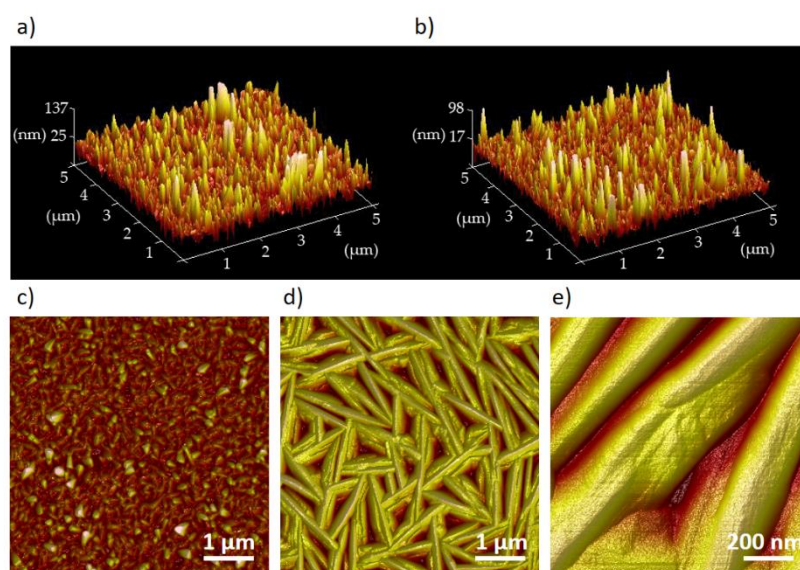


Figure 4.14. AFM images of vacuum-evaporated thin films of *N*-trimethyltriindole **61** deposited on a) bare SiO₂ (5 × 5 μm²), b) and c) PS-treated SiO₂ (5 × 5 μm²) from two different points of view, d) OTS-treated SiO₂ (5 × 5 μm²) and e) OTS-treated SiO₂ (1 × 1 μm²).

Figure 4.15 collects the AFM images taken from **62** vacuum-evaporated films. The film prepared on bare SiO₂ surface shows large round-shape grains around 1.5 μm in diameter (Figure 4.15a). The grains are not interconnected between them, which would hinder the charge transport. By treating the SiO₂ surface with PS the grains become elongated with a grain size up to 2 μm × 0.2 μm and better interconnected (Figure 4.15b). On the other hand, the AFM image of the film with OTS-treated SiO₂ surface (Figure 4.15c) shows also elongated grains but with a more irregular grain morphology and higher roughness than the PS-treated layer, which could be related to the lower hole mobilities determined for OTFT devices with OTS-treated c-Si/SiO₂ substrates in comparison to the PS-treated ones (Table 4.3).

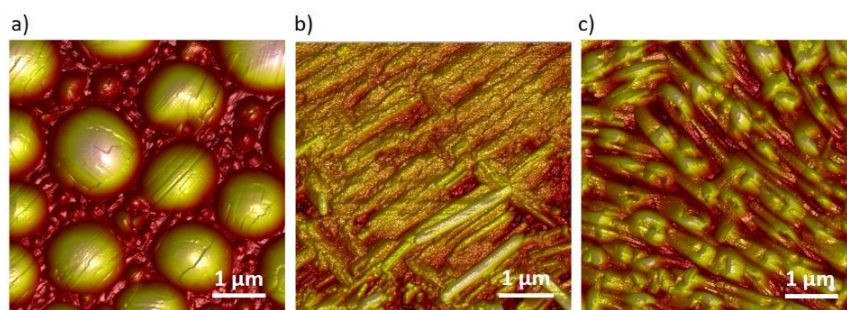


Figure 4.15. AFM images of vacuum-evaporated thin films of *N*-trihexyltriindole **62** deposited on a) bare SiO₂ (5 × 5 μm²), b) PS-treated SiO₂ (5 × 5 μm²) and c) OTS-treated SiO₂ (5 × 5 μm²).

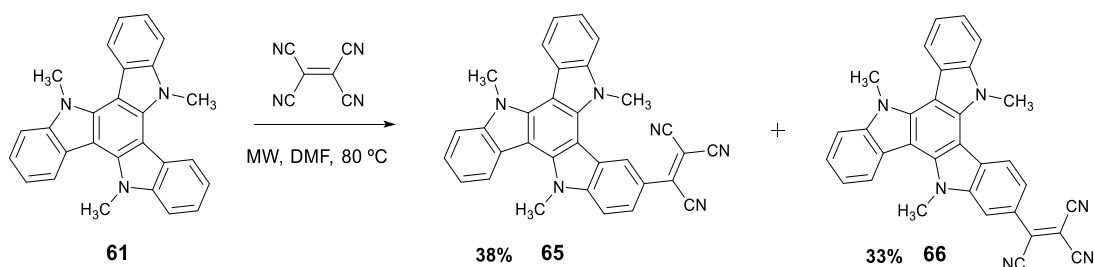
Summarizing the above presented results, it can be concluded that OTFTs based on **59** and **61**, with the shorter *N*-methyl chain, showed enhanced hole mobilities by treating the SiO₂ surface with OTS. On the contrary, those devices fabricated with the longer *N*-hexyl derivative **62** showed improved hole mobilities in PS-treated devices. Combining the XRD and AFM data, the relationship between the treatment of the dielectric surface with PS or OTS and the *N*-alkyl chain length attached to the π -conjugated core seems to determine the degree of molecular ordering, the growth mode and the grain shape characteristics of the organic semiconducting layer (Figures 4.13–4.15), and thus the device performance.

4.3. Tricyanovinyl-substituted triindole derivatives

The introduction of the tricyanovinyl group on the carbazole core (Chapter 3) afforded ambipolar and n-type materials. Given that triindole derivatives have shown enhanced hole mobilities around $10^{-2} - 10^{-1} \text{ cm}^2 \text{ V}^{-1} \text{ s}^{-1}$ with respect to those of carbazole derivatives, the aim of this section is to study the effect that the introduction of the tricyanovinyl group on the triindole core can have on its charge-transporting properties.

4.3.1. Synthesis

The synthesis of 3-tricyanovinyl-substituted triindole derivative **65** is displayed in Scheme 4.6. It should be mentioned that the first attempts to synthesize tricyanovinyl derivative **65** consisted on heating triindole **61** in anhydrous DMF with tetracyanoethylene at 50 °C. However, no formation of **65** was detected, neither increasing the reaction temperature from 50 to 100°C, nor adding additional equivalents (up to a maximum of 4 eq.) of tetracyanoethylene.



Scheme 4.6. Synthesis of tricyanovinyl derivative **65**.

When compound **61** was heated in anhydrous DMF with tetracyanoethylene under microwave irradiation the formation of the desired product **65** was accomplished (Scheme 4.6). However, formation of sub-products was observed due to the chemical nature of the triindole moiety. First, it should be mentioned that the electrophilic substitution of 9*H*-carbazole derivatives with tetracyanoethylene takes place only in the activated position 3 of the carbazole core, that is, the *para* position to the nitrogen atom. The addition of more equivalents of tetracyanoethylene does not result in the introduction of a second unit, due to the deactivation of the aromatic carbazole system as a consequence of the established charge transfer from the electron-donating carbazole to the electron-withdrawing tricyanovinyl groups.^[114a] In contrast, the treatment of triindole **61** under microwave irradiation at 80 °C led to the 3-substituted desired product **65** but also to the 2-substituted derivative **66**. The two isomers were characterized and identified by ¹H NMR. The separation and purification of both compounds was very difficult and only compound **65** was obtained in a suitable purity level after several recrystallization processes from hexane/dichloromethane mixtures. For this reason, compound **66** has not been subject of further studies in this thesis. It should be also mentioned that the introduction of additional tricyanovinyl fragments on the other peripheral benzene rings of the triindole core was also detected by mass spectroscopy in the reaction mixture.

4.3.2. Characterization of the organic semiconductor

Compound **65** exhibited a high thermal stability with a decomposition temperature of 376 °C as revealed by TGA (Appendix B). Figure 4.16 displays the UV-Vis absorption spectra of the corresponding vacuum-evaporated layer of **65**. The absorption spectra of 9-methyl-3-(1,2,2-tricyanovinyl)-9*H*-carbazole **39** is also shown for comparison. The absorption spectra of **65** displays three absorption bands with maximum absorption wavelengths at 318, 448 and 615 nm. Consistent with the extension of the conjugation in triindole derivative **65**, the absorption band in the UV zone is 20 nm bathochromically shifted in comparison to the carbazole derivative **39**, as well as the charge transfer band, that exhibits a red shift of 143 nm and shows its maximum in the red region of the spectrum.

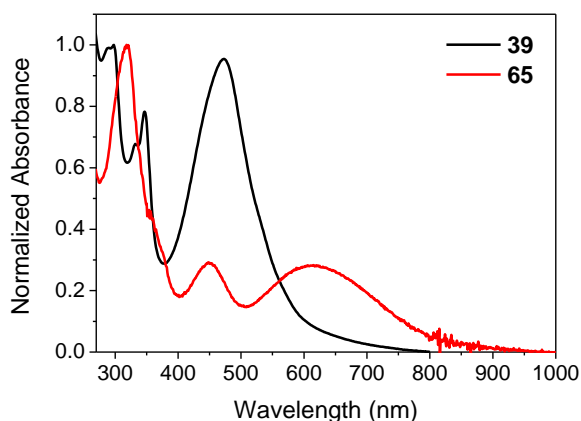


Figure 4.16. Absorption spectra of vacuum-evaporated layers (75 nm) based on **39** and **65**.

The electrochemical properties of **65** were examined by cyclic voltammetry and compared to the previous studied compounds 9-methyl-3-(1,2,2-tricyanovinyl-9*H*-carbazole **39** and *N*-trimethyltriindole **61** (Table 4.4).

Table 4.4. Electrochemical properties of **39**, **61** and **65**.

Compd.	$E_{\text{red},1}^0$ [a] (V)	$E_{\text{onset}}^{\text{red}}$ [b] (V)	$E_{\text{ox},1}^0$ [a] (V)	$E_{\text{onset}}^{\text{ox}}$ [b] (V)	EA [c] (eV)	IP [c] (eV)	E_{gap} [c] (eV)
39	-1.08	-1.00	–	1.06	4.39	6.45	2.06
61	–	–	–	0.17	2.03 [d]	5.56	3.53 [e]
65	-1.07	-0.99	0.52	0.43	4.40	5.82	1.42

[a] Standard potential of the first reduction redox couple ($E_{\text{red},1}^0$) and of the first oxidation redox couple ($E_{\text{ox},1}^0$) vs. Fc^+/Fc determined from CV in 1 mM dichloromethane solutions at a scan rate of 100 mV s^{-1} . [b] Onset reduction potential ($E_{\text{onset}}^{\text{red}}$) and onset oxidation potential ($E_{\text{onset}}^{\text{ox}}$) vs. Fc^+/Fc determined from CV in 1 mM dichloromethane solutions at a scan rate of 100 mV s^{-1} . [c] Electron affinity (EA) and ionization potential (IP) estimated from CV as $\text{EA} = E_{\text{onset vs. Fc}^+/\text{Fc}}^{\text{red}} + 5.39$, $\text{IP} = E_{\text{onset vs. Fc}^+/\text{Fc}}^{\text{ox}} + 5.39$ and $E_{\text{gap}} = \text{IP} - \text{EA}$. [d] EA estimated as $\text{EA} = \text{IP} - E_{\text{gap}}^{\text{opt}}$. [e] Optical energy gap ($E_{\text{gap}}^{\text{opt}}$) estimated from the absorption spectra.

Cyclic voltammogram of **65** exhibits two reduction and two oxidation waves, being in both cases the first one *quasi*-reversible and the second one irreversible (Figure 4.17). Comparing to tricyanovinyl derivative **39**, compound **65** shows a similar reduction standard potential of -1.07 V , suggesting that the reduction potentials are highly influenced by the tricyanovinyl fragment and not by the electron-donating moiety. On the other hand, the onset oxidation potential of **65** differs to that of **39**. Indeed, triindole derivative **65** is more easily oxidized ($E_{\text{onset}}^{\text{ox}} = 0.43 \text{ V}$) than **39** ($E_{\text{onset}}^{\text{ox}} = 1.06 \text{ V}$), according to the enhanced electron-donating nature of the triindole core **65**. In

comparison to the non-substituted parent compound **61** ($E_{\text{onset}}^{\text{ox}} = 0.17$ V), derivative **65** is less easily oxidized ($E_{\text{onset}}^{\text{ox}} = 0.43$ V) in accordance to the attached electron-withdrawing tricyanovinyl group. It should be noted that a similar difference between the onset oxidation potentials can be found for 9-methyl-3-(1,2,2-tricyanovinyl)-9H-carbazole **39** ($E_{\text{onset}}^{\text{ox}} = 1.06$ V) and the non-substituted parent compound 9-methyl-9H-carbazole **43** ($E_{\text{onset}}^{\text{ox}} = 0.77$ V). The ionization potential and electron affinity of **65** are 5.82 and 4.40 eV, respectively, and are indicative of potential p- and n-type channel conduction.

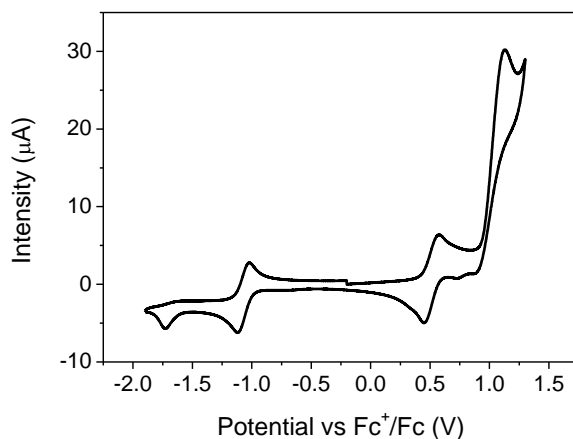


Figure 4.17. Cyclic voltammogram of compound **65** recorded at a scan rate of 100 mV s^{-1} in 1 mM dichloromethane solution.

4.3.3. Organic Thin-Film Transistors

Charge-transporting properties of **65** were studied in bottom-gate/top-contact OTFTs by using PS and OTS-treated c-Si/SiO₂ gate/dielectric substrates and Au as source and drain electrodes. The semiconducting layer was deposited by vacuum evaporation.

Devices based on **65** showed p-type behaviour (Table 4.5, Figure 4.18 and Appendix B). OTFT devices with PS- and OTS-treated substrates based on **65** exhibited similar hole mobilities of 2×10^{-4} and $1 \times 10^{-4} \text{ cm}^2 \text{ V}^{-1} \text{ s}^{-1}$, respectively. The threshold voltage (V_{th}) was slightly reduced by treating the substrate surface with OTS ($V_{\text{th}} = -4.3$ V) than by treating it with PS ($V_{\text{th}} = -8.1$ V). Contrary to the expected from cyclic voltammetry analyses, devices based on tricyanovinyl derivative **65** did not show electron transport as the previous series of tricyanovinyl derivatives presented in Chapter 3. Moreover, the hole mobility for devices of **65** decreases significantly, in

comparison to those based on the parent compound *N*-trimethyltriindole **61**, which exhibited a hole mobility as high as $6 \times 10^{-2} \text{ cm}^2 \text{ V}^{-1} \text{ s}^{-1}$.

Table 4.5. OTFT characteristics of devices based on **65** with PS and OTS-treated c-Si/SiO₂ substrates.

Compound		$\mu_{\text{h}} (\text{cm}^2 \text{ V}^{-1} \text{ s}^{-1})$ [a]	$V_{\text{th}} (\text{V})$ [b]	$I_{\text{on}}/I_{\text{off}} (\text{A/A})$ [c]
65	PS	2×10^{-4}	-8.1	$\sim 10^3$
65	OTS	1×10^{-4}	-4.3	$\sim 10^4$

[a] Electron mobility (μ_e). [b] Threshold voltage (V_{th}). [c] $I_{\text{on}}/I_{\text{off}}$ ratio. Measurements were determined in vacuum at room temperature.

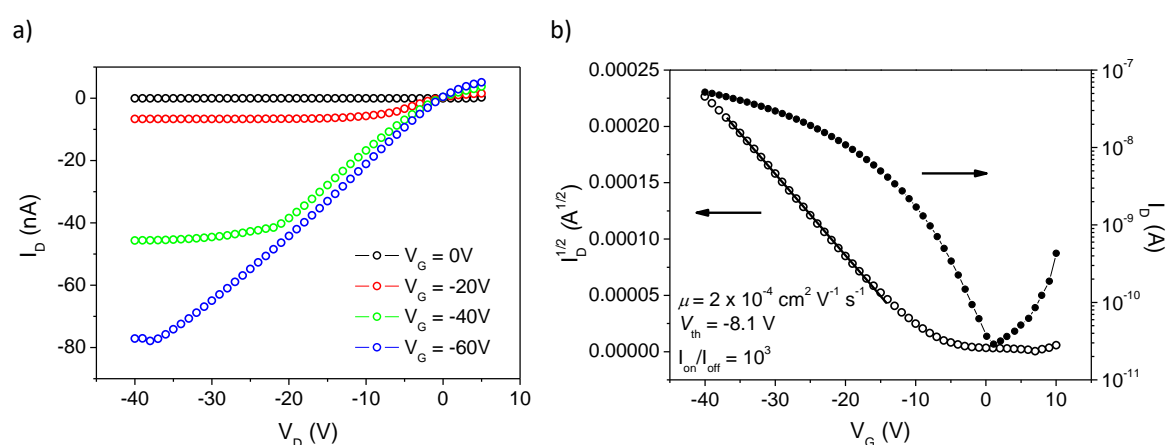


Figure 4.18. OTFT characteristics of a device fabricated with **65** as the semiconductor layer and with PS-treated c-Si/SiO₂ substrate. a) Output characteristics at different gate voltages (V_{G}). b) Transfer ($V_{\text{D}} = -40 \text{ V}$) and saturation characteristics.

It should be noted that although compounds **39** and **65** show similar IP and EA values, their molecular structure differs considerably. Considering that the supramolecular organization in the solid state influences on the charge-transporting properties, the knowledge of the molecular packing of these molecules could give insights about the charge-transporting properties of **65** and justify the obtained results. Unfortunately, until now it has not been possible to get suitable crystals from **65** to determine the single crystal structure by X-ray crystallography. Taking into account that molecules in **61** adopt a face-to-face packing in an alternate arrangement (Figure 4.2), we suggest that molecules in **65** could form also π -stacks with face-to-face interactions between triindole cores, or slipped face-to-face ones, being the tricyanovinyl fragment in an alternate position in each adjacent molecule (Figure 4.19a). DFT calculations for 9-methyl-9*H*-carbazole **39** showed that the

HOMO orbital was mainly located at the electron-donating carbazole moiety and the LUMO at the electron-withdrawing tricyanovinyl fragment (Figure 4.19b). Accordingly, a similar description could be expected for tricyanovinyl-substituted triindole derivative **65**. Thus, if tricyanovinyl fragments of neighbouring molecules are located at long distances in **65**, due to a possible alternate arrangement of triindole molecules, LUMO-LUMO interactions would not be favoured, and the electron transport would be hindered. However, further studies including X-ray diffraction analyses and theoretical calculations should be performed to confirm this hypothesis.

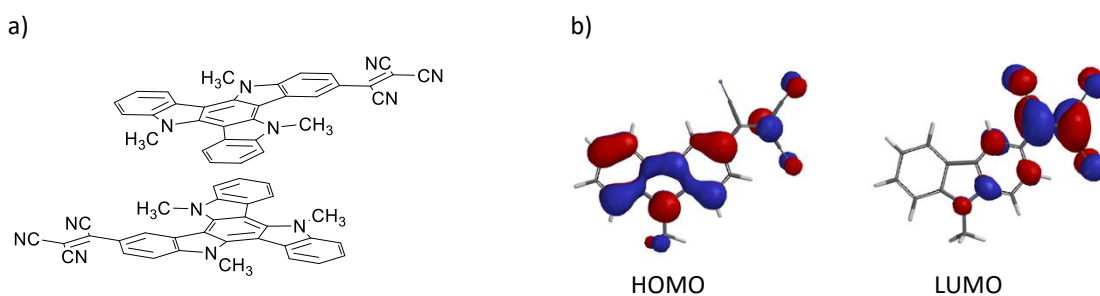
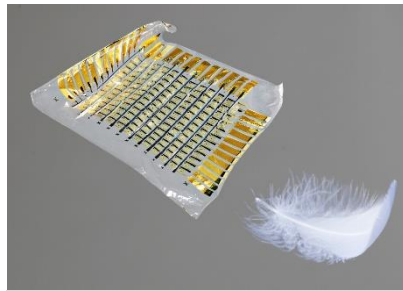


Figure 4.19. a) Schematic representation of the molecular packing proposed for molecules of **65** in the thin films. b) Computed spatial distributions of HOMO and LUMO of **39** (Reprinted from Figure 3.6).

4.4. Conclusions

All the carbazole-based compounds **43** and **58–62** presented high ionization potentials and high optical band gaps, indicating their potential hole-transporting properties and air stability. However, only compounds **59–62**, with extended π -conjugated cores with two or three fused carbazole rings, presented good device performances and air-stability and durability under air conditions, for longer periods up to 5 months, with hole mobility values ranging from 10^{-3} to $0.1 \text{ cm}^2 \text{ V}^{-1} \text{ s}^{-1}$. For indolocarbazole derivative **59**, a herringbone packing motif with $\text{CH}_3 \cdots \pi$ interactions has been described in the semiconductor layer, whereas a cofacial molecular packing with π - π interactions is observed for triindole **61**. For the latter, it has been found that in the crystal structure and in the thin film, presents a face-to-face molecular packing, and an optimal perpendicular molecular disposition to the substrate surface as determined by XRD, that can favour charge transport in the OTFT devices. *N*-Trihexyltriindole **62** exhibits a slipped cofacial molecular packing with π - π interactions but also with $\text{C-H} \cdots \pi$ interactions, that could explain the enhanced hole mobilities up to $0.1 \text{ cm}^2 \text{ V}^{-1} \text{ s}^{-1}$ for **62**-based devices. Indolo[3,2-*b*]carbazole and specially triindole units are shown to be promising π -conjugated cores for new organic semiconductors for electronic devices.

The introduction of the tricyanovinyl group on the triindole core furnished isomers **65** and **66**, substituted in positions 3 and 2 of the triindole moiety, respectively. Compound **65** exhibited a high thermal stability and suitable IP and EA values of 5.82 and 4.40 eV, respectively, to display potential ambipolar properties, similarly to the series of tricyanovinyl-substituted carbazole derivatives studied in Chapter 3. However, vacuum-evaporated OTFTs based on **65** only afforded the measurement of hole-transporting properties, with hole mobilities around $10^{-4} \text{ cm}^2 \text{ V}^{-1} \text{ s}^{-1}$, significantly lower than those obtained for the parent compound *N*-trimethyltriindole **61**. We suggest that the molecular packing of **65** could hinder the LUMO-LUMO interactions and as a consequence the electron transport. However, further studies should be undertaken to prove this statement.



by *Plastics* ^[146]

CONCLUSIONS

CONCLUSIONS

The extension of the π -conjugated carbazole system by introducing the donor moieties thienyl, phenyl or carbazole at 3,6 positions of the carbazole core has been proved to be an effective strategy to obtain materials with blue-emitting properties, which have been modulated by the introduction of the ethynylene spacer between the carbazole and the donor units. The extension of the conjugation of the carbazole system by forming bicarbazole and tricarbazole derivatives and keeping the triple bond substitution afforded emitters in the sought range of the deep-blue region in the solid state. This series of materials showed hole-transporting properties with hole mobilities up to $10^{-3} \text{ cm}^2 \text{ V}^{-1} \text{ s}^{-1}$. A blue non-doped OLED device based on 9-ethyl-3,6-bis(2-phenylethynyl)-9H-carbazole (**8**) as the emitting layer exhibited a very low turn-on voltage of only 4 V, together with a high luminance up to $1.4 \times 10^4 \text{ cd m}^{-2}$, and a very high efficiency of radiative exciton production (ϕ) of 45%.

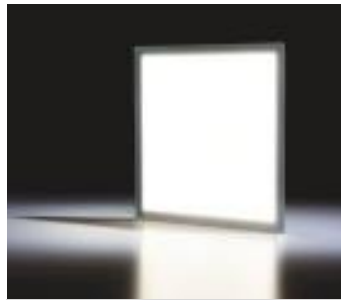
The development of new ambipolar semiconducting materials has been undertaken by preparing a series of charge-transfer radical adducts based on the coupling of the electron-donating carbazole group and the acceptor TTM radical. The introduction of electron-withdrawing groups in the carbazole core, as well as the extension of the conjugation, have been proved to be effective approaches to obtain ambipolar materials with well-balanced charge carrier mobilities. Xerographic single-layered photoreceptors fabricated with this series of radical adducts showed good xerographic photosensitivity across the visible spectrum.

The strategy of preparing push-pull compounds by maintaining the carbazole heterocycle as the donor fragment and using the tricyanovinyl unit as the electron acceptor has been successfully applied to obtain electron-transporting materials as confirmed by TOF and OTFT measurements. The introduction of the methoxy substituent in the carbazole core in the *ortho* position with respect to the tricyanovinyl unit afforded ambipolar materials. The methoxy-substitution involves a non-planar conformation of the molecules that influences the supramolecular organization in the solid state favouring the ambipolar properties. In a different way, non-methoxy substituted carbazole derivatives showed exclusively electron transport. In this case, molecules adopt a planar

conformation that favours LUMO-LUMO interactions between neighbouring molecules resulting in an improvement of the electron transport. The introduction of alkyl chains of different length on the nitrogen atom of the carbazole core, from methyl to dodecyl, yielded a series of materials that exhibited electron mobilities as active layers in OTFT devices of the same order, in the range of 9×10^{-6} to $5 \times 10^{-5} \text{ cm}^2 \text{ V}^{-1} \text{ s}^{-1}$. XRD studies revealed that all compounds show a layered organization with an antiparallel arrangement and similar minimum interlayer distances. The intermolecular interactions in the π stacks are mainly governed by the π -conjugated carbazole system and not by the *N*-alkyl chain, implying for this series of tricyanovinyl derivatives comparable electron mobilities.

The extension of the aromatic core of the carbazole unit through the formation of the related derivatives indolo[3,2-*b*]carbazole and triindole has been an effective selection to prepare organic semiconductors with high hole mobilities. OTFTs showed high device performance, as well as air stability and durability for long periods up to 5 months. In particular, the introduction of the long *N*-hexyl chains in *N*-trihexyltriindole **62** contributes with additional C–H $\cdots\pi$ interactions to those of π – π character between the triindole cores to increase the hole mobilities up to $0.1 \text{ cm}^2 \text{ V}^{-1} \text{ s}^{-1}$.

On this basis, the elucidation of the supramolecular organization and intermolecular interactions in organic semiconductors is, therefore, essential to rationalize the charge transport properties and it is shown to be a powerful guide for the future design of new organic semiconductors with improved performance.



by OSRAM ^[37]

REFERENCES

REFERENCES

- [1] <http://www.paneloled.com> (date: March 22, 2017).
- [2] H. Shirakawa, E. J. Louis, A. G. MacDiarmid, C. K. Chiang and A. J. Heeger, *J. Chem. Soc., Chem. Commun.* **1977**, 578–580.
- [3] H. Shirakawa, *Angew. Chem., Int. Ed.* **2001**, *40*, 2575–2580.
- [4] <http://nobelprize.org/chemistry/laureates/2000/index.html>.
- [5] Y. Yao, H. Dong and W. Hu, *Adv. Mater.* **2016**, *28*, 4513–4523.
- [6] L. Dou, Y. Liu, Z. Hong, G. Li and Y. Yang, *Chem. Rev.* **2015**, *115*, 12633–12665.
- [7] M. Zhu and C. Yang, *Chem. Soc. Rev.* **2013**, *42*, 4963–4976.
- [8] L. Dou, J. You, Z. Hong, Z. Xu, G. Li, R. A. Street and Y. Yang, *Adv. Mater.* **2013**, *25*, 6642–6671.
- [9] Y. Shirota and H. Kageyama, *Chem. Rev.* **2007**, *107*, 953–1010.
- [10] C. R. Newman, C. D. Frisbie, D. A. da Silva Filho, J.-L. Brédas, P. C. Ewbank and K. R. Mann, *Chem. Mater.* **2004**, *16*, 4436–4451.
- [11] J. Mei, Y. Diao, A. L. Appleton, L. Fang and Z. Bao, *J. Am. Chem. Soc.* **2013**, *135*, 6724–6746.
- [12] L. Torsi, M. Magliulo, K. Manoli and G. Palazzo, *Chem. Soc. Rev.* **2013**, *42*, 8612–8628.
- [13] A. Tsumura, H. Koezuka and T. Ando, *Appl. Phys. Lett.* **1986**, *49*, 1210–1212.
- [14] K. Takimiya, T. Yamamoto, H. Ebata and T. Izawa, *Sci. Technol. Adv. Mater.* **2007**, *8*, 273–276.
- [15] a) X. Gao and Y. Hu, *J. Mater. Chem. C* **2014**, *2*, 3099–3117; b) Y. Zhao, Y. Guo and Y. Liu, *Adv. Mater.* **2013**, *25*, 5372–5391.
- [16] D. M. De Leeuw, M. M. J. Simenon, A. R. Brown and R. E. F. Einerhand, *Synth. Met.* **1997**, *87*, 53–59.
- [17] B. A. Jones, A. Facchetti, M. R. Wasielewski and T. J. Marks, *J. Am. Chem. Soc.* **2007**, *129*, 15259–15278.
- [18] L. Dou, Y. Liu, Z. Hong, G. Li and Y. Yang, *Chem. Rev.* **2015**, *115*, 12633–12665.
- [19] T. Lei, J.-Y. Wang and J. Pei, *Chem. Mater.* **2014**, *26*, 594–603.
- [20] a) C.-H. Lee, Y.-Y. Lai, J.-Y. Hsu, P.-K. Huang and Y.-J. Cheng, *Chem. Sci.* **2017**, *8*, 2942–2951; b) J. Y. Back, T. K. An, Y. R. Cheon, H. Cha, J. Jang, Y. Kim, Y. Baek, D. S. Chung, S.-K. Kwon, C. E. Park and Y.-H. Kim, *ACS Appl. Mater. Interfaces* **2015**, *7*, 351–358; d) H. B. Akkerman, S. C. B. Mannsfeld, A. P. Kaushik, E. Verploegen, L. Burnier, A. P. Zoombelt, J. D. Staathoff, S. Hong, S. Atahan-Evrenk, X. Liu, A. Aspuru-Guzik, M. F. Toney, P. Clancy and Z. Bao, *J. Am. Chem. Soc.* **2013**, *135*, 11006–11014.
- [21] F. Garnier, R. Hajlaoui, A. El Kassmi, G. Horowitz, L. Laigre, W. Porzio, M. Armanini and F. Provasoli, *Chem. Mater.* **1998**, *10*, 3334–3339.

- [22] Z. Bao, A. J. Lovinger and A. Dodabalapur, *Appl. Phys. Lett.* **1996**, *69*, 3066–3068.
- [23] a) M. E. Roberts, S. C. B. Mannsfeld, N. Queraltó, C. Reese, J. Locklin, W. Knoll and Z. Bao, *PNAS* **2008**, *105*, 12134–12139; b) H. Klauk, M. Halik, U. Zschieschang, G. Schmid, W. Radlik and W. Weber, *J. Appl. Phys.* **2002**, *92*, 5259–5263.
- [24] a) D. Simeone, S. Cipolloni, L. Mariucci, M. Rapisarda, A. Minotti, A. Pecora, M. Cuscunà, L. Maiolo and G. Fortunato, *Thin Solid Films* **2009**, *517*, 6283–6286; b) K. Takimiya, T. Yamamoto, H. Ebata and T. Izawa, *Sci. Technol. Adv. Mater.* **2007**, *8*, 273–276.
- [25] a) M. J. Kang, I. Doi, H. Mori, E. Miyazaki, K. Takimiya, M. Ikeda and H. Kuwabara, *Adv. Mater.* **2011**, *23*, 1222–1225; b) T. Yamamoto and K. Takimiya, *J. Am. Chem. Soc.* **2007**, *129*, 2224–2225.
- [26] A. Y. Amin, A. Khassanov, K. Reuter, T. Meyer-Friedrichsen and M. Halik, *J. Am. Chem. Soc.* **2012**, *134*, 16548–16550.
- [27] Y. Sakamoto, T. Suzuki, M. Kobayashi, Y. Gao, Y. Fukai, Y. Inoue, F. Sato and S. Tokito, *J. Am. Chem. Soc.* **2004**, *126*, 8138–8140.
- [28] A. Facchetti, Y. Deng, A. Wang, Y. Koide, H. Sirringhaus, T. J. Marks and R. H. Friend, *Angew. Chem. Int. Ed.* **2000**, *39*, 4547–4551.
- [29] Z. Bao, A. J. Lovinger and J. Brown, *J. Am. Chem. Soc.* **1998**, *120*, 207–208.
- [30] B. A. Jones, M. J. Ahrens, M.-H. Yoon, A. Facchetti, T. J. Marks and M. R. Wasielewski, *Angew. Chem. Int. Ed.* **2004**, *43*, 6363–6366.
- [31] Y. Qiao, Y. Guo, C. Yu, F. Zhang, W. Xu, Y. Liu and D. Zhu, *J. Am. Chem. Soc.* **2012**, *134*, 4084–4087.
- [32] S. W. Yun, J. H. Kim, S. Shin, H. Yang, B.-K. An, L. Yang and S. Y. Park, *Adv. Mater.* **2012**, *24*, 911–915.
- [33] M. L. Tang, A. D. Reichardt, T. Siegrist, S. C. B. Manssfeld and Z. Bao, *Chem. Mater.* **2008**, *20*, 4669–4676.
- [34] M. L. Tang, A. D. Reichardt, N. Miyaki, R. M. Stoltenberg and Z. Bao, *J. Am. Chem. Soc.* **2008**, *130*, 6064–6065.
- [35] A. Bernanose, M. Comte and P. Vouaux, *J. Chim. Phys.* **1953**, *50*, 64–68.
- [36] C. W. Tang and S. A. VanSlyke, *Appl. Phys. Lett.* **1987**, *51*, 913.
- [37] <http://www.osram-oled.com/oled/en/products/orbeos-sdw-058/index.jsp> (date: March 22, 2017).
- [38] <https://www.sony.es/electronics/televisores/a1-series> (date: March 22, 2017)
- [39] <http://www.lighting.philips.com/main/products/oled> (date: March 22, 2017)
- [40] <http://www.osram-oled.com/oled/en/applications/reference-projects/cobra/index.jsp> (date: March 22, 2017).
- [41] G. M. Farinola and R. Ragni, *Chem. Soc. Rev.* **2011**, *40*, 3467–3482.
- [42] a) T. H. El-Assaad, M. Auer, R. Castañeda, K. M. Hallal, F. M. Jradi, L. Mosca, R. S. Khnayzer, D. Patra, T. V. Timofeeva, J.-L. Brédas, E. J. W. List-Kratochvil, B. Wex and B. R. Kaafarani, *J. Mater. Chem. C* **2016**, *4*, 3041–3058; b) W. Qin, Z. Yang, Y. Jiang, J. W. Y. Lam, G. Liang, H. S. Kwok and B. Z. Tang, *Chem. Mater.* **2015**, *27*, 3892–3901; c) C. He, H. Guo, Q. Peng, S. Dong and F. Li, *J. Mater. Chem. C* **2015**, *3*, 9942–9947; d) X. Zhan, N. Sun, Z. Wu, J. Tu, L. Yuan, X. Tang, Y. Xie, Q. Peng, Y. Dong, Q. Li, D. Ma and

- Z. Li, *Chem. Mater.* **2015**, *27*, 1847–1854; e) C. Liu, Q. Fu, Y. Zou, C. Yang, D. Ma and J. Qin, *Chem. Mater.* **2014**, *26*, 3074–3083.
- [43] M. Zhu and C. Yang, *Chem. Soc. Rev.* **2013**, *42*, 4963–4976.
- [44] X. Yang, X. Xu and G. Zhou, *J. Mater. Chem. C* **2015**, *3*, 913–944.
- [45] P. Stroehriegl and J. V. Grazulevicius, *Adv. Mater.* **2002**, *14*, 1439–1452.
- [46] P.-I. Shih, C.-Y. Chuang, C.-H. Chien, E. W.-G. Diao and C.-F. Shu, *Adv. Funct. Mater.* **2007**, *17*, 3141–3146.
- [47] <https://www.basf.com/es/es/we-create-chemistry/creating-chemistry-magazine/quality-of-life/the-reinvention-of-light.html> (date: March 22, 2017).
- [48] J.-F. Morin, M. Leclerc, D. Adès and A. Siove, *Macromol. Rapid. Commun.* **2005**, *26*, 761–778.
- [49] a) A. Bucinskas, D. Volyniuk, Y. Danyliv, J. V. Grazulevicius, G. Baryshnikov, B. Minaev, K. Ivaniuk, V. Cherpak and P. Stakhira, *RSC Adv.* **2015**, *5*, 78150–78159; b) M. Y. Wong, G. J. Hedley, G. Xie, L. S. Kölln, I. D. W. Samuel, A. Pertegás, H. J. Bolink and E. Zysman-Colman, *Chem. Mater.* **2015**, *27*, 6535–6542.
- [50] a) R. Singh, J. S. Meena, C.-S. Wu and F.-H. Ko, *Phys. Chem. Chem. Phys.* **2015**, *17*, 5227–5235; b) S. Chen, B. Sun, W. Hong, Z. Yan, H. Aziz, Y. Meng, J. Hollinger, D. S. Seferos and Y. Li, *J. Mater. Chem. C* **2014**, *2*, 1683–1690; c) P.-L. T. Boudreault, S. Wakim, M. L. Tang, Y. Tao, Z. Bao and M. Leclerc, *J. Mater. Chem.* **2009**, *19*, 2921–2928.
- [51] a) D. Gudeika, J. V. Grazulevicius, D. Volyniuk, G. Juska, V. Jankauskas and G. Sini, *J. Phys. Chem. C* **2015**, *119*, 28335–28346. b) S.-I. Kato, H. Noguchi, A. Kobayashi, T. Yoshihara, S. Tobita and Y. Nakamura, *J. Org. Chem.* **2012**, *77*, 9120–9133.
- [52] S. Castellanos, V. Gaidelis, V. Jankauskas, J. V. Grazulevicius, E. Brillas, F. López-Calahorra, L. Juliá and D. Velasco, *Chem. Commun.* **2010**, *46*, 5130–5132.
- [53] Y. Leng, *Materials Characterization: Introduction to Microscopic and Spectroscopic Methods*, Wiley-VCH, Weinheim, Germany, **2013**.
- [54] B. Valeur, *Molecular Fluorescence: Principles and Applications*, Wiley-VCH, **2001**.
- [55] Z. R. Grabowski, K. Rotkiewicz and W. Rettig, *Chem. Rev.* **2003**, *103*, 3899–4031.
- [56] G. A. Crosby and J. N. Demas, *J. Phys. Chem.* **1971**, *75*, 991–1024.
- [57] Y. Tao, K. Yuan, T. Chen, P. Xu, H. Li, R. Chen, C. Zheng, L. Zhang and W. Huang, *Adv. Mater.* **2014**, *26*, 7931–7958.
- [58] C. M. Cardona, W. Li, A. E. Kaifer, D. Stockdale and G. C. Bazan, *Adv. Mater.* **2011**, *23*, 2367–2371.
- [59] P. Bujak, I. Kulszewicz-Bajer, M. Zagorska, V. Maurel, I. Wielgus and A. Pron, *Chem. Soc. Rev.* **2013**, *42*, 8895–8999.
- [60] A. J. Bard and L. R. Faulkner, *Electrochemical Methods: Fundamentals and Applications*, WILEY-VCH, New York, **2001**.
- [61] a) S. Braun, W. R. Salaneck and M. Fahlman, *Adv. Mater.* **2009**, *21*, 1450–1472; b) B. W. D’Andrade, S. Datta, S. R. Forrest, P. Djurovich, E. Polikarpov and M. E. Thompson, *Org. Electron.* **2005**, *6*, 11–20.

- [62] a) A. Kokil, K. Yang and J. Kumar, *J. Polym. Sci., Part B: Polym. Phys.* **2012**, *50*, 1130–1144; b) S. N. Tiwari and N. C. Greenham, *Opt. Quant. Electron.* **2009**, *41*, 69–89.
- [63] S. M. Vaezi-Nejad, *Int. J. Electronics* **1987**, *62*, 361–384.
- [64] Y. Wen, Y. Liu, Y. Guo, G. Yu and W. Hu, *Chem. Rev.* **2011**, *111*, 3358–3406.
- [65] X.-H. Zhu, J. Peng, Y. Cao and J. Roncali, *Chem. Soc. Rev.* **2011**, *40*, 3509–3524.
- [66] B. Minaev, G. Baryshnikov and H. Agren, *Phys. Chem. Chem. Phys.* **2014**, *16*, 1719–1758.
- [67] a) K. S. Yook and J. Y. Lee, *Adv. Mater.* **2014**, *26*, 4218–4233; b) H. Sasabe and J. Kido, *Eur. J. Org. Chem.* **2013**, 7653–7663.
- [68] M. Y. Wong and E. Zysman-Colman, *Adv. Mater.* **2017**, 1605444/1–54.
- [69] M. J. Sung, H. Chubachi, R. Sato, M.-K. Shin, S.-K. Kwon, Y.-J. Pu and Y.-H. Kim, *J. Mater. Chem. C* **2017**, *5*, 1090–1094.
- [70] Y. Wen, Y. Liu, Y. Guo, G. Yu and W. Hu, *Chem. Rev.* **2011**, *111*, 3358–3406.
- [71] P.-L. T. Boudreaault, S. Wakim, N. Blouin, M. Simard, C. Tessier, Y. Tao and M. Leclerc, *J. Am. Chem. Soc.* **2007**, *129*, 9125–9136.
- [72] N. Yoshimoto, H. Brisset, J. Ackermann and C. Videlot-Ackermann, *Open J. Appl. Sci.* **2012**, *2*, 283–293.
- [73] a) M. Yu, S. Wang, S. Shao, J. Ding, L. Wang, X. Jing and F. Wang, *J. Mater. Chem. C* **2015**, *3*, 861–869; b) V. Bhalla, G. Singh, M. Kumar, C. Singh, M. Rawat and R. S. Anand, *RSC Adv.* **2013**, *3*, 14722–14730; c) P. Kotchapradist, N. Prachumrak, R. Tarsang, S. Jungsuttiwong, T. Keawin, T. Sudyoosuk and V. Promarak, *J. Mater. Chem. C* **2013**, *1*, 4916–4924; d) S. H. Kim, I. Cho, M. K. Sim, S. Park and S. Y. Park, *J. Mater. Chem.* **2011**, *21*, 9139–9148.
- [74] S.-L. Lin, L.-H. Chan, R.-H. Lee, M.-Y. Yen, W.-J. Kuo, C.-T. Chen and R.-J. Jeng, *Adv. Mater.* **2008**, *20*, 3947–3952.
- [75] a) S.-I. Kato, S. Shimizu, A. Kobayashi, T. Yoshihara, S. Tobita and Y. Nakamura, *J. Org. Chem.* **2014**, *79*, 618–629; b) M.-D. Zhang, H.-X. Xie, X.-H. Ju, L. Qin, Q.-X. Yang, H.-G. Zheng and X.-F. Zhou, *Phys. Chem. Chem. Phys.* **2013**, *15*, 634–641; c) S.-I. Kato, S. Shimizu, H. Taguchi, A. Kobayashi, S. Tobita and Y. Nakamura, *J. Org. Chem.* **2012**, *77*, 3222–3232; d) E. Sezer, M. van Hooren, A. S. Saraç and M. L. Hallensleben, *J. Polym. Sci. Part A: Polym. Chem.* **1999**, *37*, 379–381; e) M. Park, J. R. Buck and C. J. Rizzo, *Tetrahedron* **1998**, *54*, 12707–12714.
- [76] a) S. Goswami, G. Wicks, A. Rebane and K. S. Schanze, *Dalton Trans.* **2014**, *43*, 17721–17728; b) V. Promarak and S. Ruchirawat, *Tetrahedron* **2007**, *63*, 1602–1609.
- [77] a) D. Kang, D. Eom, H. Kim and P. H. Lee, *Eur. J. Org. Chem.* **2010**, 2330–2336; b) M. L. Keshtov, N. M. Belomoina, A. S. Peregudov, A. L. Rusanov and A. R. Khokhlov, *Dokl. Chem.* **2007**, *412*, 14–17.
- [78] A. Hameurlaine, W. Dehaen, H. Peng, Z. Xie and B. Z. Tang, *J. Macromol. Sci., Pure Appl. Chem.* **2004**, *41*, 295–303.
- [79] K. Smith, D. M. James, A. G. Mistry, M. R. Bye and D. J. Faulkner, *Tetrahedron* **1992**, *48*, 7479–7488.
- [80] S. H. Tucker, *J. Chem. Soc.* **1926**, *129*, 546–553.
- [81] D. Kim, J. K. Lee, S. O. Kang and J. Ko, *Tetrahedron* **2007**, *63*, 1913–1922.

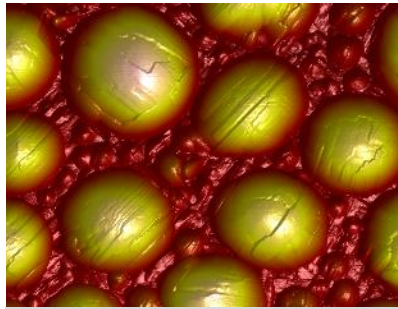
- [82] a) M. Ouyang, P. Wang, W. Yu, S. Huang, J. Sun, B. Hu, X. Lv, Z. Fu and C. Zhang, *J. Electrochem. Soc.* **2014**, *161*, H337–H342; b) N. Berton, I. Fabre-Francke, D. Bourrat, F. Chandezon and S. Sadki, *J. Phys. Chem. B* **2009**, *113*, 14087–14093.
- [83] R. Chinchilla and C. Nájera, *Chem. Rev.* **2007**, *107*, 874–922.
- [84] a) E. K. Galván-Miranda, H. M. Castro-Cruz, J. A. Arias-Orea, M. Iurlo, G. Valenti, M. Marcaccio and N. A. Macías-Ruvalcaba, *Phys. Chem. Chem. Phys.* **2016**, *18*, 15025–15038; b) R. A. Al-Balushi, A. Haque, M. Jayapal, M. K. Al-Suti, J. Husband, M. S. Khan, O. F. Koentjoro, K. C. Molloy, J. M. Skelton and P. R. Raithby, *Inorg. Chem.* **2016**, *55*, 6465–6480; c) Shanmugaraju, A. K. Bar, K.-W. Chi and P. S. Mukherjee, *Organometallics* **2010**, *29*, 2971–2980.
- [85] Z. Ruan, C. Y. K. Chan, J. W. Y. Lam, Q. Wu, Q. Li, J. Qin, B. Zhong and Z. Li, *J. Mater. Chem. C* **2014**, *2*, 633–640.
- [86] P. Wang, Y. Ju, S. Y. Tang, J. Y. Wu and H. P. Zhou, *Acta Crystallogr. Sect. E: Struct. Rep. Online* **2007**, *63*, 3671.
- [87] a) F. Niu, H. Niu, Y. Liu, J. Lian and P. Zeng, *RSC Adv.* **2011**, *1*, 415–423; b) J. N. Moorthy, P. Natarajan, P. Venkatakrishnan, D.-F. Huang and T. J. Chow, *Org. Lett.* **2007**, *9*, 5215–5218.
- [88] S. Shanmugaraju, V. Vajpayee, S. Lee, K.-W. Chi, P. J. Stang, P. S. Mukherjee, *Inorg. Chem.* **2012**, *51*, 4817–4823.
- [89] a) N. A. Kukhta, D. Volyniuk, L. Peculyte, J. Ostrauskaite, G. Juska and J. V. Grazulevicius, *Dyes Pigm.* **2015**, *117*, 122–132; b) R. R. Reghu, H. K. Bisoyi, J. V. Grazulevicius, P. Anjukandi, V. Gaidelis and V. Jankauskas, *J. Mater. Chem.* **2011**, *21*, 7811–7819.
- [90] H. Zhang, Q. Fu, W. Zeng and D. Ma, *J. Mater. Chem. C* **2014**, *2*, 9620–9624.
- [91] D. Y. Kondakov, T. D. Pawlik, T. K. Hatwar and J. P. Spindler, *J. Appl. Phys.* **2009**, *106*, 124510/1–7.
- [92] M. Segal, M. Singh, K. Rivoire, S. Difley, T. Van Voorhis and M. A. Baldo, *Nat. Mater.* **2007**, *6*, 374–378.
- [93] A. Bucinskas, G. Bagdziunas, A. Tomkeviciene, D. Volyniuk, N. Kostiv, D. Gudeika, V. Jankauskas, M. Rutkis and J. V. Grazulevicius, *RSC Adv.* **2015**, *5*, 49577–49589.
- [94] a) A. Tomkeviciene, T. Bartiuk, A. Bucinskas, J. V. Grazulevicius and V. Jankauskas, *React. Funct. Polym.* **2011**, *71*, 796–802; b) V. Vaitkeviciene, S. Grigalevicius, J. V. Grazulevicius, V. Jankauskas and V. G. Syromyatnikov, *Eur. Polym. J.* **2006**, *42*, 2254–2260.
- [95] A. Tomkeviciene, J. V. Grazulevicius, K. Kazlauskas, A. Gruodis, S. Jursenas, T.-H. Ke and C.-C. Wu, *J. Phys. Chem. C* **2011**, *115*, 4887–4897.
- [96] Q. Zhang, W. Zhu, M. Fang, F. Yin and C. Li, *Spectrochim. Acta, Part A* **2015**, *135*, 379–385.
- [97] H. Wang, G. Chen, X. Xu, H. Chen and S. Ji, *Dyes Pigm.* **2010**, *86*, 238–248.
- [98] Y. Tao, C. Yang and J. Qin, *Chem. Soc. Rev.* **2011**, *40*, 2943–2970.
- [99] a) D. Sipaviciute, D. Tavgeniene, G. Krucaite, D. Volyniuk, J. V. Grazulevicius, B. Yao, Z. Xie, B. Zhang and S. Grigalevicius, *Dyes Pigm.* **2017**, *137*, 208–213; b) C. Peng, S. Liu, X. Fu, Z. Pan, Y. Chen, F. So and K. S. Schanze, *ACS Appl. Mater. Interfaces* **2016**, *8*, 16192–16199.
- [100] I. Ratera and J. Veciana, *Chem. Soc. Rev.* **2012**, *41*, 303–349.

- [101] E. P. Tomlinson, M. E. Hay and B. W. Boudouris, *Macromolecules* **2014**, *47*, 6145–6158.
- [102] T. Kurata, K. Koshika, F. Kato, J. Kido and H. Nishide, *Chem. Commun.* **2007**, 2986–2988.
- [103] N. Crivillers, M. Paradinas, M. Mas-Torrent, S. T. Bromley, C. Rovira, C. Ocal and J. Veciana, *Chem. Commun.* **2011**, *47*, 4664–4666.
- [104] O. Armet, J. Veciana, C. Rovira, J. Riera, J. Castañer, E. Molins, J. Rius, C. Miravittles, S. Olivella and J. Brichfeus, *J. Phys. Chem.* **1987**, *91*, 5608–5616.
- [105] A. Jiménez, A. Selga, J. L. Torres and L. Juliá, *Org. Lett.* **2004**, *6*, 4583–4586.
- [106] L. Fajará, R. Papoular, M. Reig, E. Brillas, J. L. Jorda, O. Vallcorba, J. Rius, D. Velasco and L. Juliá, *J. Org. Chem.* **2014**, *79*, 1771–1777.
- [107] S. Castellanos, D. Velasco, F. López-Calahorra, E. Brillas and L. Juliá, *J. Org. Chem.* **2008**, *73*, 3759–3767.
- [108] D. Velasco, S. Castellanos, M. López, F. López-Calahorra, E. Brillas and L. Juliá, *J. Org. Chem.* **2007**, *72*, 7523–7532.
- [109] V. Gamero, D. Velasco, S. Latorre, F. López-Calahorra, E. Brillas and L. Juliá, *Tetrahedron Lett.* **2006**, *47*, 2305–2309.
- [110] a) K. Aoki, H. Akutsu, J.-I. Yamada, S. Nakatsuji, T. Kojima and Y. Yamashita, *Chem. Lett.* **2009**, *38*, 112–113; b) Y. Wang, H. Wang, Y. Liu, C.-A. Di, Y. Sun, W. Wu, G. Yu, D. Zhang and D. Zhu, *J. Am. Chem. Soc.* **2006**, *128*, 13058–13059.
- [111] M. Ballester, J. Riera, J. Castañer, C. Rovira and O. Armet, *Synthesis*, **1986**, 64.
- [112] The spectrum was simulated following the WINSIM by Dulong, D. *Public EPR Software Tools*, National Institute of Environmental Health Sciences, Bethesda, MD, **1996**.
- [113] a) Y. Wang and D. Liang, *Adv. Mater.* **2010**, *22*, 1521–1525; b) T. Malinauskas, M. Daskeviciene, G. Bubniene, I. Petrikyte, S. Raisys, K. Kazlauskas, V. Gaidelis, V. Jankauskas, R. Maldzius, S. Jursenas and V. Getautis, *Chem. Eur. J.* **2013**, *19*, 15044–15056.
- [114] a) S. Banerjee, F. Ali, P. K. Nayak and N. Agarwal, *Thin Solid Films* **2012**, *520*, 2644–2650; b) J. L. Díaz, A. Dobarro, B. Villacampa and D. Velasco, *Chem. Mater.* **2001**, *13*, 2528–2536.
- [115] a) A. Wojciechowski, M. M. M. Raposo, M. C. R. Castro, W. Kuznik, I. Fuks-Janczarek, M. Pokladko-Kowar and F. Bures, *J. Mater. Sci.: Mater. Electron.* **2014**, *25*, 1745–1750; b) S. Rodríguez González, J. Orduna, R. Alicante, B. Villacampa, K. A. McGee, J. Pina, J. Seixas de Melo, K. M. Schwaderer, J. C. Johnson, B. A. Blackorbay, J. J. Hansmeier, V. F. Bolton, T. J. Helland, B. A. Edlund, T. M. Pappenfus, J. T. López Navarrete and J. Casado, *J. Phys. Chem. B* **2011**, *115*, 10573–10585.
- [116] a) Y. A. Getmanenko, T. A. Purcell, D. K. Hwang, B. Kippelen and S. R. Marder, *J. Org. Chem.* **2012**, *77*, 10931–10937; b) X. Cai, M. W. Burand, C. R. Newman, D. A. da Silva Filho, T. M. Pappenfus, M. M. Bader, J.-L. Bredas, K. R. Mann and C. D. Frisbie, *J. Phys. Chem. B* **2006**, *110*, 14590–14597.
- [117] a) E. C.-H. Kwok, D. P.-K. Tsang, M.-Y. Chan and V. W.-W. Yam, *Chem. - Eur. J.* **2013**, *19*, 2757–2767; b) P. Qin, J. Wiberg, E. A. Gibson, M. Linder, L. Li, T. Brinck, A. Hagfeldt, B. Albinsson and L. Sun, *J. Phys. Chem. C* **2010**, *114*, 4738–4748.

- [118] a) D.-Y. Goo and S. K. Woo, *Org. Biomol. Chem.* **2016**, *14*, 122–130; b) V. Arun, P. O. V. Reddy, M. Pilania and D. Kumar, *Eur. J. Org. Chem.* **2016**, 2096–2100; c) J. H. Smitrovich and I. W. Davies, *Org. Lett.* **2004**, *6*, 533–535.
- [119] G. Bubniene, T. Malinauskas, M. Daskeviciene, V. Jankauskas and V. Getautis, *Tetrahedron*, **2010**, *66*, 3199.
- [120] H. Bässler, *Phys. Status Solidi B*, **1993**, *175*, 15–56.
- [121] a) V. I. Arkhipov, I. I. Fishchuk, A. Kadashchuk and H. Bässler, in *Photophysics of Molecular Materials*, ed. G. Lanzani, Wiley-VCH Verlag GmbH & Co. KGaA, Weinheim, **2006**, ch. 6, pp. 350–356; b) V. Mimaite, J. V. Grazulevicius, R. Laurinaviciute, D. Volyniuk, V. Jankauskas and G. Sini, *J. Mater. Chem. C* **2015**, *3*, 11660–11674.
- [122] V. Vaissier, J. M. Frost, P. R. F. Barnes and J. Nelson, *J. Phys. Chem. C* **2015**, *119*, 24337–24341.
- [123] E. G. Popova, L. A. Chetkina, B. V. Kotov, *Zhurnal Strukturnoi Khimii* **1981**, *22*, 116.
- [124] S. Fratini, D. Mayou and S. Ciuchi, *Adv. Funct. Mater.* **2016**, *26*, 2292–2315.
- [125] R. A. Marcus, *Angew. Chem., Int. Ed. Engl.* **1993**, *32*, 1111–1121.
- [126] J. E. Kuder, W. W. Limburg, J. M. Pochan and D. Wychick, *J. Chem. Soc., Perkin Trans. 2* **1977**, 1643–1651.
- [127] G. Li, X. Zhou, P. Yang, Y. Jian, T. Deng, H. Shen and Y. Bao, *Tetrahedron Lett.* **2014**, *55*, 7054–7059.
- [128] Y. Zou, M. Wan, G. Sang, M. Ye and Y. Li, *Adv. Funct. Mater.* **2008**, *18*, 2724–2732.
- [129] L. Schweighauser and H. A. Wegner, *Chem. Commun.* **2013**, *49*, 4397–4399.
- [130] a) I. Petrikyte, I. Zimmermann, K. Rakstys, M. Daskeviciene, T. Malinauskas, V. Jankauskas, V. Getautis and M. K. Nazeeruddin, *Nanoscale* **2016**, *8*, 8530–8535; b) X. Qian, L. Shao, H. Li, R. Yan, X. Wang and L. Hou, *J. Power Sources* **2016**, *319*, 39–47.
- [131] H. Zhao, L. Jiang, H. Dong, H. Li, W. Hu and B. S. Ong, *ChemPhysChem* **2009**, *10*, 2345–2348.
- [132] I. Bulut, P. Chávez, A. Mirloup, Q. Huault, A. Hébraud, B. Heinrich, S. Fall, S. Méry, R. Ziessel, T. Heiser, P. Lèveque and N. Leclerc, *J. Mater. Chem. C* **2016**, *4*, 4296–4303.
- [133] a) X. Qian, L. Lu, Y.-Z. Zhu, H.-H. Gao and J.-Y. Zheng, *Dyes Pigm.* **2015**, *113*, 737–742; b) X. Qian, Y.-Z. Zhu, J. Song, X.-P. Gao and J.-Y. Zheng, *Org. Lett.* **2013**, *15*, 6034–6037.
- [134] W.-Y. Lai, Q.-Y. He, R. Zhu, Q.-Q. Chen and W. Huang, *Adv. Funct. Mater.* **2008**, *18*, 265–276.
- [135] S. W. Shelton, T. L. Chen, D. E. Barclay and B. Ma, *Appl. Mater. Interfaces* **2012**, *4*, 2534–2540.
- [136] a) P.-Y. Su, L.-B. Huang, J.-M. Liu, Y.-F. Chen, L.-M. Xiao, D.-B. Kuang, M. Mayor and C.-Y. Su, *J. Mater. Chem. A*, **2017**, *5*, 1913–1918; b) F. J. Ramos, K. Rakstys, S. Kazim, M. Grätzel, M. K. Nazeeruddin and S. Ahmad, *RSC Adv.* **2015**, *5*, 53426–53432.
- [137] D. H. Huh, G. W. Kim, G. H. Kim, C. Kulshreshtha and J. H. Kwon, *Synth. Met.* **2013**, *180*, 79–84.
- [138] a) C. Ruiz, U. K. Pandey, R. Termine, E. M. García-Frutos, G. López-Espejo, R. Ponce Ortiz, W. Huang, T. J. Marks, A. Facchetti, M. C. Ruiz Delgado, A. Golemne and B. Gómez-Lor, *ACS Appl. Mater. Interfaces* **2016**, *8*, 26964–26971; b) E. M. García-Frutos, U. K. Pandey, R. Termine, A. Omenat, J. Barberá, J. L. Serrano, A. Golemne and B. Gómez-Lor, *Angew. Chem. Int. Ed.* **2011**, *50*, 7399–7402.

- [139] a) T. Tokuda, K. Murashiro, M. Kubo, H. Masu, M. Imanari, H. Seki, N. Aoki, Y. Ochiai, H. Kanoh and K. Hoshino, *Langmuir* **2012**, *28*, 16430–16435; b) V. Vaitkeviciene, S. Grigalevicius, J. V. Grazulevicius, V. Jankauskas and V. G. Syromyatnikov, *Eur. Polym. J.* **2006**, *42*, 2254–2260.
- [140] a) H. Shi, J. Yuan, X. Wu, X. Dong, L. Fang, Y. Miao, H. Wang and F. Cheng, *New. J. Chem.* **2014**, *38*, 2368–2378; b) B. Robinson, *J. Chem. Soc.* **1963**, 3097–3099.
- [141] a) M. Franceschin, L. Ginnari-Satriani, A. Alvino, G. Ortaggi and A. Bianco, *Eur. J. Org. Chem.* **2010**, 134–141; b) L. Ji, Q. Fang, M.-S. Yuan, Z.-Q. Liu, Y.-X. Shen and H.-F. Chen, *Org. Lett.* **2010**, *12*, 5192–5195.
- [142] E. M. García-Frutos, E. Gutierrez-Puebla, M. A. Monge, R. Ramírez, P. de Andrés, A. de Andrés, R. Ramírez and B. Gómez-Lor, *Org. Electron.* **2009**, *10*, 643–652.
- [143] G. Zhao, H. Dong, H. Zhao, L. Jiang, X. Zhang, J. Tan, Q. Meng and W. Hu, *J. Mater. Chem.* **2012**, *22*, 4409–4417.
- [144] S. Wakim, J. Bouchard, M. Simard, N. Drolet, Y. Tao and M. Leclerc, *Chem. Mater.* **2004**, *16*, 4386–4388.
- [145] F. Gallego-Gómez, E. M. García-Frutos, J. M. Villalvilla, J. A. Quintana, E. Gutierrez-Puebla, A. Monge, M. A. Díaz-García and B. Gómez-Lor, *Adv. Funct. Mater.* **2011**, *21*, 738–745.
- [146] <http://www.plasticsgl/consumer/lighter-than-a-feather/> (date: April 29, 2017).
- [147] J. Stampfl, S. Tasch, G. Leising and U. Scherf, *Synth. Met.* **1995**, *71*, 2125–2128.
- [148] G. M. Sheldrick, *Acta Crystallogr.* **2008**, *A64*, 112–122.
- [149] Spartan'14 for Windows Version 1.1.2. 1840 Von Karman Avenue, Suite 370, Irvine, CA.
- [150] S. F. Boys and F. Bernardi, *Mol. Phys.* **1970**, *19*, 553–566.
- [151] A. C. Chamberlin, C. J. Cramer and D. G. Truhlar, *J. Phys. Chem. B* **2008**, *112*, 8651–8655.
- [152] F. Biedermann and H.-J. Schneider, *Chem. Rev.* **2016**, *116*, 5216–5300.
- [153] J. Jortner, *J. Chem. Phys.* **1976**, *64*, 4860–4867.
- [154] A. Pivrikas, M. Ullah, H. Sitter and N. S. Sariciftci, *Appl. Phys. Lett.* **2011**, *98*, 092114/1–3.
- [155] G. Bagdziunas, G. Grybauskaite, N. Kostiv, K. Ivaniuk, D. Volyniuk and A. Lazauskas, *RSC Adv.* **2016**, *6*, 61544–61554.
- [156] A. Natan, N. Kuritz and L. Kronik, *Adv. Funct. Mater.* **2010**, *20*, 2077–2084.
- [157] H. M. Heitzer, T. J. Marks and M. A. Ratner, *J. Am. Chem. Soc.* **2015**, *137*, 7189–7196.
- [158] W. Volksen, R. D. Miller and G. Dubois, *Chem. Rev.* **2010**, *110*, 56–110.
- [159] M. Schwarze, W. Tress, B. Beyer, F. Gao, R. Scholz, C. Poelking, K. Ortstein, A. A. Günther, D. Kasemann, D. Andrienko and K. Leo, *Science* **2016**, *352*, 1446–1449.
- [160] N. Ueno, *Science* **2016**, *352*, 1395–1396.
- [161] S. M. Ryno, C. Risko and J.-L. Brédas, *ACS Appl. Mater. Interfaces* **2016**, *8*, 14053–14062.
- [162] D. P. McMahon and A. Troisi, *J. Phys. Chem. Lett.* **2010**, *1*, 941–946.
- [163] M. Malagoli and J. L. Brédas, *Chem. Phys. Lett.* **2000**, *327*, 13–17.
- [164] Z. Shuai, H. Geng, W. Xu, Y. Liao and J.-M. André, *Chem. Soc. Rev.* **2014**, *43*, 2662–2679.
- [165] Y. Olivier, V. Lemaure, J. L. Brédas and J. Cornil, *J. Phys. Chem. A* **2006**, *110*, 6356–6364.

- [166] a) J. Kalade, E. Montrimas, R. Maldzius and Z. Tokarski, *J. Imaging Sci. Technol.* **2005**, *49*, 28–34; b) M. Daskeviciene, V. Getautis, J. V. Grazulevicius, A. Stanisauskaite, J. Antulis, V. Gaidelis, V. Jankauskas and J. Sidaravicius, *J. Imaging Sci. Technol.* **2002**, *46*, 467–472.
- [167] H. Zhang, Q. Fu, W. Zeng and D. Ma, *J. Mater. Chem. C* **2014**, *2*, 9620–9624.
- [168] a) V. Cherpak, P. Stakhira, B. Minaev, G. Baryshnikov, E. Stromylo, I. Helzhynskyy, M. Chapran, D. Volyniuk, D. Tomkute-Luksiene, T. Malinauskas, V. Getautis, A. Tomkeviciene, J. Simokaitiene and J. V. Grazulevicius, *J. Phys. Chem. C* **2014**, *118*, 11271–11278; b) N. C. Greenham, R. H. Friend and D. D. C. Bradley, *Adv. Mater.* **1994**, *6*, 491–494.
- [169] a) A. Ghalgaoui, R. Shimizu, S. Hosseinpour, R. Álvarez-Asencio, C. McKee, C. M. Johnson and M. W. Rutland, *Langmuir* **2014**, *30*, 3075–3085; b) D. Song, H. Wang, F. Zhu, J. Yang, H. Tian, Y. Geng and D. Yan, *Adv. Mater.* **2008**, *20*, 2142–2144.



EXPERIMENTAL PART

EXPERIMENTAL PART

The fabrication and measurement of OTFTs have been carried out in the clean room facilities of the *Departament d'Enginyeria Electrònica* from the *Universitat Politècnica de Catalunya*. OLEDs have been fabricated and measured using the facilities of the Department of Polymer Chemistry and Technology at Kaunas University of Technology in Lithuania, at the Technological Center of Catalonia Eurecat and at the Institute of Chemical Research of Catalonia (ICIQ). TOF measurements have been performed at the Department of Polymer Chemistry and Technology from Kaunas University of Technology in Lithuania. The XTOF measurements have been carried out in the laboratories of the Department of Solid State Electronics from Vilnius University in Lithuania. Theoretical calculations have been performed by Dr. Gintautas Bagdziunas from Kaunas University of Technology in Lithuania.

1. Materials, solvents and reagents

All chemicals were of commercial grade and used as received. All solvents were dried and degassed by standard methods. Tetrahydrofuran was distilled from sodium/benzophenone and dichloromethane was distilled from CaH_2 . Anhydrous commercially available DMF was stored over activated 4 Å molecular sieves under nitrogen atmosphere. Reactions were monitored by thin layer chromatography (TLC) using aluminium sheets coated with silica gel 60 F₂₅₄ (Merck). Visualization of TLC plates was achieved using ultraviolet light. Flash column chromatography was performed over silica gel (grade 62, 60–200 mesh, 150 Å, Aldrich or SDS, 230–240 mesh).

2. Instrumentation and methods

NMR spectroscopy. ^1H NMR and ^{13}C NMR spectra were collected on a Varian Inova 300 MHz, a Varian Mercury 400 MHz or a Bruker 400 MHz Avance III instrument. NMR spectra have been processed with the MestReNova software. Solvent peaks were used as internal references. Signals were reported as singlet (s), doublet (d), doublet of doublet (dd) triplet (t), quadruplet (q) and multiplet (m).

Mass spectrometry. MALDI-TOF was performed on an Applied Biosystems MDS SCIEX 4800 equipment in the Reflector mode. Chemical ionization mass spectrometry (CI-MS) was carried out on a HEWLETT-PACKARD HP-5988A instrument. High resolution mass spectrometry (HRMS) was performed on a LC/MSD-TOF Agilent Technologies instrument by the electrospray (ESI-MS) technique.

UV-Vis spectroscopy. UV-Vis spectra were registered using a Varian Cary UV-Vis-NIR 500E or a 50Bio spectrophotometer.

Fourier transform infrared spectroscopy (FT-IR). ATR FT-IR spectroscopy was performed on a FT-IR Nicolet 6700 instrument. Peaks intensity is expressed as strong (s), medium (m) and weak (w).

Electron paramagnetic resonance (EPR). X-band EPR spectra were recorded in dichloromethane solution at room temperature and at 180 K with a Bruker EMX-Plus 10/12 spectrometer.

Thermogravimetric analyses (TGA). TGA were performed using a TA Instruments Q50 or a Mettler Toledo TGA/SDTA 851e instrument under nitrogen atmosphere at a heating rate of 10 °C min⁻¹ or 20 °C min⁻¹ as indicated.

Differential scanning calorimetry (DSC). DSC analyses were performed on a TA Instruments Q2000 calorimeter or a Mettler Toledo DSC-822e at a scan rate of 10 °C min⁻¹ under nitrogen atmosphere.

Fluorescence spectroscopy. Emission spectra were recorded with either an Edinburgh Instruments FLS980 spectrophotometer at room temperature or a PTI fluorimeter equipped with a 220B lamp power supply, a 815 photomultiplier detection system and a Felix 32 software. Relative quantum yield measurements (Φ_f) in solution were determined using optically-matched solutions of a standard following a literature protocol.^[56] The following two compounds were used as standards:

- 1,4-Bis(5-phenyl-2-oxazolyl)benzene dissolved in cyclohexane. The fluorescence quantum yield is 0.93 after excitation at 300 nm.
- Tris(2,2'-bipyridyl)ruthenium(II) chloride dissolved in water. The fluorescence quantum yield is 0.042 after excitation at 450 nm.

Quantum yield measurements in the solid state were determined either by using the above mentioned method^[147] or by means of an integrating sphere.

Cyclic voltammetry (CV). Cyclic voltammograms were carried out in a microcomputer-controlled potentiostat/galvanostat Autolab with PGSTAT30 equipment and GPES software. All voltammetric curves were recorded under quiescent conditions, at a scan rate of 100 mV s⁻¹ (unless otherwise indicated) and under argon atmosphere. A cylindrical three-electrode cell was used. Two different methods have been employed to carry out the cyclic voltammograms:

- **Method A:** The reference electrode was a Metrohm Ag/AgCl/KCl (3M) mounted in a Luggin capillary containing a 0.1 M solution of tetrabutylammonium perchlorate (TBAP) in dichloromethane. The counter and working electrodes were a platinum spiral and a platinum wire, respectively. All solutions were prepared in dichloromethane (1 mM). TBAP (Aldrich, electrochemical grade) was used as the supporting electrolyte. $E^0(\text{Fc}^+/\text{Fc})$ was estimated as $E^0(\text{Fc}^+/\text{Fc}) = +0.43$ V vs. Ag/AgCl/KCl (3M). The CV of compounds **23, 24, 43, 58** and **59** have been recorded using this method.
- **Method B:** The reference electrode was a Ag/Ag⁺ electrode (0.01 M AgNO₃ in acetonitrile). The counter and working electrodes were a platinum wire and a glassy-carbon electrode, respectively. Solutions were prepared in acetonitrile or dichloromethane (1 mM). Tetrabutylammonium hexafluorophosphate (TBAPF₆) (0.1 M) was used as the supporting electrolyte. $E^0(\text{Fc}^+/\text{Fc})$ was determined experimentally before recording the cyclic voltammograms of the samples. The CV of compounds **1–9, 29, Cbz-TTM, 33–36, 37–40, 45–48, 54, 60–62** and **65** have been recorded using this method.

The ionization potential (IP) and electron affinity values (EA) were estimated from the onset potential of the first oxidation and reduction peaks, respectively, as $\text{IP} = E_{\text{onset vs Fc}^+/\text{Fc}}^{\text{ox}} + 5.39$ and $\text{EA} = E_{\text{onset vs Fc}^+/\text{Fc}}^{\text{red}} + 5.39$; or from the oxidation and reduction standard potentials as $\text{IP} = E_{\text{ox vs Fc}^+/\text{Fc}}^0 + 5.39$ and $\text{EA} = E_{\text{red vs Fc}^+/\text{Fc}}^0 + 5.39$, respectively, where 5.39 eV corresponds to the formal potential of the Fc⁺/Fc redox couple in the Fermi scale.^[58,60]

Photoelectron emission method in air. Ionization potentials (IP) in the solid state were measured by the photoelectron emission method in air. Thin films for IP measurements were prepared by vacuum thermal evaporation of the organic compounds with a base pressure below 10⁻⁶ mbar on fluorine doped tin oxide coated glass slides. A negative voltage of 300 V was applied to the sample substrate. A deep UV deuterium light source ASBN-D130-CM and CM110 1/8m monochromator was used for illumination of the samples with monochromatic light. A 6517B Keithley electrometer was connected to the counter electrode for the photocurrent measurement, which was flowing in

the circuit under illumination. An energy scan of the incident photons was performed while increasing the photon energy. For measuring the IP of radicals **33–36**, the monochromator and sample camera were filled with nitrogen to reduce the light absorption at the shortwave spectrum region.

Profilometry. Thickness of thin films was determined using a Veeco DEKTAK 150 profilometer.

X-Ray diffraction of monocrystalline materials. Single-crystal analysis of the organic materials was performed on a D8 Venture system equipped with a multilayer monochromator and a Mo Microfocus ($\lambda = 0.71073 \text{ \AA}$) or Cu ($\lambda = 1.54178 \text{ \AA}$). The frames were integrated with the Bruker SAINT software package using a narrow-frame algorithm. The structures were solved and refined using the Bruker SHELXTL Software Package and some of them refined using SHELXL.^[148]

Powder X-Ray diffraction. Powder X-ray diffraction (XRD) measurements were obtained by using a PANalytical X'Pert PRO MPD θ/θ powder diffractometer of 240 millimetres of radius, in a configuration of convergent beam with a focalizing mirror and transmission geometry with a spinner glass capillary sample holder, a PIXcel detector, with Cu K α radiation ($\lambda = 1.5418 \text{ \AA}$) and work power at 45 kV and 40 mA. Samples were prepared by introduction of the powder materials in *Lindemann* glass capillaries of 0.5 or 0.7 millimetres of diameter.

X-Ray diffraction (XRD) of thin films. XRD measurements of thin films were performed using a Bruker D8 Advance diffractometer (geometry: Bragg-Brentano, theta-2theta) with one-dimensional LynxEye Detector, using monochromatic beam Cu K α 1 ($\lambda = 1.5406 \text{ \AA}$) and running conditions at 40 KV and 40 mA.

Grazing Incidence X-Ray Diffraction (GIXRD) of thin films. GIXRD measurements of the thin films of the organic materials were performed in a PANalytical X'Pert PRO MRD diffractometer with a PIXcel detector, a parabolic Göbel mirror at the incident beam and a parallel plate collimator at the diffracted beam, with Cu K α radiation ($\lambda = 1.5418 \text{ \AA}$) and work power at 45 kV and 40 mA. The angle of incidence used was $\omega \sim 0.2^\circ$.

Atomic force microscopy (AFM). AFM measurements were conducted using an AFM Dimension 3100 system attached to a Nanoscope IVa electronics unit (Bruker). AFM measurements in the tapping mode were performed on an AFM Multimode 8 system attached to a Nanoscope V electronic unit (Bruker).

2.1. Computational methods

2.1.1. Details of theoretical calculations for compounds 1–4, 6 and 8 (Chapter 1)

The geometry optimizations and single point energy calculations using density functional theory (DFT) employed the Spartan'14 software.^[149] The no symmetry constraints were employed for calculations and a default fine grid was used for all calculations. DFT calculations were performed in vacuum and at 298 K. The geometries of the compounds **1–4**, **6** and **8** were optimized by the hybrid B3LYP functional method and 6-31G(d,p) basis set. The rotation probability of the thienyl and phenyl moieties and single point energy of **1–3** was analysed via the theoretical potential energy scan experiment using the same level of theory, using rotation steps of 20°. The intermolecular interaction energies between molecules **3**, **6** and **7** in dimers were estimated using the basis set superposition effect (BSSE) concept^[150] and at wB97X-D functional with the London dispersion corrections and 6-311G(d) basis set. The dimers of molecules from X-ray analysis were generated. The six lowest excitation as the singlet-singlet and triplet-singlet electronic transitions and strengths were estimated using the ground state structure coordinates with unrestricted time-dependent density functional theory (TDDFT) B3LYP functional and 6-311G(d) basis set.

2.1.2. Details of theoretical calculations for compounds 37–40 (Chapter 3)

All structures were optimized and the molecular orbitals were generated by using the DFT semi-local hybrid functional B3LYP and 6-31+G(d) basis set with a diffuse function (+). The adiabatic IP and EA energies were estimated using the same functional and basis set and the Cramer-Truhlar quantum mechanical continuum solvation model (SM8)^[151] in dichloromethane ($\epsilon = 8.9$). The electrostatic potential map (EPM) at the same level of theory was calculated in order to understand the electron density and the strength of the bonding interactions present in the molecules. The rotation probability of the tricyanovinyl moiety and the single point energies of compounds **39** and **40** were analysed *via* the theoretical potential energy scan experiment using the same level of theory, where rotation steps of 20° were considered. The intermolecular interaction energies between molecules for compounds **39** and **40** were estimated using the basis set superposition effect (BSSE) concept and the wB97X-D functional with the London dispersion corrections and the 6-311G(d) basis set.^[152] The dimers of molecules determined from X-ray analysis were generated. For the intermolecular interactions visualization, the Mercury 3.7 program was used.

Nowadays, the Levich-Jortner theory for a hopping rate between the charged and neutral sites has been treated quantum mechanically. In this theory, the molecular vibrations are considered quantum mechanically using the Franck-Condon factors.^[153] However, most intramolecular vibrational frequencies are above the thermal energy at room temperature (*i.e.* $k_B T \approx 26$ meV). Therefore, this theory is only acceptable in the high-temperature limit if the thermal energy exceeds the vibrational energy. Thus, the simpler Marcus-type expression^[125] (eqn (1.1)) and the intermolecular component of reorganization energy (eqn (1.4)) can be employed and it was used to determine the rate of charge transfer between molecules:

$$k_i = \frac{2\pi}{\hbar} |H_i|^2 \frac{1}{\sqrt{4\pi\lambda k_B T}} \exp\left(-\frac{(\lambda + \Delta G^0)^2}{4\lambda k_B T} - \frac{eFd_i}{\epsilon k_B T}\right) \quad (1.1)$$

where k_i is the electron transfer rate constant for pathway i , H_i is the electronic coupling between the initial and final states, λ is the internal reorganization energy, ΔG^0 is the total Gibbs free energy of change for the charge transfer reaction, k_B is the Boltzmann constant and T is the absolute temperature (298 K). However, the influence of the electric field on the activation energy from Marcus theory (*i.e.* on $E_a = (\lambda + \Delta G^0)^2 / (4\lambda)$ but not on ΔG^0) was proposed. In support of this idea, Pivrikas *et al.*^[154] showed that the electric field has an impact on the activation energy of electron transport in fullerene diodes. This model showed a good agreement with the experimental data in a previous work.^[155] In this exponential component, e is the elementary charge (1.60×10^{-19} C), F is the applied external electric field, ϵ is the dielectric constant (permittivity) of the material and d_i is the distance for pathway i between neighbouring donor-donor (D–D) moieties for holes and acceptor-acceptor (A–A) moieties for electrons. The dielectric constants ϵ (permittivities) of **39** and **40** materials were estimated according to the Clausius-Mossotti equation (1.2)^[156,157] which expresses the dielectric constant as:

$$\epsilon = \left(1 + \frac{8\pi\alpha}{3V}\right) \times \left(1 - \frac{4\pi\alpha}{3V}\right)^{-1} \quad (1.2)$$

where α is the isotropic polarizability and V is the molecular volume plus the van der Waals radius of 1 Å. The isotropic polarizability was calculated by the B3LYP/6-31+G(d) method. The ϵ values were estimated to be 3.4 and 3.2 for **39** and **40** materials, respectively. These data show a good correlation with data from literature. Traditionally, the organic materials are characterized by low ϵ (*i.e.* 2–7) in the solid state.^[158] However, the influence of the electric field on ϵ was ignored to simplify the modelling. The calculated parameters are provided in Table 1.1.

Table 1.1. Computed dielectric constants, molecular volumes (with van der Waals radius of 1 Å) and static isotropic polarizabilities.

Compound	α (Å ³)	V (Å ³)	ϵ
39	39.3	368	3.4
40	40.3	403	3.2

On the other hand, the charged sites are polarized by their surrounding environment and an external electric field, which in turn would cause an additional energy shift.^[159,160] Therefore, ΔG^0 is the energy difference between the initial and final states of the charge transfer process. The Gibbs free energy was approximated to eqn (1.3):

$$\Delta G^0 = -eF\epsilon^{-1}d_i - P^\pm \quad (1.3)$$

where P^\pm is the polarization energy for holes and electrons, respectively. The polarization energy (P^+ and P^-) measures the contribution of intermolecular interactions in the solid state to hole and electron transport levels and includes both the electrostatic and polarization contributions. The P^\pm energies are defined as the difference between the solid state and gas phase values of ionization potential and electron affinity, respectively.^[161] The crystal cells of **39** and **40** were used for estimation of the vertical ionization potentials (IP) and electron affinities (EA) by using the B3LYP/6-31+G(d) method in the solid state. The polarization energies for one dimension can be described by the formula $P^+ = \frac{1}{3}(\text{IP}_{\text{cryst}} - \text{IP}_{\text{gas}})$ or $P^- = \frac{1}{3}(\text{EA}_{\text{cryst}} - \text{EA}_{\text{gas}})$, for holes and electrons, respectively.^[93] The values (P^+ and P^-) were estimated to be (-0.24, -0.20 eV) and (-0.24, -0.25 eV) for **39** and **40**, respectively.

From the literature, the computed values of external reorganization energy are very small compared to the internal reorganization energy component (*i.e.* typically lower than about 9 meV).^[162] Moreover, the values of internal reorganization energy for the modelled compounds were calculated by the adiabatic potential energy surface method^[163] and at the B3LYP/6-31+G(d) level in vacuum according to eqn (1.4):

$$\lambda = [E^\pm(g^0) - E^\pm(g^\pm)] + [E^0(g^\pm) - E^0(g^0)] \quad (1.4)$$

In this equation, E corresponds to the energy of the neutral molecule (g^0) in the geometry of cationic/anionic species (g^\pm), respectively.

The coupling integrals are one of the key parameters determining charge carrier mobility. The integrals H_i for the pathways (see Figure 3.8 in Chapter 3 and Figures A5–A7 in Appendix A) between molecules m and n were obtained by the site-energy overlap correction method (eqn (1.5))^[164] using the long-range corrected hybrid density functional wB97X-D and 6-311G(d) basis set in vacuum.

$$H_i = \frac{H_{mn}^0 - \frac{1}{2}S_{mn}(H_{mm} + H_{nn})}{1 - S_{mn}^2} \quad (1.5)$$

where H_{mn}^0 is the electronic coupling (transfer) matrix element, S_{mn} is the overlap integral, and $H_{mm(nn)}$ are the energies of the neutral and charged dimer states.

The diffusion coefficient (D) for all migrations of electrons or holes between neighbouring molecules is given by the Pauli master eqn (1.6):^[165]

$$D = \frac{1}{2N} \sum_i d_i^2 k_i p_i \quad (1.6)$$

where N is the dimensionality ($N = 3$) and d_i is the distance between the neighboring D–D for holes and A–A moieties for electrons in dimer i , and p_i is the probability of charge migration. The molecular dynamics (Monte Carlo) simulations based on the empirical force fields can be used to obtain a well-equilibrated amorphous structure of the organic solids.^[120] However, the energies of intermolecular interactions are not considered in this method and the injection sites with equal probability are used. Taking into account the intermolecular interactions, the probability of sites can be estimated by using Boltzmann distribution depending on the intermolecular interaction energy difference ΔE_i and temperature.^[155] The evolution eqn (1.7) for p_i is given by:

$$p_i = \frac{k_i}{\sum_i k_i} \times \frac{\exp\left(-\frac{\Delta E_i}{k_B T}\right)}{\sum_i \exp\left(-\frac{\Delta E_i}{k_B T}\right)} \quad (1.7)$$

The thickness of the vacuum-evaporated layers ranged from 0.8 to 5.0 μm that corresponds to the distance between the electrodes. The possible quantity of charge hopping, which means how many times carriers must hop in order to reach across the whole film thickness, was estimated to be $10^{4\pm 1}$ considering the distances between the neighbouring donor-donor (D–D) and acceptor-acceptor (A–A) moieties determined from the crystal structures (Table A1 in Appendix A). Taking into account this data, the probability cut off was proposed to be 10^{-5} for the charge mobility calculations.

The final drift mobility (μ) was calculated according to the Einstein equation (eqn (1.8)) using the single-step approximation:

$$\mu = \frac{e \cdot D}{k_B T} \quad (1.8)$$

All DFT calculations were done with the Spartan'14 program in vacuum and at 298K.^[149]

2.2. Charge transport measurements

2.2.1. TOF measurements

Samples fabrication. Samples for the charge drift mobility measurements by the time-of-flight (TOF) method were prepared by vacuum thermal evaporation with a base pressure below 10^{-6} mbar unless otherwise stated. The organic compounds were deposited on pre-cleaned indium tin oxide (ITO) coated glass substrates followed by deposition of 80 nm of aluminium using a mask. The area of the obtained devices was 0.06 cm^2 .

TOF characterization. Photo generation of charge carriers was performed by light pulse through the ITO. For hole mobility measurements a positive voltage was applied to the ITO electrode, whereas for electron mobility measurements a negative voltage was applied. A Keithley 6517B electrometer was used to apply external voltages with a pulsed third-harmonic Nd:YAG laser EKSPLA NL300 working at a pulse duration of 3–6 ns and a wavelength of 355 nm. A digital storage oscilloscope Tektronix TDS 3032C was used to record the TOF transients. The transit time (t_t) was determined by the kink on the curve of the transient in the log–log scale. The drift mobility was calculated by the formula $\mu = d^2/Ut_t$, where d is the layer thickness and U is the surface potential at the moment of illumination. Zero-field mobilities (μ_0) and the field dependence parameter (α) were calculated by the equation: $\mu = \mu_0 e^{\alpha E^{1/2}}$.

2.2.2. XTOF measurements

Samples fabrication. The samples for the charge drift mobility measurements by the xerographic time of flight (XTOF) technique were prepared by vacuum thermal evaporation (with a base pressure below 10^{-6} mbar) of the organic materials on Al coated glasses; or by casting the THF solutions of the pure materials and of the molecular mixtures of the organic materials with

bisphenol polycarbonate Z (PCZ) from Mitsubishi Gas Chemical Co, as polymer host, in weight proportion 1:1 in THF on glass plates with a conductive Al layer.

XTOF characterization. Electric field inside the layer was created by charging of a corona. Illumination with pulses of N₂ laser ($\lambda = 337$ nm) generated charge carriers at the layer surface producing a decrease up to 1–5% of the initial potential before illumination. The capacitance probe that was connected to the wide frequency band electrometer measured the rate of the surface potential decrease, dU/dt . Transient time was determined from the kink in the log-log scale dU/dt curve. Drift mobility was calculated according to the formula $\mu = d^2/U_0t_t$, where d is the layer thickness and U_0 is the surface potential at the moment of illumination. Field dependences of the hole and electron mobilities were determined according to the formula $\log\mu = \alpha E^{1/2}$.

2.3. Fabrication and measurement of the organic photoreceptor devices

Single-layered xerographic photoreceptors were prepared by casting the solutions of mixtures of the investigated compounds and bisphenol polycarbonate Z (PCZ) from Mitsubishi Gas Chemical Co, as polymer host, at a mass proportion of 1:1 in THF on the glass substrates covered with Al layer. For the photosensitivity measurements, the samples were charged by corona up to 350–450 V and illuminated with monochromatic light the intensity of which was 10^{13} quanta $\text{cm}^{-2} \text{s}^{-1}$. Photoinduced discharging curves were measured using a dynamic electrometer. The photosensitivity ($S_{1/2}$) was calculated from the time of half decay of the initial potential, residual potential (U_R) was obtained from discharge curves.^[166] Photodischarge transients were measured using xenon flash pulse illumination (1 μs pulse duration) with capacitance probe connected to the wide frequency band electrometer.

2.4. Fabrication and measurement of OLEDs

2.4.1. OLED based on compound 8 as the emitting layer

OLED fabrication. The electroluminescent device was fabricated by means of vacuum thermal evaporation of the organic compound and metal electrodes onto pre-cleaned ITO coated glass substrates with a base pressure below 10^{-6} mbar. The devices were fabricated by step-by-step deposition of the different layers. MoO₃ was used as hole-transporting layer^[167] and BPhen (Bathophenanthroline) as electron-transporting layer. Since Ca is highly reactive and corrodes quickly under aerated conditions, a Ca layer topped with a 85 nm aluminium (Al) layer was used as

the cathode. The structure consisted on ITO / MoO₃ (5 nm) / **8** (45 nm) / BPhen (15 nm) / Ca (14 nm) / Al (85 nm). The active area of the obtained devices was 2 x 3 mm².

OLED characterization. The density-voltage and luminance-voltage characteristics were measured using a Keithley 6517B electrometer and a Keithley 2400-C sourcemeter in air without passivation immediately after the preparation of the device. The brightness measurements were done using a calibrated photodiode.^[168]

2.4.2. OLEDs based on compound **23** as the emitting layer

OLED fabrication. The substrates were cleaned by ultrasonic treatment in acetone and isopropyl alcohol and subsequently dried by a nitrogen blow. After that, their surfaces were processed with ozone treatment for 30 minutes. Subsequently, PEDOT:PSS (Clevios PV P Al4083 from H.C. Starck, filtered at 0.45 μm) was spin-coated at 4500 rpm (thickness around 25 nm) onto the ITO surface and later heated at 120 °C for 20 min. After that, starting from a solution of 10 mg mL⁻¹, **23** was spin casted from different solvents on the PEDOT:PSS layer and successively heated at 50 °C for 5 min. Samples were transferred into a nitrogen filled glovebox where 10 nm of TPBi, 1 nm of LiF and 100 nm of Al were deposited by thermal evaporation on the active layer under high vacuum. The devices were put in a sample holder that protect them from oxygen and moisture and allow contacting them for measuring. The effective area of each cell was ~9 mm².

OLED characterization. The current density-voltage and luminance-voltage curves were simultaneously acquired by a Keithley 2400 unit (current) and a Konica-Minolta LS-100 (luminance).

2.5. Fabrication and measurements of OTFTs

Materials. OTFT devices were fabricated using the bottom-gate top-contact geometry. The substrate consisted in a thermally oxidized crystalline silicon wafer that provided a gate dielectric (SiO₂) of thickness 50 nm, 110 and 130 nm. The substrates were cleaned by ultrasonic treatment in acetone and isopropyl alcohol, rinsed with Milli-Q water, subsequently dried by an air blow and heated at 120 °C for 5 min.

Modification of the dielectric surface. The SiO₂ surface was treated with either a layer of polystyrene (PS) or octadecyltrichlorosilane (OTS) as a self-assembled monolayer (SAM) to improve the device performance. PS was deposited by spin coating. For this purpose, a solution of PS in

toluene (4 mg mL^{-1}) was cast onto the substrate in order to entirely cover the surface. The substrate was spun at 500 rpm for 5 s and 2500 rpm for 30 s with a P6700 spin coater and subsequently heated at $120 \text{ }^\circ\text{C}$ for 1 hour. For OTS SAM fabrication, the substrates were immersed in a 2 mM toluene solution of OTS for 24 hours at room temperature.^[169] Then, the substrates were cleaned by ultrasonic treatment in toluene, acetone and isopropyl alcohol, and subsequently dried by a nitrogen blow and heated at $100 \text{ }^\circ\text{C}$ for 10 minutes. The contact angles determined for bare SiO_2 , PS- and OTS-treated SiO_2 surfaces were determined to be 14° , 74° and 92° , respectively (Figure 1.1).

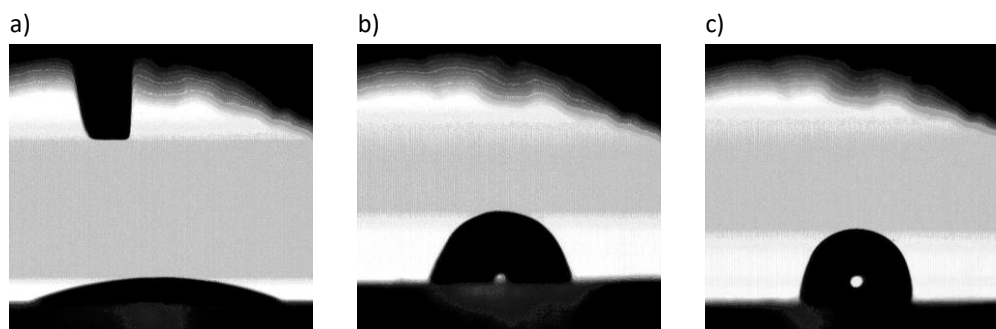


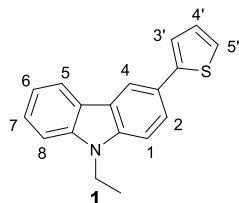
Figure 1.1. Measurement of the contact angle of a) bare SiO_2 substrate, b) PS treated substrate and c) OTS treated substrate.

OTFT fabrication. Organic materials were deposited by thermal evaporation in a vacuum system with base pressure below 10^{-6} mbar. The sublimation temperature for the organic compounds was regulated to maintain a stable deposition rate around $0.1\text{--}0.3 \text{ \AA s}^{-1}$ to obtain layers around 75 nm thick. Then, the samples were transferred to a different vacuum chamber used to evaporate the metallic contacts. Gold was used for source and drain electrodes. A metallic mask was used to define a channel length (L) and width (W) of $80 \text{ }\mu\text{m}$ and 2 mm, respectively.

OTFT characterization. The fabricated OTFTs were electrically characterized in dark either under vacuum (n-type OTFTs) or under air conditions (p-type OTFTs) as indicated. The electrical characteristics were measured using an Agilent 4156C parameter analyser or a Keitley 2636A source meter.

3. Synthetic procedures and compound characterization data

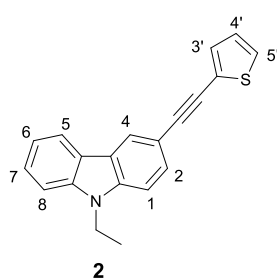
3.1. Synthesis of 9-ethyl-3-(2-thienyl)-9H-carbazole (1)



NaH (48 mg, 1.21 mmol, 60% dispersion in mineral oil) was added to a solution of **13** (249 mg, 1.00 mmol) in 8 mL of anhydrous DMF under a nitrogen atmosphere. The solution was stirred at room temperature for 45 minutes. Then, bromoethane (90 μ L, 1.21 mmol) was added and the mixture was stirred overnight at room temperature and then treated with water. The aqueous layer was extracted with dichloromethane and the organic layer was dried over anhydrous Na_2SO_4 , filtered off and the solvent was distilled off under reduced pressure. The crude was purified by flash column chromatography using hexane as the eluent to afford **1** as a white solid.

Yield: 237 mg (86%). **$^1\text{H NMR}$** (400 MHz, Acetone- d_6) δ (ppm): 8.45 (d, $^4J = 1.8$ Hz, H^4 , 1H), 8.23 (d, $^3J = 7.5$ Hz, H^5 , 1H), 7.78 (dd, $^3J = 8.5$ Hz, $^4J = 1.8$ Hz, H^2 , 1H), 7.61 (d, $^3J = 8.5$ Hz, H^1 , 1H), 7.58 (d, $^3J = 8.3$ Hz, H^8 , 1H), 7.50–7.45 (m, $\text{H}^{3'}$, H^7 , 2H), 7.39 (dd, $^3J = 5.1$ Hz, $^4J = 1.2$ Hz, $\text{H}^{5'}$, 1H), 7.25–7.21 (m, H^6 , 1H), 7.13 (dd, $^3J = 5.1$ Hz, $^3J = 3.6$ Hz, $\text{H}^{4'}$, 1H), 4.52 (q, $^3J = 7.2$ Hz, N-CH_2 , 2H), 1.42 (t, $^3J = 7.2$ Hz, CH_3 , 3H). **$^{13}\text{C NMR}$** (100 MHz, Acetone- d_6) δ (ppm): 146.4, 141.4, 140.4, 129.0, 126.9, 126.5, 124.9, 124.5, 124.2, 123.7, 122.9, 121.4, 119.9, 118.3, 110.1, 109.9, 38.1, 14.1. **UV-Vis** (THF) λ_{max} ($\epsilon / \text{dm}^3 \text{mol}^{-1} \text{cm}^{-1}$): 299 (35 925), 317 (16 734) nm. **HRMS** (ESI-MS) m/z : calcd for $\text{C}_{18}\text{H}_{16}\text{NS}$: 278.0998 ($\text{M} + \text{H}$) $^+$, found: 278.0998.

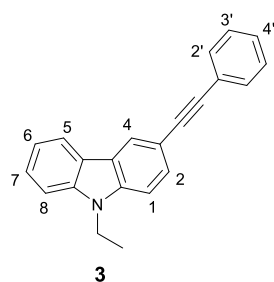
3.2. Synthesis of 9-ethyl-3-[2-(2-thienyl)ethynyl]-9H-carbazole (2)



NaH (36 mg, 0.90 mmol, 60% dispersion in mineral oil) was added to a solution of **19** (164 mg, 0.60 mmol) in 6 mL of anhydrous DMF under a nitrogen atmosphere. The solution was stirred at room temperature for 45 minutes. Then, bromoethane (67 μ L, 0.90 mmol) was added and the mixture was stirred overnight at room temperature and then treated with water. The aqueous layer was extracted with dichloromethane and the organic layer was dried over anhydrous Na_2SO_4 , filtered off and the solvent was distilled off under reduced pressure. The crude was purified by flash column chromatography using a mixture of hexane and dichloromethane (9:1 v/v) as the eluent to afford **2** as a white solid.

Yield: 99 mg (55%). **¹H NMR** (400 MHz, Acetone-*d*₆) δ (ppm): 8.35 (s, H⁴, 1H), 8.23 (d, ³*J* = 7.8 Hz, H⁵, 1H), 7.64–7.59 (m, H¹, H², H⁸, 3H), 7.53–7.49 (m, H^{5'}, H⁷, 2H), 7.34 (dd, ³*J* = 3.6 Hz, ⁴*J* = 1.0 Hz, H^{3'}, 1H), 7.28–7.24 (m, H⁶, 1H), 7.10 (dd, ³*J* = 5.2 Hz, ³*J* = 3.6 Hz, H^{4'}, 1H), 4.50 (q, ³*J* = 7.2 Hz, N–CH₂, 2H), 1.41 (t, ³*J* = 7.2 Hz, CH₃, 3H). **¹³C NMR** (100 MHz, Acetone-*d*₆) δ (ppm): 141.4, 140.7, 132.3, 129.7, 128.2, 128.0, 127.2, 124.6, 124.5, 123.9, 123.2, 121.5, 120.3, 113.5, 110.1, 110.0, 95.2, 81.1, 38.2, 14.1. **UV-Vis** (THF) λ_{max} (ϵ / dm³ mol⁻¹ cm⁻¹): 304 (37 944), 324 (29 519) nm. **HRMS** (ESI-MS) *m/z*: calcd for C₂₀H₁₆N: 302.0998 (M + H)⁺, found: 302.1011.

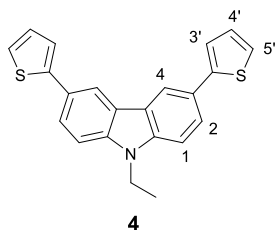
3.3. Synthesis of 9-ethyl-3-(2-phenylethynyl)-9H-carbazole (3)



NaH (40 mg, 1.00 mmol, 60% dispersion in mineral oil) was added to a solution of **21** (182 mg, 0.68 mmol) in 6 mL of anhydrous DMF under a nitrogen atmosphere. The solution was stirred at room temperature for 45 minutes. Then, bromoethane (75 μ L, 1.00 mmol) was added and the mixture was stirred overnight at room temperature and then treated with water. The aqueous layer was extracted with dichloromethane and the organic layer was dried over anhydrous Na₂SO₄, filtered off and the solvent was distilled off under reduced pressure. The crude was purified by flash column chromatography using a mixture of hexane and dichloromethane (9:1 v/v) as the eluent to afford **3** as a white solid.

Yield: 136 mg (68%). **¹H NMR** (400 MHz, Acetone-*d*₆) δ (ppm): 8.36 (d, ⁴*J* = 1.5 Hz, H⁴, 1H), 8.23 (d, ³*J* = 7.8 Hz, H⁵, 1H), 7.65 (d, ³*J* = 8.5 Hz, ⁴*J* = 1.5 Hz, H², 1H), 7.63–7.56 (m, H¹, H⁸, H^{2'}, 4H), 7.53–7.49 (m, H⁷, 1H), 7.45–7.36 (m, H^{3'}, H^{4'}, 3H), 7.28–7.24 (m, H⁶, 1H), 4.52 (q, ³*J* = 7.2 Hz, N–CH₂, 2H), 1.42 (t, ³*J* = 7.2 Hz, CH₃, 3H). **¹³C NMR** (100 MHz, Acetone-*d*₆) δ (ppm): 141.4, 140.6, 132.1, 130.0, 129.4, 128.8, 127.2, 124.8, 124.6, 123.9, 123.3, 121.4, 120.3, 114.0, 110.0, 91.7, 88.1, 38.2, 14.1. **UV-Vis** (THF) λ_{max} (ϵ / dm³ mol⁻¹ cm⁻¹): 299 (42 835), 317 (26 018) nm. **HRMS** (ESI-MS) *m/z*: calcd for C₂₂H₁₈N: 296.1434 (M + H)⁺, found: 296.1442.

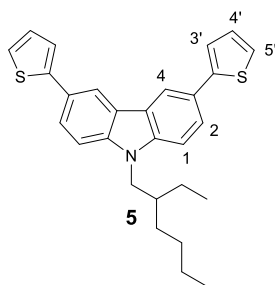
3.4. Synthesis of 9-ethyl-3,6-di-2-thienyl-9H-carbazole (4)



NaH (22 mg, 0.55 mmol, 60% dispersion in mineral oil) was added to a solution of **14** (119 mg, 0.36 mmol) in 3 mL of anhydrous DMF under a nitrogen atmosphere. The solution was stirred at room temperature for 45 minutes. Then, bromoethane (41 μ L, 0.55 mmol) was added and the mixture was stirred overnight at room temperature and then treated with water. The aqueous layer was extracted with dichloromethane and the organic layer was dried over anhydrous Na_2SO_4 , filtered off and the solvent was distilled off under reduced pressure. The crude was purified by flash column chromatography using a mixture of hexane and dichloromethane (10:1 v/v) as the eluent to afford **4** as a light brown solid.

Yield: 85 mg (66%). **$^1\text{H NMR}$** (400 MHz, $\text{DMSO-}d_6$) δ (ppm): 8.59 (d, $^4J = 1.8$ Hz, H^4 , 2H), 7.78 (dd, $^3J = 8.5$ Hz, $^4J = 1.8$ Hz, H^2 , 2H), 7.66 (d, $^3J = 8.5$ Hz, H^1 , 2H), 7.55 (dd, $^3J = 3.6$ Hz, $^4J = 1.1$ Hz, $\text{H}^{3'}$, 2H), 7.50 (dd, $^3J = 5.1$ Hz, $^4J = 1.1$ Hz, $\text{H}^{5'}$, 2H), 7.16 (dd, $^3J = 5.1$ Hz, $^3J = 3.6$ Hz, $\text{H}^{4'}$, 2H), 4.47 (q, $^3J = 7.1$ Hz, N-CH_2 , 2H), 1.34 (t, $^3J = 7.1$ Hz, CH_3 , 3H). **$^{13}\text{C NMR}$** (100 MHz, CDCl_3) δ (ppm): 145.8, 140.1, 128.1, 126.1, 124.8, 123.9, 123.5, 122.3, 118.2, 109.1, 37.9, 14.0. **UV-Vis** (THF) λ_{max} ($\epsilon / \text{dm}^3 \text{mol}^{-1} \text{cm}^{-1}$): 315 (42 710), 337 (23 377) nm. **HRMS** (ESI-MS) m/z : calcd for $\text{C}_{22}\text{H}_{18}\text{NS}_2$: 360.0875 ($\text{M} + \text{H}$) $^+$, found: 360.0865.

3.5. Synthesis of 9-(2-ethylhexyl)-3,6-di-2-thienyl-9H-carbazole (5)

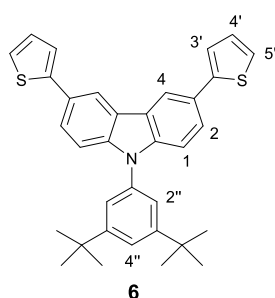


NaH (17 mg, 0.43 mmol, 60% dispersion in mineral oil) was added to a solution of **14** (119 mg, 0.36 mmol) in 6 mL of anhydrous DMF under a nitrogen atmosphere. The solution was stirred at room temperature for 45 minutes. Then, 2-ethylhexyl bromide (76 μ L, 0.43 mmol) was added and the mixture was stirred overnight at room temperature and then treated with water. The aqueous layer was extracted with dichloromethane and the organic layer was dried over anhydrous Na_2SO_4 , filtered off and the solvent was distilled off under reduced pressure. The crude was purified by flash column chromatography using a mixture of hexane and dichloromethane (9:1 v/v) as the eluent to afford **5** as a white solid.

Yield: 90 mg (56%). **$^1\text{H NMR}$** (400 MHz, $\text{Acetone-}d_6$) δ (ppm): 8.55 (d, $^4J = 1.5$ Hz, H^4 , 2H), 7.79 (dd, $^3J = 8.5$ Hz, $^4J = 1.5$ Hz, H^2 , 2H), 7.57 (d, $^3J = 8.5$ Hz, H^1 , 2H), 7.48 (d, $^3J = 3.6$ Hz, $\text{H}^{3'}$, 2H), 7.39 (d, $^3J =$

5.0 Hz, H^{5'}, 2H), 7.13 (dd, ³J = 5.0 Hz, ³J = 3.6 Hz, H^{4'}, 2H), 4.31 (d, ³J = 7.5 Hz, N-CH₂, 2H), 2.16–2.08 (m, CH, 1H), 1.48–1.19 (m, 4 × CH₂, 8H), 0.93 (t, ³J = 7.4 Hz, CH₃, 3H), 0.83 (t, ³J = 7.2 Hz, CH₃, 3H). ¹³C NMR (100 MHz, CDCl₃) δ (ppm): 145.8, 141.0, 128.1, 126.0, 124.7, 123.8, 123.3, 122.2, 118.1, 109.6, 47.8, 39.6, 31.2, 29.0, 24.6, 23.2, 14.2, 11.1. **UV-Vis** (THF) λ_{max} (ε / dm³ mol⁻¹ cm⁻¹): 314 (40 978), 335 (23 532) nm. **HRMS** (ESI-MS) *m/z*: calcd for C₂₈H₃₀NS₂, 444.1814 (M + H)⁺, found: 444.1817.

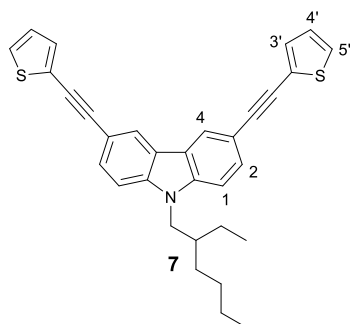
3.6. Synthesis of 9-(3,5-di-*tert*-butylphenyl)-3,6-di-2-thienyl-9*H*-carbazole (6)



A mixture of **14** (381 mg, 1.15 mmol), 1-bromo-3,5-di-*tert*-butylbenzene (937 mg, 3.48 mmol), anhydrous K₂CO₃ (339 mg, 2.45 mmol) and Cu powder (10 mg, 0.16 mmol) was refluxed in anhydrous DMF (5 mL) under nitrogen atmosphere for 24 h. After, the reaction mixture was filtered through Celite and diluted with water. The aqueous layer was extracted with dichloromethane and the organic layer was dried over anhydrous Na₂SO₄, filtered off and the solvent was distilled off under reduced pressure. The crude was purified by flash column chromatography using hexane and dichloromethane (10:1 v/v) as the eluent to give compound **6** as a white solid.

Yield: 320 mg (54%). ¹H NMR (400 MHz, CDCl₃) δ (ppm): 8.41 (d, ⁴J = 1.8 Hz, H⁴, 2H), 7.71 (dd, ³J = 8.5 Hz, ⁴J = 1.8 Hz, H², 2H), 7.53 (t, ⁴J = 1.8 Hz, H^{4''}, 1H), 7.43 (d, ³J = 8.5 Hz, H¹, 2H), 7.41 (d, ⁴J = 1.8 Hz, H^{2''}, 2H), 7.38 (dd, ³J = 3.6 Hz, ⁴J = 1.1 Hz, H^{3'}, 2H), 7.28 (dd, ³J = 5.1 Hz, ⁴J = 1.1 Hz, H^{5'}, 2H), 7.13 (dd, ³J = 5.1 Hz, ³J = 3.6 Hz, H^{4'}, 2H), 1.41 (s, 6 × CH₃, 18H). ¹³C NMR (100 MHz, CDCl₃) δ (ppm): 152.9, 145.7, 141.1, 136.8, 128.2, 127.0, 125.0, 124.0, 123.8, 122.4, 121.6, 121.1, 118.0, 110.6, 35.3, 31.6. **UV-Vis** (THF) λ_{max} (ε / dm³ mol⁻¹ cm⁻¹): 313 (54 696), 335 (27 368) nm. **HRMS** (ESI-MS) *m/z*: calcd for C₃₄H₃₄NS₂: 520.2127 (M + H)⁺, found: 520.2148.

3.7. Synthesis of 9-(2-ethylhexyl)-3,6-bis[2-(2-thienyl)ethynyl]-9*H*-carbazole (7)

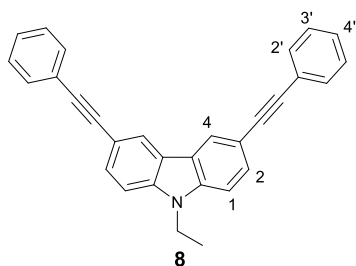


NaH (63 mg, 1.58 mmol, 60% dispersion in mineral oil) was added to a solution of **20** (505 mg, 1.33 mmol) in 15 mL of anhydrous DMF under a nitrogen atmosphere. The solution was stirred at room temperature for 45 minutes. Then, 2-ethylhexyl bromide (281 μL, 1.58 mmol) was added and the mixture was stirred overnight at room temperature and then treated with water. The aqueous layer

was extracted with dichloromethane and the organic layer was dried over anhydrous Na₂SO₄, filtered off and the solvent was distilled off under reduced pressure. The crude was purified by flash column chromatography using a mixture of hexane and dichloromethane (9:1 v/v) as the eluent to afford **7** as a pale yellow solid.

Yield: 300 mg (46%). **¹H NMR** (400 MHz, Acetone-*d*₆) δ (ppm): 8.43 (s, H⁴, 2H), 7.65 (dd, ³*J* = 8.5 Hz, ⁴*J* = 1.5 Hz, H², 2H), 7.62 (d, ³*J* = 8.5 Hz, H¹, 2H), 7.52 (dd, ³*J* = 5.2 Hz, ⁴*J* = 1.1 Hz, H^{5'}, 2H), 7.35 (dd, ³*J* = 3.6 Hz, ⁴*J* = 1.1 Hz, H^{3'}, 2H), 7.11 (dd, ³*J* = 5.2 Hz, ³*J* = 3.6 Hz, H^{4'}, 2H), 4.35 (d, ³*J* = 7.6 Hz, N-CH₂, 2H), 2.15–2.08 (m, CH, 1H), 1.47–1.17 (m, 4 × CH₂, 8H), 0.93 (t, ³*J* = 7.5 Hz, CH₃, 3H), 0.81 (t, ³*J* = 7.2 Hz, CH₃, 3H). **¹³C NMR** (100 MHz, CDCl₃) δ (ppm): 141.1, 131.5, 129.7, 127.2, 126.9, 124.2, 124.1, 122.6, 113.7, 109.5, 94.3, 81.2, 47.8, 39.5, 31.1, 28.9, 24.5, 23.1, 14.1, 11.0. **UV-Vis** (THF) λ_{\max} (ϵ / dm³ mol⁻¹ cm⁻¹): 312 (53 400), 336 (39 341) nm. **HRMS** (ESI-MS) *m/z*: calcd for C₃₂H₃₀NS₂: 492.1814 (M + H)⁺, found: 492.1799.

3.8. Synthesis of 9-ethyl-3,6-bis(2-phenylethynyl)-9H-carbazole (**8**)

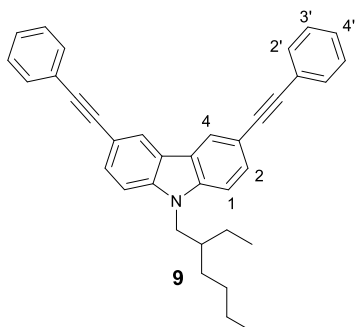


NaH (66 mg, 1.65 mmol, 60% dispersion in mineral oil) was added to a solution of **22** (400 mg, 1.09 mmol) in 6 mL of anhydrous DMF under a nitrogen atmosphere. The solution was stirred at room temperature for 45 minutes. Then, bromoethane (123 μ L, 1.65 mmol) was added and the mixture was stirred overnight at room temperature and then treated with water. The aqueous layer

was extracted with dichloromethane and the organic layer was dried over anhydrous Na₂SO₄, filtered off and the solvent was distilled off under reduced pressure. The crude was purified by flash column chromatography using a mixture of hexane and dichloromethane (5:1 v/v) as the eluent to afford **8** as a white solid.

Yield: 311 mg (72%). **¹H NMR** (400 MHz, DMSO-*d*₆) δ (ppm): 8.50 (d, ⁴*J* = 1.5 Hz, H⁴, 2H), 7.72 (d, ³*J* = 8.5 Hz, H¹, 2H), 7.67 (dd, ³*J* = 8.5 Hz, ⁴*J* = 1.5 Hz, H², 2H), 7.59–7.57 (m, H^{2'}, 4H), 7.47–7.39 (m, H^{3'}, H^{4'}, 6H), 4.50 (q, ³*J* = 7.1 Hz, N-CH₂, 2H), 1.35 (t, ³*J* = 7.1 Hz, CH₃, 3H). **¹³C NMR** (100 MHz, Acetone-*d*₆) δ (ppm): 141.0, 132.1, 130.6, 129.4, 128.9, 125.0, 124.7, 123.4, 114.7, 110.4, 91.4, 88.4, 38.4, 14.1. **UV-Vis** (THF) λ_{\max} (ϵ / dm³ mol⁻¹ cm⁻¹): 312 (55 546), 336 (38 101) nm. **HRMS** (ESI-MS) *m/z*: calcd for C₃₀H₂₂N: 396.1747 (M + H)⁺, found: 396.1766.

3.9. Synthesis of 9-(2-ethylhexyl)-3,6-bis(2-phenylethynyl)-9H-carbazole (9)

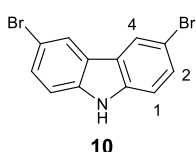


NaH (65 mg, 1.63 mmol, 60% dispersion in mineral oil) was added to a solution of **22** (400 mg, 1.09 mmol) in 6 mL of anhydrous DMF under a nitrogen atmosphere. The solution was stirred at room temperature for 45 minutes. Then, 2-ethylhexyl bromide (290 μ L, 1.63 mmol) was added and the mixture was stirred overnight at room temperature and then treated with water. The aqueous layer was extracted with dichloromethane and the organic layer was

dried over anhydrous Na_2SO_4 , filtered off and the solvent was distilled off under reduced pressure. The crude was purified by flash column chromatography using a mixture of hexane and dichloromethane (20:1 v/v) as the eluent to afford **9** as a pale yellow solid.

Yield: 317 mg (61%). $^1\text{H NMR}$ (400 MHz, Acetone- d_6) δ (ppm): 8.45 (d, $^4J = 1.5$ Hz, H^4 , 2H), 7.68 (dd, $^3J = 8.5$ Hz, $^4J = 1.5$ Hz, H^2 , 2H), 7.64 (d, $^3J = 8.5$ Hz, H^1 , 2H), 7.60–7.57 (m, $\text{H}^{2'}$, 4H), 7.46–7.37 (m, $\text{H}^{3'}$, $\text{H}^{4'}$, 6H), 4.38 (d, $^3J = 7.6$ Hz, N- CH_2 , 2H), 2.17–2.10 (m, CH, 1H), 1.49–1.20 (m, 4 \times CH_2 , 8H), 0.94 (t, $^3J = 7.5$ Hz, CH_3 , 3H), 0.82 (t, $^3J = 7.2$ Hz, CH_3 , 3H). $^{13}\text{C NMR}$ (100 MHz, CDCl_3) δ (ppm): 141.0, 131.6, 129.8, 128.5, 128.0, 124.2, 124.0, 122.6, 114.0, 109.4, 90.7, 88.0, 47.7, 39.5, 31.1, 28.9, 24.5, 23.1, 14.1, 11.0. **UV-Vis** (THF) λ_{max} ($\epsilon / \text{dm}^3 \text{mol}^{-1} \text{cm}^{-1}$): 312 (64 737), 336 (44 587) nm. **HRMS** (ESI-MS) m/z : calcd for $\text{C}_{36}\text{H}_{34}\text{N}$: 480.2686 ($\text{M} + \text{H}^+$), found: 480.2692.

3.10. Synthesis of 3,6-dibromo-9H-carbazole (10)

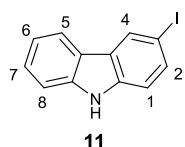


A solution of NBS (10.75 g, 60.4 mmol) in dichloromethane (300 mL) was added slowly to a stirred solution of 9H-carbazole (5.05 g, 30.2 mmol) in dichloromethane (300 mL), containing silica gel (120 g). The mixture was stirred

overnight in the dark at room temperature. Then, the mixture was filtered and the silica gel was washed thoroughly with dichloromethane. The combined filtrate was washed with water, dried over anhydrous Na_2SO_4 , filtered off, and the solvent was distilled off under reduced pressure. The resulting solid was recrystallized from ethanol to give **10** as a white solid.

Yield: 4.83 g (49%). $^1\text{H NMR}$ (400 MHz, Acetone- d_6) δ (ppm): 10.66 (s, NH, 1H), 8.37 (d, $^4J = 1.9$ Hz, H^4 , 2H), 7.55 (dd, $^3J = 8.6$ Hz, $^4J = 1.9$ Hz, H^2 , 2H), 7.51 (d, $^3J = 8.6$ Hz, H^1 , 2H).

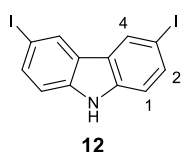
3.11. Synthesis of 3-iodo-9H-carbazole (**11**)



9H-Carbazole (4.00 g, 23.9 mmol) was dissolved in glacial acetic acid (100 mL) at reflux. Next, potassium iodide (2.66 g, 16.0 mmol) and potassium iodate (3.85 g, 18.0 mmol) were added stepwise observing the evolution of iodine gas. The reaction mixture was stirred under reflux for 30 minutes. Then, the hot solution was decanted to separate the undissolved KIO_3 and cooled down to ambient temperature. The formation of a precipitate was observed. The solid was isolated by vacuum filtration, washed with a 5% $\text{Na}_2\text{S}_2\text{O}_3$ solution and then with water, and dried. The product was recrystallized from methanol to afford **11** as a light brown solid.

Yield: 4.10 g (58%). $^1\text{H NMR}$ (400 MHz, Acetone- d_6) δ (ppm): 10.49 (s, NH, 1H), 8.49 (d, $^4J = 1.7$ Hz, H^4 , 1H), 8.16 (d, $^3J = 7.9$ Hz, H^5 , 1H), 7.67 (dd, $^3J = 8.5$ Hz, $^4J = 1.7$ Hz, H^2 , 1H), 7.53 (d, $^3J = 8.2$ Hz, H^8 , 1H), 7.45–7.40 (m, H^7 , 1H), 7.39 (d, $^3J = 8.5$ Hz, H^1 , 1H), 7.23–7.19 (m, H^6 , 1H). **CI-MS** m/z : calcd for $\text{C}_{12}\text{H}_9\text{IN}$: 294.0 (M + H) $^+$, found: 294.6.

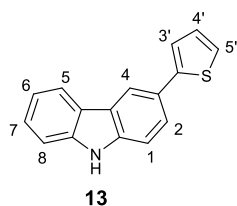
3.12. Synthesis of 3,6-diiodo-9H-carbazole (**12**)



9H-Carbazole (100 mg, 0.60 mmol) was dissolved in glacial acetic acid (3 mL) at reflux. Next, potassium iodide (134 mg, 0.81 mmol) and potassium iodate (197 mg, 0.92 mmol) were added stepwise observing the evolution of iodine gas. The reaction mixture was stirred under reflux for 20 minutes. Then, the hot solution was decanted to separate the undissolved KIO_3 and the solution was cooled down to ambient temperature and the formation of a precipitate was observed. The solid was isolated by vacuum filtration, washed with a 5% $\text{Na}_2\text{S}_2\text{O}_3$ solution, water, and dried. The product was purified by flash column chromatography using a mixture of hexane and dichloromethane (7:2 v/v) as the eluent to give **12** as a white solid.

Yield: 167 mg (67%). $^1\text{H NMR}$ (400 MHz, Acetone- d_6) δ (ppm): 10.63 (s, NH, 1H), 8.55 (d, $^4J = 1.7$ Hz, H^4 , 2H), 7.69 (dd, $^3J = 8.5$ Hz, $^4J = 1.7$ Hz, H^2 , 2H), 7.24 (d, $^3J = 8.5$ Hz, H^1 , 2H).

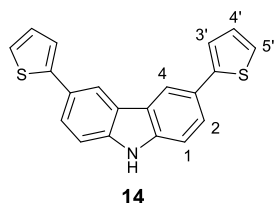
3.13. Synthesis of 3-(2-thienyl)-9H-carbazole (13)



A mixture of **11** (1.00 g, 3.41 mmol), 2-(tributylstannyl)thiophene (1.30 mL, 4.10 mmol) and Pd(PPh₃)₄ (196 mg, 0.17 mmol) in anhydrous DMF (10 mL) was heated at 100 °C for 24 h under a nitrogen atmosphere. Then, the reaction mixture was cooled down to room temperature, treated with water and the product was extracted with dichloromethane. The organic layer was dried over anhydrous Na₂SO₄, filtered off and the solvent was distilled off under reduced pressure. The crude was purified by flash column chromatography using a mixture of hexane and ethyl acetate (10:1 v/v) as the eluent to give compound **13** as a white solid.

Yield: 490 mg (58%). **¹H NMR** (400 MHz, Acetone-*d*₆) δ (ppm): 10.42 (s, NH, 1H), 8.44 (d, ⁴*J* = 1.8 Hz, H⁴, 1H), 8.20 (d, ³*J* = 7.8 Hz, H⁵, 1H), 7.72 (dd, ³*J* = 8.4 Hz, ⁴*J* = 1.8 Hz, H², 1H), 7.55 (d, ³*J* = 8.4 Hz, H¹, 1H), 7.53 (d, ³*J* = 8.0 Hz, H⁸, 1H), 7.45 (dd, ³*J* = 3.6 Hz, ⁴*J* = 1.1 Hz, H^{3'}, 1H), 7.43–7.39 (m, H⁷, 1H), 7.37 (dd, ³*J* = 5.1 Hz, ⁴*J* = 1.1 Hz, H^{5'}, 1H), 7.23–7.19 (m, H⁶, 1H), 7.12 (dd, ³*J* = 5.1 Hz, ³*J* = 3.6 Hz, H^{4'}, 1H). **¹³C NMR** (100 MHz, Acetone-*d*₆) δ (ppm): 146.5, 141.5, 140.5, 128.9, 126.9, 126.6, 124.9, 124.5 (2C), 123.9, 122.9, 121.2, 120.0, 118.2, 112.2, 111.9. **HRMS** (ESI-MS) *m/z*: calcd for C₁₆H₁₂NS 250.0685 (M + H)⁺, found: 250.0680.

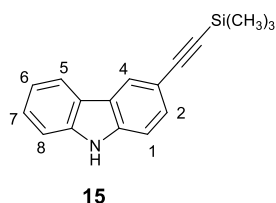
3.14. Synthesis of 3,6-di-2-thienyl-9H-carbazole (14)



A mixture of **10** (1.75 g, 5.38 mmol), 2-thienylboronic acid (1.50 g, 11.7 mmol) and Pd(PPh₃)₄ (312 mg, 0.27 mmol) in 10 mL of aqueous K₂CO₃ 2M and 30 mL of THF under a nitrogen atmosphere was refluxed for 24 h. Then, the mixture was cooled down to ambient temperature and treated with water. The product was extracted with dichloromethane and the organic layer was dried over anhydrous Na₂SO₄, filtered off and the solvent was distilled off under reduced pressure. The crude was purified by flash column chromatography using a mixture of hexane and dichloromethane (6:1 v/v) as the eluent to give **14** as a light brown solid.

Yield: 1.32 g (74%). **¹H NMR** (400 MHz, Acetone-*d*₆) δ (ppm): 10.54 (s, NH, 1H), 8.54 (d, ⁴*J* = 1.8 Hz, H⁴, 2H), 7.75 (dd, ³*J* = 8.5 Hz, ⁴*J* = 1.8 Hz, H², 2H), 7.57 (d, ³*J* = 8.5 Hz, H¹, 2H), 7.48 (dd, ³*J* = 3.6 Hz, ⁴*J* = 1.1 Hz, H^{3'}, 2H), 7.39 (dd, ³*J* = 5.1 Hz, ⁴*J* = 1.1 Hz, H^{5'}, 2H), 7.13 (dd, ³*J* = 5.1 Hz, ³*J* = 3.6 Hz, H^{4'}, 2H).

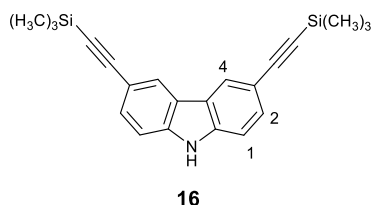
3.15. Synthesis of 3-[2-(trimethylsilyl)ethynyl]-9H-carbazole (**15**)



11 (2.01 g, 6.86 mmol), CuI (169 mg, 0.89 mmol) and Pd(PPh₃)₂Cl₂ (239 mg, 0.34 mmol) were mixed in 50 mL of anhydrous THF under a nitrogen atmosphere. Then, triethylamine (2.0 mL, 14.3 mmol) and ethynyltrimethylsilane (1.5 mL, 10.8 mmol) were added and the mixture was stirred at room temperature overnight. After, the solvent was distilled off under reduced pressure and the crude was purified by flash column chromatography using a mixture of hexane and dichloromethane (9:1 v/v) as the eluent to afford **15** as a pale yellow solid.

Yield: 1.13 g (63%). ¹H NMR (400 MHz, Acetone-*d*₆) δ (ppm): 10.54 (s, NH, 1H), 8.25 (s, H⁴, 1H), 8.19 (d, ³J = 7.6 Hz, H⁵, 1H), 7.53 (d, ³J = 8.2 Hz, H⁸, 1H), 7.50 (d, ³J = 8.4 Hz, H¹, 1H), 7.47 (dd, ³J = 8.4 Hz, ⁴J = 1.4 Hz, H², 1H), 7.44–7.40 (m, H⁷, 1H), 7.24–7.20 (m, H⁶, 1H), 0.25 (s, Si(CH₃)₃, 9H). ¹³C NMR (100 MHz, Acetone-*d*₆) δ (ppm): 141.4, 140.8, 130.1, 127.1, 124.9, 124.0, 123.5, 121.3, 120.3, 114.1, 112.0, 111.9, 107.9, 91.5, 0.26. HRMS (ESI-MS) *m/z*: calcd for C₁₇H₁₈NSi: 264.1203 (M + H)⁺, found: 264.1202.

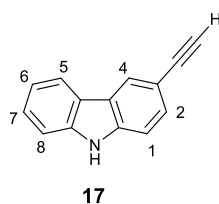
3.16. Synthesis of 3,6-bis[2-(trimethylsilyl)ethynyl]-9H-carbazole (**16**)



12 (2.00 g, 4.77 mmol), CuI (120 mg, 0.63 mmol) and Pd(PPh₃)₂Cl₂ (168 mg, 0.24 mmol) were mixed in 25 mL of anhydrous THF under a nitrogen atmosphere. Then, triethylamine (2.30 mL, 16.5 mmol) and ethynyltrimethylsilane (1.98 mL, 14.3 mmol) were added and the mixture was stirred at room temperature overnight. After, the solvent was distilled off under reduced pressure and the crude was purified by flash column chromatography using a mixture of hexane and ethyl acetate (9:1 v/v) as the eluent to afford **16** as a pale yellow solid.

Yield: 1.10 g (65%). ¹H NMR (400 MHz, Acetone-*d*₆) δ (ppm): 10.74 (s, NH, 1H), 8.34 (s, H⁴, 2H), 7.54 (m, H¹, H², 4H), 0.25 (s, 2 × Si(CH₃)₃, 18H). CI-MS *m/z*: calcd for C₂₂H₂₆NSi₂: 360.2 (M + H)⁺, found: 360.2.

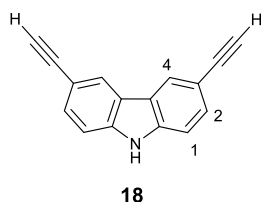
3.17. Synthesis of 3-ethynyl-9H-carbazole (17)



15 (211 mg, 0.80 mmol) and anhydrous K_2CO_3 (2.47 g, 17.9 mmol) were dissolved in methanol (120 mL). The reaction mixture was stirred at room temperature overnight. The solvent was distilled off under reduced pressure and then the residue was treated with dichloromethane. The excess of K_2CO_3 was filtered off and the solvent was removed under reduced pressure. The crude was purified by flash column chromatography using hexane and dichloromethane (4:1 v/v) as the eluent to afford **17** as a white solid.

Yield: 135 mg (88%). 1H NMR (400 MHz, Acetone- d_6) δ (ppm): 10.54 (s, NH, 1H), 8.28 (s, H^4 , 1H), 8.17 (d, $^3J = 7.6$ Hz, H^5 , 1H), 7.55–7.50 (m, H^1 , H^2 , H^8 , 3H), 7.45–7.41 (m, H^7 , 1H), 7.24–7.20 (m, H^6 , 1H), 3.51 (s, $C\equiv C-H$, 1H).

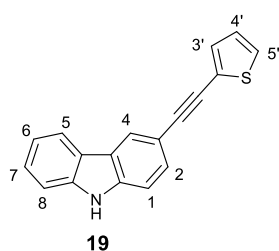
3.18. Synthesis of 3,6-diethynyl-9H-carbazole (18)



16 (1.10 g, 3.06 mmol) and anhydrous K_2CO_3 (2.11 g, 15.3 mmol) were dissolved in methanol (180 mL). The reaction mixture was stirred at room temperature overnight. After termination of the reaction, the solvent was distilled off under reduced pressure. The residue was treated with water and the product was extracted with ethyl acetate. The organic layer was dried over $MgSO_4$, filtered off and the solvent was distilled off under reduced pressure. The crude was purified by flash column chromatography using hexane and ethyl acetate (6:1 v/v) as the eluent to afford **18** as a white solid.

Yield: 0.56 g (85%). 1H NMR (400 MHz, Acetone- d_6) δ (ppm): 10.74 (s, NH, 1H), 8.34 (s, H^4 , 2H), 7.54 (m, H^1 , H^2 , 4H), 3.54 (s, $C\equiv C-H$, 2H). **CI-MS** m/z : calcd for $C_{16}H_{10}N$: 216.1 ($M + H$) $^+$, found: 216.2.

3.19. Synthesis of 3-[2-(2-thienyl)ethynyl]-9H-carbazole (19)

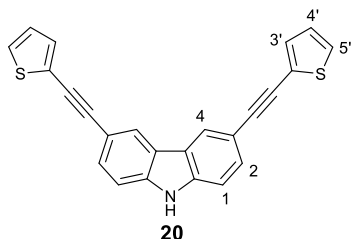


17 (474 mg, 2.48 mmol), CuI (61 mg, 0.32 mmol) and $Pd(PPh_3)_2Cl_2$ (84 mg, 0.12 mmol) were mixed in 8 mL of anhydrous THF under a nitrogen atmosphere. Then, triethylamine (1.21 mL, 8.68 mmol) and 2-iodothiophene (0.60 mL, 5.43 mmol) were added and the mixture was stirred at room temperature overnight. After, the solvent was distilled off

under reduced pressure and the crude was purified by flash column chromatography using a mixture of hexane and dichloromethane (5:1 v/v) as the eluent to afford **19** as a white solid.

Yield: 309 mg (46%). **¹H NMR** (400 MHz, Acetone-*d*₆) δ (ppm): 10.58 (s, NH, 1H), 8.34 (s, H⁴, 1H), 8.21 (d, ³*J* = 7.8 Hz, H⁵, 1H), 7.58–7.54 (m, H¹, H², H⁸, 3H), 7.51 (dd, ³*J* = 5.2 Hz, ⁴*J* = 0.9 Hz, H^{5'}, 1H), 7.46–7.42 (m, H⁷, 1H), 7.33 (dd, ³*J* = 3.6 Hz, ⁴*J* = 0.9 Hz, H^{3'}, 1H), 7.26–7.22 (m, H⁶, 1H), 7.10 (dd, ³*J* = 5.2 Hz, ³*J* = 3.6 Hz, H^{4'}, 1H). **¹³C NMR** (100 MHz, Acetone-*d*₆) δ (ppm): 141.4, 140.8, 132.2, 129.7, 128.2, 128.0, 127.2, 124.6, 124.5, 124.2, 123.4, 121.3, 120.3, 113.6, 112.1, 112.0, 95.3, 81.0. **HRMS** (ESI-MS) *m/z*: calcd for C₁₈H₁₂NS: 274.0685 (M + H)⁺, found: 274.0685.

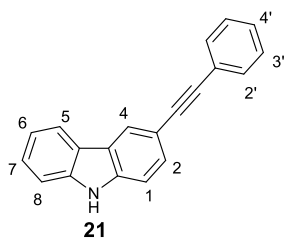
3.20. Synthesis of 3,6-bis[2-(2-thienyl)ethynyl]-9H-carbazole (**20**)



18 (441 mg, 2.05 mmol), CuI (51 mg, 0.27 mmol) and Pd(PPh₃)₂Cl₂ (70 mg, 0.10 mmol) were mixed in 8 mL of anhydrous THF under a nitrogen atmosphere. Then, triethylamine (1.00 mL, 7.18 mmol) and 2-iodothiophene (0.68 mL, 6.16 mmol) were added and the mixture was stirred at room temperature overnight. After, the solvent was distilled off under reduced pressure and the crude was purified by flash column chromatography using a mixture of hexane and dichloromethane (3:1 v/v) as the eluent to give **20** as a white solid.

Yield: 544 mg (70%). **¹H NMR** (400 MHz, Acetone-*d*₆) δ (ppm): 10.83 (s, NH, 1H), 8.43 (s, H⁴, 2H), 7.62–7.58 (m, H¹, H², 4H), 7.52 (dd, ³*J* = 5.2, ⁴*J* = 1.2 Hz, H^{5'}, 2H), 7.35 (dd, ³*J* = 3.6, ⁴*J* = 1.2 Hz, H^{3'}, 2H), 7.11 (dd, ³*J* = 5.2 Hz, ³*J* = 3.6 Hz, H^{4'}, 2H). **¹³C NMR** (100 MHz, Acetone-*d*₆) δ (ppm): 141.3, 132.4, 130.4, 128.3, 128.2, 124.9, 124.5, 123.7, 114.4, 112.5, 95.0, 81.3. **HRMS** (ESI-MS) *m/z*: calcd for C₂₄H₁₄NS₂: 380.0562 (M + H)⁺, found: 380.0547.

3.21. Synthesis of 3-(2-phenylethynyl)-9H-carbazole (**21**)

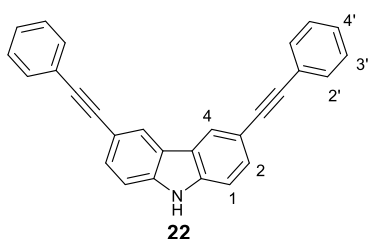


11 (1.00 g, 3.41 mmol), CuI (86 mg, 0.45 mmol) and Pd(PPh₃)₂Cl₂ (119 mg, 0.17 mmol) were mixed in 8 mL of anhydrous THF under a nitrogen atmosphere. Then, triethylamine (1.60 mL, 11.5 mmol) and phenylacetylene (0.57 mL, 5.19 mmol) in anhydrous THF were added and the mixture was stirred at room temperature overnight. After, the solvent was distilled off under reduced pressure and the crude was purified by flash column

chromatography using a mixture of hexane and dichloromethane (3:1 v/v) as the eluent to give **21** as a light brown solid.

Yield: 618 mg (68%). $^1\text{H NMR}$ (400 MHz, Acetone- d_6) δ (ppm): 10.57 (s, NH, 1H), 8.34 (s, H⁴, 1H), 8.20 (d, $^3J = 7.9$ Hz, H⁵, 1H), 7.59–7.54 (m, H¹, H², H⁸, H^{2'}, 5H), 7.46–7.35 (m, H⁷, H^{3'}, H^{4'}, 4H), 7.25–7.21 (m, H⁶, 1H). **HRMS** (ESI-MS) m/z : calcd for C₂₀H₁₄N: 268.1121 (M + H)⁺, found: 268.1124.

3.22. Synthesis of 3,6-bis(2-phenylethynyl)-9H-carbazole (**22**)

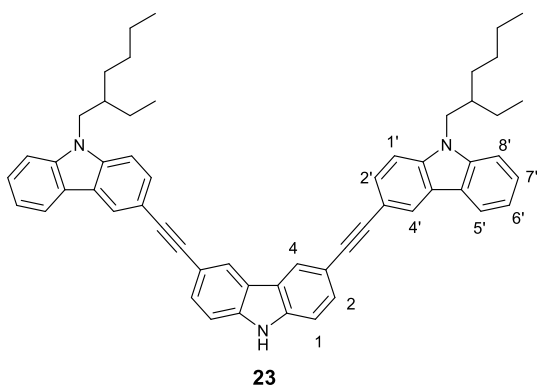


22 (1.19 g, 2.84 mmol), CuI (70 mg, 0.37 mmol) and Pd(PPh₃)₂Cl₂ (98 mg, 0.14 mmol) were mixed in 8 mL of anhydrous THF under a nitrogen atmosphere. Then, triethylamine (1.38 mL, 9.90 mmol) and phenylacetylene (0.97 mL, 8.83 mmol) were added and the mixture was stirred at room temperature overnight. After, the

solvent was distilled off under reduced pressure and the crude was purified by flash column chromatography using a mixture of hexane and dichloromethane (5:1 v/v) as the eluent to give **22** as a pale yellow solid.

Yield: 620 mg (59%). $^1\text{H NMR}$ (400 MHz, Acetone- d_6) δ (ppm): 10.79 (s, NH, 1H), 8.43 (H⁴, 2H), 7.63 (dd, $^3J = 8.4$ Hz, $^4J = 1.5$ Hz, H², 2H), 7.60–7.56 (m, H¹, H^{2'}, 6H), 7.45–7.36 (m, H^{3'}, H^{4'}, 6H). **HRMS** (ESI-MS) m/z : calcd for C₂₈H₁₈N: 368.1434 (M + H)⁺, found: 368.1432.

3.23. Synthesis of 3,6-bis[2-(9-(2-ethylhexyl)-9H-carbazol-3-yl)ethynyl]-9H-carbazole (**23**)



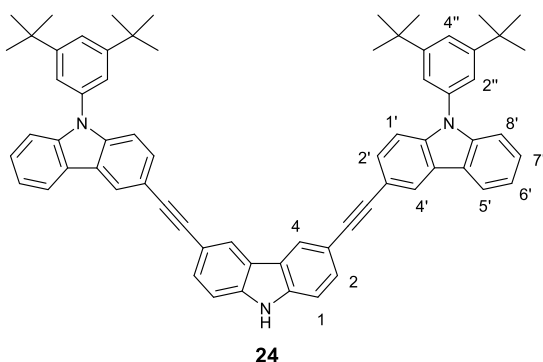
25 (1.19 g, 2.94 mmol), Pd(PPh₃)₂Cl₂ (35 mg, 0.05 mmol) and CuI (25 mg, 0.13 mmol) were dissolved in 10 mL of anhydrous THF under nitrogen atmosphere. Then, triethylamine (0.48 mL, 3.43 mmol) and a solution of **18** (0.21 g, 0.98 mmol) in THF were added and stirred at room temperature for 10 min. After termination of the reaction, the reaction mixture was treated with

water. The aqueous layer was extracted with ethyl acetate and the organic layer was dried over MgSO₄, filtered off and the solvent was distilled off under reduced pressure. The crude was purified

by flash column chromatography using a mixture of hexane and ethyl acetate (9:1 v/v) as the eluent to afford **23** as a white solid.

Yield: 0.23 g (31%). **¹H NMR** (400 MHz, Acetone-*d*₆) δ (ppm): 10.74 (s, NH, 1H), 8.46 (s, H⁴, 2H), 8.39 (d, ⁴*J* = 0.8 Hz, H^{4'}, 2H), 8.25 (d, ³*J* = 7.9 Hz, H^{5'}, 2H), 7.69–7.58 (m, H¹, H², H^{1'}, H^{2'}, H^{8'}, 10H), 7.53–7.48 (m, H^{7'}, 2H), 7.29–7.24 (m, H^{6'}, 2H), 4.35 (d, ³*J* = 7.6 Hz, 2 × N–CH₂, 4H), 2.18–2.10 (m, 2 × CH, 2H), 1.50–1.19 (m, 8 × CH₂, 16H), 0.94 (t, ³*J* = 7.4 Hz, 2 × CH₃, 6H), 0.83 (t, ³*J* = 7.2 Hz, 2 × CH₃, 6H). **¹³C NMR** (100 MHz, CDCl₃) δ (ppm): 141.4, 140.6, 139.3, 130.0, 129.3, 126.1, 124.1, 124.0, 123.3, 123.0, 122.6, 120.6, 119.4, 115.4, 113.8, 110.9, 109.3, 109.2, 89.3, 88.6, 47.7, 39.5, 31.2, 28.9, 24.6, 23.2, 14.2, 11.1. **UV-Vis** (CH₂Cl₂) λ_{\max} (ϵ / dm³ mol⁻¹ cm⁻¹): 305 (84 451), 325 (71 237), 349 (53 501) nm. **HRMS** (ESI-MS) *m/z*: calcd for C₅₆H₅₆N₃: 770.4469 (M + H)⁺, found: 770.4437.

3.24. Synthesis of 3,6-bis[2-(9-(3,5-di-*tert*-butylphenyl)-9*H*-carbazol-3-yl)ethynyl]-9*H*-carbazole (**24**)



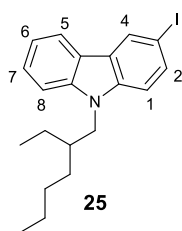
Method A. **26** (0.74 g, 1.53 mmol), Pd(PPh₃)₂Cl₂ (18 mg, 0.026 mmol) and CuI (13 mg, 0.07 mmol) were dissolved in 10 mL of anhydrous THF under nitrogen atmosphere. Then, triethylamine (0.25 mL, 1.78 mmol) and a solution of **18** (0.11 g, 0.51 mmol) in THF were added and stirred at room temperature for 10 min. After termination of the reaction, the reaction mixture was treated with water. The aqueous layer was extracted with ethyl acetate and the organic layer was dried over MgSO₄, filtered off and the solvent was distilled off under reduced pressure. The crude was purified by flash column chromatography using a mixture of hexane and THF (9:1 v/v) as the eluent to afford **24** as a white solid. **Yield:** 0.07 g (15%).

Method B. **28** (0.73 g, 1.92 mmol), Pd(PPh₃)₂Cl₂ (21 mg, 0.03 mmol) and CuI (15 mg, 0.08 mmol) were dissolved in 10 mL of anhydrous THF under nitrogen atmosphere. Then, triethylamine (0.32 mL, 2.24 mmol) and a solution of **12** (0.27 g, 0.64 mmol) in THF were added and stirred at room temperature for 10 min. After termination of the reaction, the reaction mixture was treated with water. The aqueous layer was extracted with ethyl acetate and the organic layer was dried over MgSO₄, filtered off and the solvent was distilled off under reduced pressure. The crude was

purified by flash column chromatography using a mixture of hexane and ethyl acetate (4:1 v/v) as the eluent to afford **24**. **Yield:** 0.14 g (24%).

¹H NMR (400 MHz, Acetone-*d*₆) δ (ppm): 10.76 (s, NH, 1H), 8.48–8.47 (m, H⁴, H^{4'}, 4H), 8.33 (d, ³*J* = 7.8 Hz, H⁵, 2H), 7.69–7.65 (m, H², H^{2'}, H^{4''}, 6H), 7.61 (d, ³*J* = 8.4 Hz, H¹ or H^{1'}, 2H), 7.50 (d, ⁴*J* = 1.7 Hz, H^{2''}, 4H), 7.49–7.43 (m, H⁷, H⁸, H¹ or H^{1'}, 6H), 7.36–7.32 (m, H^{6'}, 2H), 1.44 (s, 12 × CH₃, 36H). **¹³C NMR** (100 MHz, Acetone-*d*₆) δ (ppm): 153.8, 142.3, 141.1, 140.9, 137.5, 130.4, 130.3, 127.5, 124.6, 124.4, 124.3, 123.7, 123.7, 122.6, 121.9, 121.5, 121.2, 115.9, 115.4, 112.3, 111.0, 110.9, 89.8, 89.4, 35.8, 31.7. **UV-Vis** (CH₂Cl₂) λ_{max} (ϵ / dm³ mol⁻¹ cm⁻¹): 305 (80 919), 324 (69 718), 349 (54 247) nm. **MS** (MALDI-TOF) *m/z*: calcd for C₆₈H₆₃N₃: 921.5 (M⁺), found: 921.5.

3.25. Synthesis of 9-(2-ethylhexyl)-3-iodo-9*H*-carbazole (**25**)

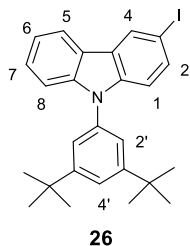


NaH (42 mg, 1.04 mmol, 60% dispersion in mineral oil) was added to a solution of **11** (250 mg, 0.85 mmol) in 5 mL of anhydrous DMF under a nitrogen atmosphere. The solution was stirred at room temperature for 30 minutes. Then, 2-ethylhexyl bromide (185 μ L, 1.04 mmol) was added and the mixture was stirred at 80 °C for 30 minutes. The mixture was cooled down to room temperature and then treated

with water. The aqueous layer was extracted with dichloromethane and the organic layer was dried over anhydrous Na₂SO₄, filtered off and the solvent was distilled off under reduced pressure. The crude was purified by flash column chromatography using hexane as the eluent to afford **25** as an oil.

Yield: 290 mg (84%). **¹H NMR** (400 MHz, Acetone-*d*₆) δ (ppm): 8.50 (d, ⁴*J* = 1.7 Hz, H⁴, 1H), 8.18 (d, ³*J* = 7.8 Hz, H⁵, 1H), 7.72 (dd, ³*J* = 8.6 Hz, ⁴*J* = 1.7 Hz, H², 1H), 7.56 (d, ³*J* = 8.3 Hz, H⁸, 1H), 7.51–7.47 (m, H⁷, 1H), 7.43 (d, ³*J* = 8.6 Hz, H¹, 1H), 7.25–7.21 (m, H⁶, 1H), 4.30 (d, ³*J* = 7.6 Hz, N–CH₂, 2H), 2.14–2.07 (m, CH, 1H), 1.46–1.17 (m, 4 × CH₂, 8H), 0.91 (t, ³*J* = 7.5 Hz, CH₃, 3H), 0.81 (t, ³*J* = 7.2 Hz, CH₃, 3H).

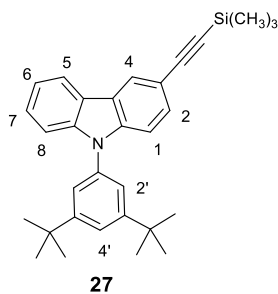
3.26. Synthesis of 9-(3,5-di-*tert*-butylphenyl)-3-iodo-9*H*-carbazole (**26**)



A mixture of **11** (4.50 g, 15.35 mmol), 1-bromo-3,5-di-*tert*-butylbenzene (12.40 g, 46.05 mmol), anhydrous K_2CO_3 (4.24 g, 30.70 mmol) and Cu powder (0.13 g, 1.99 mmol) was refluxed in 35 ml of anhydrous DMF under nitrogen atmosphere for 72 h. After, the reaction mixture was filtered through Celite and diluted with water. The product was extracted with ethyl acetate and the organic layer was washed thoroughly with water until the aqueous layer was neutral. The organic extract was dried over anhydrous $MgSO_4$, filtered off and the solvent was distilled off under reduced pressure. The residue was purified by column chromatography using hexane as the eluent to afford **26** as a white solid.

Yield: 1.51 g (21%). **1H NMR** (400 MHz, Acetone- d_6) δ (ppm): 8.59 (d, $^4J = 1.7$ Hz, H^4 , 1H), 8.27 (d, $^3J = 7.8$ Hz, H^5 , 1H), 7.71 (dd, $^3J = 8.6$ Hz, $^4J = 1.7$ Hz, H^2 , 1H), 7.67 (t, $^4J = 1.7$ Hz, $H^{4'}$, 1H), 7.50–7.45 (m, $H^{2'}$, H^7 , 3H), 7.41 (d, $^3J = 8.2$ Hz, H^8 , 1H), 7.33–7.29 (m, H^6 , 1H), 7.26 (d, $^3J = 8.6$ Hz, H^1 , 1H), 1.42 (s, $6 \times CH_3$, 18H). **^{13}C NMR** (100 MHz, Acetone- d_6) δ (ppm): 153.8, 141.8, 141.0, 137.3, 135.1, 130.0, 127.8, 126.7, 122.8, 122.6, 121.8, 121.5, 121.2, 113.0, 110.8, 82.6, 35.8, 31.7. **HRMS** (ESI-MS) m/z : calcd for $C_{26}H_{29}IN$: 482.1339 ($M + H$) $^+$, found: 482.1348.

3.27. Synthesis of 9-(3,5-di-*tert*-butylphenyl)-3-[2-(trimethylsilyl)ethynyl]-9*H*-carbazole (**27**)

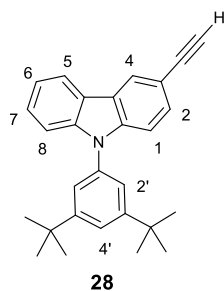


26 (1.33 g, 2.76 mmol), $Pd(PPh_3)_2Cl_2$ (0.10 g, 0.14 mmol) and CuI (0.07 g, 0.36 mmol) were dissolved in 10 mL of anhydrous THF under nitrogen atmosphere. Then, triethylamine (1.35 mL, 9.68 mmol) and ethynyl-trimethylsilane (0.78 mL, 5.50 mmol) dissolved in THF were added and stirred at room temperature for 10 min. After termination of the reaction, the reaction mixture was treated with water. The aqueous layer was extracted with ethyl acetate and the organic layer was dried over $MgSO_4$, filtered off and the solvent was distilled off under reduced pressure. The crude was purified by flash column chromatography using a mixture of hexane and THF (9:1 v/v) as the eluent to afford **27** as a light brown solid.

Yield: 1.23 g (98%). **1H NMR** (400 MHz, Acetone- d_6) δ (ppm): 8.35 (d, $^4J = 1.6$ Hz, H^4 , 1H), 8.30 (d, $^3J = 7.7$ Hz, H^5 , 1H), 7.67 (t, $^4J = 1.8$ Hz, $H^{4'}$, 1H), 7.52 (dd, $^3J = 8.5$ Hz, $^4J = 1.6$ Hz, H^2 , 1H), 7.49–7.45 (m, $H^{2'}$, H^7 , 3H), 7.41 (d, $^3J = 8.1$ Hz, H^8 , 1H), 7.38 (d, $^3J = 8.5$ Hz, H^1 , 1H), 7.34–7.30 (m, H^6 , 1H), 1.42 (s, 6

× CH₃, 18H), 0.27 (s, Si(CH₃)₃, 9H). ¹³C NMR (100 MHz, Acetone-*d*₆) δ (ppm): 153.8, 142.3, 141.4, 137.3, 130.6, 127.6, 125.0, 124.1, 123.6, 122.6, 121.8, 121.5, 121.3, 115.1, 110.9, 110.8, 107.4, 92.2, 35.8, 31.7, 0.2. HRMS (ESI-MS) *m/z*: calcd for C₃₁H₃₈NSi: 452.2768 (M + H)⁺, found: 452.2759.

3.28. Synthesis of 9-(3,5-di-*tert*-butylphenyl)-3-ethynyl-9*H*-carbazole (**28**)

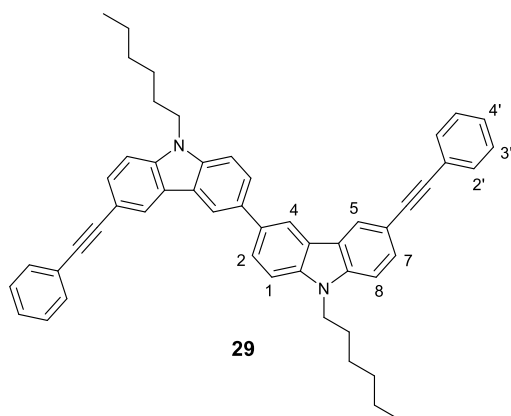


27 (1.2 g, 2.66 mmol) and anhydrous K₂CO₃ (1.84 g, 13.31 mmol) were dissolved in methanol (180 mL). The reaction mixture was stirred at room temperature for 24 h. After termination of the reaction, the solvent was distilled off under reduced pressure. The residue was treated with water and the product was extracted with ethyl acetate. The organic layer was dried over MgSO₄, filtered off and the solvent was distilled off under reduced pressure.

The crude was purified by flash column chromatography using hexane as the eluent to afford **28** as a white solid.

Yield: 0.81 g (80%). ¹H NMR (400 MHz, Acetone-*d*₆) δ (ppm): 8.38 (d, ⁴*J* = 1.6 Hz, H⁴, 1H), 8.28 (d, ³*J* = 7.8 Hz, H⁵, 1H), 7.67 (t, ⁴*J* = 1.8 Hz, H^{4'}, 1H), 7.55 (dd, ³*J* = 8.5 Hz, ⁴*J* = 1.6 Hz, H², 1H), 7.49–7.45 (m, H⁷, H^{2'}, 3H), 7.42 (d, ³*J* = 8.3 Hz, H⁸, 1H), 7.39 (d, ³*J* = 8.5 Hz, H¹, 1H), 7.34–7.30 (m, H⁶, 1H), 3.57 (s, C≡C–H, 1H), 1.42 (s, 6 × CH₃, 18H). ¹³C NMR (100 MHz, Acetone-*d*₆) δ (ppm): 153.3, 141.7, 140.9, 136.8, 130.3, 127.3, 124.9, 123.7, 123.0, 122.2, 121.4, 121.3, 121.0, 113.9, 110.6, 110.5, 85.0, 78.0, 35.4, 31.4. HRMS (ESI-MS) *m/z*: calcd for C₂₈H₃₀N: 380.2373 (M + H)⁺, found: 380.2363.

3.29. Synthesis of 9,9'-dihexyl-6,6'-bis(2-phenylethynyl)-3,3'-bi-9*H*-carbazole (**29**)

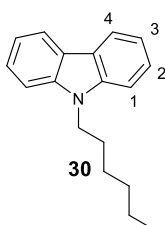


32 (135 mg, 0.18 mmol), CuI (6 mg, 0.03 mmol) and Pd(PPh₃)₂Cl₂ (7 mg, 0.01 mmol) were dissolved in 8 mL of anhydrous THF under nitrogen atmosphere. Then, triethylamine (0.08 mL, 0.57 mmol) and phenylacetylene (0.06 mL, 0.54 mmol) were added and the reaction mixture was stirred at room temperature for 24 h. Afterwards, the solvent was distilled off under reduced pressure and the crude

was purified by column chromatography using a mixture of hexane and dichloromethane (4:1 v/v) as the eluent to afford **29** as a pale yellow solid.

Yield: 72 mg (57%). **¹H NMR** (400 MHz, CDCl₃) δ (ppm): 8.42–8.40 (m, H⁴, H⁵, 4H), 7.85 (dd, ³J = 8.5 Hz, ⁴J = 1.7 Hz, H², 2H), 7.67 (dd, ³J = 8.5 Hz, ⁴J = 1.6 Hz, H⁷, 2H), 7.61–7.58 (m, H^{2'}, 4H), 7.51 (d, ³J = 8.5 Hz, H¹, 2H), 7.40–7.30 (m, H⁸, H^{3'}, H^{4'}, 8H), 4.34 (t, ³J = 7.2 Hz, 2 \times N–CH₂, 4H), 1.96–1.89 (m, 2 \times CH₂, 4H), 1.47–1.27 (m, 6 \times CH₂, 12H), 0.89 (t, ³J = 7.0 Hz, 2 \times CH₃, 6H). **¹³C NMR** (100 MHz, CDCl₃) δ (ppm): 140.7, 140.1, 133.7, 131.6, 129.5, 128.5, 127.9, 126.0, 124.3, 124.1, 123.2, 123.2, 119.1, 113.4, 109.3, 109.0, 91.1, 87.7, 43.5, 31.7, 29.1, 27.1, 22.7, 14.2. **UV-Vis** (THF) λ_{max} (ϵ / dm³ mol⁻¹ cm⁻¹): 313 (86 011), 337 (52 747) nm. **HRMS** (ESI-MS) m/z : calcd for C₅₂H₄₉N₂: 701.3890 (M + H)⁺, found 701.3897.

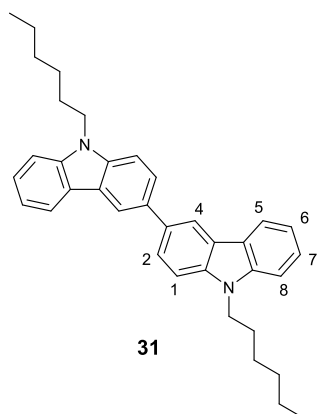
3.30. Synthesis of 9-hexyl-9H-carbazole (30)



NaH (0.96 g, 24.0 mmol, 60% dispersion in mineral oil) was added to a solution of 9H-carbazole (1.99 g, 11.9 mmol) in 14 mL of anhydrous DMF under a nitrogen atmosphere. The solution was stirred at room temperature for 30 minutes. Then, 1-bromohexane (2.51 mL, 17.9 mmol) was added and the mixture was stirred overnight at room temperature and then treated with water. The aqueous layer was extracted with dichloromethane and the organic layer was dried over anhydrous Na₂SO₄, filtered off and the solvent was distilled off under reduced pressure. The crude was purified by flash column chromatography using a mixture of hexane and dichloromethane (10:1 v/v) as the eluent to afford **30** as white solid.

Yield: 2.80 g (94%). **¹H NMR** (400 MHz, Acetone-*d*₆) δ (ppm): 8.13 (d, ³J = 7.8 Hz, H⁴, 2H), 7.56 (d, ³J = 8.2 Hz, H¹, 2H), 7.47–7.43 (m, H², 2H), 7.21–7.17 (m, H³, 2H), 4.42 (t, ³J = 7.2 Hz, N–CH₂, 2H), 1.91–1.83 (m, CH₂, 2H), 1.45–1.24 (m, 3 \times CH₂, 6H), 0.84 (t, ³J = 7.1 Hz, CH₃, 3H).

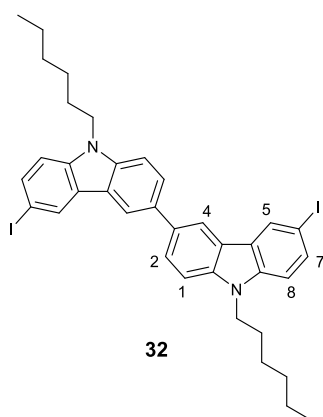
3.31. Synthesis of 9,9'-dihexyl-3,3'-bi-9H-carbazole (31)



30 (4.00 g, 15.9 mmol) and anhydrous iron(III) trichloride (10.33 g, 63.7 mmol) were dissolved in anhydrous chloroform (30 mL) under nitrogen atmosphere. The reaction mixture was stirred at room temperature for 30 min. After, the solution was diluted with methanol and the solvent was distilled off under reduced pressure. The crude was purified by flash column chromatography using a mixture of hexane and dichloromethane as the eluent to afford **31** as a white solid.

Yield: 1.63 g (41%). $^1\text{H NMR}$ (400 MHz, CDCl_3) δ (ppm): 8.42 (d, $^4J = 1.8$ Hz, H^4 , 2H), 8.20 (d, $^3J = 7.6$ Hz, H^5 , 2H), 7.84 (dd, $^3J = 8.4$ Hz, $^4J = 1.8$ Hz, H^4 , 2H), 7.52–7.47 (m, H^1 , H^7 , 4H), 7.44 (d, $^3J = 8.0$ Hz, H^8 , 2H), 7.28–7.24 (m, H^6 , 2H), 4.35 (t, $^3J = 7.2$ Hz, $2 \times \text{N-CH}_2$, 4H), 1.96–1.89 (m, $2 \times \text{CH}_2$, 4H), 1.48–1.27 (m, $6 \times \text{CH}_2$, 12H), 0.89 (t, $^3J = 7.0$ Hz, $2 \times \text{CH}_3$, 6H). $^{13}\text{C NMR}$ (100 MHz, CDCl_3) δ (ppm): 141.0, 139.7, 133.5, 125.8, 125.7, 123.5, 123.2, 120.6, 119.1, 118.9, 109.0, 108.9, 43.4, 31.8, 29.2, 27.2, 22.7, 14.2.

3.32. Synthesis of 9,9'-dihexyl-6,6'-diiodo-3,3'-bi-9H-carbazole (32)



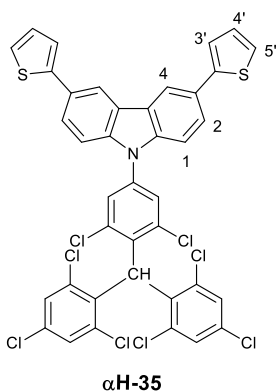
31 (300 mg, 0.60 mmol) was dissolved in glacial acetic acid (10 mL) at reflux. Next, potassium iodide (136 mg, 0.82 mmol) and potassium iodate (197 mg, 0.92 mmol) were added stepwise observing the evolution of iodine gas. The reaction mixture was stirred under reflux for 15 min. Then, the hot solution was decanted to separate the undissolved KIO_3 . After, the solution was cooled down to ambient temperature, diluted with an aqueous sodium bicarbonate solution and the product was extracted with dichloromethane. The combined

organic extract was dried over anhydrous Na_2SO_4 , filtered off and the solvent was distilled off under reduced pressure. The crude was purified by flash column chromatography using, first, hexane, and then a mixture of hexane and ethyl acetate of increasing polarity, from 50:1 to 10:1 (v/v) as the eluent. Compound **32** was obtained as a brown solid.

Yield: 152 mg (34%). $^1\text{H NMR}$ (400 MHz, CDCl_3) δ (ppm): 8.49 (d, $^4J = 1.7$ Hz, H^5 , 2H), 8.33 (d, $^4J = 1.7$ Hz, H^4 , 2H), 7.83 (dd, $^3J = 8.5$ Hz, $^4J = 1.7$ Hz, H^2 , 2H), 7.72 (dd, $^3J = 8.5$ Hz, $^4J = 1.7$ Hz, H^7 , 2H),

7.48 (d, $^3J = 8.5$ Hz, H¹, 2H), 7.22 (d, $^3J = 8.5$ Hz, H⁸, 2H), 4.31 (t, $^3J = 7.3$ Hz, 2 × N-CH₂, 4H), 1.93–1.85 (m, 2 × CH₂, 4H), 1.43–1.25 (m, 6 × CH₂, 12H), 0.88 (t, $^3J = 7.0$ Hz, 2 × CH₃, 6H). ¹³C NMR (100 MHz, CDCl₃) δ (ppm): 140.2, 139.7, 134.0, 133.6, 129.4, 126.3, 125.7, 122.3, 119.1, 111.0, 109.3, 81.3, 43.5, 31.7, 29.1, 27.1, 22.7, 14.2.

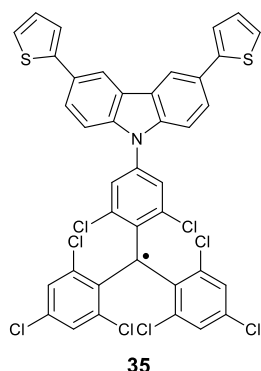
3.33. Synthesis of [4-(3,6-di-2-thienyl-9-carbazolyl)-2,6-dichlorophenyl]bis(2,4,6-trichlorophenyl)methane (α H-35)



A mixture of **14** (613 mg, 1.85 mmol), TTM (852 mg, 1.54 mmol), and anhydrous Cs₂CO₃ (1.30 g, 3.99 mmol) in DMF (10 mL) was stirred at 150 °C under a nitrogen atmosphere in the dark for 4 h. Then, the resulting mixture was cooled down to room temperature, poured into an excess of diluted aqueous HCl acid and extracted with CH₂Cl₂. The organic layer was washed with water, dried over anhydrous Na₂SO₄, filtered off, and the solvent was distilled off under reduced pressure. The residue was chromatographed in silica gel by using a mixture of hexane and dichloromethane (4:1 v/v) as the eluent to give α H-35 as a green solid.

Yield: 545 mg (42%). ¹H NMR (400 MHz, CDCl₃) δ (ppm): 8.36 (d, $^4J = 1.6$ Hz, H⁴, 2H), 7.73 (dd, $^3J = 8.5$ Hz, $^4J = 1.6$ Hz, H², 2H), 7.63 (d, $^4J = 2.2$ Hz, ph, 1H), 7.50 (d, $^4J = 2.2$ Hz, ph, 1H), 7.44 (d, $^3J = 8.5$ Hz, H¹, 2H), 7.44 (d, $^4J = 2.2$ Hz, ph, 1H), 7.42 (d, $^4J = 2.2$ Hz, ph, 1H), 7.39 (dd, $^3J = 3.5$ Hz, $^4J = 0.7$ Hz, H^{3'}, 2H), 7.32–7.29 (m, H^{5'}, ph, 4H), 7.13 (dd, $^3J = 5.0$ Hz, $^3J = 3.5$ Hz, H^{4'}, 2H), 6.87 (s, CH, 1H). ¹³C NMR (100 MHz, CDCl₃) δ (ppm): 145.1, 140.1, 138.7, 138.1, 138.1, 137.9, 137.7, 137.4, 134.4, 134.1, 134.1, 134.0, 130.3, 130.2, 128.7, 128.3, 128.1, 128.1, 126.5, 125.4, 124.4, 124.3, 122.8, 118.2, 110.3, 50.2.

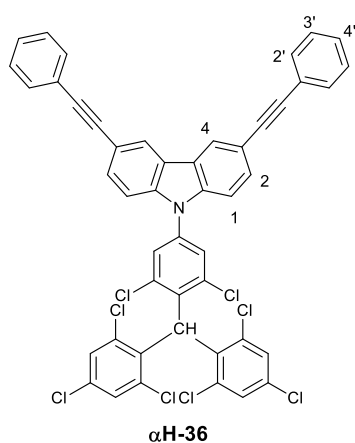
3.34. Synthesis of [4-(3,6-di-2-thienyl-9-carbazolyl)-2,6-dichlorophenyl]bis(2,4,6-trichlorophenyl)methyl radical (**35**)



chloroform as the eluent to give radical adduct **35** as a green solid.

Yield: 67 mg (67%). **IR** (KBr) ν (cm^{-1}): 3099 (w), 3068 (w), 1573 (m), 1553 (m), 1523 (m), 1477 (m), 1423 (w), 1369 (w), 1319 (w), 1285 (w), 1258 (m), 1228 (m), 1181 (m), 1136 (m), 1082 (m), 1019 (m), 925 (w), 870 (w), 857 (m), 795 (s), 755 (w), 724 (w), 686 (s), 665 (w), 656 (w). **UV-Vis** (CHCl_3) λ_{max} ($\epsilon / \text{dm}^3 \text{mol}^{-1} \text{cm}^{-1}$): 267 (36 879), 316 (41 898), 376 (33 876), 626 (3752) nm. **HRMS** (ESI-MS) m/z : calcd for $\text{C}_{39}\text{H}_{18}\text{Cl}_8\text{NS}_2$: 843.8394 (M) $^-$, found: 843.8385.

3.35. Synthesis of {4-[3,6-bis(phenylethynyl)-9-carbazolyl]-2,6-dichlorophenyl}bis(2,4,6-trichlorophenyl)methane (αH -**36**)

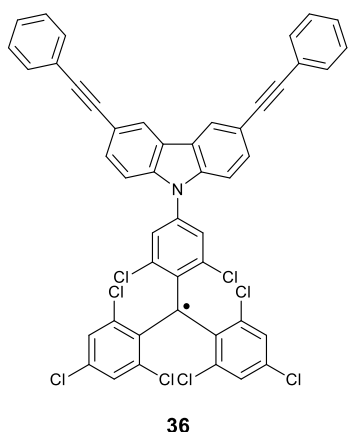


dichloromethane (7:3 v/v) as the eluent to give αH -**36** as a green solid.

Yield: 64 mg (16%). **$^1\text{H NMR}$** (400 MHz, CDCl_3) δ (ppm): 8.31 (d, $^4J = 1.6$ Hz, H^4 , 2H), 7.64 (dd, $^3J = 8.5$ Hz, $^4J = 1.6$ Hz, H^2 , 2H), 7.61–7.58 (m, $\text{H}^{2'}$, ph, 5H), 7.47 (d, $^4J = 2.2$ Hz, ph, 1H), 7.44 (d, $^4J = 2.2$ Hz, ph, 1H), 7.42 (d, $^4J = 2.2$ Hz, ph, 1H), 7.40–7.34 (m, H^1 , $\text{H}^{3'}$, $\text{H}^{4'}$, 8H), 7.32 (d, $^4J = 2.2$ Hz, ph,

1H), 7.29 (d, $^4J = 2.2$ Hz, ph, 1H), 6.87 (s, CH, 1H). ^{13}C NMR (100 MHz, CDCl_3) δ (ppm): 140.2, 138.9, 138.2, 138.1, 138.0, 137.4, 137.3, 137.2, 134.9, 134.1, 134.0, 131.7, 130.5, 130.3, 130.3, 128.7, 128.7, 128.5, 128.3, 128.2, 126.7, 124.4, 123.7, 123.5, 116.2, 110.0, 90.1, 88.6, 50.2.

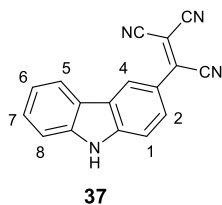
3.36. Synthesis of {4-[3,6-bis(phenylethynyl)-9-carbazolyl]-2,6-dichlorophenyl}bis(2,4,6-trichlorophenyl)methyl radical (36)



An aqueous solution of tetrabutylammonium hydroxide (1.5 M, 0.151 mL, 0.23 mmol) was added to a solution of $\alpha\text{H-36}$ (100 mg, 0.11 mmol) in THF (10 mL) under an Ar atmosphere and the mixture was stirred (4 h) at room temperature. Then, chloranil (77 mg, 0.31 mmol) was added and stirring was extended (45 min). The reaction mixture was poured into diluted hydrochloric acid and filtered. The precipitate was washed with water, dried and chromatographed in silica gel with a mixture of hexane and chloroform as the eluent to give radical adduct **36** as a green solid.

Yield: 88 mg (88%). **IR** (KBr) ν (cm^{-1}): 3060 (w), 3030 (w), 2210 (w), 1594 (w), 1573 (m), 1556 (m), 1522 (m), 1494 (m), 1476 (s), 1454 (w), 1382 (w), 1369 (w), 1351 (m), 1319 (w), 1279 (m), 1226 (m), 1181 (m), 1138 (m), 1082 (w), 1026 (w), 925 (w), 888 (w), 857 (s), 814 (s), 799 (s), 752 (s), 725 (w), 712 (w), 688 (s), 664 (m). **UV-Vis** (CHCl_3) λ_{max} ($\epsilon / \text{dm}^3 \text{mol}^{-1} \text{cm}^{-1}$): 264 (59 630), 286 (49 880), 313 (73 860), 375 (43 520), 609 (4820) nm. **HRMS** (ESI-MS) m/z : calcd for $\text{C}_{47}\text{H}_{22}\text{Cl}_8\text{N}$: 879.9266 (M) $^{\cdot-}$, found: 879.9244.

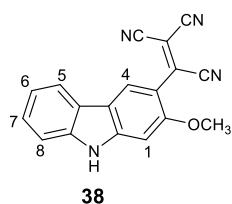
3.37. Synthesis of 3-(1,2,2-tricyanovinyl)-9H-carbazole (37)



9H-Carbazole (300 mg, 1.79 mmol) was dissolved in 10 mL of anhydrous DMF under nitrogen atmosphere. Then, tetracyanoethylene (284 mg, 2.22 mmol) was added and the solution was stirred at 50 °C for 52 h. The cooled mixture was poured into a water/ice solution and the product was extracted with ethyl acetate. The organic layer was dried over anhydrous Na_2SO_4 , filtered off and the solvent was distilled off under reduced pressure. The crude was purified by flash column chromatography using first a mixture of hexane and ethyl acetate (3:1 v/v) followed by 100% ethyl acetate as the eluent to give compound **37** as a red solid.

Yield: 176 mg (37%). **¹H NMR** (400 MHz, Acetone-*d*₆) δ (ppm): 11.27 (s, NH, 1H), 8.94 (d, ⁴*J* = 2.0 Hz, H⁴, 1H), 8.32 (d, ³*J* = 7.9 Hz, H⁵, 1H), 8.21 (dd, ³*J* = 8.8 Hz, ⁴*J* = 2.0 Hz, H², 1H), 7.82 (d, ³*J* = 8.8 Hz, H¹, 1H), 7.67 (d, ³*J* = 8.2 Hz, H⁸, 1H), 7.58–7.54 (m, H⁷, 1H), 7.39–7.35 (m, H⁶, 1H). **¹³C NMR** (100 MHz, DMSO-*d*₆) δ (ppm): 143.9, 140.7, 140.7, 127.7, 126.9, 123.9, 123.3, 122.0, 121.1, 121.0, 119.7, 115.0, 113.4, 113.3, 112.6, 112.2, 86.3. **UV-Vis** (CH₂Cl₂) λ_{\max} (ϵ / dm³ mol⁻¹ cm⁻¹): 288 (19 044), 320 (9929), 332 (13 218), 466 (27 062) nm. **HRMS** (ESI-MS) *m/z*: calcd for C₁₇H₉N₄: 269.0822 (M + H)⁺, found: 269.0818.

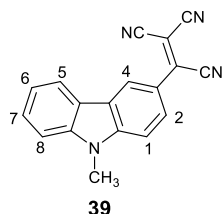
3.38. Synthesis of 2-methoxy-3-(1,2,2-tricyanovinyl)-9H-carbazole (38)



42 (300 mg, 1.52 mmol) was dissolved in 10 mL of anhydrous DMF under a nitrogen atmosphere. Then, tetracyanoethylene (241 mg, 1.88 mmol) was added and the solution was stirred at 50 °C for 48 h. The cooled mixture was poured into a water/ice solution and the product was extracted with ethyl acetate. The organic layer was dried over anhydrous Na₂SO₄, filtered off and the solvent was distilled off under reduced pressure. The crude was purified by flash column chromatography using a mixture of hexane and dichloromethane (1:4 v/v) as the eluent to give compound **38** as a red solid.

Yield: 185 mg (41%). **¹H NMR** (400 MHz, Acetone-*d*₆) δ (ppm): 10.91 (s, NH, 1H), 8.58 (s, H⁴, 1H), 8.14 (d, ³*J* = 7.8 Hz, H⁵, 1H), 7.55 (d, ³*J* = 8.1 Hz, H⁸, 1H), 7.45–7.41 (m, H⁷, 1H), 7.31 (s, H¹, 1H), 7.30–7.26 (m, H⁶, 1H), 4.09 (s, O–CH₃, 3H). **¹³C NMR** (100 MHz, DMSO-*d*₆) δ (ppm): 156.9, 145.7, 140.6, 138.4, 126.3, 124.2, 122.2, 120.6, 120.0, 117.2, 114.6, 112.9, 112.5, 111.7, 110.6, 94.2, 91.6, 56.3. **UV-Vis** (CH₂Cl₂) λ_{\max} (ϵ / dm³ mol⁻¹ cm⁻¹): 295 (19 147), 311 (16 782), 325 (11 702), 464 (19 580) nm. **HRMS** (ESI-MS) *m/z*: calcd for C₁₈H₉N₄O: 297.0782 (M – H)⁻, found: 297.0784.

3.39. Synthesis of 9-methyl-3-(1,2,2-tricyanovinyl)-9H-carbazole (39)

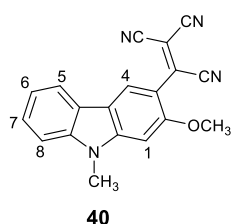


43 (1.00 g, 5.52 mmol) was dissolved in 10 mL of anhydrous DMF under a nitrogen atmosphere. Then, tetracyanoethylene (876 mg, 6.84 mmol) was added and the solution was stirred at 50 °C for 48 h. The cooled mixture was poured into a water/ice solution and the product was extracted with chloroform. The organic layer was dried over anhydrous Na₂SO₄, filtered off and the solvent was distilled off under reduced pressure. The crude was purified by flash column

chromatography using a mixture of hexane and dichloromethane (1:4 v/v) as the eluent to give compound **39** as a red solid.

Yield: 424 mg (27%). **¹H NMR** (400 MHz, Acetone-*d*₆) δ (ppm): 8.93 (d, ⁴*J* = 2.1 Hz, H⁴, 1H), 8.33 (d, ³*J* = 7.8 Hz, H⁵, 1H), 8.27 (dd, ³*J* = 8.9 Hz, ⁴*J* = 2.1 Hz, H², 1H), 7.87 (d, ³*J* = 8.9 Hz, H¹, 1H), 7.72 (d, ³*J* = 8.2 Hz, H⁸, 1H), 7.66–7.62 (m, H⁷, 1H), 7.43–7.39 (m, H⁶, 1H), 4.07 (s, N–CH₃, 3H). **UV-Vis** (CH₂Cl₂) λ_{\max} (ϵ / dm³ mol⁻¹ cm⁻¹): 290 (19 667), 317 (9197), 329 (11 038), 342 (15 986), 490 (32 090) nm. **HRMS** (ESI-MS) *m/z*: calcd for C₁₈H₁₁N₄: 283.0978 (M + H)⁺, found: 283.0976.

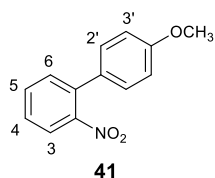
3.40. Synthesis of 2-methoxy-9-methyl-3-(1,2,2-tricyanovinyl)-9H-carbazole (**40**)



40 (380 mg, 1.80 mmol) was dissolved in 10 mL of anhydrous DMF under a nitrogen atmosphere. Then, tetracyanoethylene (297 mg, 2.32 mmol) was added and the solution was stirred at 50 °C for 72 h. The cooled mixture was poured into a water/ice solution and the product was extracted with ethyl acetate. The organic layer was dried over anhydrous Na₂SO₄, filtered off and the solvent was distilled off under reduced pressure. The crude was purified by flash column chromatography using first a mixture of hexane and dichloromethane (1:1 v/v) followed by 100% dichloromethane as the eluent to give compound **40** as a dark green solid.

Yield: 353 mg (63%). **¹H NMR** (400 MHz, DMSO-*d*₆) δ (ppm): 8.57 (s, H⁴, 1H), 8.10 (d, ³*J* = 7.7 Hz, H⁵, 1H), 7.64 (d, ³*J* = 8.2 Hz, H⁸, 1H), 7.53–7.49 (m, H⁷, 1H), 7.44 (s, H¹, 1H), 7.33–7.29 (m, H⁶, 1H), 4.08 (s, O–CH₃, 3H), 3.93 (s, N–CH₃, 3H). **¹³C NMR** (100 MHz, DMSO-*d*₆) δ (ppm): 157.2, 146.3, 141.6, 138.2, 126.3, 124.0, 121.8, 120.9, 120.0, 116.6, 114.6, 112.9, 112.4, 110.5, 110.1, 93.1, 91.6, 56.5, 29.6. **UV-Vis** (CH₂Cl₂) λ_{\max} (ϵ / dm³ mol⁻¹ cm⁻¹): 293 (17 947), 319 (12 003), 334 (11 220), 486 (22 627) nm. **HRMS** (ESI-MS) *m/z*: calcd for C₁₉H₁₃N₄O: 313.1084 (M + H)⁺, found: 313.1090.

3.41. Synthesis of 4'-methoxy-2-nitro-1,1'-biphenyl (**41**)

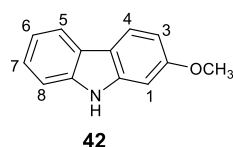


A mixture of 1-bromo-2-nitrobenzene (4.27 g, 21.14 mmol), 4-methoxyphenylboronic acid (3.38 g, 22.24 mmol) and Pd(PPh₃)₄ (1.22 g, 1.06 mmol) in 25 mL of aqueous K₂CO₃ 2M and 30 mL of benzene under a nitrogen atmosphere was stirred at 90 °C for 2 h. Then, the mixture was cooled down to ambient temperature, treated with water and neutralized. The product was extracted with dichloromethane and the organic layer was dried over anhydrous Na₂SO₄, filtered off and the

solvent was distilled off under reduced pressure. The crude was purified by flash column chromatography using a mixture of hexane and ethyl acetate (from 50:1 to 20:1 v/v) as the eluent to give **41** as a yellow oil.

Yield: 4.15 g (86%). **¹H NMR** (400 MHz, CDCl₃) δ (ppm): 7.80 (d, ³J = 8.0 Hz, H³, 1H), 7.61–7.56 (m, H⁵, 1H), 7.46–7.42 (m, H⁴, H⁶, 2H), 7.27–7.24 (m, H^{2'}, 2H), 6.97–6.94 (m, H^{3'}, 2H), 3.85 (s, O–CH₃, 3H). **CI-MS** *m/z*: calcd for C₁₃H₁₂NO₃: 230.1 (M + H)⁺, found: 230.4.

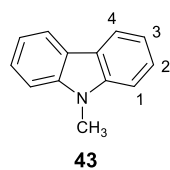
3.42. Synthesis of 2-methoxy-9H-carbazole (**42**)



A mixture of **41** (3.95 g, 17.23 mmol) in 9 mL of triethyl phosphite was heated at 160 °C under a nitrogen atmosphere for 2h. After cooling down to room temperature, hexane was added and the mixture was stirred for 10 min. The product was collected by vacuum filtration yielding compound **42** as a white solid.

Yield: 2.39 g (70%). **¹H NMR** (400 MHz, Acetone-*d*₆) δ (ppm): 10.18 (s, NH, 1H), 7.99 (d, ³J = 7.8 Hz, H⁵, 1H), 7.96 (d, ³J = 8.6 Hz, H⁴, 1H), 7.44 (d, ³J = 8.1 Hz, H⁸, 1H), 7.31–7.26 (m, H⁷, 1H), 7.15–7.11 (m, H⁶, 1H), 7.03 (d, ⁴J = 2.3 Hz, H¹, 1H), 6.81 (dd, ³J = 8.6 Hz, ⁴J = 2.3 Hz, H³, 1H), 3.86 (s, O–CH₃, 3H). **¹³C NMR** (100 MHz, Acetone-*d*₆) δ (ppm): 160.1, 142.4, 141.0, 125.0, 124.2, 121.6, 120.0, 119.7, 117.7, 111.4, 108.8, 95.4, 55.7.

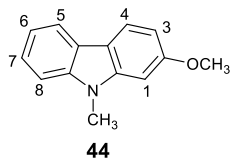
3.43. Synthesis of 9-methyl-9H-carbazole (**43**)



NaH (2.63 g, 65.8 mmol, 60% dispersion in mineral oil) was added to a solution of 9H-carbazole (10.0 g, 59.8 mmol) in 40 mL of anhydrous DMF under a nitrogen atmosphere. The solution was stirred at room temperature for 30 minutes. Then, iodomethane (4.1 mL, 65.8 mmol) was added and the mixture was stirred at room temperature for 30 minutes. After, the mixture was treated with cold water and the formation of a precipitate was observed. The solid was isolated by vacuum filtration, dried and recrystallized from methanol to afford **43** as white crystalline needles.

Yield: 8.8 g (81%). **¹H NMR** (300 MHz, CDCl₃) δ (ppm): 8.10 (d, ³J = 7.8 Hz, H⁴, 2H), 7.51–7.46 (m, H², 2H), 7.41 (d, ³J = 8.1 Hz, H¹, 2H), 7.26–7.21 (m, H³, 2H), 3.86 (s, N–CH₃, 3H).

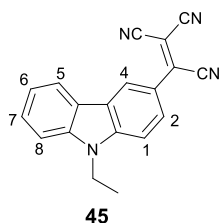
3.44. Synthesis of 2-methoxy-9-methyl-9H-carbazole (44)



NaH (445 mg, 11.13 mmol, 60% dispersion in mineral oil) was added to a solution of **42** (1.96 g, 9.94 mmol) in 18 mL of anhydrous DMF under a nitrogen atmosphere. The solution was stirred at room temperature for 30 minutes. Then, iodomethane (693 μ L, 11.13 mmol) was added and the mixture was stirred at room temperature for 45 minutes and then treated with water. The aqueous layer was extracted with dichloromethane and the organic layer was dried over anhydrous Na_2SO_4 , filtered off and the solvent was distilled off under reduced pressure. The crude was purified by flash column chromatography using a mixture of hexane and dichloromethane (9:1 v/v) as the eluent to give compound **44** as a white solid.

Yield: 1.86 g (89%). $^1\text{H NMR}$ (400 MHz, Acetone- d_6) δ (ppm): 8.01 (d, $^3J = 7.8$ Hz, H^5 , 1H), 7.98 (d, $^3J = 8.5$ Hz, H^4 , 1H), 7.46 (d, $^3J = 8.2$ Hz, H^8 , 1H), 7.39–7.34 (m, H^7 , 1H), 7.18–7.14 (m, H^6 , 1H), 7.08 (d, $^4J = 2.2$ Hz, H^1 , 1H), 6.82 (dd, $^3J = 8.5$ Hz, $^4J = 2.2$ Hz, H^3 , 1H), 3.92 (s, O- CH_3 , 3H), 3.87 (s, N- CH_3 , 3H). $^{13}\text{C NMR}$ (100 MHz, CDCl_3) δ (ppm): 159.3, 142.5, 141.2, 124.5, 123.1, 121.1, 119.5, 119.1, 116.8, 108.3, 107.4, 93.0, 55.8, 29.2.

3.45. Synthesis of 9-ethyl-3-(1,2,2-tricyanovinyl)-9H-carbazole (45)

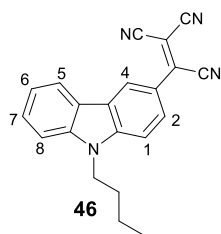


9-Ethyl-9H-carbazole (200 mg, 1.02 mmol) was dissolved in 8 mL of anhydrous DMF under a nitrogen atmosphere. Then, tetracyanoethylene (161 mg, 1.26 mmol) was added and the solution was stirred at 50 $^\circ\text{C}$ for 80 h. The cooled mixture was poured into a water/ice solution and the product was extracted with ethyl acetate. The organic layer was dried over anhydrous Na_2SO_4 , filtered off and the solvent was distilled off under reduced pressure. The crude was purified by flash column chromatography using a mixture of hexane and ethyl acetate (from 10:1 to 5:1 v/v) as the eluent to give compound **45** as a red solid.

Yield: 199 mg (66%). $^1\text{H NMR}$ (400 MHz, DMSO- d_6) δ (ppm): 8.83 (d, $^4J = 2.1$ Hz, H^4 , 1H), 8.32 (d, $^3J = 7.5$ Hz, H^5 , 1H), 8.15 (dd, $^3J = 8.9$ Hz, $^4J = 2.1$ Hz, H^2 , 1H), 7.95 (d, $^3J = 8.9$ Hz, H^1 , 1H), 7.78 (d, $^3J = 8.2$ Hz, H^8 , 1H), 7.64–7.59 (m, H^7 , 1H), 7.40–7.36 (m, H^6 , 1H), 4.55 (q, $^3J = 7.2$ Hz, N- CH_2 , 2H), 1.36 (t, $^3J = 7.2$ Hz, CH_3 , 3H). $^{13}\text{C NMR}$ (100 MHz, DMSO- d_6) δ (ppm): 143.7, 141.1, 141.0, 128.2, 127.4, 124.2, 123.5, 122.3, 121.7, 121.7, 120.2, 115.4, 113.8, 113.7, 111.3, 111.0, 87.1, 38.2, 14.2. **UV-Vis**

(CH₂Cl₂) λ_{\max} (ϵ / dm³ mol⁻¹ cm⁻¹): 292 (13 018), 319 (6734), 330 (8106), 342 (11 489), 493 (22 860) nm. **HRMS** (ESI-MS) m/z : calcd for C₁₉H₁₃N₄: 297.1135 (M + H)⁺, found: 297.1146.

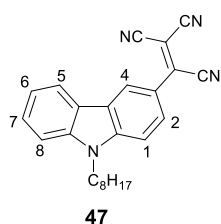
3.46. Synthesis of 9-butyl-3-(1,2,2-tricyanovinyl)-9H-carbazole (46)



49 (476 mg, 2.13 mmol) was dissolved in 10 mL of anhydrous DMF under a nitrogen atmosphere. Then, tetracyanoethylene (327 mg, 2.55 mmol) was added and the solution was heated to 50 °C for 52 h. The cooled mixture was poured into a water/ice solution and the product was extracted with ethyl acetate. The organic layer was dried over anhydrous Na₂SO₄, filtered off and the solvent was distilled off under reduced pressure. The crude was purified by flash column chromatography using a mixture of hexane and ethyl acetate (from 10:1 to 5:1 v/v) as the eluent to give compound **46** as a red solid.

Yield: 336 mg (49%). **¹H NMR** (400 MHz, DMSO-*d*₆) δ (ppm): 8.83 (d, ⁴*J* = 2.0 Hz, H⁴, 1H), 8.32 (d, ³*J* = 7.6 Hz, H⁵, 1H), 8.14 (dd, ³*J* = 8.9 Hz, ⁴*J* = 2.0 Hz, H², 1H), 7.95 (d, ³*J* = 8.9 Hz, H¹, 1H), 7.78 (d, ³*J* = 8.3 Hz, H⁸, 1H), 7.63–7.59 (m, H⁷, 1H), 7.40–7.36 (m, H⁶, 1H), 4.51 (t, ³*J* = 7.1 Hz, N–CH₂, 2H), 1.82–1.75 (m, CH₂, 2H), 1.35–1.25 (m, CH₂, 2H), 0.88 (t, ³*J* = 7.4 Hz, CH₃, 3H). **¹³C NMR** (100 MHz, DMSO-*d*₆) δ (ppm): 143.8, 141.0, 140.5, 127.7, 126.8, 123.8, 122.9, 121.8, 121.2, 121.1, 119.7, 114.9, 113.4, 113.3, 111.1, 110.8, 86.5, 42.7, 30.6, 19.7, 13.6. **UV-Vis** (CH₂Cl₂) λ_{\max} (ϵ / dm³ mol⁻¹ cm⁻¹): 292 (12 168), 319 (6261), 330 (7654), 343 (11 156), 494 (21 858) nm. **HRMS** (ESI-MS) m/z : calcd for C₂₁H₂₀N₅: 342.1713 (M + NH₄)⁺, found: 342.1713.

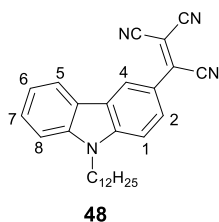
3.47. Synthesis of 9-octyl-3-(1,2,2-tricyanovinyl)-9H-carbazole (47)



50 (481 mg, 1.72 mmol) was dissolved in 10 mL of anhydrous DMF under a nitrogen atmosphere. Then, tetracyanoethylene (264 mg, 2.06 mmol) was added and the solution was stirred at 50 °C for 72 h. The cooled mixture was poured into a water/ice solution and the product was extracted with ethyl acetate. The organic layer was dried over anhydrous Na₂SO₄, filtered off and the solvent was distilled off under reduced pressure. The crude was purified by flash column chromatography using first hexane followed by a mixture of hexane and ethyl acetate (from 10:1 to 2:1 v/v) as the eluent to give compound **47** as a red solid.

Yield: 272 mg (42%). **¹H NMR** (400 MHz, CDCl₃) δ (ppm): 8.82 (d, ⁴*J* = 2.0 Hz, H⁴, 1H), 8.26 (dd, ³*J* = 9.0 Hz, ⁴*J* = 2.0 Hz, H², 1H), 8.16 (d, ³*J* = 7.8 Hz, H⁵, 1H), 7.63–7.58 (m, H⁷, 1H), 7.51 (d, ³*J* = 9.0 Hz, H¹, 1H), 7.50 (d, ³*J* = 8.2 Hz, H⁸, 1H), 7.42–7.38 (m, H⁶, 1H), 4.35 (t, ³*J* = 7.2 Hz, N–CH₂, 2H), 1.94–1.87 (m, CH₂, 2H), 1.42–1.20 (m, 5 × CH₂, 10H), 0.86 (t, ³*J* = 6.8 Hz, CH₃, 3H). **¹³C NMR** (100 MHz, CDCl₃) δ (ppm): 144.7, 141.6, 140.9, 128.2, 127.5, 124.4, 124.3, 122.7, 122.0, 121.4, 120.1, 114.6, 113.2, 112.8, 110.3, 110.3, 84.5, 44.0, 31.9, 29.4, 29.2, 29.1, 27.4, 22.7, 14.2. **UV-Vis** (CH₂Cl₂) λ_{max} (ϵ / dm³ mol⁻¹ cm⁻¹): 292 (13 641), 319 (7207), 330 (8665), 343 (12 618), 494 (25 256) nm. **HRMS** (ESI-MS) *m/z*: calcd for C₂₅H₂₈N₅: 398.2339 (M + NH₄)⁺, found: 398.2340.

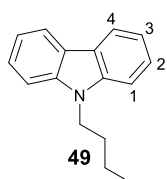
3.48. Synthesis of 9-dodecyl-3-(1,2,2-tricyanovinyl)-9H-carbazole (48)



51 (671 mg, 2.00 mmol) was dissolved in 10 mL of anhydrous DMF under a nitrogen atmosphere. Then, tetracyanoethylene (307 mg, 2.40 mmol) was added and the solution was stirred at 50 °C for 72 h. The cooled mixture was poured into a water/ice solution and the product was extracted with ethyl acetate. The organic layer was dried over anhydrous Na₂SO₄, filtered off and the solvent was distilled off under reduced pressure. The crude was purified by flash column chromatography using first hexane followed by a mixture of hexane and ethyl acetate (from 10:1 to 5:1 v/v) as the eluent to give compound **48** as a red solid.

Yield: 409 mg (47%). **¹H NMR** (400 MHz, CDCl₃) δ (ppm): 8.82 (d, ⁴*J* = 2.1 Hz, H⁴, 1H), 8.26 (dd, ³*J* = 9.0 Hz, ⁴*J* = 2.1 Hz, H², 1H), 8.16 (d, ³*J* = 7.8 Hz, H⁵, 1H), 7.63–7.58 (m, H⁷, 1H), 7.51 (d, ³*J* = 9.0 Hz, H¹, 1H), 7.49 (d, ³*J* = 8.2 Hz, H⁸, 1H), 7.42–7.38 (m, H⁶, 1H), 4.35 (t, ³*J* = 7.2 Hz, N–CH₂, 2H), 1.94–1.87 (m, CH₂, 2H), 1.42–1.20 (m, 9 × CH₂, 18H), 0.88 (t, ³*J* = 6.9 Hz, CH₃, 3H). **¹³C NMR** (100 MHz, CDCl₃) δ (ppm): 144.7, 141.6, 140.9, 128.2, 127.5, 124.4, 124.3, 122.6, 122.0, 121.4, 120.0, 114.6, 113.2, 112.8, 110.3, 110.3, 84.5, 44.0, 32.0, 29.7, 29.6, 29.6, 29.5, 29.4, 29.1, 27.4, 22.8, 14.3. **UV-Vis** (CH₂Cl₂) λ_{max} (ϵ / dm³ mol⁻¹ cm⁻¹): 292 (13 534), 319 (6486), 330 (8046), 343 (12 148), 494 (23 595) nm. **HRMS** (ESI-MS) *m/z*: calcd for C₂₉H₃₆N₅: 454.2965 (M + NH₄)⁺, found: 454.2957.

3.49. Synthesis of 9-butyl-9H-carbazole (49)

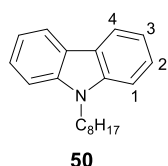


NaH (526 mg, 13.15 mmol, 60% dispersion in mineral oil) was added to a solution of 9H-carbazole (2.00 g, 11.96 mmol) in 15 mL of anhydrous DMF under a nitrogen atmosphere. The solution was stirred at room temperature for 30 minutes. Then,

1-bromobutane (1.41 mL, 13.15 mmol) was added and the mixture was stirred at 80 °C for 1 h. Then, the mixture was cooled down to ambient temperature and treated with water. The aqueous layer was extracted with ethyl acetate and the organic layer was dried over anhydrous Na₂SO₄, filtered off and the solvent was distilled off under reduced pressure. The crude product was purified by recrystallization from ethanol to afford **49** as a white solid.

Yield: 2.30 g (86%). **¹H NMR** (400 MHz, CDCl₃) δ (ppm): 8.11 (d, ³J = 7.8 Hz, H⁴, 2H), 7.49–7.45 (m, H², 2H), 7.41 (d, ³J = 8.1 Hz, H¹, 2H), 7.25–7.21 (m, H³, 2H), 4.32 (t, ³J = 7.2 Hz, N–CH₂, 2H), 1.91–1.83 (m, CH₂, 2H), 1.46–1.37 (m, CH₂, 2H), 0.96 (t, ³J = 7.4 Hz, CH₃, 3H). **HRMS** (ESI-MS) *m/z*: calcd for C₁₆H₁₈N: 224.1434 (M + H)⁺, found: 224.1436.

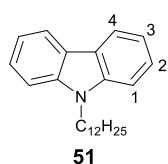
3.50. Synthesis of 9-octyl-9H-carbazole (**50**)



NaH (526 mg, 13.15 mmol, 60% dispersion in mineral oil) was added to a solution of 9H-carbazole (2.00 g, 11.96 mmol) in 15 mL of anhydrous DMF under a nitrogen atmosphere. The solution was stirred at room temperature for 30 minutes. Then, 1-bromooctane (2.27 mL, 13.15 mmol) was added and the mixture was stirred at 80 °C for 1 h. Then, the mixture was cooled down to ambient temperature and treated with water. The aqueous layer was extracted with ethyl acetate and the organic layer was dried over anhydrous Na₂SO₄, filtered off and the solvent was distilled off under reduced pressure. The crude product was purified by flash column chromatography using hexane as the eluent to give **50** as an oil.

Yield: 2.64 g (79%). **¹H NMR** (400 MHz, CDCl₃) δ (ppm): 8.10 (d, ³J = 7.8 Hz, H⁴, 2H), 7.48–7.44 (m, H², 2H), 7.41 (d, ³J = 8.2 Hz, H¹, 2H), 7.24–7.21 (m, H³, 2H), 4.30 (t, ³J = 7.3 Hz, N–CH₂, 2H), 1.91–1.83 (m, CH₂, 2H), 1.43–1.24 (m, 5 × CH₂, 10H), 0.86 (t, ³J = 6.9 Hz, CH₃, 3H). **HRMS** (ESI-MS) *m/z*: calcd for C₂₀H₂₆N: 280.2060 (M + H)⁺, found: 280.2065.

3.51. Synthesis of 9-dodecyl-9H-carbazole (**51**)

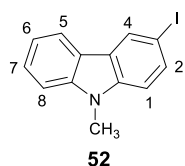


NaH (526 mg, 13.15 mmol, 60% dispersion in mineral oil) was added to a solution of 9H-carbazole (2.00 g, 11.96 mmol) in 15 mL of anhydrous DMF under a nitrogen atmosphere. The solution was stirred at room temperature for 30 minutes. Then, 1-bromododecane (3.16 mL, 13.15 mmol) was added and the mixture was stirred at 80 °C for 1 h. Then, the mixture was cooled down to ambient temperature and treated with water. The aqueous layer was extracted with ethyl acetate and the organic layer was dried over

anhydrous Na₂SO₄, filtered off and the solvent was distilled off under reduced pressure. The crude product was purified by flash column chromatography using hexane as the eluent to give **51** as an oil.

Yield: 3.38 g (84%). **¹H NMR** (400 MHz, CDCl₃) δ (ppm): 8.11 (d, ³J = 7.8 Hz, H⁴, 2H), 7.49–7.44 (m, H², 2H), 7.41 (d, ³J = 8.0 Hz, H¹, 2H), 7.25–7.21 (m, H³, 2H), 4.30 (t, ³J = 7.3 Hz, N–CH₂, 2H), 1.91–1.83 (m, CH₂, 2H), 1.43–1.24 (m, 9 × CH₂, 18H), 0.88 (t, ³J = 6.9 Hz, CH₃, 3H). **HRMS** (ESI-MS) *m/z*: calcd for C₂₄H₃₄N: 336.2686 (M + H)⁺, found: 336.2690.

3.52. Synthesis of 3-iodo-9-methyl-9H-carbazole (**52**)

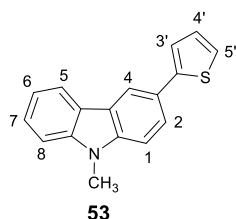


NaH (240 mg, 6.00 mmol, 60% dispersion in mineral oil) was added to a solution of **11** (1.60 g, 5.46 mmol) in anhydrous DMF (10 mL) under nitrogen atmosphere. The solution was stirred at room temperature for 30 minutes. Then, iodomethane (374 μ L, 6.00 mmol) was added and the mixture was stirred at room temperature

for 30 minutes and then treated with water. The aqueous layer was extracted with dichloromethane and the organic layer was dried over anhydrous Na₂SO₄, filtered off and the solvent was distilled off under reduced pressure. The crude was purified by flash column chromatography using a mixture of hexane and ethyl acetate (20:1 v/v) as the eluent to give **52** as an oil.

Yield: 1.45 g (86%). **¹H NMR** (400 MHz, Acetone-*d*₆) δ (ppm): 8.49 (d, ⁴J = 1.7 Hz, H⁴, 1H), 8.17 (d, ³J = 7.6 Hz, H⁵, 1H), 7.74 (dd, ³J = 8.6 Hz, ⁴J = 1.7 Hz, H², 1H), 7.55 (d, ³J = 8.2 Hz, H⁸, 1H), 7.53–7.48 (m, H⁷, 1H), 7.42 (d, ³J = 8.6 Hz, H¹, 1H), 7.26–7.22 (m, H⁶, 1H), 3.91 (s, N–CH₃, 3H). **CI-MS** *m/z*: calcd for C₁₃H₁₁IN: 308.0 (M + H)⁺, found: 308.0.

3.53. Synthesis of 9-methyl-3-(2-thienyl)-9H-carbazole (**53**)



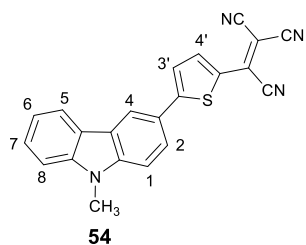
A mixture of **52** (771 mg, 2.51 mmol), 2-(tributylstannyl)thiophene (1.12 g, 3.00 mmol) and Pd(PPh₃)₄ (139 mg, 0.12 mmol) in anhydrous DMF (10 mL) was heated at 100 °C for 24 h under a nitrogen atmosphere. Then, the reaction mixture was cooled down to room temperature, treated with water and the product was extracted with dichloromethane. The organic layer was

dried over anhydrous Na₂SO₄, filtered off and the solvent was distilled off under reduced pressure.

The crude was purified by flash column chromatography using a mixture of hexane and dichloromethane (9:1 v/v) as the eluent to give compound **53** as a white solid.

Yield: 343 mg (52%). **¹H NMR** (400 MHz, CDCl₃) δ (ppm): 8.32 (d, ⁴J = 1.8 Hz, H⁴, 1H), 8.14 (d, ³J = 7.7 Hz, H⁵, 1H), 7.75 (dd, ³J = 8.5 Hz, ⁴J = 1.8 Hz, H², 1H), 7.52–7.48 (m, H⁷, 1H), 7.41 (d, ³J = 8.1 Hz, H⁸, 1H), 7.40 (d, ³J = 8.5 Hz, H¹, 1H), 7.35 (dd, ³J = 3.6 Hz, ⁴J = 1.0 Hz, H^{3'}, 1H), 7.28–7.24 (m, H^{5'} and H⁶, 2H), 7.11 (dd, ³J = 5.1 Hz, ³J = 3.6 Hz, H^{4'}, 1H), 3.87 (s, N–CH₃, 3H). **¹³C NMR** (100 MHz, CDCl₃) δ (ppm): 146.0, 141.6, 140.7, 128.1, 126.2, 125.9, 124.5, 123.8, 123.3, 122.9, 122.2, 120.6, 119.3, 118.0, 108.9, 108.8, 29.4. **HRMS** (ESI-MS) *m/z*: calcd for C₁₇H₁₄NS: 264.0841 (M + H)⁺, found: 264.0843.

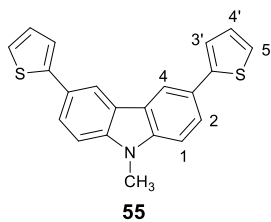
3.54. Synthesis of 9-methyl-3-[5-(1,2,2-tricyanovinyl)thiophen-2-yl]-9H-carbazole (**54**)



53 (195 mg, 0.74 mmol) and tetracyanoethylene (117 mg, 0.91 mmol) were dissolved in 4 mL of anhydrous DMF in a microwave vial and the system was purged with nitrogen. The sealed vial was heated at 80 °C for 2 h under microwave irradiation. TLC control of the reaction revealed that it was not completed, so tetracyanoethylene (58 mg, 0.45 mmol) was added and the solution was heated for an additional 1 h. Then, the reaction mixture was poured into a water/ice solution and the formation of a green precipitate was observed. The solid was isolated by vacuum filtration, dried and recrystallized from hexane/dichloromethane to afford compound **54** as a dark green solid.

Yield: 237 mg (88%). **¹H NMR** (400 MHz, DMSO-*d*₆) δ (ppm): 8.83 (d, ⁴J = 1.9 Hz, H⁴, 1H), 8.35 (d, ³J = 7.5 Hz, H⁵, 1H), 8.20 (d, ³J = 4.4 Hz, H^{3'}, 1H), 8.05 (d, ³J = 4.4 Hz, H^{4'}, 1H), 8.00 (d, ³J = 8.7 Hz, ⁴J = 1.9 Hz, H², 1H), 7.76 (d, ³J = 8.7 Hz, H¹, 1H), 7.67 (d, ³J = 7.8 Hz, H⁸, 1H), 7.57–7.53 (m, H⁷, 1H), 7.32–7.28 (m, H⁶, 1H), 3.94 (s, N–CH₃, 3H). **UV-Vis** (CH₂Cl₂) λ_{\max} (ϵ / dm³ mol⁻¹ cm⁻¹): 294 (22 059), 342 (7965), 377 (6183), 566 (36 974) nm. **HRMS** (ESI-MS) *m/z*: calcd for C₂₂H₁₂N₄S: 364.0777 (M)⁺, found: 364.0779.

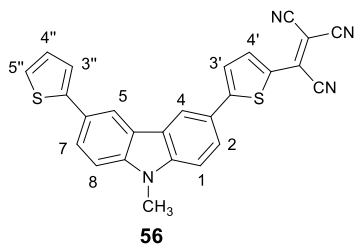
3.55. Synthesis of 9-methyl-3,6-di-2-thienyl-9H-carbazole (55)



NaH (33 mg, 0.83 mmol, 60% dispersion in mineral oil) was added to a solution of **14** (252 mg, 0.76 mmol) in anhydrous DMF (10 mL) under nitrogen atmosphere. The solution was stirred at room temperature for 30 minutes. Then, iodomethane (52 μ L, 0.83 mmol) was added and the mixture was stirred at room temperature for 30 minutes and then treated with water. The aqueous layer was extracted with dichloromethane and the organic layer was dried over anhydrous Na_2SO_4 , filtered off and the solvent was distilled off under reduced pressure. The crude was purified by flash column chromatography using a mixture of hexane and dichloromethane (5:1 v/v) as the eluent to give **55** as a white solid.

Yield: 215 mg (82%). **$^1\text{H NMR}$** (400 MHz, CDCl_3) δ (ppm): 8.35 (d, $^4J = 1.8$ Hz, H^4 , 2H), 7.77 (dd, $^3J = 8.5$ Hz, $^4J = 1.8$ Hz, H^2 , 2H), 7.40 (d, $^3J = 8.5$ Hz, H^1 , 2H), 7.37 (dd, $^3J = 3.5$ Hz, $^4J = 1.0$ Hz, $\text{H}^{3'}$, 2H), 7.27 (dd, $^3J = 5.1$ Hz, $^4J = 1.0$ Hz, $\text{H}^{5'}$, 2H), 7.12 (dd, $^3J = 5.1$ Hz, $^3J = 3.5$ Hz, $\text{H}^{4'}$, 2H), 3.88 (s, N- CH_3 , 3H). **$^{13}\text{C NMR}$** (100 MHz, CDCl_3) δ (ppm): 145.8, 141.1, 128.2, 126.2, 124.8, 123.9, 123.3, 122.3, 118.1, 109.1, 29.5. **HRMS** (ESI-MS) m/z : calcd for $\text{C}_{21}\text{H}_{16}\text{NS}_2$: 346.0719 ($\text{M} + \text{H}$) $^+$, found: 346.0732.

3.56. Synthesis of 9-methyl-6-(2-thienyl)-3-[5-(1,2,2-tricyanovinyl)thiophen-2-yl]-9H-carbazole (56)

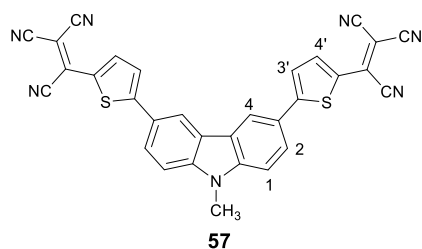


55 (169 mg, 0.49 mmol) was dissolved in 6 mL of anhydrous DMF under a nitrogen atmosphere. Then, tetracyanoethylene (63 mg, 0.49 mmol) was added and the solution was stirred at 50 $^\circ\text{C}$ for 48 h. Then, the cooled mixture was poured into a water/ice solution. The aqueous layer was extracted with dichloromethane and the organic layer was dried over anhydrous Na_2SO_4 , filtered off and the solvent was distilled off under reduced pressure. The crude was purified by flash column chromatography using first a mixture of hexane and dichloromethane (from 2:1 to 1:2 v/v) followed by 100% dichloromethane to give **56** as a green solid.

Yield: 110 mg of **56** (50%). A small amount of **57** (8 mg, yield: 3%) was also obtained. **$^1\text{H NMR}$** (400 MHz, CDCl_3) δ (ppm): 8.50 (d, $^4J = 1.8$ Hz, H^4 or H^5 , 1H), 8.40 (d, $^4J = 1.8$ Hz, H^4 or H^5 , 1H), 8.10 (d, $^3J = 4.4$ Hz, $\text{H}^{3'}$, 1H), 7.87 (dd, $^3J = 8.7$ Hz, $^4J = 1.8$ Hz, H^2 or H^7 , 1H), 7.83 (dd, $^3J = 8.7$ Hz, $^4J = 1.8$ Hz, H^2 or H^7 , 1H), 7.64 (d, $^3J = 4.4$ Hz, $\text{H}^{4'}$, 1H), 7.47 (d, $^3J = 8.7$ Hz, H^1 or H^8 , 1H), 7.45 (d, $^3J =$

8.7 Hz, H¹ or H⁸, 1H), 7.42 (dd, ³J = 3.6 Hz, ⁴J = 1.0 Hz, H^{3''}, 1H), 7.31 (dd, ³J = 5.2 Hz, ⁴J = 1.0 Hz, H^{5''}, 1H), 7.14 (dd, ³J = 5.2 Hz, ³J = 3.6 Hz, H^{4''}, 1H), 3.93 (s, N-CH₃, 3H). **HRMS** (ESI-MS) *m/z*: calcd for C₂₆H₁₅N₄S₂: 447.0733 (M + H)⁺, found: 447.0720.

3.57. Synthesis of 9-methyl-3,6-bis[5-(1,2,2-tricyanovinyl)thiophen-2-yl]-9H-carbazole (57)

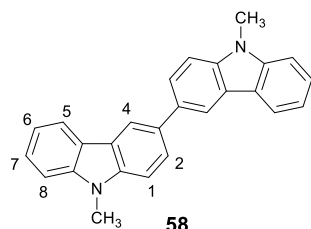


55 (59 mg, 0.17 mmol) was dissolved in 4 mL of anhydrous DMF under a nitrogen atmosphere. Then, tetracyanoethylene (65 mg, 0.51 mmol) was added and the solution was stirred at 50 °C for 24 h. Then, additional tetracyanoethylene (65 mg, 0.51 mmol) was added and the

reaction mixture was stirred for another 48 h. The cooled mixture was poured into a water/ice solution and the formation of a green precipitate was observed. The solid was isolated by vacuum filtration, washed thoroughly with dichloromethane and dried to afford compound **57** as a dark green solid.

Yield: 69 mg (74%). **MS** (MALDI-TOF) *m/z*: calcd for C₃₁H₁₄N₇S₂: 548.1 (M + H)⁺, found: 548.1.

3.58. Synthesis of 9,9'-dimethyl-9H,9H'-[3,3']bicarbazole (58)



43 (5.6 g, 31.1 mmol) was dissolved in anhydrous CHCl₃ (70 mL) under nitrogen atmosphere. Subsequently, FeCl₃ (13.7 g, 84.5 mmol) was added and the reaction mixture was stirred at room temperature for 30 minutes. Then, the mixture was poured into methanol and the formation of a precipitate was observed. The solid was isolated by

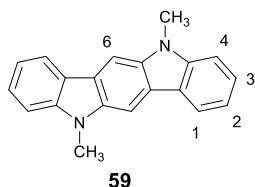
vacuum filtration, washed thoroughly with methanol and then dried. The crude was purified by flash column chromatography using a mixture of hexane and dichloromethane (1:1 v/v) as the eluent to give compound **58** as a white solid.

Yield: 4.3 g (73%). **¹H NMR** (400 MHz, DMSO-*d*₆) δ (ppm): 8.55 (d, ⁴J = 1.7 Hz, H⁴, 2H), 8.26 (d, ³J = 7.6 Hz, H⁵, 2H), 7.89 (dd, ³J = 8.5 Hz, ⁴J = 1.7 Hz, H², 2H), 7.67 (d, ³J = 8.5 Hz, H¹, 2H), 7.58 (d, ³J = 8.2 Hz, H⁸, 2H), 7.50–7.46 (m, H⁷, 2H), 7.24–7.21 (m, H⁶, 2H), 3.92 (s, 2 × N-CH₃, 6H). **UV-Vis** (CH₂Cl₂) λ_{max} (ε / dm³ mol⁻¹ cm⁻¹): 303 (76 660), 343 (9003), 356 (6582) nm. **¹³C NMR** (100 MHz, DMSO-*d*₆)

δ (ppm): 141.1, 139.7, 132.2, 125.8, 125.0, 122.7, 122.3, 120.4, 118.7, 118.2, 109.4, 109.2, 29.1.

HRMS (ESI-MS) m/z : calcd for $C_{26}H_{21}N_2$: 361.1699 ($M+H$)⁺, found: 361.1684.

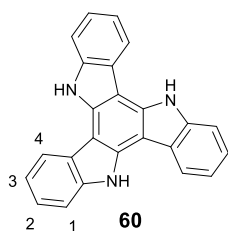
3.59. Synthesis of 5,11-dihydro-5,11-dimethylindolo[3,2-*b*]carbazole (**59**)



NaH (12 mg, 0.52 mmol) was added to a solution of **64** (60 mg, 0.23 mmol) in anhydrous DMF under nitrogen atmosphere. The solution was stirred at room temperature for 30 minutes. Then, iodomethane (32 μ L, 0.52 mmol) was added and the mixture was stirred at room temperature for 30 minutes and then treated with water. The aqueous layer was extracted with dichloromethane and the organic layer was dried over anhydrous Na_2SO_4 . The solvent was removed by evaporation and the crude was purified by flash column chromatography using a mixture of hexane and dichloromethane (4:1 v/v) to give compound **59** as a yellow solid.

Yield: 55 mg (83%). **¹H NMR** (400 MHz, $CDCl_3$) δ (ppm): 8.20 (d, $^3J = 8.0$ Hz, H^1 , 2H), 8.02 (s, H^6 , 2H), 7.53–7.49 (m, H^3 , 2H), 7.42 (d, $^3J = 8.0$ Hz, H^4 , 2H), 7.26–7.22 (m, H^2 , 2H), 3.96 (s, 2 \times N- CH_3 , 6H). **¹³C NMR** (100 MHz, $CDCl_3$) δ (ppm): 142.3, 136.9, 125.8, 123.0, 122.9, 120.3, 118.2, 108.3, 98.7, 29.5. **UV-Vis** (CH_2Cl_2) λ_{max} ($\epsilon / dm^3 mol^{-1} cm^{-1}$): 283 (52 268), 325 (31 095), 341 (62 044), 394 (4805), 416 (6814) nm. **HRMS** (ESI-MS) m/z : calcd for $C_{20}H_{17}N_2$: 285.1386 ($M+H$)⁺, found: 285.1382.

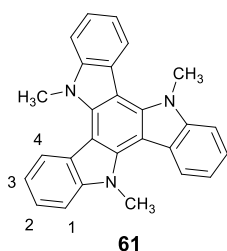
3.60. Synthesis of 10,15-dihydro-5H-diindolo[3,2-*a*:3',2'-*c*]carbazole (**60**)



A solution of 2-oxindole (7.00 g, 52.6 mmol) in $POCl_3$ (35 mL) was stirred under reflux for 6 h. After cooling down to room temperature, the mixture was poured into ice-water, and neutralized with an aqueous 1M NaOH solution. Then, the precipitate was filtered off, washed thoroughly with water and dried. The product was purified by flash column chromatography using a mixture of hexane and ethyl acetate (5:1 v/v) as the eluent to give **60** as a white solid.

Yield: 3.15 g (52%). **¹H NMR** (400 MHz, $DMSO-d_6$) δ (ppm): 11.85 (s, NH, 3H), 8.67 (d, $^3J = 7.3$ Hz, H^4 , 3H), 7.72 (d, $^3J = 7.7$ Hz, H^1 , 3H), 7.40–7.36 (m, H^2 , 3H), 7.34–7.31 (m, H^3 , 3H). **¹³C NMR** (100 MHz, $DMSO-d_6$) δ (ppm): 138.5, 133.8, 122.4, 122.2, 119.9, 119.1, 111.0, 100.6. **UV-Vis** (CH_2Cl_2) λ_{max} ($\epsilon / dm^3 mol^{-1} cm^{-1}$): 273 (33068), 306 (60 233), 317 (37 893), 337 (9404) nm. **HRMS** (ESI-MS) m/z : calcd for $C_{24}H_{16}N_3$: 346.1339 ($M+H$)⁺, found: 346.1342.

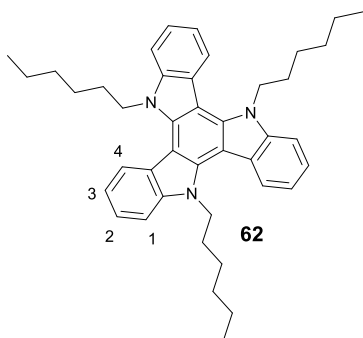
3.61. Synthesis of 10,15-dihydro-5,10,15-trimethyl-5*H*-diindolo[3,2- α :3',2'-*c*]carbazole (61)



NaH (98 mg, 4.05 mmol) was added to a solution of **60** (0.28 g, 0.81 mmol) in anhydrous DMF under inert atmosphere. The solution was stirred at room temperature for 30 minutes. Then, iodomethane (166 μ L, 2.67 mmol) was added and the mixture was stirred at room temperature for 30 minutes and then treated with H₂O. The aqueous layer was extracted with dichloromethane and the organic layer was dried over anhydrous Na₂SO₄, filtered off and the solvent was distilled off under reduced pressure. The crude was purified by flash column chromatography using a mixture of hexane and dichloromethane (5:1 v/v) as the eluent to give compound **61** as a white solid.

Yield: 0.26 g (84%). **¹H NMR** (400 MHz, CDCl₃) δ (ppm): 8.47 (d, ³*J* = 8.0 Hz, H⁴, 3H), 7.59 (d, ³*J* = 8.0 Hz, H¹, 3H), 7.49–7.45 (m, H², 3H), 7.37–7.33 (m, H³, 3H), 4.48 (s, 3 \times N–CH₃, 9H). **¹³C NMR** (100 MHz, CDCl₃) δ (ppm): 142.1, 139.2, 123.0 (2C), 121.9, 120.0, 109.8, 102.7, 36.1. **UV-Vis** (CH₂Cl₂) λ_{\max} (ϵ / dm³ mol⁻¹ cm⁻¹): 256 (41 445), 317 (79 023), 334 (34 367), 353 (12 429) nm. **HRMS** (ESI-MS) *m/z*: calcd for C₂₇H₂₂N₃: 388.1808 (M+H)⁺, found: 388.1810.

3.62. Synthesis of 5,10,15-trihexyl-10,15-dihydro-5*H*-diindolo[3,2- α :3',2'-*c*]carbazole (62)

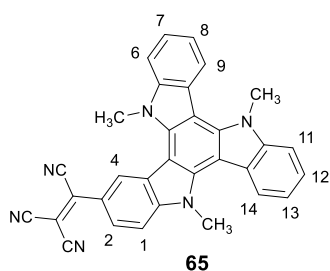


NaH (828 mg, 20.7 mmol, 60% dispersion in mineral oil) was added to a solution of **60** (781 mg, 2.26 mmol) in anhydrous DMF under nitrogen atmosphere. The solution was stirred at room temperature for 45 minutes. Then, 1-bromohexane (1.61 mL, 11.5 mmol) was added and the mixture was stirred overnight and then treated with water. The aqueous layer was extracted with dichloromethane and the organic layer was dried over anhydrous Na₂SO₄, filtered off and the solvent was distilled off under reduced pressure. The crude was purified by flash column chromatography using a mixture of hexane and dichloromethane (8:1 v/v) as the eluent to give **62** as a white solid.

Yield: 1.186 g (88%). **¹H NMR** (400 MHz, CDCl₃) δ (ppm): 8.29 (d, ³*J* = 8.0 Hz, H⁴, 3H), 7.64 (d, ³*J* = 7.7 Hz, H¹, 3H), 7.47–7.43 (m, H², 3H), 7.36–7.32 (m, H³, 3H), 4.92 (t, ³*J* = 7.2 Hz, 3 \times N–CH₂, 6H), 2.02–1.94 (m, 3 \times CH₂, 6H), 1.35–1.20 (m, 9 \times CH₂, 18H), 0.81 (t, ³*J* = 7.1 Hz, 3 \times CH₃, 9H). **¹³C NMR**

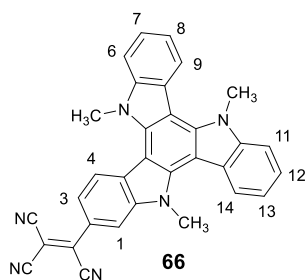
(100 MHz, CDCl₃) δ (ppm): 141.2, 139.0, 123.6, 122.8, 121.6, 119.8, 110.6, 103.3, 47.2, 31.6, 29.9, 26.5, 22.6, 14.1. **UV-Vis** (CH₂Cl₂) λ_{\max} (ϵ / dm³ mol⁻¹ cm⁻¹): 258 (35 733), 318 (71 631), 335 (30 624), 354 (10 943) nm.

3.63. Synthesis of 10,15-dihydro-5,10,15-trimethyl-3-(1,2,2-tricyanovinyl)-5H-diindolo-[3,2-*a*:3',2'-*c*]carbazole (65)



61 (298 mg, 0.77 mmol) and tetracyanoethylene (198 mg, 1.55 mmol) were dissolved in 5 mL of anhydrous DMF in a microwave vial and the system was purged with nitrogen. The sealed vial was heated at 80 °C for 1 h under microwave irradiation. TLC control of the reaction revealed that it was not completed, so tetracyanoethylene (198 mg, 1.55 mmol) was added and the solution was heated for an additional 2 h. Then, the reaction mixture was poured into a water/ice solution. The aqueous layer was extracted with dichloromethane and the organic layer was dried over anhydrous Na₂SO₄, filtered off and the solvent was distilled off under reduced pressure. The crude was subjected to flash column chromatography using first a mixture of hexane and dichloromethane (1:1 v/v) followed by 100% dichloromethane as the eluent affording different fractions containing compounds **65** and **66** in different proportions. Fractions containing **65** as the main product were joined and the resulting solid was purified after several recrystallization processes from hexane/dichloromethane mixtures. Compound **65** was obtained as a green solid.

Yield: 142 mg (38%). **¹H NMR** (400 MHz, CDCl₃) δ (ppm): 9.08 (d, ⁴*J* = 2.0 Hz, H⁴, 1H), 8.49 (d, ³*J* = 7.8 Hz, H⁹ or H¹⁴, 1H), 8.43 (d, ³*J* = 8.1 Hz, H⁹ or H¹⁴, 1H), 8.23 (dd, ³*J* = 8.9 Hz, ⁴*J* = 2.0 Hz, H², 1H), 7.65–7.59 (m, H¹, H⁶ and H¹¹, 3H), 7.57–7.53 (m, H⁷ and H¹², 2H), 7.42–7.38 (m, H⁸ and H¹³, 2H), 4.52 (s, N–CH₃, 3H), 4.49 (s, N–CH₃, 3H), 4.44 (s, N–CH₃, 3H). **UV-Vis** (CH₂Cl₂) λ_{\max} (ϵ / dm³ mol⁻¹ cm⁻¹): 316 (78 316), 351 (30 877), 429 (18 099), 584 (16 218) nm. **HRMS** (ESI-MS) *m/z*: calcd for C₃₂H₂₀N₆: 488.1744 (M)⁺, found: 488.1739.



Compound **66** was obtained as a blue solid as a mixture with compound **65** in a proportion of 78% as determined by ¹H NMR.

Yield: 123 mg (33%). **¹H NMR** (400 MHz, CDCl₃) δ (ppm): 8.47–8.40 (m, H⁹ and H¹⁴, 2H), 8.30 (d, ⁴*J* = 2.0 Hz, H¹, 1H), 8.06 (dd, ³*J* = 8.6 Hz, ⁴*J* = 2.0 Hz, H³, 1H), 7.65–7.61 (m, H⁶ and H¹¹, 2H), 7.56–7.51 (m, H⁴, H⁷ and

H¹², 3H), 7.43–7.38 (m, H⁸ and H¹³, 2H), 4.50 (s, 2 × N–CH₃, 6H), 4.41 (s, N–CH₃, 3H). **CI-MS** *m/z*: calcd for C₃₂H₂₁N₆: 489.2 (M + H)⁺, found: 489.5.

RESUM

RESUM

Introducció

La recerca i el desenvolupament de materials moleculars amb aplicacions en el camp de l'electrònica va començar a finals del segle passat. Al 1977, A. J. Heeger, A. G. MacDiarmid i H. Shirakawa van descobrir que la conductivitat elèctrica del poliacetilè es podia incrementar dopant-lo amb halògens.^[2] Pel descobriment i desenvolupament dels polímers conductors, van rebre el Premi Nobel de Química l'any 2000.^[3,4] Actualment, el desenvolupament de nous semiconductors orgànics amb capacitat de transport de càrrega presenta un gran interès per a un ampli ventall d'aplicacions, entre les quals destaquen els transistors orgànics de capa prima (OTFTs), els díodes emissors de llum orgànics (OLEDs) i les cel·les solars orgàniques.^[5-8] En comparació amb els materials inorgànics, l'ús de semiconductors orgànics és interessant degut al seu fàcil processament, la possibilitat de recobrir grans superfícies de dispositius electrònics flexibles, la lleugeresa i el baix cost. Els semiconductors orgànics inclouen tant polímers com molècules de baix pes molecular. Aquestes últimes presenten procediments sintètics, de purificació i de caracterització més senzills, degut al seu baix pes molecular i a què presenten una estructura ben definida.^[9] A més, les seves propietats òptiques i electròniques poden ser modulades fàcilment mitjançant el disseny molecular.

Els materials orgànics emprats com a capes actives en dispositius electrònics i optoelectrònics consisteixen en sistemes conjugats de tipus π . Aquests materials estan involucrats en diferents processos, com la introducció de portadors de càrregues en el sistema, transport de càrrega a través dels materials actius i recollida de les càrregues. D'acord amb la naturalesa dels portadors de càrrega, els semiconductors orgànics es poden classificar en transportadors de forats (tipus p) o d'electrons (tipus n). Quan els portadors de càrrega s'indueixen en la capa activa del semiconductor orgànic, és a dir, en les molècules conjugades, les càrregues es deslocalitzen ràpidament en el corresponent sistema orbital de tipus π , la qual cosa facilita el transport de càrrega entre molècules. Per tant, el transport de càrrega intermolecular s'afavoreix com major sigui el solapament orbital entre molècules veïnes.^[10] El transport de càrrega per a sistemes

orgànics desordenats es pot explicar a partir de l'anomenat model de *hopping*.^[9] En aquest model, els portadors de càrrega, és a dir, els forats i els electrons, estan relacionats amb les corresponents espècies radicalàries catiònica i aniònica, respectivament. En el cas del transport de forats, els electrons es transfereixen seqüencialment d'una molècula neutra a un catió radical a través de l'orbital molecular ocupat de més alta energia (HOMO), mentre que en el cas del transport d'electrons, els electrons es transfereixen seqüencialment d'un anió radical a una molècula neutra a través de l'orbital molecular desocupat de més baixa energia (LUMO).

El sistema conjugat és el responsable de les propietats electròniques i optoelectròniques dels semiconductors orgànics, les quals poden ser modulades fàcilment introduint grups donadors o acceptors d'electrons. A més, la introducció de cadenes laterals influeix en la solubilitat i en la formació de les capes primes basades en els semiconductors orgànics. Per tant, l'estructura química dels materials orgànics determina els nivells energètics HOMO i LUMO, així com la corresponent diferència energètica, la solubilitat i les interaccions intermoleculares, les quals influeixen en l'empaquetament molecular a l'estat sòlid. Tenint en compte aquests aspectes, la selecció de l'estructura del nucli conjugat és clau per tal d'aconseguir dispositius que presentin eficiències elevades.^[11] Tanmateix, també ho és el processament dels materials, el disseny dels dispositius i el control de la morfologia de les capes.

Aquesta tesi tracta sobre la preparació i caracterització de nous semiconductors orgànics per a la seva aplicació com a capes actives en OTFTs i OLEDs. Els OTFTs són dispositius que amplifiquen i commuten els senyals elèctrics i s'utilitzen actualment com a components en circuits electrònics i es troben en sensors, llibres electrònics i en dispositius OLED, entre d'altres. A més, també permeten avaluar les propietats de transport de càrrega dels semiconductors orgànics.

El desenvolupament dels OTFTs durant els últims anys ha donat lloc a valors de mobilitat de l'ordre dels obtinguts pel silici amorf ($0.1 - 1 \text{ cm}^2 \text{ V}^{-1} \text{ s}^{-1}$), i inclús a valors que s'apropen a les mobilitats del silici cristal·lí ($> 10 \text{ cm}^2 \text{ V}^{-1} \text{ s}^{-1}$).^[11] Cal destacar que en termes de mobilitat i estabilitat a l'aire, el desenvolupament dels materials transportadors de forats ha estat superior que pel que fa als transportadors d'electrons o ambipolars, els quals també es requereixen com a components en transistors ambipolars o en circuits complementaris.

Per al disseny dels semiconductors orgànics s'ha de tenir en compte que les interaccions de tipus π entre molècules condueixen a valors de mobilitat més elevats. Per tant, es requereixen materials altament conjugats. L'estructura química dels materials orgànics determina també

l'estabilitat i durabilitat dels dispositius fabricats. De fet, molts OTFTs mostren degradació quan operen a l'aire, la qual cosa requereix encapsular el dispositiu. Per tal que els semiconductors de tipus p siguin estables enfront el dopatge oxidatiu que pot ocasionar l'oxigen atmosfèric, han de presentar energies d'ionització elevades.^[14] Per al disseny de semiconductors de tipus n es requereixen materials amb afinitats electròniques elevades (> 4.0 eV), per tal de facilitar la injecció de càrregues i estabilitat a l'aire.^[10,15] Els nivells energètics HOMO i LUMO es poden modular dissenyant molècules de transferència de càrrega. Els OTFTs ambipolars, que són aquells que presenten tant transport de forats com d'electrons, es classifiquen segons la composició de la capa activa. Aquesta pot consistir en la combinació d'un semiconductor de tipus p i un de tipus n, o bé, d'un sol component. Per als OTFTs ambipolars on la capa activa es basa en un sol component, els materials han de tenir energies d'ionització i afinitats electròniques superiors a 5.0 eV i a 4.0 eV, respectivament, per tal d'aconseguir un transport de forats i d'electrons estable, així com facilitar la injecció de càrregues a la capa activa.^[18]

La morfologia de les capes també influeix en el funcionament dels OTFTs. En principi, les capes cristal·lines presenten mobilitats majors que les capes amorfes.^[10] La tècnica d'evaporació tèrmica al buit permet obtenir capes cristal·lines altament ordenades. Cal destacar que el processament dels semiconductors orgànics per solució, com per exemple utilitzant la tècnica de *spin coating*, acostuma a comportar capes amb dominis amorfs. Per tant, els OTFTs preparats en aquesta tesi s'han fabricat mitjançant la tècnica d'evaporació tèrmica al buit.

Els OLEDs es basen en el principi d'electroluminiscència, que consisteix en un fenomen físic pel qual els materials emeten llum en resposta a l'aplicació d'un camp elèctric. Avui en dia els OLEDs s'empren en aplicacions comercials com en les pantalles planes de dispositius i en sistemes d'il·luminació artificial. De totes maneres, cal encara millorar les eficiències, la puresa del color i els temps d'operació dels dispositius per tal de produir dispositius industrials eficients.

Els OLEDs que emeten llum a la zona del blau de l'espectre electromagnètic comporten un gran interès, degut a què els materials emissors en el blau, conjuntament amb els emissors en el verd i en el vermell, s'utilitzen en pantalles de dispositius electrònics que integren tots els colors i en OLEDs de llum blanca.^[41] Tenint en compte que els OLEDs de llum blava presenten menors eficiències que els OLEDs de llum verda i vermella, avui en dia molts recursos científics es destinen a desenvolupar nous materials luminescents en el blau.^[42] El funcionament dels OLEDs amb materials emissors a la zona del blau està subjecte a les grans diferències energètiques entre els

corresponents nivells HOMO i LUMO, cosa que dificulta la injecció de càrregues a la capa emissora. Per una altra banda, la poca sensibilitat de l'ull humà en aquesta part de l'espectre electromagnètic en disminueix l'eficàcia.^[43] A més, els OLEDs que emeten a la zona del blau són més propensos a degradar-se i per tant mostren una menor estabilitat i temps d'operació més curts.^[44]

Els OLEDs de llum blava fluorescents poden fabricar-se dopant una matriu amb el fluoròfor corresponent per tal d'evitar el *quenching* de la fluorescència o bé utilitzant el fluoròfor com a capa activa no dopada.^[43] Tot i que les capes dopades poden donar lloc a dispositius amb eficiències elevades, la intrínseca separació entre les fases pot deteriorar el funcionament del dispositiu i a més es necessita un control molt estricte de la concentració del dopant. Per tant, en general, l'ús de capes emissores no dopades és més convenient per a aplicacions pràctiques.

El color de l'emissió d'un dispositiu OLED es pot descriure mitjançant les coordenades cromàtiques (x , y) segons la *Comission Internationale de l'Éclairage* (CIE). Si es considera l'ús dels OLEDs per a pantalles de dispositius que reproduïen tots els colors, les coordenades CIE estàndards per al blau són ($x = 0.14$, $y = 0.08$) o ($x = 0.15$, $y = 0.06$), tal i com especifiquen el Comitè de Sistemes de Televisió Nacional (NTSC per les seves sigles en anglès) i la Unió Europea de Radiodifusió (EBU), respectivament.^[44] Per tant, és encara necessari desenvolupar OLEDs eficients que emetin a la zona del blau, i en particular, que presentin la coordenada CIE y inferior a 0.1.

Per tal d'actuar com a capes emissores eficients, els fluoròfors han de presentar un sistema conjugat amb rendiments quàntics alts, una estabilitat tèrmica elevada i la capacitat de donar lloc a capes contínues i estables morfològicament. Per aquest motiu es requereixen materials moleculars amorfs, amb temperatures de transició vítria per sobre de temperatura ambient.^[45] Una estratègia per obtenir materials amorfs es basa en introduir substituents voluminosos en el sistema conjugat, per tal de dificultar un empaquetament ordenat de les molècules. En general, els rendiments quàntics de fluorescència són alts en solució, però disminueixen considerablement en estat sòlid degut als processos d'agregació. Per tal de reduir el *quenching* de fluorescència en estat sòlid, una estratègia consisteix en utilitzar estructures moleculars que no siguin planes, introduint substituents rígids i voluminosos que dificultin les interaccions intermoleculars en estat sòlid. Seguint aquestes estratègies, alguns exemples recents de dispositius OLEDs de llum blava basats en l'antracè o el fluorè, han derivat en valors d'eficiències quàntiques externes (EQE) de fins el $\sim 6\%$.^[42b-d]

Objectius

Els objectius d'aquesta tesi se centren en la preparació i caracterització de nous semiconductors orgànics basats en l'heterocicle 9H-carbazole per a la seva aplicació com a capes actives en dispositius electrònics i optoelectrònics. El carbazole és un material de partida econòmic, relativament fàcil de funcionalitzar i que presenta una estabilitat tèrmica elevada.^[48] Cal destacar també que els derivats del carbazole presenten rendiments quàntics de fluorescència elevats i propietats de transport de forats excel·lents, per la qual cosa són candidats adients per a OLEDs^[49] i OTFTs.^[50]

Aquest treball està enfocat en primer terme en el disseny molecular, síntesi i caracterització dels materials orgànics, seguit de l'estudi de les seves propietats tèrmiques, òptiques, electroquímiques i de transport de càrrega, i finalitza amb l'aplicació dels materials preparats com a capes actives en OLEDs i OTFTs. Els objectius principals i l'organització d'aquest treball es descriuen a continuació.

El primer capítol d'aquesta tesi (Capítol 1) tracta sobre la preparació i caracterització d'una sèrie de derivats del carbazole amb emissió a la zona del blau de l'espectre electromagnètic, per a la seva aplicació com a capes emissores en OLEDs. Per tal d'obtenir materials emissors a la zona del blau amb propietats de transport de forats, s'ha considerat l'extensió del sistema π del nucli carbazole mitjançant la introducció de grups donadors a les posicions 3 i 6. A més, tenint en compte que els espaïadors conjugats de tipus π poden modular significativament la connectivitat de les molècules, en termes de conjugació, i les propietats fotofísiques,^[51] l'efecte de la inserció del triple enllaç com a connector entre el carbazole i les unitats donadores també s'ha analitzat. Com a última variació estructural i amb l'objectiu d'obtenir materials moleculars amorfs, s'ha considerat introduir substituents voluminosos en l'àtom de nitrogen del nucli carbazole. A través de l'estudi de les propietats dels materials preparats, es pretén seleccionar els candidats més adequats per a estudiar-los com a capes emissores en el blau en OLEDs. La relació entre l'estructura i les propietats que presenten els materials s'ha analitzat mitjançant la resolució de les estructures cristal·lines corresponents per difracció de raigs X de monocristall i càlculs teòrics.

L'objectiu principal dels Capítols 2 i 3 és el desenvolupament de nous materials semiconductors orgànics de tipus n i ambipolars. Pel seu disseny, s'ha de tenir en compte que es requereixen afinitats electròniques elevades per tal de facilitar la injecció d'electrons i estabilitat a l'aire. Per tal d'obtenir derivats de tipus n i ambipolars, l'estratègia seguida en aquesta tesi

consisteix en la modificació de les propietats de transport de forats característiques del nucli donador d'electrons carbazole, mitjançant la introducció de grups acceptors d'electrons per tal de disminuir el nivell energètic del LUMO, és a dir, augmentar l'afinitat electrònica.

El Capítol 2 es basa en un treball desenvolupat prèviament en el grup de recerca, en el qual la introducció dels grups carbazole o indole en el radical tris(2,4,6-triclorofenil)metil (TTM) va permetre obtenir derivats radicals amb transferència de càrrega intramolecular que van mostrar propietats de transport de càrrega ambipolars, amb mobilitats de forats i d'electrons de l'ordre de $10^{-4} - 10^{-3} \text{ cm}^2 \text{ V}^{-1} \text{ s}^{-1}$.^[52] Amb l'objectiu de desenvolupar nous derivats amb mobilitats superiors i amb un millor balanç de càrregues de forats i d'electrons, es va considerar desenvolupar una sèrie de compostos basada en el radical [4-(*N*-carbazolil)-2,6-diclorofenil]bis(2,4,6-triclorofenil)metil (Cbz-TTM). En aquesta nova sèrie de radicals, s'han introduït diferents grups amb diferent caràcter donador d'electrons en les posicions 3 i 6 del nucli carbazole per tal de modular el caràcter *push-pull* dels materials resultants i estudiar el seu efecte en les propietats de transport de càrrega mitjançant la tècnica *Xerographic Time-of-flight* (XTOF). A més, els radicals preparats es van estudiar com a capes actives en fotoreceptors xerogràfics.

El Capítol 3 es basa en la modificació de les propietats de transport de forats característiques dels derivats del carbazole mitjançant la introducció del grup fortament acceptor d'electrons triclanovinil, el qual dóna lloc a un sistema de tipus *push-pull* amb una elevada afinitat electrònica. S'han seguit diferents aproximacions per tal de desenvolupar tres sèries de derivats del carbazole que incorporen el grup triclanovinil. En la primera sèrie de compostos, s'han introduït grups donadors d'electrons en el nucli carbazole per modular-ne el seu caràcter donador. La segona sèrie consisteix en la introducció de cadenes alquíliques de diferent longitud en el nitrogen del carbazole dels triclanovinil derivats. La última sèrie es basa en l'extensió del sistema π del carbazole mitjançant la introducció de l'heterocicle tiofè com a pont conjugat entre el nucli carbazole i el grup triclanovinil. S'ha analitzat l'efecte de la introducció dels substituents en el nucli carbazole en termes de propietats tèrmiques, òptiques, electroquímiques i de transport de càrrega. A més, la relació entre l'estructura molecular dels semiconductors i les propietats de transport de càrrega determinades mitjançant la tècnica TOF i la fabricació i mesura de OTFTs s'ha examinat mitjançant estudis de difracció de raigs X i per càlculs teòrics.

Tot i que fins l'actualitat el desenvolupament de materials de tipus p ha resultat superior que el corresponent als materials de tipus n i ambipolars, encara es requereixen nous tipus de

materials conjugats per OTFTs de tipus p per tal de millorar el funcionament dels dispositius. Amb aquesta idea en ment, el Capítol 4 s'ha centrat en una sèrie de materials derivats del carbazole transportadors de forats, en els quals l'extensió del sistema conjugat carbazole s'ha variat progressivament per tal d'estudiar el seu efecte en les propietats de transport de càrrega. D'aquesta manera, s'ha sintetitzat i caracteritzat una sèrie de compostos basats en els nuclis carbazole, 3,3'-bicarbazole, indolo-[3,2-*b*]carbazole i triindole. Els nuclis indolo-[3,2-*b*]carbazole i triindole mostren estructures moleculars més extenses que el carbazole i el 3,3'-bicarbazole. Per tant, s'espera que presentin un ordre molecular superior en l'estat sòlid, i per tant, millor transport de càrrega. A més, l'efecte de la longitud de la cadena alquíllica en els àtoms de nitrogen del triindole també s'ha analitzat. El Capítol 4 tracta no només del funcionament dels OTFTs d'aquesta sèrie de compostos basats en el carbazole, sinó que també pretén determinar l'empaquetament molecular en les capes dels semiconductors orgànics dels dispositius mitjançant estudis de difracció de raigs X. Per tant, l'objectiu d'aquest capítol és determinar la correlació del funcionament dels dispositius amb l'ordre molecular en les capes semiconductores en funció del disseny del nucli conjugat dels semiconductors orgànics.

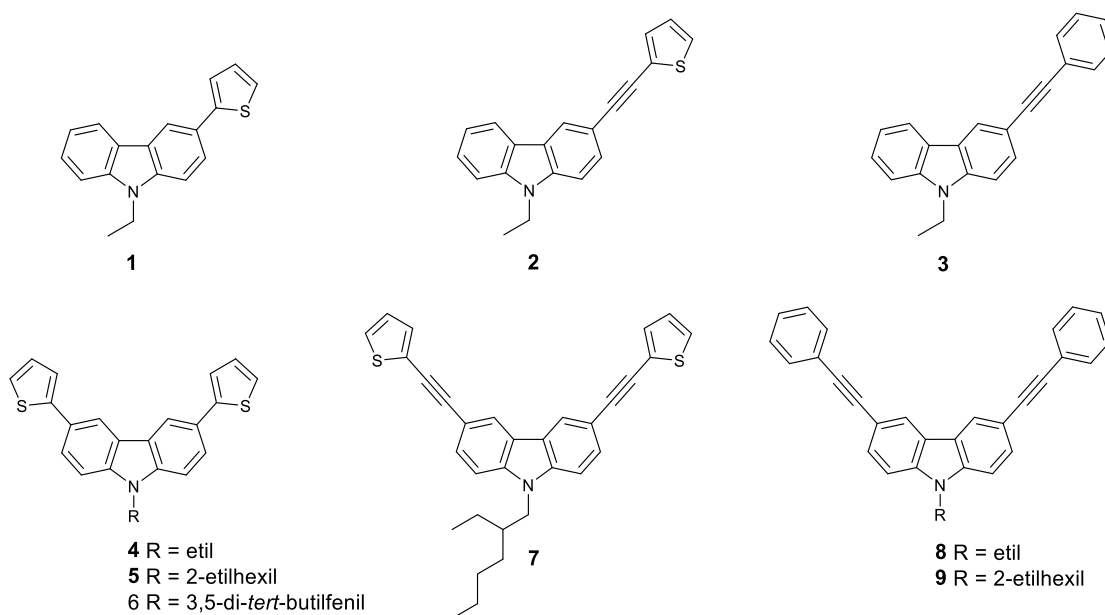
Resultats i discussió

Capítol 1. Derivats del carbazole com a capes emissores en OLEDs de llum blava

Els materials emissors en la zona del blau de l'espectre electromagnètic presenten un gran interès en el camp dels OLEDs ja que conjuntament amb materials emissors en la zona del verd i del vermell, s'utilitzen en pantalles de dispositius electrònics que integren tots els colors i en OLEDs de llum blanca. De fet, actualment es requereix desenvolupar OLEDs eficients que emetin a la zona del blau, i en particular, que presentin la coordenada CIE y inferior a 0.1.

D'entre els materials luminescents amb emissió en el blau, els derivats del carbazole són candidats atractius com a capes emissores en OLEDs de llum blava no dopats.^[73] Els materials basats en el carbazole destaquen per les seves propietats luminescents i de transport de forats. Aquest heterocicle mostra una banda d'emissió a la zona de l'ultravioleta de l'espectre, la longitud d'ona d'emissió de la qual es pot modular fàcilment desplaçant-la a energies més baixes mitjançant l'extensió del seu sistema conjugat.

L'objectiu d'aquest capítol és preparar una família de derivats del carbazole que presentin emissió en la zona del blau de l'espectre electromagnètic i propietats de transport de forats per tal de ser estudiats com a capes emissores en OLEDs. Com a primera aproximació, es va considerar l'extensió del sistema conjugat del carbazole mitjançant la introducció de grups donadors d'electrons en les posicions 3 i 6, en concret el tiofè i el fenil, per tal d'obtenir sistemes amb emissió a la zona del blau de l'espectre. A més, es va analitzar l'efecte de la inserció del triple enllaç com a connector entre el carbazole i els grups donadors. Per tal d'obtenir materials amorfs, es van introduir els grups etil, 2-etilhexil o 3,5-di-*tert*-butilfenil en el nitrogen del carbazole. Tenint en compte aquestes consideracions es va preparar la primera sèrie de compostos **1–9** (Esquema 1).



Esquema 1. Estructura química dels derivats **1–9**.

L'estructura cristal·lina dels compostos **3**, **6** i **7** es va determinar per difracció de raigs X de monocristall. En les tres estructures cristal·lines, els grups fenil i tiofè no són coplanars amb el carbazole. Però els derivats que incorporen el triple enllaç entre el grup carbazole i la unitat donadora tiofè o fenil (**3** i **7**) són els que presenten una major desviació de la planaritat, sent el derivat monosubstituint **3**, que conté el grup feniletinil, el que mostra una desviació major de 63.3°. En l'empaquetament molecular del compost **3**, s'observen interaccions intermoleculars de tipus C–H... π , però no de tipus π – π . Només el tienil derivat **6**, que no presenta el triple enllaç en la seva estructura, mostra interaccions intermoleculars de tipus π – π , tot i que cal destacar que les molècules veïnes es troben lleugerament desplaçades les unes respecte les altres.

Les propietats tèrmiques es van analitzar mitjançant anàlisi termogravimètric (TGA) i calorimetria d'escombratge diferencial (DSC). A partir de l'anàlisi termogravimètric es va determinar que les temperatures de descomposició per a la sèrie de compostos **1–9** es troben entre 257–349°C. Considerant l'aplicació d'aquests materials com a capes emissores en OLEDs, el compost disubstituint amb els grups feniletinil **8** és l'únic derivat que va presentar una temperatura de transició vítria per sobre de temperatura ambient, cosa que el converteix en l'únic candidat d'aquesta sèrie de compostos per a ser estudiat com a capa emissora en OLEDs.

Es van enregistrar els espectres d'absorció i d'emissió dels compostos **1–9** en solució i en fase sòlida, observant una banda d'emissió a la zona de l'UV-blau de l'espectre en solució i un desplaçament a longituds d'ona majors en les mesures en fase sòlida (398–421 nm), mantenint l'emissió en la zona del blau de l'espectre. Es van determinar els rendiments quàntics de fluorescència, tant en solució com en fase sòlida. En solució, es van obtenir rendiments quàntics de l'ordre de 0.05–0.33, mentre que en fase sòlida el rendiment quàntic disminueix per a tots els compostos (0.05–0.12). Cal destacar que els derivats que incorporen el grup feniletinil mostren en general un desplaçament hipsocròmic de la banda d'absorbància i d'emissió i un rendiment quàntic superior respecte els derivats que presenten el grup tiofè. En l'estat sòlid el rendiment quàntic de fluorescència pot disminuir degut a la presència d'interaccions intermoleculares de tipus $\pi-\pi$ i processos de desactivació no radiatius.^[87] Cal destacar que l'angle de torsió de 63.3° del grup fenil respecte el carbazole en el compost **3** dificulta l'empaquetament entre molècules veïnes i per tant es podria esperar que els derivats que incorporen el grup feniletinil presentin majors rendiments quàntics.

L'anàlisi de les propietats òptiques i electroquímiques va permetre determinar que els compostos **1–9** presenten potencials d'ionització elevats, que són adients per a proporcionar una conducció de tipus p. Les propietats de transport de càrrega per a aquesta sèrie de compostos es van estudiar mitjançant la tècnica *Time of Flight* (TOF), donant lloc a mobilitats de forats en el rang de 10^{-5} fins a 10^{-3} cm² V⁻¹ s⁻¹.

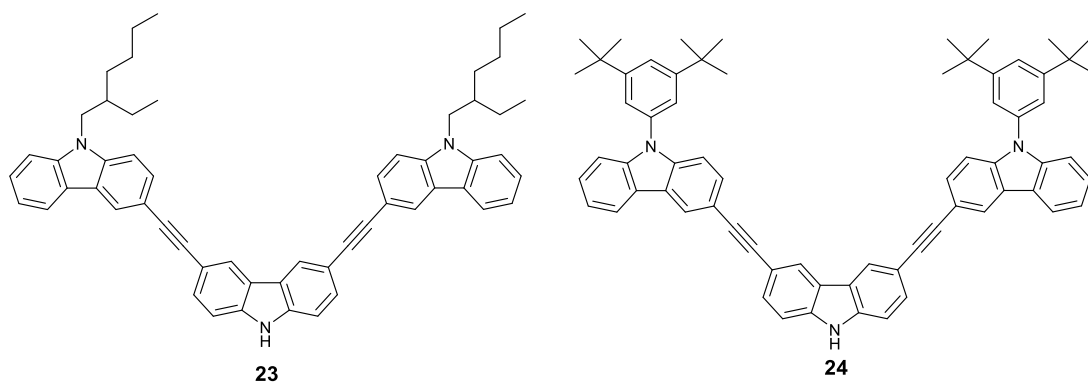
El compost **8** es va seleccionar com a candidat per a ser estudiat com a capa emissora en OLEDs, ja que presenta una elevada estabilitat tèrmica i una temperatura de transició vítria per sobre de temperatura ambient, que és clau per a una correcta operació dels dispositius. A més, el compost **8** presenta emissió a la zona del blau amb un pic màxim d'emissió centrat a 402 nm i coordenades CIE de (0.21, 0.18). Per una altra banda, tot i que tots els compostos **1–9** presenten

rendiments quàntics de fluorescència en l'estat sòlid baixos, el del compost **8** es troba entre els valors més alts de la sèrie.

Tenint en compte aquestes consideracions, es va fabricar un dispositiu OLED amb l'estructura ITO/MoO₃ (5 nm)/**8** (45 nm)/BPhen (15 nm)/Ca (14 nm)/Al (85 nm), en què totes les capes es van dipositar per evaporació tèrmica al buit. El MoO₃ es va utilitzar com a capa transportadora de forats^[90] i el BPhen com a capa transportadora d'electrons. El dispositiu va mostrar un voltatge al qual comença a funcionar de només 4 V, indicant una injecció de càrrega, transport i recombinació eficients. Es va determinar un màxim de luminància de 14305 cd m⁻² als 12 V, una eficiència de corrent màxima de 3.3 cd A⁻¹, i una eficiència quàntica externa de 1.0%. Tot i que la configuració del dispositiu es pot optimitzar, aquests resultats indiquen que el compost **8** mostra un funcionament en OLEDs competitiu en comparació amb els dispositius descrits a la literatura basats en derivats del carbazole emissors en el blau.^[73]

Per a aquest dispositiu basat en el compost **8** com a capa emissora, l'eficiència de la conversió dels excitons generats elèctricament en llum va resultar ser del 45%, que supera el límit teòric del 25% corresponent a l'eficiència de producció d'excitons singlet que s'assumeix pels OLEDs fluorescents. Es van realitzar càlculs teòrics per tal d'explicar el mecanisme pel qual té lloc l'emissió en aquest sistema i explicar aquest fenomen. Els càlculs teòrics indiquen que l'emissió prové dels estats S₁ i S₂ del carbazole **8**, juntament amb la contribució de la transferència d'energia del triplet T₅ a l'estat S₁ a través d'un procés de conversió entre sistemes invers (*reverse intersystem crossing*, RISC), ja que la diferència energètica entre aquests estats és només de 85 meV.^[92]

Com s'ha comentat anteriorment, actualment es requereixen OLEDs que presentin emissió a la zona del blau de l'espectre, però que a més presentin una coordenada CIE y inferior a 0.1. Amb aquest objectiu en ment, es va considerar preparar una sèrie de compostos basats en el derivat **8** que presentessin una banda d'emissió desplaçada a longituds d'ona superiors, sent la coordenada CIE y inferior a 0.1. Es van preparar dos compostos basats en el derivat **8**, en què es van substituir els grups fenil per unitats de carbazole per tal d'extendre la conjugació del sistema i augmentar els rendiments quàntics d'emissió en l'estat sòlid. Es van introduir substituents voluminosos en els àtoms de nitrogen dels carbazoles perifèrics, el 2-etilhexil i el 3,5-di-tert-butilfenil, donant lloc als compostos **23** i **24** (Esquema 2), respectivament, per tal d'obtenir materials moleculars amorfs i rendiments quàntics de fluorescència superiors.



Esquema 2. Estructura química dels derivats del carbazole **23** i **24**.

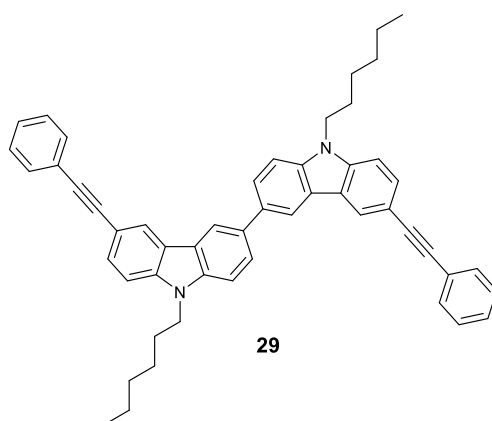
La introducció de tres unitats de carbazole a l'estructura molecular permet obtenir materials amb una estabilitat tèrmica i una temperatura de transició vítria superiors que els derivats **1–9**. Els espectres d'emissió en estat sòlid dels compostos **23** i **24** mostren una banda d'emissió centrada a 410 i 398 nm, respectivament. Les coordenades CIE pel compost **23** són (0.17, 0.07) i pel compost **24** (0.18, 0.11). És a dir, la coordenada CIE y és inferior a 0.1 tal i com es pretenia. Els compostos **23** i **24** presenten rendiments quàntics de fluorescència en solució de 0.39 i 0.31, respectivament. En estat sòlid, el rendiment quàntic de fluorescència pel derivat *N*-alquilat **23** es manté inalterat respecte el determinat en solució, mentre que pel derivat *N*-aril **24** decau considerablement fins a un valor de 0.11. Per tant, la introducció del grup 2-etilhexil en els àtoms de nitrogen de les unitats de carbazole perifèriques ha demostrat ser més eficient per evitar el quenching de la fluorescència en estat sòlid que el grup 3,5-di-*tert*-butilfenil.

Els valors de potencial d'ionització i d'afinitat electrònica estimats per voltamperometria cíclica dels compostos **23** i **24** són ~ 5.9 i ~ 2.6 eV, respectivament, del mateix ordre que els valors obtinguts pels derivats **1–9**. El compost **23** va mostrar un valor de mobilitat de forats de l'ordre de $10^{-4} \text{ cm}^2 \text{ V}^{-1} \text{ s}^{-1}$ mitjançant la tècnica *Xerographic Time of Flight* (XTOF), mentre que pel compost **24** no va ser possible la seva determinació degut a l'elevada dispersivitat que van mostrar els transitoris mesurats.

El compost **23** presenta un rendiment quàntic de fluorescència en estat sòlid elevat, la banda d'emissió centrada a 410 nm, en la zona del blau de l'espectre, i la coordenada CIE y inferior a 0.1. Per tant, es van preparar dispositius OLED en què el compost **23** es va utilitzar com a capa emissora. L'estructura dels dispositius preparats va consistir en ITO/PEDOT:PSS (25 nm)/**23** (25–55 nm)/TPBi (10 nm)/LiF (1 nm)/Al (100 nm). El compost **23** es va dipositar per *spin coating* a partir

d'una solució en clorobenzè i es van preparar dispositius amb diferents gruixos de capes de 25 a 55 nm. Tots els dispositius van presentar un potencial molt baix al qual comencen a funcionar, d'entre 2.6 i 3.6 V, indicant que les barreres d'injecció des de les capes transportadores de càrregues són petites en el dispositiu. La luminància augmenta segons el voltatge aplicat, arribant al valor màxim per sota de 5 V. Els valors màxims de luminància depenen del gruix de la capa del compost **23**, obtenint-se el ratio òptim entre luminància i eficiència de corrent quan el gruix de la capa és de 50 nm, amb valors de 39.46 cd m^{-2} i 0.17 cd A^{-1} , respectivament.

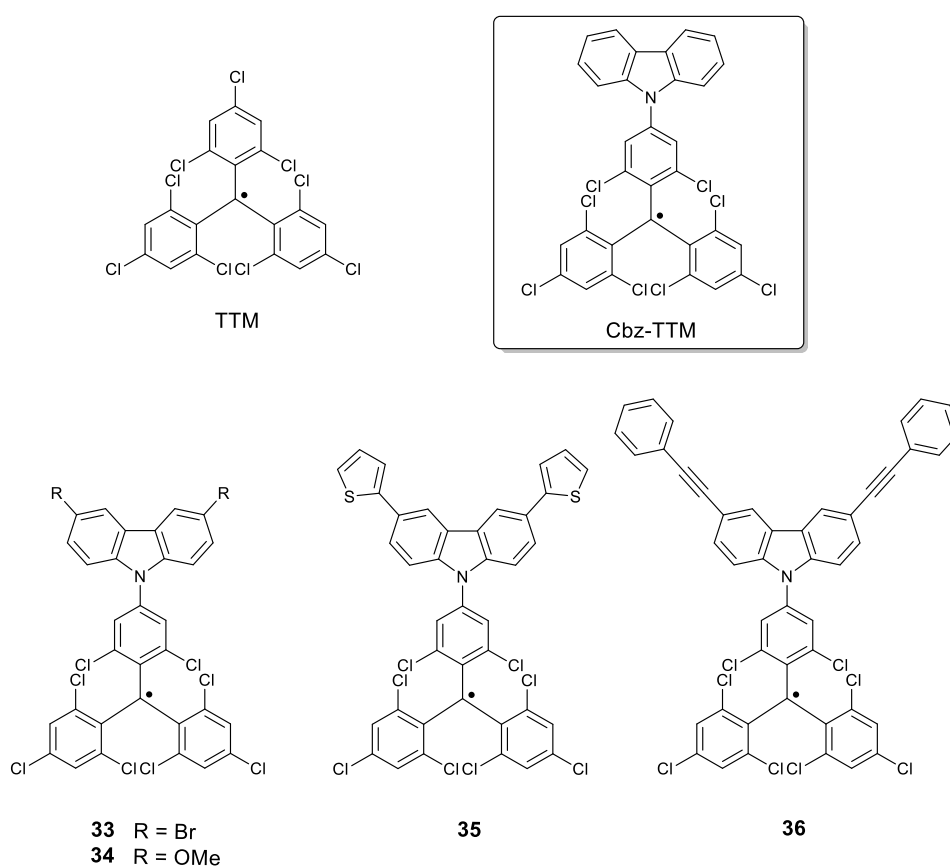
Per últim, es va considerar preparar un nou derivat amb emissió a la zona del blau de l'espectre en l'estat sòlid i que també presentés la coordenada CIE y inferior a 0.1. En aquest cas, es va considerar estendre la conjugació del sistema π del compost **8** substituint el nucli carbazole pel 3,3'-bicarbazole, mantenint els grups perifèrics feniletinil. Es va preparar el compost **29** (Esquema 3), el qual presenta una elevada estabilitat tèrmica i un comportament amorf amb una temperatura de transició vítria de $59 \text{ }^\circ\text{C}$. L'estudi de les propietats òptiques indica que el compost **29** mostra les coordenades CIE en la zona del blau requerida (0.17, 0.10). A més, el rendiment quàntic de fluorescència en estat sòlid mesurat pel compost **23** és 0.21, el qual és superior al del compost **8** ($\Phi_f = 0.11$). El compost **29** presenta un potencial d'ionització i afinitat electrònica de 5.87 i 2.52 eV, respectivament. A més, a partir de la tècnica TOF, s'ha determinat que presenta una mobilitat de forats de $1.7 \times 10^{-3} \text{ cm}^2 \text{ V}^{-1} \text{ s}^{-1}$. Per tant, el compost **29** manté les característiques necessàries per a actuar com a component en dispositius OLED i per aquest motiu, actualment, s'està analitzant com a capa emissora en OLEDs.



Esquema 3. Estructura química del derivat del carbazole **29**.

Capítol 2. Radicals estables derivats del carbazole amb transport de càrrega ambipolar

L'obtenció de semiconductors orgànics que puguin presentar ambdós tipus de mobilitats, de forats i d'electrons, són d'especial interès en el camp de l'electrònica per les seves potencials aplicacions, com per exemple en transistors orgànics (OTFTs) ambipolars. Prèviament, en el grup de recerca es van estudiar les propietats semiconductoras del radical Cbz-TTM mitjançant la tècnica *Xerographic Time-of-Flight* (XTOF), obtenint valors de mobilitat de forats i d'electrons de l'ordre de $10^{-4} - 10^{-3} \text{ cm}^2 \text{ V}^{-1} \text{ s}^{-1}$.^[52] En aquest treball, s'han estudiat les propietats de transport de càrrega d'una nova sèrie de derivats basada en el Cbz-TTM, en què s'ha variat la capacitat donadora d'electrons i l'extensió del sistema π del nucli carbazole, i per tant el caràcter de tipus *push-pull* dels radicals resultants (**33–36**) (Esquema 4).



Esquema 4. Estructura química dels radicals Cbz-TTM i **33–36**.

El radical neutre TTM presenta una estabilitat elevada en estat sòlid, degut a l'impediment estèric causat pels sis àtoms de clor que envolten el carboni trivalent.^[104,105] Aquesta estabilitat es

transfereix als adductes resultants de la introducció de l'heterocicle carbazole. Els estudis d'EPR han confirmat el caràcter radicalari dels nous derivats i la seva estabilitat en estat sòlid i en condicions ambient durant llargs períodes de temps quan són emmagatzemats protegint-los de la llum. Per una altra banda, aquesta sèrie de derivats presenta una elevada estabilitat tèrmica amb temperatures de descomposició superiors a 260 °C.

Es van enregistrar els espectres d'absorbància i d'emissió en solució per als compostos Cbz-TTM i **33–36**. Tots els compostos presenten una zona d'absorció a la zona de l'UV i una banda d'absorció a la zona del vermell, que es pot atribuir al procés de transferència de càrrega intramolecular des del fragment donador d'electrons, el carbazole, al grup acceptor d'electrons, el TTM. Cal destacar que el radical **34**, que incorpora els grups metoxi a l'anell del carbazole, presenta un desplaçament major de la banda d'absorció de transferència de càrrega a energies menors de tota la sèrie de compostos, d'acord amb el major caràcter donador d'electrons del grup metoxi. Els espectres d'emissió enregistrats en ciclohexà mostren una banda d'emissió a la zona del vermell per a tots els compostos, el màxim d'emissió de la qual depèn també de la naturalesa dels substituents del nucli carbazole. El radical no substituït Cbz-TTM presenta el rendiment quàntic de fluorescència més elevat de tota la sèrie de radicals, i va disminuint segons la capacitat donadora d'electrons dels substituents del carbazole.

Les propietats electroquímiques es van analitzar per voltamperometria cíclica. Els voltamperogrames cíclics mostren processos d'oxidació i de reducció quasi-reversibles per a tota la sèrie de radicals. El radical **34**, que incorpora el grup donador d'electrons metoxi a la seva estructura, és l'espècie que mostra més facilitat per oxidar-se i més dificultat per reduir-se. Per contra, la introducció d'àtoms acceptors d'electrons com el bromo a les posicions 3 i 6 del nucli carbazole (**33**) produeix un increment del potencial estàndard d'oxidació en comparació amb el radical Cbz-TTM. Cal destacar que els potencials estàndards d'oxidació depenen considerablement dels substituents del nucli carbazole, mentre que els potencials estàndard de reducció de tota la sèrie de derivats són molt similars, independentment de la substitució del carbazole, i molt propers al del radical TTM, suggerint que els potencials estàndard de reducció d'aquests adductes estan influenciats pel fragment TTM, però no pel grup carbazole. D'acord amb aquests resultats, els potencials d'ionització d'aquesta sèrie de radicals depenen de la naturalesa dels substituents del nucli carbazole i es troben en el rang de 5.7 a 6.0 eV, mentre que les afinitats electròniques tenen valors similars i propers a 4.4 eV. Els potencials d'ionització determinats en estat sòlid es troben en el rang de 5.6 a 5.9 eV i confirmen els resultats obtinguts per voltamperometria cíclica. Tots els

radicals presentats aquí presenten les condicions adients per actuar com a semiconductors ambipolars, ja que els dispositius que incorporen un sol component com a capa activa requereixen semiconductors amb potencials d'ionització superiors a 5.0 eV i afinitats electròniques superiors a 4.0 eV per tal d'aconseguir un transport de forats i d'electrons eficient i estabilitat a l'aire.

El transport de càrrega dels semiconductors **33–36** es va estudiar mitjançant la tècnica XTOF. Les capes del semiconductor orgànic es van dipositar per evaporació tèrmica al buit o bé per solució sobre un substrat de vidre recobert amb una capa d'alumini. La mesura d'aquestes mostres mitjançant la tècnica XTOF va permetre determinar mobilitats, tant d'electrons com de forats per a tota la sèrie de materials, en el rang de 10^{-7} a 10^{-2} $\text{cm}^2 \text{V}^{-1} \text{s}^{-1}$. Els valors de mobilitat més elevats corresponen als dispositius on el semiconductor orgànic es va dipositar per evaporació tèrmica al buit.

Es va observar un efecte considerable de la naturalesa dels substituents del nucli carbazole en les propietats de transport de càrrega dels materials preparats. La introducció de substituents acceptors d'electrons en el nucli carbazole afavoreix el transport de càrrega ambipolar, augmentant tant els valors de mobilitats d'electrons com de forats respecte el radical no substituït Cbz-TTM. En aquest sentit, s'ha de mencionar que el radical bromo derivat **33** presenta el major valor de mobilitat d'electrons de tota la sèrie de 1.7×10^{-2} $\text{cm}^2 \text{V}^{-1} \text{s}^{-1}$, sense perdre les propietats de transport de forats. Tenint en compte que els materials basats en el carbazole s'han definit normalment com a transportadors de forats, el transport d'electrons determinat pel radical Cbz-TTM i la sèrie de nous radicals presentada aquí, ha d'estar relacionat amb la presència del fragment radical TTM, que es pot reduir fàcilment i de forma reversible, com indiquen les voltamperometries cícliques.

L'augment de la capacitat donadora d'electrons del carbazole mitjançant la introducció dels grups metoxi a les posicions 3 i 6 en el radical **34** no ha donat lloc a variacions significatives dels valors de mobilitat de forats i d'electrons en comparació amb el radical no substituït Cbz-TTM. De fet, el radical **34** mostra mobilitats de forats i d'electrons lleugerament inferiors a les del Cbz-TTM. El derivat **35**, que incorpora el grup donador d'electrons tiofè en el nucli carbazole, presenta una mobilitat d'electrons elevada de 1.3×10^{-3} $\text{cm}^2 \text{V}^{-1} \text{s}^{-1}$, però una mobilitat d'electrons de només 7×10^{-7} $\text{cm}^2 \text{V}^{-1} \text{s}^{-1}$. Cal destacar que tots els radicals estudiats mostren un comportament ambipolar amb valors similars tant d'electrons com de forats, excepte el derivat **35**, que té una mobilitat d'electrons considerablement menor. Al contrari, l'extensió de la conjugació del carbazole amb el

grup feniletinil en el radical **36** va permetre obtenir un sistema ambipolar amb mobilitats de forats i electrons més similars inclús que en el cas del Cbz-TTM. Cal destacar que el radical **36** presenta el valor de mobilitat de forats més elevat de tota la sèrie, que és $3 \times 10^{-3} \text{ cm}^2 \text{ V}^{-1} \text{ s}^{-1}$.

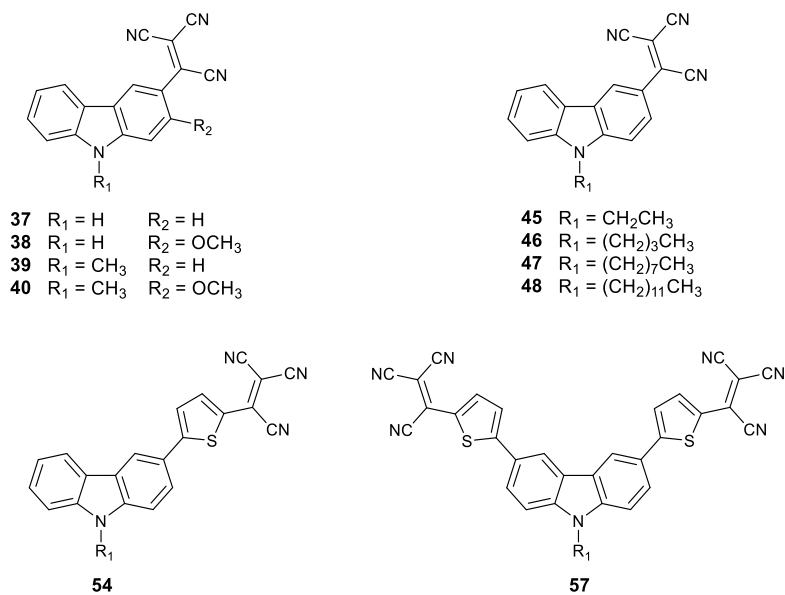
Aquests resultats suggereixen que la introducció de grups acceptors d'electrons, com en el cas del compost **33**, i l'extensió de la conjugació del nucli carbazole a través de les posicions 3 i 6, com en el cas del compost **36**, milloren les propietats de transport de forats i d'electrons respecte les del derivat no substituït Cbz-TTM.

Tenint en compte les propietats ambipolars de transport de càrrega dels radicals **33–36**, es van preparar fotoreceptors xerogràfics utilitzant aquests materials com a capa activa. Els dispositius basats en el bromo derivat **33** van mostrar els millors resultats, aconseguint una fotosensibilitat elevada en una àmplia regió de l'espectre òptic amb el màxim a 600 nm.

Capítol 3. Derivats del carbazole que incorporen el grup tricivanovinil com a semiconductors de tipus n i ambipolars

Mantenint l'objectiu d'obtenir nous semiconductors de tipus n o ambipolars, el Capítol 3 se centra en modificar les propietats de transport de forats característiques del carbazole mitjançant la introducció del grup acceptor d'electrons tricivanovinil. D'aquesta manera, es pretén obtenir sistemes de tipus *push-pull* amb una afinitat electrònica elevada. Al llarg d'aquest capítol s'han preparat tres sèries de tricivanovinil derivats i s'ha estudiat l'efecte dels substituents del carbazole en les seves propietats tèrmiques, òptiques, electroquímiques i de transport de càrrega (Esquema 5).

En primer lloc s'ha preparat una sèrie de tricivanovinil derivats (**37–40**) en què la capacitat donadora d'electrons del nucli carbazole s'ha modulada a través de la metilació del nitrogen i per la introducció en la posició 2 del grup donador d'electrons metoxi. En segon lloc, tenint en compte que la introducció de cadenes flexibles afecta en el tipus d'empaquetament molecular en l'estat sòlid i per tant pot influir en les propietats de transport de càrrega, s'ha dissenyat una segona sèrie de tricivanovinil derivats, els quals difereixen en la llargada de la cadena alquílica del nitrogen del carbazole (**45–48**), incloent les cadenes etil, butil, octil i dodecil. Per últim, s'ha considerat l'extensió del sistema conjugat del carbazole per introducció del grup tiofè com a pont conjugat entre el carbazole i el grup tricivanovinil (**54 i 57**) per tal d'afavorir el solapament orbitalic entre molècules veïnes i millorar el transport de càrrega.



Esquema 5. Estructura química dels tricivanil derivats **37–40**, **45–48**, **54** i **57**.

S'han determinat les estructures cristal·lines dels derivats **39**, **40** i **45–48** per difracció de raigs X de monocristall. Les molècules dels derivats **39** i **45–48** mostren una estructura gairebé planar formant un angle entre el carbazole i el grup tricivanil de 1.31–6.36°, mentre que el derivat metoxi-substituint **40** presenta un angle de 48.30°, degut a l'impediment estèric que causa el grup metoxi.

Aquesta família de tricivanil derivats mostra una elevada estabilitat tèrmica amb temperatures de descomposició superiors a 248 °C i una naturalesa cristal·lina, tal i com es deriva dels anàlisis de TGA i de DSC. Els espectres d'absorbància dels compostos **37–40** i **45–48** en clorur de metilè mostren una zona d'absorció a l'UV amb el màxim d'absorbància centrat al voltant de 290 nm, corresponent al nucli carbazole, i una segona banda d'absorció a la zona del visible centrada en el rang de 464 a 490 nm, que es pot atribuir al procés de transferència de càrrega intramolecular des del fragment donador d'electrons carbazole al grup acceptor d'electrons tricivanil. La introducció del grup ric en electrons tiofè entre el nucli carbazole i el grup tricivanil implica un desplaçament de la banda de transferència de càrrega a energies menors, de fins a 76 nm pel derivat **54**, indicant un augment de la conjugació del sistema. El fort caràcter donador-acceptor d'aquestes molècules permet el recobriment de la zona de l'UV i del visible de l'espectre electromagnètic.

Les voltamperometries cícliques per a aquestes sèries de compostos mostren dos processos de reducció, sent el primer quasi-reversible per a tots ells, i un procés d'oxidació irreversible. D'acord amb el major caràcter donador d'electrons del grup metoxi, els compostos **38** i **40** presenten valors d'afinitat electrònica i potencial d'ionització menors que els seus anàlegs no substituïts **37** i **39**. Els derivats *N*-alquilats **45–48** presenten un comportament idèntic al derivat metilat **39**. El compost **54** que incorpora el grup ric en electrons tiofè presenta un potencial d'oxidació inferior en comparació al compost **39**. Els potencials d'ionització i les afinitats electròniques es troben al voltant de 6.2–6.4 eV i 4.3–4.5 eV, respectivament, indicant que aquests compostos són candidats tant per al transport de forats com d'electrons.

Les propietats de transport de càrrega de les capes preparades per evaporació tèrmica al buit dels compostos **37–40** s'han analitzat mitjançant la tècnica *Time-of-Flight* (TOF). La introducció del grup acceptor d'electrons tricivanil en el nucli carbazole implica que s'observi transport d'electrons. Les capes basades en els derivats **37** i **39** només van mostrar transport d'electrons. El derivat *N*-metil **39** presenta el valor més alt de mobilitat d'electrons d'aquesta sèrie de $7.2 \times 10^{-4} \text{ cm}^2 \text{ V}^{-1} \text{ s}^{-1}$. Ara bé, cal destacar que la introducció del grup donador d'electrons metoxi en la posició *orto* respecte el grup tricivanil en els compostos **38** i **40** va permetre detectar tant transport d'electrons com de forats. El derivat alquilat **40** mostra valors de mobilitats d'electrons i de forats més similars entre ells de 9.3×10^{-5} i $2.4 \times 10^{-4} \text{ cm}^2 \text{ V}^{-1} \text{ s}^{-1}$, respectivament, que el seu anàleg no alquilat **38**.

Per tal d'intentar correlacionar les propietats de transport de càrrega determinades per la tècnica TOF per a la sèrie de compostos **37–40** es van realitzar càlculs teòrics DFT. En primer lloc, es van determinar les energies de reorganització per forats i electrons per als compostos **39** i **40**, tenint en compte la geometria que adopten en l'estat sòlid. Les energies de reorganització per a forats i electrons són similars pel que fa al compost metoxi substituït **40**, però difereixen considerablement pel compost **39**, apuntant a que el compost **40** pot presentar característiques de transport de càrrega més similars per forats i electrons.

Es van dur a terme càlculs teòrics per tal d'estimar les mobilitats dels compostos **39** i **40**. A partir de les corresponents estructures cristal·lines i tenint en compte les interaccions intermoleculares entre molècules veïnes, es van generar una sèrie de rutes possibles per al transport de les càrregues entre les molècules. Les rutes seleccionades van ser aquelles en què les molècules

mostren interaccions de tipus π - π , que són les que mostren interaccions intermoleculares més fortes, és a dir, energies d'interacció majors.

Les integrals d'acoblament calculades entre molècules veïnes pel compost **39** són superiors per electrons que per forats, indicant que pel compost **39** el transport d'electrons és afavorit en front del transport de forats. Per una altra banda, pel compost metoxi-substituint **40**, les integrals d'acoblament per a forats són superiors que per a electrons, indicant en aquest cas que el transport de forats està més afavorit. Ara bé, el compost **40** presenta valors d'acoblament electrònic per a forats entre molècules veïnes similars als obtinguts pel compost **39**. D'acord amb els resultats experimentals obtinguts per la tècnica TOF, el compost **39** no presenta mobilitat de forats, mentre que el compost **40** presenta mobilitats de forats superiors a les d'electrons. Per explicar aquest fenomen cal tenir en compte que els compostos **39** i **40** presenten una diferència important en les energies de reorganització de forats (64.4 vs 249 meV, respectivament) i que pel compost **39** s'observa una regió de Marcus invertida (*i.e.* $\lambda < \Delta G$) pel que fa a la mobilitat de forats. En aquest cas, la baixa energia de reorganització del compost **39** redueix la mobilitat de forats.

Les mobilitats de forats i d'electrons calculades per als compostos **39** i **40** corresponen a les determinades experimentalment a partir de les mesures de TOF. A partir de la tècnica TOF no es va poder determinar transport de forats per al compost **39**, mentre que per càlculs teòrics es va calcular una mobilitat de forats baixa de l'ordre de $10^{-6} \text{ cm}^2 \text{ V}^{-1} \text{ s}^{-1}$. Aquests resultats mostren que el transport de càrrega a través de les capes dels compostos **37-40** depèn considerablement de l'organització supramolecular, que està influenciada per la substitució amb el grup metoxi del carbazole en la posició *orto* respecte el grup tricivanil. De fet, el grup tricivanil en el compost **40** es troba fora del pla molecular degut a l'impediment estèric causat pel grup metoxi. Tenint en compte, a partir de la realització de càlculs teòrics, que l'HOMO es troba localitzat en el carbazole tant pel compost **39** com pel **40**, l'estructura no planar del derivat **40** implica interaccions cofacials entre els nuclis carbazole de molècules veïnes, mentre que pel compost **39** l'estructura planar mostra interaccions cofacials, però en què les molècules veïnes es troben lleugerament desplaçades. Des del punt de vista del transport de càrrega, els càlculs teòrics apunten a què la regió de Marcus invertida pel compost **39** podria explicar l'increment de la mobilitat de forats observada pel compost **40** en comparació amb el compost **39**. Per una altra banda, considerant que el LUMO es troba principalment localitzat en el grup tricivanil, es pot esperar un major solapament entre els orbitals LUMO de molècules veïnes pel compost planar **39** que pel **40**, ja que els grups tricivanil estan més propers en l'espai en el compost **39**. Aquesta característica es pot

corroborar amb els majors valors d'acoblament electrònic calculats per electrons pel compost **39** que per forats.

Les propietats de transport de càrrega dels compostos **39** i **45–48** es van estudiar mitjançant la fabricació i mesura de OTFTs. Els dispositius fabricats amb aquesta sèrie de compostos van presentar transport d'electrons i valors de mobilitat d'electrons molt similars en el rang de 9×10^{-6} a $5 \times 10^{-5} \text{ cm}^2 \text{ V}^{-1} \text{ s}^{-1}$, sense mostrar un efecte important de la mobilitat amb la llargada de la cadena alquílica. Per tal de correlacionar les propietats de transport de càrrega amb l'empaquetament molecular i ordre de les capes, s'han estudiat les capes semiconductoras per difracció de raigs X.

Primer cal dir que l'empaquetament molecular en aquesta sèrie de compostos depèn de la llargada de la cadena alquílica. Les molècules amb cadenes més curtes (**39**, **45** i **46**) adopten un empaquetament de tipus *herringbone*, mentre que les molècules amb les cadenes alquíliques més llargues (**47** i **48**) presenten interaccions de tipus cofacial. De totes maneres, cal destacar que per a tots els compostos, les molècules presenten interaccions de tipus π amb distàncies intermoleculares en el rang de 3.28 a 3.40 Å, les quals són adients per a un transport de càrrega eficient considerant el model de *hopping*. L'anàlisi dels difractogrames de raigs X d'incidència rasant de les capes dels compostos **39** i **45–48** indica, per una banda, que el tipus d'empaquetament molecular determinat per monocristall es correspon al de les capes, excepte pel derivat **39**. Per una altra banda, els resultats suggereixen que les molècules estan orientades amb la direcció de les interaccions π - π sent paral·lela a la superfície del substrat, disposició que es considera favorable per a un transport de càrrega òptim en OTFTs. Degut a què tots els compostos presenten interaccions de tipus π amb distàncies intermoleculares similars, controlades pel nucli carbazole i no per la cadena alquílica, aquesta sèrie de tricivanil derivats **39** i **45–48** presenta valors de mobilitats d'electrons comparables.

Els OTFTs basats amb els compostos **54** i **57**, que incorporen el grup tiofè com a pont conjugat entre el nucli carbazole i el grup tricivanil, van donar lloc a mobilitats d'electrons de l'ordre de $2\text{--}5 \times 10^{-5} \text{ cm}^2 \text{ V}^{-1} \text{ s}^{-1}$, que són similars a les obtingudes pel derivat **39**, que no conté el grup tiofè.

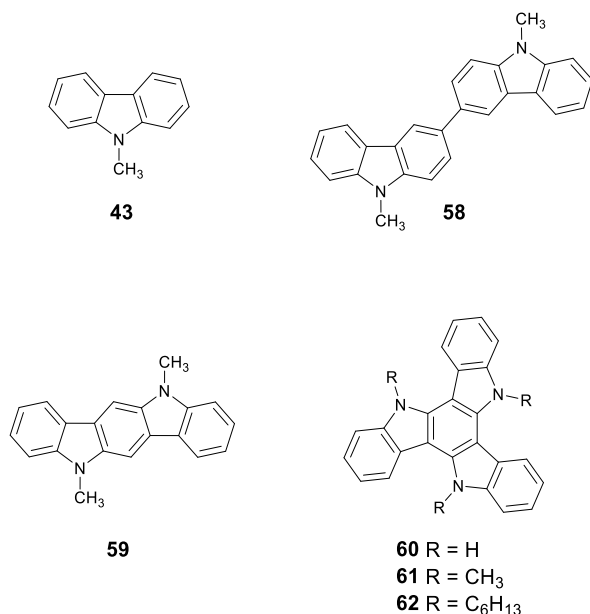
Capítol 4. Derivats del carbazole amb extensió del sistema conjugat com a capes actives en OTFTs de tipus p

Tot i que fins l'actualitat els OTFTs de tipus p han aconseguit un desenvolupament superior que els de tipus n o ambipolars, encara es requereixen nous materials transportadors de forats per tal de millorar les propietats dels OTFTs, com per exemple la seva estabilitat a l'aire. En aquest sentit, la selecció del nucli conjugat és clau, ja que permet modular les propietats òptiques i electròniques i inclús determinar la durabilitat i estabilitat a l'aire dels dispositius fabricats.

Aquest capítol es basa en l'estudi de les propietats de transport de càrrega d'una sèrie de derivats del carbazole que difereixen en l'extensió del sistema conjugat, incloent el nucli carbazole, el 3,3'-bicarbazole, l'indolo[3,2-*b*]carbazole i el triindole. L'indolo[3,2-*b*]carbazole i el triindole presenten sistemes de tipus π extensos en què dues o tres unitats de carbazole, respectivament, comparteixen un anell aromàtic. Durant els últims anys, els derivats de l'indolocarbazole han rebut una atenció especial en el camp de l'electrònica basada en materials orgànics, i alguns estudis recents han demostrat el gran potencial d'aquest tipus de materials com a capes actives en OTFTs.^[50c,131] Per una altra banda, el triindole presenta una estructura molecular major que la de l'indolocarbazole. Per tant, es pot esperar un ordre molecular superior i un transport de càrrega més eficient. Alguns derivats del triindole s'han estudiat com a capes actives i transportadores de forats en OLEDs i cel·les solars.^[130a,135-136] Les propietats de transport de càrrega del *N*-trimetiltriindole es troben descrites a la literatura mitjançant la tècnica *Space Charge Limited Current* (SCLC), donant lloc a mobilitats de forats en el rang de 1×10^{-4} a $1 \times 10^{-3} \text{ cm}^2 \text{ V}^{-1} \text{ s}^{-1}$.^[135]

La primera part d'aquest capítol s'ha centrat en l'estudi de les propietats de transport de càrrega d'aquesta sèrie de derivats del carbazole en OTFTs i la seva correlació amb l'ordre molecular de les capes semiconductor. Amb aquest objectiu en ment, s'han preparat els derivats 9-metil-9*H*-carbazole **43**, el 9,9'-dimetil-3,3'-bi-9*H*-carbazole **58**, el 5,11-dimetilindolo[3,2-*b*]carbazole **59** i el *N*-trimetiltriindole **61** (Esquema 6). A més, s'ha estudiat l'efecte de la llargada de la cadena alquíllica en els àtoms de nitrogen del nucli triindole en les propietats de transport de càrrega. Així, també s'han avaluat com a capes actives en OTFTs el triindole derivat no alquilat **60** i el *N*-trihexyltriindole **62**.

L'anàlisi de les propietats òptiques i electroquímiques van permetre determinar que els compostos **43** i **58-62** presenten potencials d'ionització alts i diferències energètiques entre els nivells HOMO i LUMO elevades, adients per als semiconductors de tipus p.



Esquema 6. Estructura química dels derivats del carbazole **43** i **58–62**.

Les propietats de transport de càrrega es van determinar utilitzant els materials orgànics preparats com a capes semiconductoras en OTFTs, en què la superfície del SiO₂ es va tractar prèviament al dipòsit del semiconductor orgànic amb poliestirè o bé amb octadeciltriclorosilà (OTS). Els derivats de l'indolocarbazole **59**, i del triindole **61** i **62**, que presenten un sistema π més extens que el carbazole o el bicarbazole, van presentar les millors propietats de transport de càrrega de tota la sèrie. Els OTFTs basats en l'indolocarbazole **59** i el *N*-trimetiltriindole **61** van mostrar els valors de mobilitat de forats més elevats en els dispositius tractats amb OTS, que van ser de fins a 8×10^{-2} i $6 \times 10^{-2} \text{ cm}^2 \text{ V}^{-1} \text{ s}^{-1}$, respectivament. En canvi, els OTFTs basats en el *N*-trihexiltriindole **62** van mostrar valors de mobilitat de forats més elevats al tractar la superfície del SiO₂ amb poliestirè, donant lloc a una mobilitat de fins a $0.1 \text{ cm}^2 \text{ V}^{-1} \text{ s}^{-1}$, que a més correspon al valor més alt determinat per a tota la sèrie. Cal destacar que tots els dispositius van mostrar una elevada durabilitat i estabilitat a l'aire durant períodes de fins a 5 mesos.

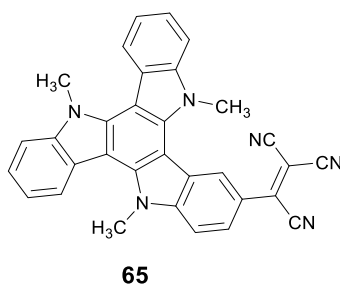
Els difractograms obtinguts per DRX d'incidència rasant indiquen que les capes primes preparades a partir dels compostos **59**, **61** i **62** són ordenades. Un anàlisi conjunt de l'estructura cristal·lina, el difractograma de raigs X del material en pols i els difractograms de raigs X de les capes primes fabricades ha permès determinar la disposició de les molècules dels compostos **59**, **61** i **62** a les capes semiconductoras dels OTFTs. Primer de tot cal dir que l'empaquetament molecular determinat per les capes correspon al determinat per DRX de monocristall. Per

l'indolocarbazole **59**, les molècules adopten un empaquetament de tipus *herringbone* amb interaccions intermoleculares de tipus C–H⋯ π . Les molècules es troben pràcticament perpendiculars respecte el substrat amb un angle de 68° mantenint l'empaquetament de tipus *herringbone*. L'estructura cristal·lina del *N*-trimetiltriindole **61** es troba descrita a la literatura.^[142] Les molècules presenten un empaquetament de tipus cofacial i mostren interaccions de tipus π – π entre les molècules de triindole adjacents. Cal destacar que a les capes, les molècules del triindole **61**, mantenint l'empaquetament de tipus cofacial, es troben totalment perpendiculars respecte la superfície del substrat, disposició que es considera favorable per a un transport de càrrega eficient en OTFTs. Pel compost *N*-trihexiltriindole **62**, les molècules presenten un empaquetament de tipus cofacial amb un lleuger desplaçament entre molècules veïnes i mostren no només interaccions de tipus π – π , sinó que també de tipus C–H⋯ π degut a la presència de la cadena *N*-hexil. A les capes, mantenint l'empaquetament de tipus cofacial, les molècules formen un cert angle respecte la superfície del substrat i estan orientades amb la direcció de les interaccions π – π sent paral·lela a la superfície del substrat. Per tant, les interaccions intermoleculares addicionals de tipus C–H⋯ π degudes a la cadena *N*-hexil afegides a les interaccions de tipus π – π entre els nuclis triindole, donen lloc a un augment de la mobilitat de fins a 0.1 cm² V⁻¹ s⁻¹.

Cal destacar que els *N*-metil derivats **59** i **61**, que presenten la cadena alquíllica més curta, mostren mobilitats majors en els dispositius tractats amb OTS, mentre que el derivat *N*-hexil **62**, amb la cadena alquíllica més llarga, presenta mobilitats majors en els dispositius tractats amb poliestirè. Aquests resultats suggereixen que la longitud de la cadena alquíllica del semiconductor orgànic té un efecte important en el creixement de la capa semiconductora i per tant en la morfologia i en el grau d'orientació de les capes segons el tractament de la superfície del dielèctric. En aquest sentit, els estudis de microscòpia de forces atòmiques (AFM) indiquen que el tractament de la superfície del SiO₂ amb poliestirè o amb OTS afecta el tamany i la forma dels grans, i els estudis de difracció de raigs X (DRX) també indiquen que afecta al grau d'ordenació de les capes.

En el Capítol 3, la introducció del grup tricivanil en el nucli carbazole va permetre obtenir materials de tipus n amb mobilitats d'electrons de l'ordre de 10⁻⁵ cm² V⁻¹ s⁻¹ en OTFTs. Degut a què els derivats del triindole mostren mobilitats de forats més elevades que els derivats del carbazole, es va considerar estudiar l'efecte de la introducció del grup tricivanil en el nucli triindole en les propietats de transport de càrrega. Amb aquest objectiu en ment, es va preparar el derivat **65** que incorpora el grup tricivanil en la posició 3 del triindole (Esquema 7). El compost **65** presenta una elevada estabilitat tèrmica. L'espectre d'absorbància del film corresponent mostra tres bandes

d'absorció amb màxims a 318, 448 i 615 nm. D'acord amb l'extensió de la conjugació en el triindole **65**, tant la banda d'absorció de la zona de l'UV com la de transferència de càrrega es troben desplaçades 20 nm i 143 nm, respectivament, a energies menors, en comparació amb el derivat del carbazole **39** que també conté el grup tricivaninil. Les voltamperometries cícliques indiquen que el compost **65** presenta un potencial estàndard de reducció de -1.07 V, que és similar al determinat pel derivat **39**, suggerint que els potencials de reducció estan influenciats pel fragment tricivaninil i no pel grup donador d'electrons carbazole o triindole. Per una altra banda, el potencial d'oxidació del compost **65** és inferior que pel compost **39**, d'acord amb el major caràcter donador d'electrons del triindole. En comparació amb el derivat *N*-trimetiltriindole **61**, el derivat **65** s'oxida menys fàcilment degut a la presència del grup acceptor d'electrons tricivaninil. El potencial d'ionització i l'afinitat electrònica per al compost **65** són 5.82 i 4.40 eV, respectivament, indicant el seu comportament potencial com a semiconductor ambipolar.



Esquema 7. Estructura química del tricivaninil derivat **65**.

Els OTFTs basats en el compost **65** només van presentar transport de forats, amb valors de mobilitat de forats de $1-2 \times 10^{-4} \text{ cm}^2 \text{ V}^{-1} \text{ s}^{-1}$. En contra de l'esperat a partir de l'anàlisi de les voltamperometries cícliques, els dispositius no van mostrar transport d'electrons com els tricivaninil derivats presentats en el Capítol 3. Aquests resultats suggereixen que el tipus d'empaquetament molecular en el compost **65** podria dificultar les interaccions entre els orbitals LUMO de molècules veïnes i per tant el transport d'electrons. De totes maneres cal realitzar més estudis, incloent estudis de difracció de raigs X i càlculs teòrics, per tal de confirmar aquesta hipòtesi.

Conclusions

S'han preparat tres sèries de materials basats en el carbazole que presenten emissió en la zona del blau de l'espectre. El triple enllaç entre el grup carbazole i les unitats donadores (fenil o tiofè) en els compostos **1–9** influeix en l'estructura molecular i en conseqüència en el corresponent empaquetament molecular i modula les propietats òptiques. L'extensió de la conjugació del sistema carbazole en els tricarbazoles **23** i **24**, mantenint els triples enllaços, així com en el bicarbazole **29**, va donar lloc a sistemes emissors en el blau de l'espectre electromagnètic en l'estat sòlid amb la coordenada CIE y sent inferior a 0.1. La introducció de grups alquil i voluminosos en l'àtom de nitrogen del nucli carbazole va donar lloc a materials moleculars amorfs. Aquesta família de compostos va mostrar propietats de transport de forats, amb mobilitats de forats de fins a $10^{-3} \text{ cm}^2 \text{ V}^{-1} \text{ s}^{-1}$. El dispositiu OLED basat en el compost **8** com a capa emissora va mostrar un potencial al qual comença a funcionar de només 4 V, una elevada luminància de fins a $1.4 \times 10^4 \text{ cd m}^{-2}$, i una eficiència de conversió dels excitons generats elèctricament en llum molt elevada del 45%.

S'han analitzat les propietats de transport de càrrega d'una sèrie de radicals neutres i estables basats en l'acoblament del radical tris(2,4,6-triclorofenil)metil, acceptor d'electrons, amb l'heterocicle carbazole, donador d'electrons, amb substituents de diferents característiques electròniques. L'extensió de la conjugació del nucli carbazole o la introducció de grups acceptors d'electrons ha conduït a valors de mobilitats de forats i d'electrons superiors respecte a les obtingudes prèviament pel derivat Cbz-TTM.

S'ha estudiat el transport de càrrega de tres sèries de derivats de tipus *push-pull* basats en el carbazole que contenen el grup acceptor d'electrons tricivanil. Tots els compostos mostren una alta estabilitat tèrmica i bandes d'absorció a la zona de l'UV i del visible de l'espectre electromagnètic. A més, tots els tricivanil derivats són candidats potencials per a actuar com a transportadors de forats i d'electrons segons les seves propietats electroquímiques. Les mesures de TOF i la fabricació i mesura de OTFTs confirmen que la substitució del nucli carbazole amb el grup acceptor d'electrons tricivanil és una estratègia efectiva per aconseguir materials transportadors d'electrons. Els compostos **38** i **40**, que incorporen el grup donador d'electrons metoxi en la posició *orto* respecte el grup tricivanil, van presentar propietats ambipolars, mentre que els derivats **37** i **39** només van mostrar transport d'electrons. L'anàlisi de les estructures cristal·lines conjuntament amb els càlculs teòrics realitzats suggereixen que les propietats de transport de càrrega de les capes d'aquesta sèrie de derivats està influenciada per l'organització

supramolecular. De fet, les molècules que incorporen el grup metoxi presenten una conformació no planar que afavoreix les propietats ambipolars. Els compostos **39** i **45–48**, que difereixen en la llargada de la cadena alquílica del nitrogen del nucli carbazole han presentat valors similars de mobilitats d'electrons en el rang de 9×10^{-6} a $5 \times 10^{-5} \text{ cm}^2 \text{ V}^{-1} \text{ s}^{-1}$ com a capes actives en OTFTs. Els estudis de difracció de raigs X indiquen que tots els compostos presenten interaccions de tipus π controlades pel nucli carbazole amb distàncies intermoleculares del mateix ordre, independentment de la llargada de la cadena alquílica, implicant que tota aquesta sèrie de tricivanovinil derivats presenti mobilitats d'electrons comparables. La introducció del grup tiofè com a pont conjugat entre el carbazole i el grup tricivanovinil ha donat lloc a mobilitats d'electrons similars pels dispositius basats en els compostos **54** i **57** respecte els basats en el compost **39**, que no conté el grup tiofè.

S'ha preparat una sèrie de derivats del carbazole que difereixen en l'extensió del sistema π . Els derivats del carbazole **43** i **58–62** presenten potencials d'ionització elevats i diferències energètiques entre els nivells HOMO i el LUMO elevades, indicant el seu potencial comportament com a capes transportadores de forats i estabilitat a l'aire. De totes maneres, només els materials **59**, **61** i **62**, amb sistemes π més extensos, presenten millors propietats de transport de càrrega. Cal destacar que els OTFTs fabricats amb aquests compostos mostren una elevada estabilitat i durabilitat a l'aire durant períodes de fins a 5 mesos, amb valors de mobilitat de forats en el rang de 10^{-3} a $0.1 \text{ cm}^2 \text{ V}^{-1} \text{ s}^{-1}$. L'indolocarbazole **59** presenta un empaquetament molecular de tipus *herringbone* amb interaccions de tipus $\text{CH}_3 \cdots \pi$. El triindole **61** presenta un empaquetament de tipus cofacial amb interaccions de tipus π - π . Cal destacar que les molècules d'aquest compost presenten una disposició òptima en les capes, ja que es troben completament perpendiculars respecte la superfície del substrat, tal i com mostren els estudis de DRX, cosa que pot afavorir el transport de càrrega. El compost **62** presenta també un empaquetament de tipus cofacial en què les molècules es troben lleugerament desplaçades, mostrant interaccions de tipus $\text{C-H} \cdots \pi$ causades per la cadena hexil addicional a les de tipus π - π entre els nuclis de triindole, que pot explicar les elevades mobilitats de forats obtingudes per als OTFTs basats en aquest compost, de $0.1 \text{ cm}^2 \text{ V}^{-1} \text{ s}^{-1}$. La introducció del grup tricivanovinil en el nucli triindole va permetre obtenir el derivat **65** substituït a la posició 3 del triindole. El compost **65** presenta una elevada estabilitat tèrmica i valors de potencials d'ionització i d'afinitat electrònica adients per tal d'actuar com a semiconductor ambipolar. Els OTFTs preparats amb el compost **65** van permetre mesurar mobilitats de forats, amb valors al voltant de $10^{-4} \text{ cm}^2 \text{ V}^{-1} \text{ s}^{-1}$.

LIST OF PUBLICATIONS

LIST OF PUBLICATIONS

Scientific publications

13. "A study of the properties, reactivity and antitumoral activity of novel *N*-methylated-3-thiazolyl or 3-thienyl carbazoles"
Org. Biomol. Chem., to be submitted on May 2017.
M. Reig, D. Velasco, R. Bosque, C. López, M. Font-Bardia, C. Calvis, R. Messeguer, L. Baldomà and J. Badía.
12. "Dependence of the *N*-alkyl chain length on the charge carrier mobility in a series of tricyanovinyl-substituted carbazole-based materials"
J. Mater. Chem. C, to be submitted on May 2017.
M. Reig, J. Puigdollers and D. Velasco.
11. "Twisted intramolecular charge transfer in a carbazole-based chromophore. The stable [(4-*N*-carbazolyl)-2,3,5,6-tetrachlorophenyl]bis(2,3,5,6-tetrachlorophenyl)methyl radical"
New Journal of Chemistry, submitted (Manuscript ID: NJ-ART-03-2017-000733).
A. Gilabert, L. Fajarí, I. Sirés, M. Reig, E. Brillas, D. Velasco, J. M. Anglada and L. Juliá.
10. "Tuning the ambipolar charge transport properties of tricyanovinyl-substituted carbazole-based materials"
Phys. Chem. Chem. Phys. **2017**, *19*, 6721–6730.
M. Reig, G. Bagdziunas, D. Volyniuk, J. V. Grazulevicius and D. Velasco.
9. "Easy accessible blue luminescent carbazole-based materials for Organic Light-Emitting Diodes"
Dyes Pigm. **2017**, *137*, 24–35.
M. Reig, C. Gozálviz, R. Bujaldón, G. Bagdziunas, K. Ivaniuk, N. Kostiv, D. Volyniuk, J. V. Grazulevicius and D. Velasco.
8. "Stable All-Organic Radicals with Ambipolar Charge Transport"
Chem. – Eur. J. **2016**, *22*, 18551–18558.
M. Reig, C. Gozálviz, V. Jankauskas, V. Gaidelis, J. V. Grazulevicius, L. Fajarí, L. Juliá and D. Velasco.

7. "New solution-processable carbazole derivatives as deep blue emitters for Organic Light-Emitting Diodes"
RSC Adv. **2016**, *6*, 9247–9253.
M. Reig, G. Bubniene, W. Cambarau, V. Jankauskas, V. Getautis, E. Palomares, E. Martínez-Ferrero and D. Velasco.
6. "Spatially Close Azo Dyes with Sub-Nanosecond Switching Speeds and Exceptional Temporal Resolution"
Chem. – Eur. J. **2015**, *21*, 14292–14296.
J. Garcia-Amorós, A. Cuadrado, M. Reig, V. D. Waele, O. Poizat and D. Velasco.
5. "Molecular order of air-stable p-type Organic Thin-Film Transistors by tuning the extension of the π -conjugated core: the cases of Indolo[3,2-*b*]carbazole and Triindole semiconductors"
J. Mater. Chem. C **2015**, *3*, 506–513. (*Inside cover*)
M. Reig, J. Puigdollers and D. Velasco.
4. "A photoswitchable bis-azo derivative with a high temporal resolution"
Chem. Commun. **2014**, *50*, 11462–11464.
J. Garcia-Amorós, M. Reig, A. Cuadrado, M. Ortega, S. Nonell and D. Velasco.
3. "Molecular photo-oscillators based on highly accelerated heterocyclic azo dyes in nematic liquid crystals"
Chem. Commun. **2014**, *50*, 6704–6706. (*Inside cover*)
J. Garcia-Amorós, M. Reig, M. Cidália R. Castro, A. Cuadrado, M. Manuela M. Raposo and D. Velasco.
2. "Charge Transfer States in Stable Neutral and Oxidized Radical Adducts from Carbazole Derivatives"
J. Org. Chem. **2014**, *79*, 1771–1777.
L. Fajarí, R. Papoular, M. Reig, E. Brillas, J. Jorda, O. Vallcorba, J. Rius, D. Velasco and L. Juliá.
1. "Fastest molecular photochromic switches based on nanosecond isomerising benzothiazolium azophenolic salts"
J. Mater. Chem. C **2014**, *2*, 474-480.
J. Garcia-Amorós, A. Bučinskas, M. Reig, S. Nonell and D. Velasco.

Poster presentations in conferences

15. "Amplification of the optical mechanotransducing abilities of carbazole-containing liquid crystal elastomers"
J. Garcia-Amorós, D. Heras, M. Reig and D. Velasco.
Liquid Crystals, Gordon Research Conference, University of New England, Biddeford, ME, 2017.
14. "Influence of the crystallinity of the organic thin film layer in OTFTs"
A. Cuadrado, R. Bujaldón, M. Reig and D. Velasco.
13th International Conference on Organic Electronics, Saint-Petersburg, Russia, 2017.
13. "p-Type Organic Thin-Film Transistors from indolo[3,2-b]carbazole and triindole as semiconductor active layers"
M. Reig, J. Puigdollers and D. Velasco.
7th International Conference on Molecular Electronics, Strasbourg, France, 2014.
12. "Emission wavelength dependence on solid media nature"
M. Reig and D. Velasco.
7th International Conference on Molecular Electronics, Strasbourg, France, 2014.
11. "Polysiloxane Liquid Single Crystal Elastomers: Flexible Substrates and Emitters"
M. Reig, C. Gozálviz, J. Garcia-Amorós, E. Martínez, L. Julià and D. Velasco.
Advanced Materials World Congress, AMWC 2013, Çeşme, Turkey, 2013.
10. "Air-Stable Organic Thin-Film Transistors based on fused carbazole units. Importance of the existence of a large π -conjugated core"
M. Reig, A. Marsal, J. Puigdollers and D. Velasco.
11th International Symposium on Functional π -Electron Systems, Arcachon (Bordeaux Area), Aquitaine, France, 2013.
9. "Double Fluorescence Carbazole Systems: UV and Red Emission from Solution to an Aggregated State"
M. Reig and D. Velasco.
11th International Symposium on Functional π -Electron Systems, Arcachon (Bordeaux Area), Aquitaine, France, 2013.

8. "Stable radical carbazole-TTM adducts as ambipolar charge carriers"
C. Gozávez, J. Neff, M. Reig, S. Galindo, C. Voz, J. Puigdollers, L. Julià and D. Velasco.
11th International Symposium on Functional π -Electron Systems, Arcachon (Bordeaux Area), Aquitaine, France, 2013.
7. "n-Type Organic Thin-Film Transistors based on a Push-Pull Carbazole System"
M. Reig, C. Gozávez, A. Marsal, J. Puigdollers, L. Julià and D. Velasco.
5th International Symposium on Flexible Organic Electronics, ISFOE 2012, Thessaloniki, Greece, 2012.
6. "Red-Emission from Charge Transfer States stabilized by Aggregation Processes in Dual Luminescent Carbazole Systems"
M. Reig, F. López-Calahorra and D. Velasco.
5th International Symposium on Flexible Organic Electronics, ISFOE 2012, Thessaloniki, Greece, 2012.
5. "Blue-emitting carbazole derivatives as possible active materials for OLEDs"
C. Gozávez, M. Reig, J. Garcia-Amorós and D. Velasco.
5th International Conference on Molecular Materials, MOLMAT 2012, Barcelona, Spain, 2012.
4. "Platinum(II) complexes derived from Carbazoles. A new step for the design of luminescent antitumoral agents"
M. Reig, D. Velasco and C. López.
11th International Symposium on Applied Bioinorganic Chemistry, ISABC 2011, Barcelona, Spain, 2011.
3. "Dual Luminescence of Push-Pull Carbazole Derivatives"
M. Reig, C. Gozávez, J. Garcia-Amorós and D. Velasco.
11th European Conference on Molecular Electronics, ECME 2011, Barcelona, Espanya, 2011.
2. "Easy accessible blue-emitting carbazole derivatives"
C. Gozávez, M. Reig, S. Cheylan, J. Garcia-Amorós and D. Velasco.
11th European Conference on Molecular Electronics, ECME 2011, Barcelona, Espanya, 2011.

1. “ β -substituted porphyrins derived from Hemin-IX as fluorescent molecules for organic light emitting devices”

J. Garcia-Amorós, M. Reig, S. Cheylan and D. Velasco.

IVth International Conference on Molecular Materials, MOLMAT 2010, Montpellier, France, 2010.

APPENDIX A

APPENDIX A

1. Figures

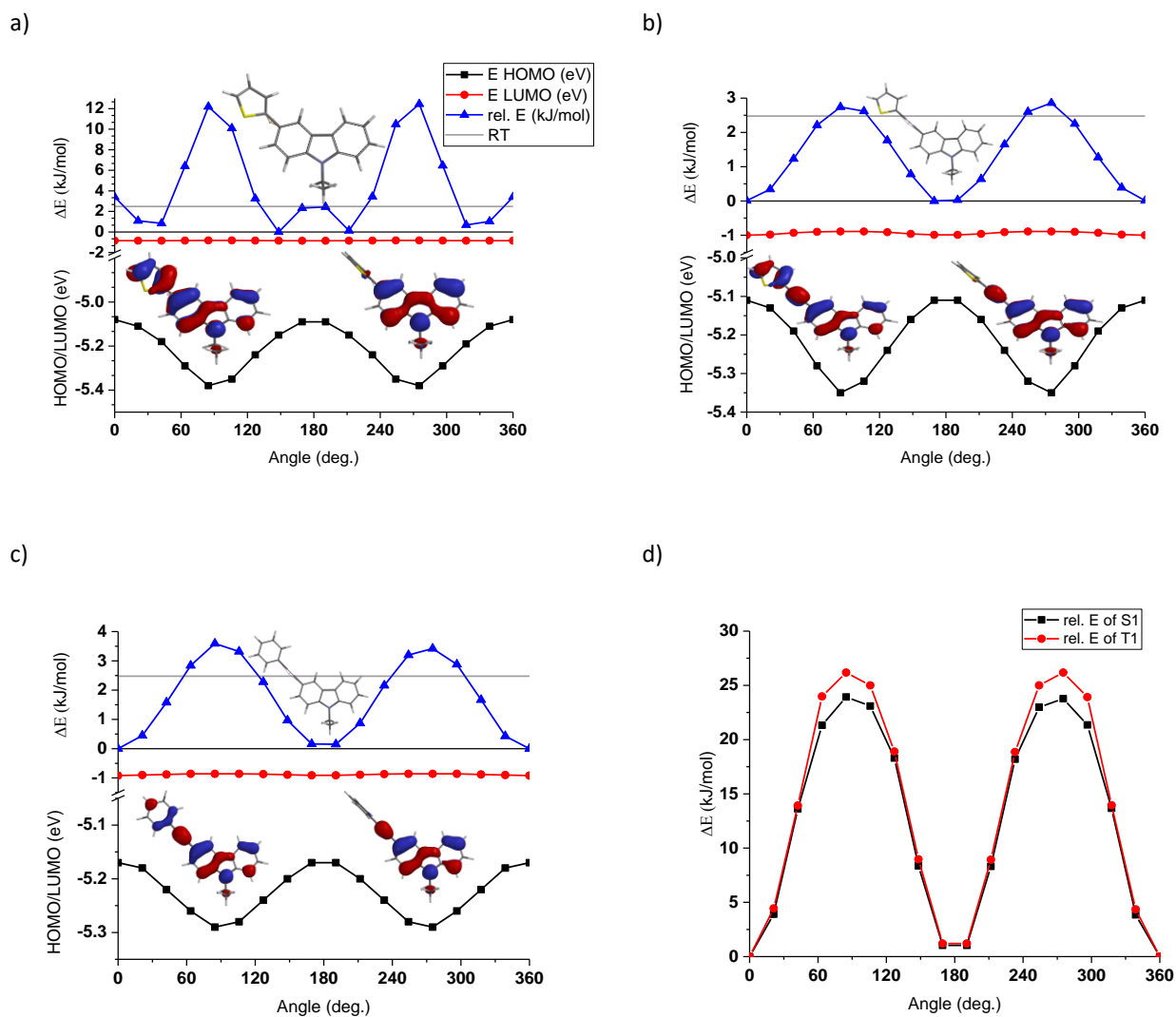


Figure A1. PES scans results of compounds a) **1**, b) **2** and c) **3** and snapshots of HOMO orbitals when the respective moieties are parallel (0 and 180°) and perpendicular (90 and 270°) to each other. Line of $k_B T$ energy is shown in grey. d) PES scans results of S_1 and T_1 excited states of **3**.

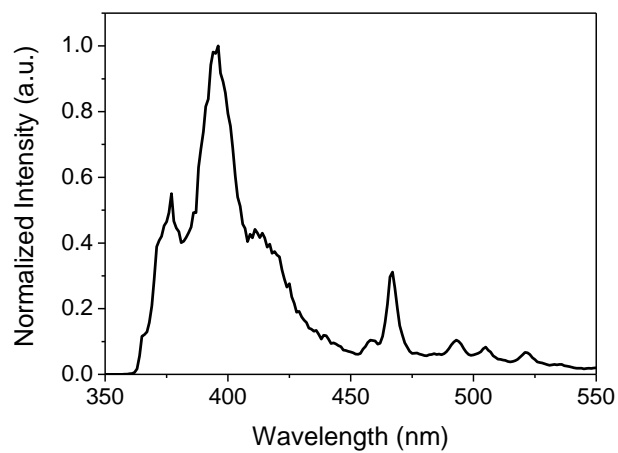


Figure A2. Phosphorescence spectrum of compound **8** recorded in THF at 10 μM at 77K.

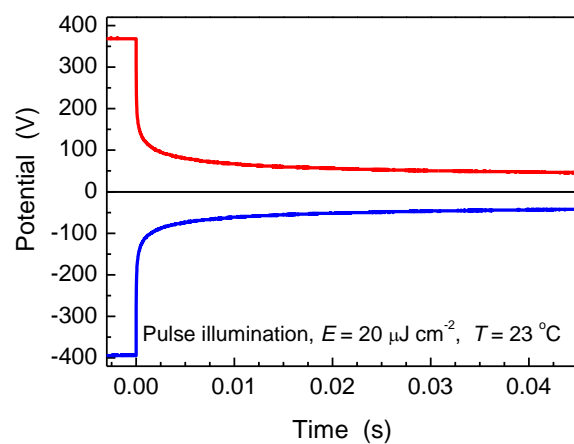


Figure A3. Discharge transients of the layer of **33**/PCZ (1:1) at positive and negative charging by pulse illumination.

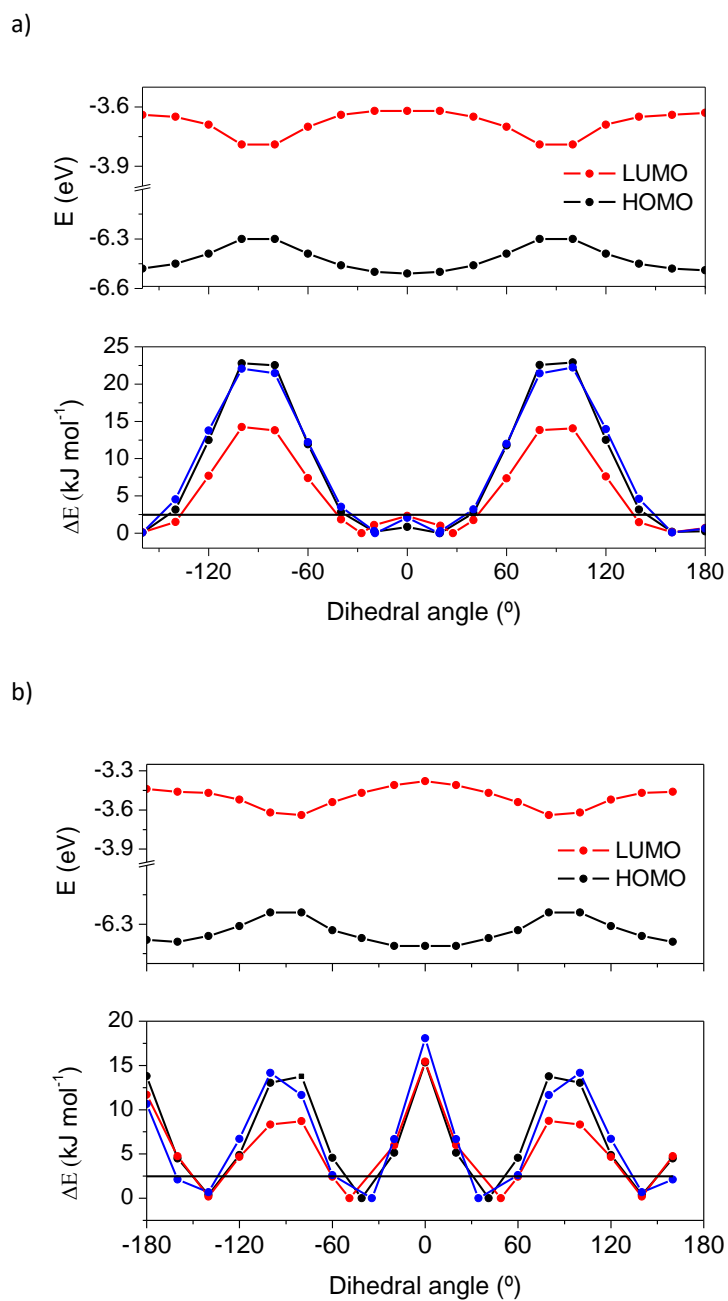


Figure A4. PES scans results of the neutral (black), cationic (red) and anionic (blue) states of molecules a) **39** and b) **40**. Line of $k_B T$ energy is shown in black.

- Possible carrier hopping pathways between molecules for **39** and **40** and intermolecular interactions (section 3.2 of Chapter 3)

The most effective carrier hopping pathways for compounds **39** and **40**, which were selected for the charge mobility calculations, are shown in Figure 3.8 of Chapter 3. However, other possible carrier hopping pathways between neighbouring molecules were also considered although they were finally removed from the modeling of mobility for the reasons mentioned below.

Adjacent molecules in pathway 2 of compound **39** from the crystal structure described here and the previously reported one^[123] are connected via electrostatic C–H...NC hydrogen bonding (Figures A5 and A6). They show the highest coupling integrals for holes and electrons, but they are relatively unstable (*i.e.* the interaction energies are -17.7 and -15.4 kJ mol⁻¹, respectively) and present a lower probability in the amorphous state (Table A1). Neighbouring molecules in pathway 3 are connected via four C–H...NC intermolecular bonds, showing higher stability than in pathway 2, but displaying the lowest coupling integrals, which do not exceed the values of 20 meV.

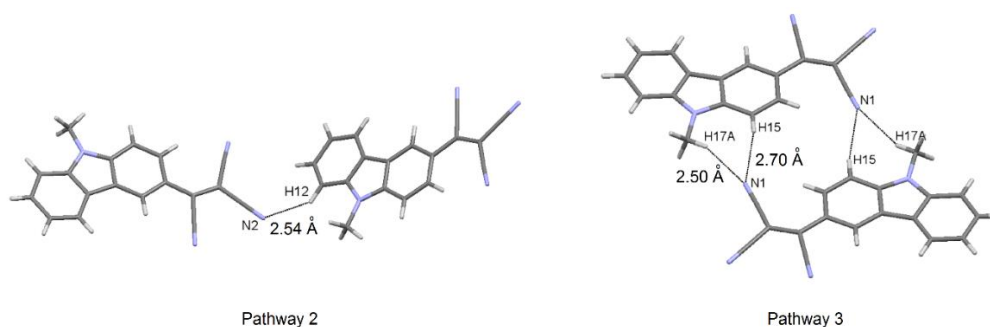


Figure A5. Possible carrier hopping pathways between neighbouring molecules and intermolecular interactions for the crystal structure of **39** reported here.

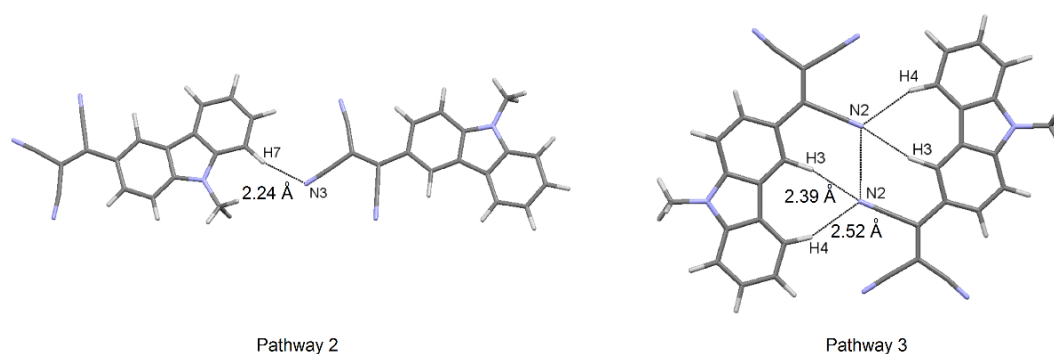


Figure A6. Possible carrier hopping pathways between neighbouring molecules and intermolecular interactions for the previously reported crystal structure^[123] of **39**.

For compound **40**, neighbouring molecules in pathway 3 are connected via dipole-dipole interactions between CN groups, whereas dimers 4 and 5 via C–H⋯NC hydrogen bonding (Figure A7). Pathways 3–5 of compound **40** were excluded for the charge mobility calculations because neighbouring molecules show lower interaction energies (-33.0 , -25.2 and -25.0 kJ mol $^{-1}$, respectively) than in pathways 1 and 2, together with very low probabilities, *i.e.* they do not exceed the value of 10^{-13} (Table A1).

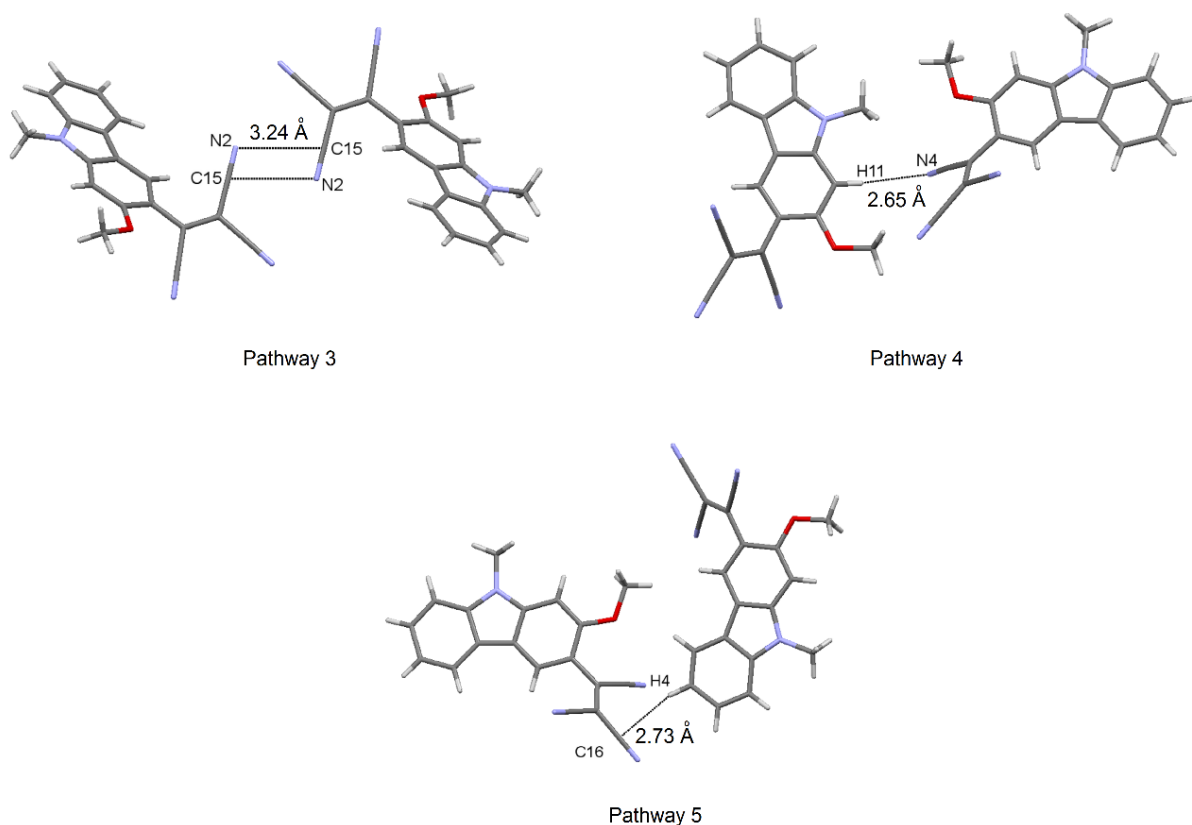


Figure A7. Possible carrier hopping pathways between neighbouring molecules and intermolecular interactions for the crystal structure of **40**.

2. Tables

Table A1. Theoretical calculation data of hole and electron mobilities of **39** and **40**. The data of the selected pathways for the calculation of charge carrier mobilities are shown in bold.

Compd.	Pathway	d(D–D) [d] (Å)	d(A–A) [d] (Å)	H_h [e] (meV)	H_e [e] (meV)	E_i [f] (kJ mol ⁻¹)	p_i [g]
39 ^[a]	1	7.56	3.42	47.4	140	-111	~1
	2	11.2	12.8	236	269	-17.7	4.1×10^{-17}
	3	8.11	7.90	8.7	8.5	-40.4	4.0×10^{-13}
39 ^[b]	1	5.07	4.81	83.2	166	-76.9	~1
	2	13.6	13.5	242	299	-15.4	1.7×10^{-11}
	3	11.0	7.56	6.9	12.9	-44.7	2.3×10^{-6}
40 ^[c]	1	4.60	8.32	63.1	21.8	-99.7	0.76
	2	3.87	9.84	121	8.4	-96.8	0.24
	3	13.6	9.58	26.3	88.5	-33.0	1.6×10^{-12}
	4	9.51	8.94	65.0	405	-25.2	6.8×10^{-14}
	5	10.3	8.56	16.8	38.3	-25.0	6.1×10^{-14}

[a] Data estimated from the here reported crystal structure of **39** ($\lambda_+ = 64.4$ meV, $\lambda_- = 310$ meV). [b] Data estimated from the previously reported crystal structure^[123] of **39**. [c] Data estimated from the crystal structure of **40** ($\lambda_+ = 249$ meV, $\lambda_- = 369$ meV). [d] Distance for pathway *i* between neighbouring donor-donor (D–D) for holes and acceptor-acceptor (A–A) moieties for electrons. [e] Coupling integrals for holes (H_h) and for electrons (H_e). [f] Interaction energy between neighbouring molecules. [g] Probability of charge migration.

